SPECTRAL DESCRIPTION OF LOW FREQUENCY OCEANIC VARIABILITY

by

Xiaoyun Zang
M.Sc., Massachusetts Institute of Technology
Woods Hole Oceanographic Institution, 1998
M.Sc., Institute of Atmospheric Physics, Academia Sinica, 1995
B.Sc., Nanjing Institute of Meteorology, 1992

Submitted to the Joint Program in Physical Oceanography
in partial fulfillment of the requirements for the degree of
Doctor of Philosophy in Physical Oceanography
at the
MASSACHUSETTS INSTITUTE OF TECHNOLOGY
and the
WOODS HOLE OCEANOGRAPHIC INSTITUTION
February 2000

Author .....
Joint Program in Physical Oceanography
Massachusetts Institute of Technology
Woods Hole Oceanographic Institution
February 25 2000

Certified by .....
Carl Wunsch
Cecil and Ida Green Professor of Physical Oceanography
Massachusetts Institute of Technology
Thesis Supervisor

Accepted by .....
Brechner Owens
Chairman, Joint Committee for Physical Oceanography
Massachusetts Institute of Technology
Woods Hole Oceanographic Institution

SPECTRAL DESCRIPTION OF LOW FREQUENCY OCEANIC VARIABILITY

by

Xiaoyun Zang

Submitted in partial fulfillment of the requirements for the degree of Doctor of Philosophy at the Massachusetts Institute of Technology
and the Woods Hole Oceanographic Institution
February 25 2000

Abstract

A simple dynamic model is used with various observations to provide an approximate spectral description of low frequency oceanic variability. Such a spectrum has wide application in oceanography, including the optimal design of observational strategy for the deployment of floats, the study of Lagrangian statistics and the estimate of uncertainty for heat content and mass flux. Analytic formulas for the frequency and wavenumber spectra of any physical variable, and for the cross spectra between any two different variables for each vertical mode of the simple dynamic model are derived. No heat transport exists in the model. No momentum flux exists either if the energy distribution is isotropic. It is found that all model spectra are related to each other through the frequency and wavenumber spectrum of the stream-function for each mode, $\Phi(k, l, \omega, n, \phi, \lambda)$, where (k, l) represent horizontal wavenumbers, ω stands for frequency, n is vertical mode number, and (ϕ, λ) are latitude and longitude, respectively. Given $\Phi(k, l, \omega, n, \phi, \lambda)$, any model spectrum can be estimated. In this study, an inverse problem is faced: $\Phi(k, l, \omega, n, \phi, \lambda)$ is unknown; however, some observational spectra are available. I want to estimate $\Phi(k, l, \omega, n, \phi, \lambda)$ if it exists.

Estimated spectra of the low frequency variability are derived from various measurements: (i) The vertical structure of and kinetic energy and potential energy is inferred from current meter and temperature mooring measurements, respectively. (ii) Satellite altimetry measurements produce the geographic distributions of surface kinetic energy magnitude and the frequency and wavenumber spectra of sea surface height. (iii) XBT measurements yield the temperature wavenumber spectra and their depth dependence. (v) Current meter and temperature mooring measurements provide the frequency spectra of horizontal velocities and temperature.

It is found that a simple form for $\Phi(k, l, \omega, n, \phi, \lambda)$ *does* exist and an analytical formula for a geographically varying $\Phi(k, l, \omega, n, \phi, \lambda)$ is constructed. Only the energy magnitude depends on location. The wavenumber spectral shape, frequency spectral shape and vertical mode structure are universal. This study shows that motion within the large-scale low-frequency spectral band is primarily governed by quasi-geostrophic dynamics and all observations can be simplified as a certain function of $\Phi(k, l, \omega, n, \phi, \lambda)$.

The low frequency variability is a broad-band process and Rossby waves are particular parts of it. Although they are an incomplete description of oceanic variability in the North Pacific, real oceanic motions with energy levels varying from about 10-40% of the total in each frequency band are indistinguishable from the simplest theoretical Rossby wave description. At higher latitudes, as the linear waves slow, they disappear altogether. Non-equatorial latitudes display some energy with frequencies too high for consistency with linear theory; this energy produces a positive bias if a lumped average westward phase speed is computed for all the motions present.

Thesis Supervisor: Carl Wunsch
Title: Cecil and Ida Green Professor of Physical Oceanography
Massachusetts Institute of Technology

Acknowledgments

First, I would like to thank my advisor, Carl Wunsch, for pointing out the topic of this thesis, giving me the freedom to pursue it independently, and generously exposing me to his own work. I am extremely grateful to him for the constructive criticism about my research and how to be a good scientist. His dedication to science inspires me to work harder. My sincere graditute goes to my thesis committee, Arthur Baggereor, Nelson Hogg, Ruixin Huang and Detlef Stammer for reading my thesis carefully and many valuable comments. Breck Owen kindly agreed to chair my thesis defense.

Many people at MIT and WHOI have made contributions to this work. In particular, I benefit greatly from the illuminating discussions with Glenn Flierl and Joe Pedlosky. Charmine King and Linda Meinke kindly help me with computing and data processing. The education office also provided me numerous assistance. Special thanks go to Wen Xu and Yanwu Zhang for discussions on signal processing and stochastic estimation.

I am indebted to my many fellow students: Francois Primeau, Juan Bottela, Galen Mckinley, Alex Ganachaud, Judith Wells, Albert Fisher, and Brian Arbic for their support and friendship.

Many friends at MIT gave me lots of personal helps, especially, Guangyu Fu and Weiran Xu, Jubao Zhang, Ji-yong Wang and Haiyan Zhang, Shi Jiang, Bingjin Ni, Yanqing Du, Yunfei Chen, Leslie Loo, Yijian Chen and Yuanlong Hu. Without their help, my life at MIT would have been much less colourful.

Last but certainly not least, I want to thank my wife, Bibo Lai, and my parents. Their love and support always accompany with me no matter where I am. Without their support, this thesis would not have been completed.

This work is supported financially by National Science Foundation through grants OCE-9529545, Jet Propulsion Laboratory, California Institute of Technology through contract 958125, and University of Texas-Austin through contract UTA-98-0222.

Contents

Chapter 1

Introduction

The general circulation of the ocean varies on all time and space scales. One of the main hindrances to understanding the climate change is the lack of a quantitative description of the natural variability of the ocean. This thesis is intended to produce a quantitative algebraic spectral description of low frequency oceanic variability. By the expression "low frequency variability", I mean the time-dependent motions with a time scale longer than the inertial period and shorter than a few years, and a spatial scale ranging from tens of km to thousands of km. Because the data used in this study typically span a few years, "very low frequency variability"—the decadal and even longer-period variability—is not considered here. Because of the strong inhomogeneity of eddy energy level, the wavenumber spectral representation is not a complete one for the basin scale in the ocean. However, in the open ocean away from major boundary currents, within the spatial scale of about 1000 km, the energy level does not change much with location, and the observed wavenumber spectra suggest that energy of time-dependent motions is dominated by motions with spatial scales of a few hundreds km. Therefore, the wavenumber spectral representation is still very useful within the scale of about 1000 km. Here I am only concerned with mesoscale eddies in the regions away from major currents and the equator. Such a spectral description has broad application. It allows one to describe the oceanic state concisely, to test the ocean general circulation model conveniently, to readily compare

theory with observations and to easily design observational strategy.

My method is analogous to that of Garrett and Munk (1972) applied to internal waves. Using linear dynamics under the hypothesis of spatial homogeneity, horizontal isotropy and vertical symmetry of the wave field, Garrett and Munk (1972) patched together a universal simple algebraic representation of the distribution of internal wave energy in wavenumber/frequency space in the deep ocean, which has become known as the Garrett-Munk spectrum. Later Garrett and Munk (1975) gave an improved version. The task for low frequency variability is much more difficult than the case for internal waves, because low frequency variability exhibits large geographical variations of energy level and strong anisotropy.

The general circulation of the ocean is a multi-dimensional and multi-variate process. In the last few decades, thanks to the advancement of measurement technology, oceanographers have obtained measurements for sea surface height, temperature, horizontal velocities, pressure, etc. at different places, depths and times. It is important to find out whether all these different data types can be related to each other. If so, this large amount of data can be described concisely. The fundamental idea of my work is summarized in figure 1-1. As displayed there, both the data and model provide estimates of the true oceanic state and each model spectrum is related to the others through the frequency and wavenumber spectrum of the stream-function for each mode, $\Phi(k, l, \omega, n, \phi, \lambda)$, where (k, l) are horizontal wavenumbers; ω is frequency; n represents vertical mode number; and (ϕ, λ) stand for latitude and longitude, respectively. Given $\Phi(k, l, \omega, n, \phi, \lambda)$, each model spectrum can be estimated and compared with the corresponding spectrum of observations. Here an inverse problem is faced: $\Phi(k, l, \omega, n, \phi, \lambda)$ is unknown and some observational spectra are available; I want to estimate $\Phi(k, l, \omega, n, \phi, \lambda)$ from the observations if $\Phi(k, l, \omega, n, \phi, \lambda)$ exists. We don't know, a priori, if there exists a simple form for $\Phi(k, l, \omega, n, \phi, \lambda)$. Because neither the data nor the model is a perfect representation of the true time-dependent motions in the ocean. The data are contaminated by instrument noises and aliased by

high frequency and small scale motions such as tides and internal waves. Moreover, the available data are short time series. Thus, the spectrum of the data is a biased estimate of the true spectrum of the underlying oceanic process. There are many drawbacks of my model as described in chapter 2. In my simple model, it is assumed that oceanic processes are linear and homogeneous in space; the background is at rest; there is no forcing and the depth of the ocean is uniform. None of these assumptions is true for the actual ocean. Therefore, it is unclear whether each spectrum of measurements is consistent with the corresponding model spectrum. If they are consistent, $\Phi(k, l, \omega, n, \phi, \lambda)$ will exist and all spectra of measurements can be simplified as a certain function of $\Phi(k, l, \omega, n, \phi, \lambda)$.

Assuming that the energy distribution is horizontally isotropic, Zang (1998) constructed a simple form for $\Phi(k, l, \omega, n, \phi, \lambda)$. A new version of the model is developed here without the assumption of isotropy. This thesis is made up of nine chapters. In chapter 2, a simple linearized model for low frequency variability is introduced and the solutions of the model are derived. Based on these solutions, analytic formulas for model spectra are obtained in chapter 3. In chapter 4, the observed properties of low frequency oceanic variability are presented. The emphasis is on answering the following questions: how is the low frequency variability energy distributed among horizontal wavenumber, direction, frequency, vertical mode and geography? and does there exist some kind of universal spectral description for low frequency variability in the ocean. In chapter 5, a simple analytic algebraic representation of $\Phi(k, l, \omega, n, \phi, \lambda)$ is constructed. Application of the spectrum is given in chapter 6. In chapter 7, a directional form of $\Phi(k, l, \omega, n, \phi, \lambda)$ is produced, which can differentiate westward-going energy from eastward-going energy. Chapter 8 presents the observed dispersion relationship for North Pacific Rossby wave motions. The conclusion and discussion are presented in chapter 9. In appendix A, the relationship between Rossby waves and topography is studied.

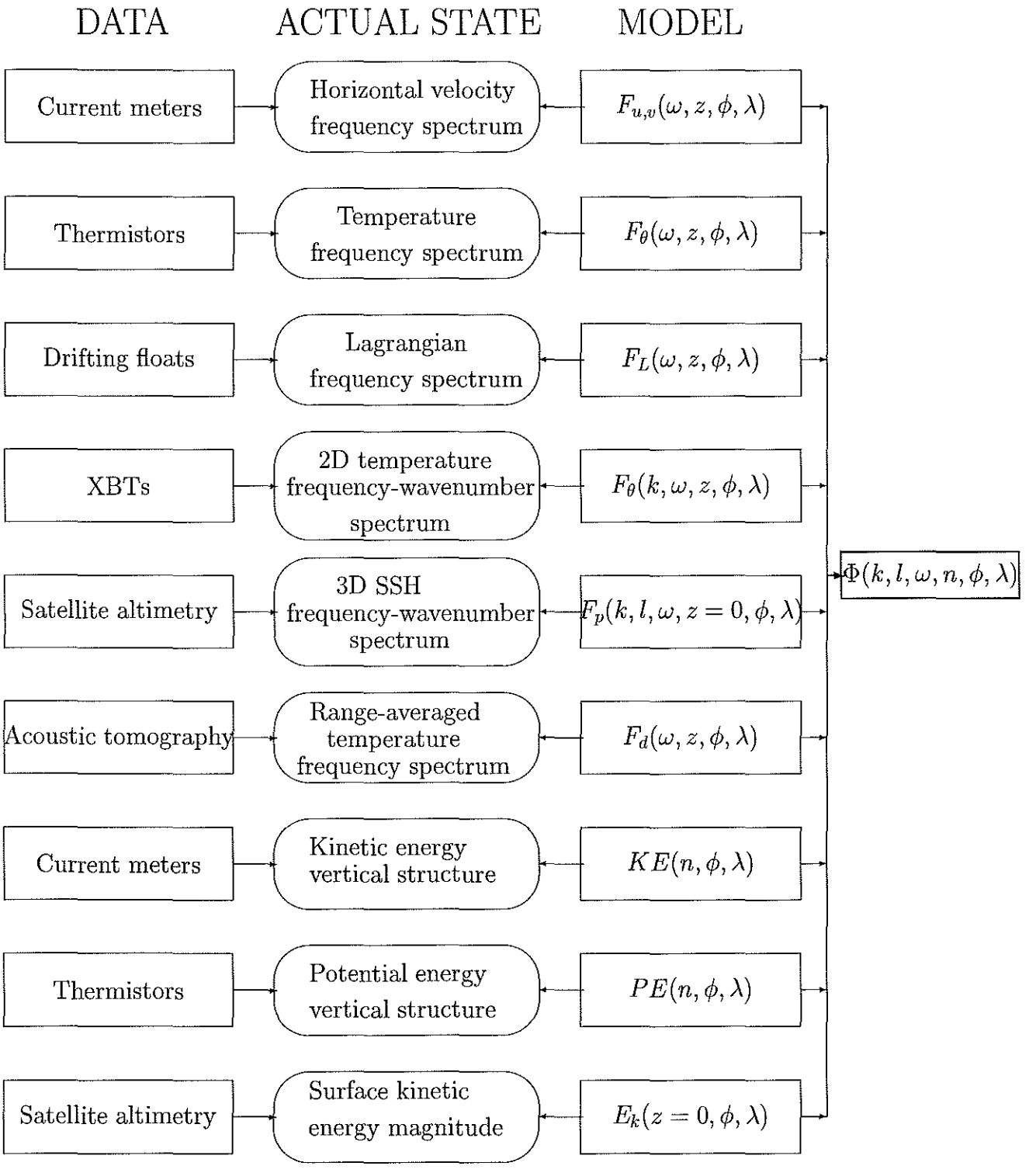

Figure 1-1: All measurements and models of the ocean are connected to each other through $\Phi(k, l, \omega, n, \phi, \lambda)$. Given $\Phi(k, l, \omega, n, \phi, \lambda)$, one can calculate all model spectra.

Chapter 2

Dynamic model for low frequency motion

2.1 The governing equations

Away from the equator and beneath the upper mixed layer, the time-dependent motions of the continuously stratified ocean can be described by the following standard linearized equations as a first-order approximation (e.g., Gill, 1982):

$$\frac{\partial u}{\partial t} - fv = -\frac{1}{\rho_0}\frac{\partial p}{\partial x}, \tag{2.1}$$

$$\frac{\partial v}{\partial t} + fu = -\frac{1}{\rho_0}\frac{\partial p}{\partial y}, \tag{2.2}$$

$$0 = -\frac{\partial p}{\partial z} - \rho g, \tag{2.3}$$

$$\frac{\partial \rho}{\partial t} + w\frac{\partial \rho_0(z)}{\partial z} = 0, \tag{2.4}$$

$$\frac{\partial u}{\partial x} + \frac{\partial v}{\partial y} + \frac{\partial w}{\partial z} = 0. \tag{2.5}$$

Here it is assumed that the mean velocities are zero, i.e., $u_0 = v_0 = w_0 = 0$. Equations (2.1) and (2.2) are the horizontal momentum equations; equation (2.3) is the hydrostatic equation; equation (2.4) is the density conservation equation and equation (2.5)

is the continuity equation. The variables u, v and w are the perturbation velocities; ρ is the perturbation density, p is the perturbation pressure; f is the Coriolis parameter and $\rho_0(z)$ is the density of the resting ocean. In the Boussinesq approximation, ρ_0 is treated as constant in equations (2.1) and (2.2). The dynamic effect of salinity variations has been simply neglected here. Because of the limitations of the data, the low frequency and large scale variations of salinity and their dynamic effect are still unclear. As discussed in detail by Pedlosky (1987), equations (2.1) to (2.5) are good representations of mesoscale eddies which have length scale of hundreds of km. For the motions with horizontal length scale comparable to or greater than the radius of the earth, spherical coordinates should be used instead and the horizontal variations of the basic density field cannot be ignored.

A single equation in p can be obtained from equation (2.1) to (2.5),

$$\left(\frac{\partial^2}{\partial t^2}+f^2\right)\left[\frac{\partial^3 p}{\partial x^2\partial t}+\frac{\partial^3 p}{\partial y^2\partial t}+(\frac{\partial^2}{\partial t^2}+f^2)\frac{\partial}{\partial z}(\frac{1}{N^2}\frac{\partial^2 p}{\partial z\partial t})\right]+\beta\left(f^2\frac{\partial p}{\partial x}-\frac{\partial^3 p}{\partial x\partial t^2}-2f\frac{\partial^2 p}{\partial y\partial t}\right)=0, \tag{2.6}$$

where

$$N^2(z)=-\frac{g}{\rho_0}\frac{\partial \rho}{\partial z}, \tag{2.7}$$

and

$$\beta=\frac{\partial f}{\partial y}. \tag{2.8}$$

Separating variables, Eq. (2.6) is,

$$p(x,y,z,t)=\sum_{n=0}^{n=+\infty} p_n(x,y,z,t)=\sum_{n=0}^{n=+\infty} P_n(x,y,t)F_n(z), \tag{2.9}$$

a sum over orthonormal vertical modes, with $F_n(z)$ satisfying,

$$\frac{d}{dz}\left(\frac{1}{N^2(z)}\frac{dF_n(z)}{dz}\right)=-r_n^2F_n(z), \tag{2.10}$$

where r_n^2 is a separation constant. The horizontal structure is governed by,

$$(\frac{\partial^2}{\partial t^2}+f^2)[\frac{\partial^3 P_n}{\partial x^2 \partial t}+\frac{\partial^3 P_n}{\partial y^2 \partial t}-r_n^2(\frac{\partial^2}{\partial t^2}+f^2)\frac{\partial P_n}{\partial t}]+\beta(f^2\frac{\partial P_n}{\partial x}-\frac{\partial^3 P_n}{\partial x \partial t^2}-2f\frac{\partial^2 P_n}{\partial y \partial t})=0. \tag{2.11}$$

Sometimes a second vertical structure function, $G_n(z)$ is useful. Define,

$$G_n(z)=\frac{1}{N^2(z)}\frac{dF_n(z)}{dz}. \tag{2.12}$$

where,

$$\frac{d^2 G_n(z)}{dz^2}+r_n^2 N^2(z) G_n(z)=0. \tag{2.13}$$

Eqs. (2.10, 2.13) are readily solved numerically. Analytic solutions to the vertical equation are available for a few forms of $N(z)$, including $N(z)$=constant, and the exponential profile,

$$N(z)=N_0 e^{az}, \tag{2.14}$$

(Garrett and Munk, 1972), which more closely resembles actual buoyancy profiles in the ocean. Following these authors, I will adopt (2.14) where $N_0 = 0.007$ s^{-1} and $a = 0.001$ m^{-1} in dimensional form, as a zero-order fit below about 1 km.

2.2 Vertical representation

In contrast to the internal wave case, observations strongly suggest the presence of vertical standing modes for low frequency variability. The rigid-lid upper and lower boundary conditions are used here:

$$w(z)=0,\ z=0,\ -h. \tag{2.15}$$

Or,

$$G_n(z)=0,\ z=0,\ -h. \tag{2.16}$$

In this study, I assume there is no topography and take h=4500 m.

The solution to equation (2.13) (Garrett and Munk, 1972) is

$$G_n(z) = A_n J_0(\frac{N_0 r_n}{a} e^{az}) + B_n Y_0(\frac{N_0 r_n}{a} e^{az}), \tag{2.17}$$

where $J_0(z)$, $Y_0(z)$ are the Bessel function of the first kind. Boundary conditions require

$$J_0(\xi_{-h})Y_0(\xi_0) - J_0(\xi_0)Y_0(\xi_{-h}) = 0, \tag{2.18}$$

and

$$B_n = \frac{J_0(N_0 r_n/a)}{Y_0(N_0 r_n/a)} A_n, \tag{2.19}$$

where,

$$\xi = \frac{N_0 r_n}{a} e^{az}, \qquad \xi_0 = \frac{N_0 r_n}{a}, \qquad \xi_{-h} = \frac{N_0 r_n}{a} e^{-ah}. \tag{2.20}$$

Mode No.	Eigenvalue (r_n)	gravity-wave phase speed (c_n)	Equivalent Depth (h_n)
0	0	∞	∞
1	0.402 (s/m)	2.48 (m/s)	63 (cm)
2	0.861 (s/m)	1.16 (m/s)	14 (cm)
3	1.319 (s/m)	0.76 (m/s)	6 (cm)

Table 2-1: Eigenvalue, gravity-wave phase speed and equivalent depth.

The first four eigenvalues, r_n, are listed in Table 2-1. The Rossby radius of deformation for the n-th mode can be obtained from r_n through

$$R_n = \frac{1}{f r_n}. \tag{2.21}$$

Chelton et al. (1998) computed the global $1° \times 1°$ climatologies of the first baroclinic gravity wave phase speed c_1 and the Rossby radius of deformation R_1 from climatological average temperature and salinity profiles. The value of c_1 ranges from about 1.5 m/s at high latitudes to 3.0 m/s near the equator. The geographical variability of R_1 is dominated by an inverse dependence on f. They also discussed the effects

of earth rotation, stratification, and water depth on c_n and R_n in terms of WKBJ approximation.

Substitution of equation (2.19) into (2.17) yields

$$G_n(z) = A_n W_n(z), \tag{2.22}$$

with

$$W_n(z) = J_0(\frac{N_0 r_n}{a} e^{az}) - \frac{J_0(N_0 r_n/a)}{Y_0(N_0 r_n/a)} Y_0(\frac{N_0 r_n}{a} e^{az}), \tag{2.23}$$

Also,

$$F_n(z) = -\frac{1}{r_n^2}\frac{dG_n}{dz} = -\frac{A_n}{r_n^2}\frac{dW_n(z)}{dz}. \tag{2.24}$$

Following custom, I normalize the vertical solution by setting

$$\int_{-h}^{0} F_n^2(z)dz = 1. \tag{2.25}$$

Substitution of equation (2.24) into equation (2.25) yields

$$\frac{A_n^2}{r_n^4}\int_{-h}^{0}(\frac{dW_n(z)}{dz})^2 dz = 1. \tag{2.26}$$

By using the properties of Bessel function (Abramowitz and Stegun, 1964), I obtain

$$\int_{-h}^{0}(\frac{dW_n(z)}{dz})^2 dz = ab_n, \tag{2.27}$$

where

$$b_n = \int_{\xi_{-1}}^{\xi_0} \xi\Gamma_n^2(\xi)d\xi = \frac{2}{\pi^2}[Y_0^{-2}(\xi_0) - Y_0^{-2}(\xi_{-1})]. \tag{2.28}$$

The vertical normalization yields

$$A_n = \frac{r_n^2}{\sqrt{ab_n}} \tag{2.29}$$

The normalized vertical eigenfunctions are

$$F_n(z) = \sqrt{\frac{1}{ab_n}}\frac{dW_n(z)}{dz} = N_0 r_n e^{az}\sqrt{\frac{1}{ac_n}}[\frac{J_0(\xi_0)}{Y_0(\xi_0)}Y_1(\xi) - J_1(\xi)], \tag{2.30}$$

$$G_n(z) = \frac{r_n^2}{\sqrt{ab_n}}W_n(z), \tag{2.31}$$

which satisfy the orthogonal conditions

$$\int_{-h}^{0} F_m(z)F_n(z)dz = \delta_{nm}, \tag{2.32}$$

$$\int_{-h}^{0} N^2(z)G_m(z)G_n(z)dz = r_n^2\delta_{nm}. \tag{2.33}$$

where δ_{nm} is the Kronecker delta function. Note that the units of $F_n(z)$ and $G_n(z)$ are $\mathrm{m}^{-1/2}$ and $\mathrm{s}^2\mathrm{m}^{-3/2}$, respectively. The normalized vertical eigenfunctions $F_n(z)$ and $G_n(z)$ are plotted in figure 2-1 for n=0 to 3. An important property in figure 2-1 is the near–surface intensification of $F_n(z)$ for n=1 to 3. Because the vertical structure of the horizontal kinetic energy is proportional to $F_n^2(z)$, the vertical structure of baroclinic horizontal kinetic energy will correspondingly show a near–surface intensification.

2.3 Horizontally propagating waves

The horizontal structure of each mode is represented in the form of propagating waves:

$$P_n(x,y,t) = \int_{-\infty}^{+\infty}\int_{-\infty}^{+\infty}\int_{-\infty}^{+\infty}\tilde{p}(k,l,\omega,n)e^{i2\pi(kx+ly-\omega t)}dkdld\omega, \tag{2.34}$$

where (k,l) stand for horizontal wavenumber; and ω represents frequency. In order to compare with the measurements readily, the cyclical frequencies and wavenumbers are used here. The units of cyclical frequencies and wavenumbers are cycles per day and cycles per kilometer, respectively. Substitution of equation (2.34) into (2.11)

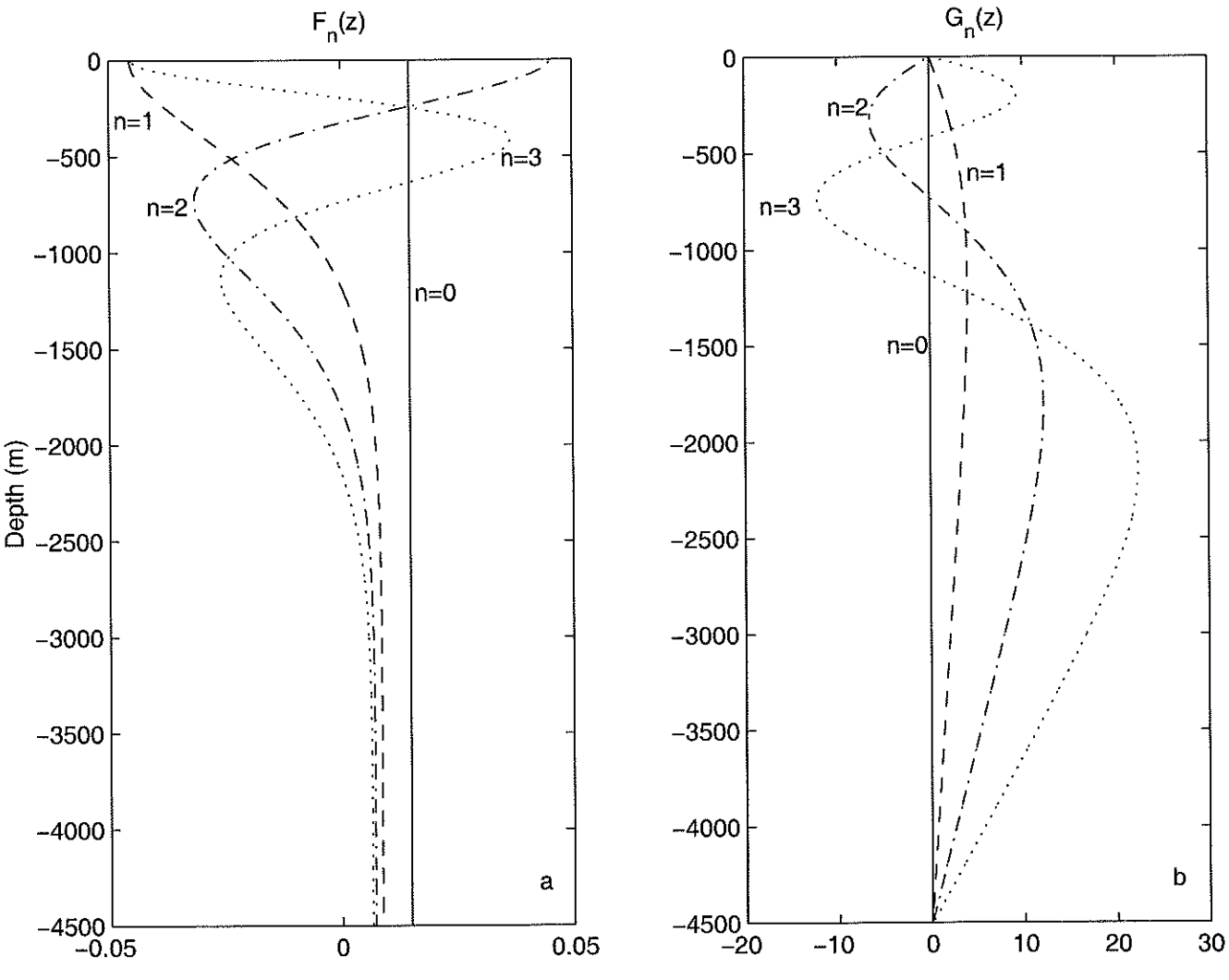

Figure 2-1: The vertical eigenfunctions $F_n(z)$ and $G_n(z)$ for modes n=0 to 3.

yields the dispersion relation

$$2\pi\omega(f^2-(2\pi\omega)^2)[(2\pi k)^2+(2\pi l)^2+r_n^2(f^2-(2\pi\omega)^2)]+\beta([(f^2-(2\pi\omega)^2)2\pi k+8\pi^2 fl\omega]=0. \tag{2.35}$$

For low frequency, $2\pi\omega << f$, equation (2.35) can be simplified as

$$\omega[(2\pi k)^2+(2\pi l)^2+f^2r_n^2]+\beta k=0. \tag{2.36}$$

For any given mode at a fixed latitude, there is a maximum frequency (shortest period) for planetary waves given by

$$\omega_{n-max}=\frac{\beta R_n}{4\pi}. \tag{2.37}$$

Recall that the vertical structure of the pressure for each mode is represented by the function $F_n(z)$. Therefore, the full solution for each mode in pressure is

$$p_n(x,y,z,t)=\int_{-\infty}^{+\infty}\int_{-\infty}^{+\infty}\int_{-\infty}^{+\infty}[\tilde{p}(k,l,\omega,n)F_n(z)e^{i2\pi(kx+ly-\omega t)}]dkdld\omega. \tag{2.38}$$

The low frequency oceanic variability is a broad-band process and consists of Rossby waves, eddies, etc. Rossby waves are particular parts of it in that the frequency and wavenumber of Rossby waves must satisfy the dispersion relation, equation (2.36). The full solution for Rossby waves for each mode in pressure is

$$p_{n_r}(x,y,z,t)=\int_{-\infty}^{+\infty}\int_{-\infty}^{+\infty}\int_{-\infty}^{+\infty}[\tilde{p}(k,l,\omega,n)F_n(z)\delta(\omega-\frac{\beta k}{(2\pi k)^2+(2\pi l)^2+f^2r_n^2})e^{i2\pi(kx+ly-\omega t)}]dkdld\omega, \tag{2.39}$$

where δ is the delta function.

For low frequency variability, the horizontal momentum equations can be approximated by the geostrophic relations:

$$fv=\frac{1}{\rho_0}\frac{\partial p}{\partial x}, \tag{2.40}$$

$$fu = -\frac{1}{\rho_0}\frac{\partial p}{\partial y}. \tag{2.41}$$

So the complete wave solutions for the horizontal velocities for each mode are

$$u_n(x,y,z,t) = -\int_{-\infty}^{+\infty}\int_{-\infty}^{+\infty}\int_{-\infty}^{+\infty}\left[\frac{i2\pi l\tilde{p}(k,l,\omega,n)F_n(z)}{\rho_0 f}\right]e^{i2\pi(kx+ly-\omega t)}dkdld\omega, \tag{2.42}$$

$$v_n(x,y,z,t) = \int_{-\infty}^{+\infty}\int_{-\infty}^{+\infty}\int_{-\infty}^{+\infty}\left[\frac{i2\pi k\tilde{p}(k,l,\omega,n)F_n(z)}{\rho_0 f}\right]e^{i2\pi(kx+ly-\omega t)}dkdld\omega. \tag{2.43}$$

The solutions for the density and vertical velocity can be derived from the hydrostatic equation and the density conservation equation. The complete wave solutions for the density and vertical velocity are

$$\rho_n(x,y,z,t) = -\int_{-\infty}^{+\infty}\int_{-\infty}^{+\infty}\int_{-\infty}^{+\infty}\left[\frac{\tilde{p}(k,l,\omega,n)N^2(z)G_n(z)}{g}\right]e^{i2\pi(kx+ly-\omega t)}dkdld\omega, \tag{2.44}$$

$$w_n(x,y,z,t) = \int_{-\infty}^{+\infty}\int_{-\infty}^{+\infty}\int_{-\infty}^{+\infty}\left[\frac{i2\pi\omega\tilde{p}(k,l,\omega,n)G_n(z)}{\rho_0}\right]e^{i2\pi(kx+ly-\omega t)}dkdld\omega. \tag{2.45}$$

One frequently used variable, the vertical displacement ζ, is related to the vertical velocity through

$$w = \frac{\partial\zeta}{\partial t}. \tag{2.46}$$

Equation (2.46) yields the solution for each mode in vertical displacement

$$\zeta_n(x,y,z,t) = \int_{-\infty}^{+\infty}\int_{-\infty}^{+\infty}\int_{-\infty}^{+\infty}-\left[\frac{\tilde{p}(k,l,\omega,n)G_n(z)}{\rho_0}\right]e^{i2\pi(kx+ly-\omega t)}dkdld\omega, \tag{2.47}$$

The vertical displacement is not directly measured in the real ocean but is inferred from temperature time series by

$$\zeta(x,y,z,t) = -\frac{\theta(x,y,z,t)}{\partial\theta_0/\partial z}. \tag{2.48}$$

From equation (2.48), the solution for each mode in temperature can be derived

$$\theta_n(x,y,z,t) = \int_{-\infty}^{+\infty}\int_{-\infty}^{+\infty}\int_{-\infty}^{+\infty}\left[\frac{\tilde{p}(k,l,\omega,n)G_n(z)}{\rho_0}\frac{\partial\theta_0}{\partial z}\right]e^{i2\pi(kx+ly-\omega t)}dkdld\omega. \tag{2.49}$$

As shown in equation (2.48), the temperature variations in my model are attributed only to the vertical advection of the mean vertical temperature profile. Therefore, my model cannot represent sea surface temperature changes because of the rigid-lid approximation. It cannot be applied to the mixed layer either. In the mixed layer, horizontal advection, mixing and atmospheric thermal forcing play an important role in the temperature changes.

2.4 Summary

In this chapter, a simple dynamic model is introduced and analytic solutions to the model are obtained. For simplification, define

$$\tilde{\psi}(k,l,\omega,n) = \frac{\tilde{p}(k,l,\omega,n)}{\rho_0 f}, \tag{2.50}$$

which represents the Fourier transform of the stream-function for each mode. If the signal is real, $\tilde{\psi}^*(k,l,\omega,n) = \tilde{\psi}(-k,-l,-\omega,n)$, where * stands for complex conjugate. The solutions for each mode can be summarized as

$$p_n(x,y,z,t) = \int_{-\infty}^{+\infty}\int_{-\infty}^{+\infty}\int_{-\infty}^{+\infty}\tilde{\psi}(k,l,\omega,n)p_a(k,l,\omega,z,n)e^{i2\pi(kx+ly-\omega t)}dkdld\omega, \tag{2.51}$$

$$u_n(x,y,z,t) = \int_{-\infty}^{+\infty}\int_{-\infty}^{+\infty}\int_{-\infty}^{+\infty}\tilde{\psi}(k,l,\omega,n)u_a(k,l,\omega,z,n)e^{i2\pi(kx+ly-\omega t)}dkdld\omega, \tag{2.52}$$

$$v_n(x,y,z,t) = \int_{-\infty}^{+\infty}\int_{-\infty}^{+\infty}\int_{-\infty}^{+\infty}\tilde{\psi}(k,l,\omega,n)v_a(k,l,\omega,z,n)e^{i2\pi(kx+ly-\omega t)}dkdld\omega, \tag{2.53}$$

$$w_n(x,y,z,t) = \int_{-\infty}^{+\infty}\int_{-\infty}^{+\infty}\int_{-\infty}^{+\infty}\tilde{\psi}(k,l,\omega,n)w_a(k,l,\omega,z,n)e^{i2\pi(kx+ly-\omega t)}dkdld\omega, \tag{2.54}$$

$$\rho_n(x,y,z,t) = \int_{-\infty}^{+\infty}\int_{-\infty}^{+\infty}\int_{-\infty}^{+\infty}\tilde{\psi}(k,l,\omega,n)\rho_a(k,l,\omega,z,n)e^{i2\pi(kx+ly-\omega t)}dkdld\omega, \tag{2.55}$$

$$\zeta_n(x,y,z,t) = \int_{-\infty}^{+\infty}\int_{-\infty}^{+\infty}\int_{-\infty}^{+\infty}\tilde{\psi}(k,l,\omega,n)\zeta_a(k,l,\omega,z,n)e^{i2\pi(kx+ly-\omega t)}dkdld\omega, \tag{2.56}$$

$$\theta_n(x,y,z,t) = \int_{-\infty}^{+\infty}\int_{-\infty}^{+\infty}\int_{-\infty}^{+\infty}\tilde{\psi}(k,l,\omega,n)\theta_a(k,l,\omega,z,n)e^{i2\pi(kx+ly-\omega t)}dkdld\omega, \tag{2.57}$$

where I have defined

$$p_a(k,l,\omega,z,n) = \rho_0 f F_n(z), \tag{2.58}$$

$$u_a(k,l,\omega,z,n) = -i2\pi l F_n(z), \tag{2.59}$$

$$v_a(k,l,\omega,z,n) = i2\pi k F_n(z), \tag{2.60}$$

$$w_a(k,l,\omega,z,n) = i2\pi\omega f G_n(z), \tag{2.61}$$

$$\rho_a(k,l,\omega,z,n) = -\frac{\rho_0 f}{g} N^2(z) G_n(z), \tag{2.62}$$

$$\zeta_a(k,l,\omega,z,n) = -f G_n(z), \tag{2.63}$$

$$\theta_a(k,l,\omega,z,n) = f\frac{\partial\theta_0}{\partial z} G_n(z). \tag{2.64}$$

Chapter 3

Spectra of the model

In chapter 2, a simple dynamic model is introduced and the solutions to it are derived. In this chapter, I will obtain the analytic formulas for the frequency and wavenumber spectra of horizontal velocities, pressure, sea surface height, temperature, etc. for each mode based on the solutions obtained in chapter 2. The formula for the frequency spectrum of the range–averaged temperature from tomographic data will also be derived. The frequency and horizontal wavenumber spectra to be obtained in this chapter are for **each mode**. In chapter 5, I will compare the model spectrum with the corresponding observations by adding up the contributions from the first few important modes.

3.1 Covariance

Let $h(x, y, z, t, n)$ represent the solution to the model for the n-th mode, where $h(x, y, z, t, n)$ is any one of the dependent variables $u_n(x, y, z, t)$, $v_n(x, y, z, t)$, etc., which can be written as

$$h(x,y,z,t,n) = \int_{-\infty}^{+\infty}\int_{-\infty}^{+\infty}\int_{-\infty}^{+\infty}\tilde{\psi}(k,l,\omega,n)h_a(k,l,\omega,z,n)e^{i2\pi(kx+ly-\omega t)}dkdld\omega, \quad (3.1)$$

where the characteristic factor $h_a(k,l,\omega,z,n)$ correspondingly stands for any of the variables $u_a(k,l,\omega,z,n)$, $v_a(k,l,\omega,z,n)$, etc.

For a spatially homogeneous and temporally stationary process,

$$< \tilde{\psi}(k,l,\omega,n)\tilde{\psi}^*(k^{'},l^{'},\omega^{'},n) >= \delta(k^{'}-k)\delta(l^{'}-l)\delta(\omega^{'}-\omega) < |\tilde{\psi}(k,l,\omega,n)|^2 > . \quad (3.2)$$

where the angle bracket represents ensemble average. Define

$$\Phi(k,l,\omega,n) =< |\tilde{\psi}(k,l,\omega,n)|^2 >, \quad (3.3)$$

which is the three-dimensional frequency and wavenumber spectrum of the stream-function for each vertical mode. For a real signal, $\Phi(-k,-l,-\omega,n) = \Phi(k,l,\omega,n)$. For a spatially homogeneous and temporally stationary process, the auto-covariance function of $h(x,y,z,t,n)$ is

$$R_h(r_x,r_y,\tau,z,n) = \int_{-\infty}^{+\infty}\int_{-\infty}^{+\infty}\int_{-\infty}^{+\infty} h_a(k,l,\omega,z,n)h_a^*(k,l,\omega,z,n)\Phi(k,l,\omega,n)e^{-i2\pi(kr_x+lr_y-\omega\tau)}dkdld\omega. \quad (3.4)$$

Define another variable $s(x,y,z,t,n)$, which is different from $h(x,y,z,t,n)$, to be the solution to the model, then $s(x,y,z,t,n)$ can be written as

$$s(x,y,z,t,n) = \int_{-\infty}^{+\infty}\int_{-\infty}^{+\infty}\int_{-\infty}^{+\infty} \tilde{\psi}(k,l,\omega,n)s_a(k,l,\omega,z,n)e^{i2\pi(kx+ly-\omega t)}dkdld\omega. \quad (3.5)$$

By definition, the cross-covariance function between $h(x,y,z,t,n)$ and $s(x,y,z,t,n)$ for a homogeneous and stationary process can be written as

$$R_{hs}(r_x,r_y,\tau,z,n) = \int_{-\infty}^{+\infty}\int_{-\infty}^{+\infty}\int_{-\infty}^{+\infty} h_a(k,l,\omega,z,n)s_a^*(k,l,\omega,z,n)\Phi(k,l,\omega,n)e^{-i2\pi(kr_x+lr_y-\omega\tau)}dkdld\omega. \quad (3.6)$$

3.2 Three-dimensional spectra

The three-dimensional spectra for u, v, etc. for each mode are

$$\Upsilon_{p,u,v,w,\rho,\theta,\zeta}(k,l,\omega,n,z) = [|p_a|^2, |u_a|^2, |v_a|^2, |w_a|^2, |\rho_a|^2, |\theta_a|^2, |\zeta_a|^2]\Phi(k,l,\omega,n). \quad (3.7)$$

If the full three-dimensional spectrum of any variable for each mode is known, one can estimate $\Phi(k,l,\omega,n)$ through equation (3.7). For example, given the three-dimensional spectrum of pressure for each mode, $\Phi(k,l,\omega,n)$ can be obtained through

$$\Phi(k,l,\omega,n) = \frac{\Upsilon_p(k,l,\omega,n,z)}{|p_a(k,l,\omega,n,z)|^2}. \quad (3.8)$$

The reader is reminded the function $p_a(k,l,\omega,n,z)$ is defined in equation (2.58). The full three-dimensional spectra of each mode are very hard to obtain for low frequency oceanic variability. TOPEX/POSEIDON altimeter data provide nearly simultaneous observations of global sea surface height every 9.91 days, from which one can obtain the three-dimensional spectrum of sea surface elevation. Pressure perturbations at sea surface are related to sea elevation changes through (Wunsch and Stammer, 1998)

$$P(x,y,z=0,t) = g\rho\eta(x,y,t). \quad (3.9)$$

One thus can infer the three-dimensional spectrum of the pressure perturbations at sea surface. However, the vertical structure of pressure is unclear. Besides satellite measurements, a sparse array of current meter and acoustic moorings can yield estimates of directional spectra. Munk (unpublished manuscript, 1988) showed how to get a handle on the directional wave energy distribution by interpreting the cross-spectra of travel times of acoustic transmissions.

3.3 Two-dimensional spectra

The k, l-spectra

The two-dimensional (k, l) spectra for u, v, etc. for each mode are

$$\Upsilon_{u,v,p,\theta,\zeta}(k,l,n,z) = \int_{-\infty}^{+\infty}[|u_a|^2, |v_a|^2, |p_a|^2, |\theta_a|^2, |\zeta_a|^2]\Phi(k,l,\omega,n)d\omega. \quad (3.10)$$

The k, ω-spectra

The two-dimensional (k, ω) spectra for u, v, etc. for each mode are

$$\Upsilon_{u,v,p,\theta,\zeta}(k,\omega,n,z) = \int_{-\infty}^{+\infty}[|u_a|^2, |v_a|^2, |p_a|^2, |\theta_a|^2, |\zeta_a|^2]\Phi(k,l,\omega,n)dl. \quad (3.11)$$

The l, ω-spectra

The two-dimensional (l, ω) spectra for u, v, etc. for each mode are

$$\Upsilon_{u,v,p,\theta,\eta}(l,\omega,n,z) = \int_{-\infty}^{+\infty}[|u_a|^2, |v_a|^2, |p_a|^2, |\theta_a|^2, |\eta_a|^2]\Phi(k,l,\omega,n)dk. \quad (3.12)$$

Two-dimensional spectra in the ocean can be obtained from a few repeated XBT lines and alongtrack altimeter data.

3.4 One-dimensional spectra

ω-spectra

The one-dimensional frequency spectra for u, v, etc. for each mode are

$$\Upsilon_{u,v,p,\theta,\zeta}(\omega,n,z) = \int_{-\infty}^{+\infty}\int_{-\infty}^{+\infty}[|u_a|^2, |v_a|^2, |p_a|^2, |\theta_a|^2, |\zeta_a|^2]\Phi(k,l,\omega,n)dkdl. \quad (3.13)$$

The one-dimensional frequency spectra of u, v are related to the three-dimensional spectra of pressure through

$$\Upsilon_{u,v}(\omega,n,z) = \int_{-\infty}^{+\infty}\int_{-\infty}^{+\infty}\left[\frac{\Upsilon_p(k,l,\omega,n,z)(2\pi l)^2}{f^2\rho_0^2}, \frac{\Upsilon_p(k,l,\omega,n,z)(2\pi k)^2}{f^2\rho_0^2}\right] dkdl. \quad (3.14)$$

k-spectra

The one-dimensional zonal-wavenumber spectra for u, v, etc., for each mode are

$$\Upsilon_{u,v,p,\theta,\zeta}(k,n,z) = \int_{-\infty}^{+\infty}\int_{-\infty}^{+\infty}[|u_a|^2, |v_a|^2, |p_a|^2, |\theta_a|^2, |\zeta_a|^2]\Phi(k,l,\omega,n)dld\omega. \quad (3.15)$$

l-spectra

The one-dimensional meridional-wavenumber spectra for each mode are

$$\Upsilon_{u,v,p,\theta,\zeta}(l,n,z) = \int_{-\infty}^{+\infty}\int_{-\infty}^{+\infty}[|u_a|^2, |v_a|^2, |p_a|^2, |\theta_a|^2, |\zeta_a|^2]\Phi(k,l,\omega,n)dkd\omega. \quad (3.16)$$

Given the three-dimensional spectrum of pressure, one can calculate the wavenumber spectrum of velocity through

$$\Upsilon_{u,v}(k,n,z) = \int_{-\infty}^{+\infty}\int_{-\infty}^{+\infty}\left[\frac{\Upsilon_p(k,l,\omega,n,z)(2\pi l)^2}{f^2\rho_0^2}, \frac{\Upsilon_p(k,l,\omega,n,z)(2\pi k)^2}{f^2\rho_0^2}\right] dld\omega, \quad (3.17)$$

and

$$\Upsilon_{u,v}(l,n,z) = \int_{-\infty}^{+\infty}\int_{-\infty}^{+\infty}\left[\frac{\Upsilon_p(k,l,\omega,n,z)(2\pi l)^2}{f^2\rho_0^2}, \frac{\Upsilon_p(k,l,\omega,n,z)(2\pi k)^2}{f^2\rho_0^2}\right] dkd\omega. \quad (3.18)$$

3.5 Horizontal coherence

For two points at the same depth separated horizontally by a vector

$$\vec{R} = \vec{X}_j - \vec{X}_i = (r_x, r_y), \quad (3.19)$$

the cross spectrum between $h(x,y,z,t,n)$ and $s(x+r_x, y+r_y, z, t, n)$ at these two points is

$$\Upsilon_{hs}(r_x, r_y, \omega, z, n) = \int_{-\infty}^{+\infty}\int_{-\infty}^{+\infty} h_a(k,l,\omega,n,z)s_a^*(k,l,\omega,n,z)\Phi(k,l,\omega,n)e^{-i(kr_x+lr_y)}dkdl. \quad (3.20)$$

By definition, the coherence is

$$C_{hs}(r_x, r_y, \omega, z, n) = \frac{\int_{-\infty}^{+\infty}\int_{-\infty}^{+\infty} h_a s_a^* \Phi(k,l,\omega,n) e^{-i(kr_x+lr_y)} dkdl}{\sqrt{\int_{-\infty}^{+\infty}\int_{-\infty}^{+\infty} |h_a|^2 \Phi(k,l,\omega,n) dkdl \int_{-\infty}^{+\infty}\int_{-\infty}^{+\infty} |s_a|^2 \Phi(k,l,\omega,n) dkdl}}. \tag{3.21}$$

If the horizontal separation is zero, the cross spectrum becomes

$$\Upsilon_{hs}(0,0,\omega,z,n) = \int_{-\infty}^{+\infty}\int_{-\infty}^{+\infty} h_a(k,l,\omega,n,z) s_a^*(k,l,\omega,n,z) \Phi(k,l,\omega,n) dkdl. \tag{3.22}$$

Substitution of h and s with u, v and θ into the above equation gives

$$\Upsilon_{uv}(0,0,\omega,z,n) = \int_{-\infty}^{+\infty}\int_{-\infty}^{+\infty} u_a(k,l,\omega,n,z) v_a^*(k,l,\omega,n,z) \Psi(k,l,\omega,n) dkdl, \tag{3.23}$$

$$\Upsilon_{u\theta}(0,0,\omega,z,n) = \int_{-\infty}^{+\infty}\int_{-\infty}^{+\infty} u_a(k,l,\omega,n,z) \theta_a^*(k,l,\omega,n,z) \Phi(k,l,\omega,n) dkdl, \tag{3.24}$$

$$\Upsilon_{v\theta}(0,0,\omega,z,n) = \int_{-\infty}^{+\infty}\int_{-\infty}^{+\infty} v_a(k,l,\omega,n,z) \theta_a^*(k,l,\omega,n,z) \Phi(k,l,\omega,n) dkdl. \tag{3.25}$$

Because $u_a(k,l,\omega,n,z)$ is an odd function of l; $v_a(k,l,\omega,n,z)$ is an odd function of k; $\theta(k,l,\omega,n,z)$ is independent of k; and l and $\Phi(k,l,\omega,n) = \Phi(-k,-l,-\omega,n)$, it is easy to prove that

$$\Upsilon_{u\theta}(0,0,\omega,z,n) = \Upsilon_{v\theta}(0,0,\omega,z,n) = 0, \tag{3.26}$$

$$C_{u\theta}(0,0,\omega,z,n) = C_{v\theta}(0,0,\omega,z,n) = 0. \tag{3.27}$$

3.6 Energy level

kinetic energy

The kinetic energy for each mode at depth z is

$$E_k(n,z) = \frac{1}{2}[< |u_n(x,y,z,t)|^2 > + < |v_n(x,y,z,t)|^2 >]$$

$$= \frac{1}{2}\int_{-\infty}^{+\infty}\int_{-\infty}^{+\infty}\int_{-\infty}^{+\infty}(|u_a|^2+|v_a|^2)\Phi(k,l,\omega,n)dkdld\omega, \qquad (3.28)$$

and the kinetic energy per unit surface area for each mode is

$$\begin{aligned} KE(n) &= \int_{-h}^{0} E_k(n,z)dz \\ &= \frac{1}{2}\int_{-\infty}^{+\infty}\int_{-\infty}^{+\infty}\int_{-\infty}^{+\infty}\int_{-h}^{0}(|u_a|^2+|v_a|^2)\Phi(k,l,\omega,n)dzdkdld\omega. \end{aligned} \qquad (3.29)$$

potential energy

The potential energy per unit surface area for each mode is

$$\begin{aligned} PE(n) &= \frac{1}{2}\int_{-h}^{0} N^2(z) < |\zeta_n(x,y,z,t)|^2 > dz \\ &= \frac{1}{2}\int_{-\infty}^{+\infty}\int_{-\infty}^{+\infty}\int_{-\infty}^{+\infty}\int_{-h}^{0} N^2|\zeta_a|^2\Phi(k,l,\omega,n)dzdkdld\omega. \end{aligned} \qquad (3.30)$$

temperature variance

Since potential energy is inferred from the temperature perturbation, the temperature variance is frequently used as a substitute for potential energy. The temperature variance for each mode at depth z is:

$$\sigma_\theta^2(n,z) = \int_{-\infty}^{+\infty}\int_{-\infty}^{+\infty}\int_{-\infty}^{+\infty}|\theta_a|^2\Phi(k,l,\omega,n)dkdld\omega. \qquad (3.31)$$

total energy

The total energy per unit surface area for each mode is

$$\begin{aligned} TE(n) &= KE(n)+PE(n) \\ &= \frac{1}{2}\int_{-\infty}^{+\infty}\int_{-\infty}^{+\infty}\int_{-\infty}^{+\infty}\int_{-h}^{0}(|u_a|^2+|v_a|^2+N^2|\zeta_a|^2)\Phi(k,l,\omega,n)dkdld\omega. \end{aligned} \qquad (3.32)$$

3.7 Heat and momentum transport

By definition, the heat transport of each mode at depth z can be written as

$$\begin{aligned} < u_n\theta_n >= R_{u\theta}(0,0,0,n,z) &= \int_{-\infty}^{+\infty}\int_{-\infty}^{+\infty}\int_{-\infty}^{+\infty} u_a(k,l,\omega,n,z)\theta_a^*(k,l,\omega,n,z)\Phi(k,l,\omega,n)dkdld\omega \\ &= \int_{-\infty}^{+\infty} \Upsilon_{u\theta}(0,0,\omega,z,n)d\omega, \end{aligned} \tag{3.33}$$

$$\begin{aligned} < v_n\theta_n >= R_{v\theta}(0,0,0,n,z) &= \int_{-\infty}^{+\infty}\int_{-\infty}^{+\infty}\int_{-\infty}^{+\infty} v_a(k,l,\omega,n,z)\theta_a^*(k,l,\omega,n,z)\Phi(k,l,\omega,n)dkdld\omega \\ &= \int_{-\infty}^{+\infty} \Upsilon_{v\theta}(0,0,\omega,z,n)d\omega. \end{aligned} \tag{3.34}$$

Substitution of equation (3.26) into equation (3.33) and (3.34) yields

$$< u_n\theta_n >=< v_n\theta_n >= 0. \tag{3.35}$$

There is no heat transport for the simple linear dynamic model with a flat bottom because two components of horizontal velocity and temperature are in spatial quadrature.

The momentum transport is

$$\begin{aligned} < u_nv_n >= R_{uv}(0,0,0,n,z) &= \int_{-\infty}^{+\infty}\int_{-\infty}^{+\infty}\int_{-\infty}^{+\infty} u_a(k,l,\omega,n,z)v_a^*(k,l,\omega,n,z)\Phi(k,l,\omega,n)dkdld\omega \\ &= -F_n^2(z)\int_{-\infty}^{+\infty}\int_{-\infty}^{+\infty}\int_{-\infty}^{+\infty} 4\pi^2 kl\Phi(k,l,\omega,n)dkdld\omega. \end{aligned} \tag{3.36}$$

If $\Phi(k,l,\omega,n)$ is isotropic, the momentum transport $< u_nv_n >$ is zero because k and l are odd functions.

3.8 Acoustic tomography data

Most of the data types we use measure velocity or temperature, etc. at a point. Tomographic data differ in that they integrate spatially through the ocean thus fil-

tering out high wavenumbers. Assuming that a preliminary inversion of the data has been done, tomographic observations are reduced to a purely horizontal average of temperature at fixed depths (Munk et al., 1996).

Suppose the acoustic ray path is along the east-west direction and the equivalent horizontal tomographic path length is L. Then it is readily shown that the frequency spectral density of the tomographic temperature average is

$$\Upsilon_d(\omega, z, n) = \int_{-\infty}^{+\infty}\int_{-\infty}^{+\infty} \theta_a \theta_a^* \Phi(k, l, \omega, n) W(k, L) dk dl. \tag{3.37}$$

where

$$W(k, L) = \frac{sin^2(\pi k L)}{(\pi k L)^2} \tag{3.38}$$

represents the spatial filtering.

Equation (3.37) suggests that tomographic measurements filter out short waves along the direction of acoustic ray path and have no effect on the waves propagating perpendicular to the acoustic ray path. Therefore, one can estimate the directional property of the energy density $\Phi(k, l, \omega, n)$ by comparing the frequency spectra of tomographic data with identical path length and different orientation.

3.9 Summary

Analytic formulas for the spectra of a simple model are derived in this chapter. The spectrum for each mode can be summarized as

(1) The three-dimensional spectrum for p

$$\Upsilon_p(k, l, \omega, n, z) = \rho_0^2 f^2 F_n^2(z) \Phi(k, l, \omega, n), \tag{3.39}$$

(2) The three-dimensional spectrum for η

$$\Upsilon_\eta(k, l, \omega, n) = \frac{f^2}{g^2} F_n^2(z = 0) \Phi(k, l, \omega, n), \tag{3.40}$$

(3) The three-dimensional spectrum for u and v

$$\Upsilon_{u,v}(k,l,\omega,n,z) = [4\pi^2 l^2, 4\pi^2 k^2] F_n^2(z) \Phi(k,l,\omega,n), \tag{3.41}$$

(4) The three-dimensional spectrum for θ and ζ

$$\Upsilon_{\theta,\zeta}(k,l,\omega,n,z) = \left[f^2 G_n^2(z) (\frac{\partial \theta_0}{\partial z})^2, f^2 G_n^2(z) \right] \Phi(k,l,\omega,n), \tag{3.42}$$

(5) The three-dimensional spectrum for w and ρ

$$\Upsilon_{w,\rho}(k,l,\omega,n,z) = \left[4\pi^2 \omega^2 f^2 G_n^2(z), \frac{\rho_0^2 f^2 N^4(z) G_n^2(z)}{g^2} \right] \Phi(k,l,\omega,n), \tag{3.43}$$

(6) The zonal-wavenumber/frequency spectrum for p

$$\Upsilon_p(k,\omega,n,z) = \rho_0^2 f^2 F_n^2(z) \int_{-\infty}^{+\infty} \Phi(k,l,\omega,n) dl, \tag{3.44}$$

(7) The meridional-wavenumber/frequency spectrum for p

$$\Upsilon_p(l,\omega,n,z) = \rho_0^2 f^2 F_n^2(z) \int_{-\infty}^{+\infty} \Phi(k,l,\omega,n) dk, \tag{3.45}$$

(8) The frequency spectrum for u, v, p and θ

$$\Upsilon_{u,v,p,\theta}(\omega,n,z) = \int_{-\infty}^{+\infty} \int_{-\infty}^{+\infty} \left[4\pi^2 l^2 F_n^2(z), 4\pi^2 k^2 F_n^2(z), \rho_0^2 f^2 F_n^2(z), f^2 G_n^2(z) (\frac{\partial \theta_0}{\partial z})^2 \right] \Phi(k,l,\omega,n) dk dl, \tag{3.46}$$

(9) The frequency spectrum for horizontally averaged temperature

$$\Upsilon_d(\omega,z,n) = \int_{-\infty}^{+\infty} \int_{-\infty}^{+\infty} f^2 G_n^2(z) (\frac{\partial \theta_0}{\partial z})^2 W(k,L) \Phi(k,l,\omega,n) dk dl, \tag{3.47}$$

(10) The zonal-wavenumber spectrum for u, v, p and θ

$$\Upsilon_{u,v,p,\theta}(k,n,z) = \int_{-\infty}^{+\infty} \int_{-\infty}^{+\infty} \left[4\pi^2 l^2 F_n^2(z), 4\pi^2 k^2 F_n^2(z), \rho_0^2 f^2 F_n^2(z), f^2 G_n^2(z) (\frac{\partial \theta_0}{\partial z})^2 \right] \Phi(k,l,\omega,n) dl d\omega, \tag{3.48}$$

(11) The meridional-wavenumber spectrum for u, v, p and θ

$$\Upsilon_{u,v,p,\theta}(l,n,z) = \int_{-\infty}^{+\infty}\int_{-\infty}^{+\infty}\left[4\pi^2 l^2 F_n^2(z), 4\pi^2 k^2 F_n^2(z), \rho_0^2 f^2 F_n^2(z), f^2 G_n^2(z)(\frac{\partial\theta_0}{\partial z})^2\right]\Phi(k,l,\omega,n)dkd\omega, \tag{3.49}$$

(12) The kinetic energy for each mode at depth z

$$E_k(n,z) = F_n^2(z)\int_{-\infty}^{+\infty}\int_{-\infty}^{+\infty}\int_{-\infty}^{+\infty}2\pi^2(k^2+l^2)\Phi(k,l,\omega,n)dkdld\omega, \tag{3.50}$$

(13) The kinetic energy per unit surface area for each mode

$$KE(n) = \int_{-\infty}^{+\infty}\int_{-\infty}^{+\infty}\int_{-\infty}^{+\infty}2\pi^2(k^2+l^2)\Phi(k,l,\omega,n)dkdld\omega, \tag{3.51}$$

(14) The potential energy per unit surface area for each mode

$$PE(n) = \int_{-\infty}^{+\infty}\int_{-\infty}^{+\infty}\int_{-\infty}^{+\infty}\frac{f^2 r_n^2}{2}\Phi(k,l,\omega,n)dkdld\omega, \tag{3.52}$$

(15) The total energy per unit surface area for each mode

$$TE(n) = \int_{-\infty}^{+\infty}\int_{-\infty}^{+\infty}\int_{-\infty}^{+\infty}[2\pi^2(k^2+l^2)+\frac{f^2 r_n^2}{2}]\Phi(k,l,\omega,n)dkdld\omega, \tag{3.53}$$

(16) The ratio of kinetic energy to potential energy per unit surface area for each mode

$$\frac{KE(n)}{PE(n)} = \frac{\int_{-\infty}^{+\infty}\int_{-\infty}^{+\infty}\int_{-\infty}^{+\infty}2\pi^2(k^2+l^2)\Phi(k,l,\omega,n)dkdld\omega}{\int_{-\infty}^{+\infty}\int_{-\infty}^{+\infty}\int_{-\infty}^{+\infty}(f^2 r_n^2/2)\Phi(k,l,\omega,n)dkdld\omega}, \tag{3.54}$$

(17) The heat flux for each mode

$$< u_n\theta_n >=< v_n\theta_n >= 0, \tag{3.55}$$

(18) The momentum flux for each mode

$$< u_n v_n >= -F_n^2(z)\int_{-\infty}^{+\infty}\int_{-\infty}^{+\infty}\int_{-\infty}^{+\infty}4\pi^2 kl\Phi(k,l,\omega,n)dkdld\omega. \tag{3.56}$$

If $\Phi(k, l, \omega, n)$ is isotropic, the momentum transport $< u_n v_n >$ is zero.

The general circulation of the ocean is a multi-dimensional and multi-variate process. In spite of its complexity, the above equations suggest that different spectra for different variables are connected to each other through the intermediate variable $\Phi(k, l, \omega, n)$, which is the three-dimensional spectrum of the stream-function for each mode. Once $\Phi(k, l, \omega, n)$ is known, one can estimate the frequency and wavenumber spectra for any variable at any depth. Accordingly, the correlation functions, time and space scales of temperature, velocities, etc. can be obtained.

Chapter 4

Observed spectra of low frequency oceanic variability

The observed spectra of low frequency variability in the ocean will be reviewed in this chapter. "Low frequency variability" is defined as the time-dependent motions with time scales longer than the inertial period and shorter than a few years and spatial scales between about 10 km and 1000 km. Emphases are put on answering the following questions: How does the variability of sea surface height, horizontal velocities and temperature depend on horizontal wavenumbers, frequency, direction, vertical mode and geography? Which characteristic features of low frequency variability are independent of geography? Which ones are geography–dependent, and how do they depend on geography? I will summarize the various observations and give a zero order description of the low frequency oceanic variability.

4.1 Horizontal inhomogeneity

The most striking property of low frequency oceanic variability is that kinetic energy varies strongly with position. This strong spatial variation implies that a spectral representation can not be a complete one because it vitiates the necessary condition for the simple spectral representation: spatial homogeneity. However, if the kinetic

energy does not change much within the scale where the dominant energy of the spectral representation occurs, the spectrum is still a useful representation.

The spatial variation inferred from altimetry and current meter moorings is used as first approximation. Figure 4-1.a (taken from Wunsch, 1997) shows surface kinetic energy from the current meters in the North Pacific; figure 4-1.b (taken from Stammer, 1997a) shows the surface kinetic energy from the altimeter in the North Pacific; and figure 4-1.c shows the surface kinetic energy from the empirical formula, equation (4.1). Figure 4-2 is the same as figure 4-1 except in the North Atlantic. There is rough agreement between the two estimates.

The zonal averages between 0° and 360°E of eddy kinetic energy K_E and sea surface slope $K_{sl} = K_E \sin^2\phi$ are provided as a function of latitude in figure 4-3 (taken from Stammer 1997a). The zonal averaged K_E decreases from maximum amplitude near the equator to minimum amplitude in high latitudes. In terms of K_{sl}, values remain almost constant in the low latitudes between 25°S and 25°N. This implies that equatorwards of 25° the zonally averaged K_E is approximately in inverse proportion to $\sin^2\phi$.

According to the figures 4-1.a and 4-1.b, the surface eddy kinetic energy in the North Pacific can be regarded as being composed of four parts: (1) the background part, (2) the low latitude part (south of the energetic currents) where $K_E \propto (1/\sin^2\theta)$, (3) the high energy source with a center around (35°N, 150°E), and (4) the low energy area in the north North Pacific. The surface eddy kinetic energy in the North Pacific is expressed as

$$\begin{aligned} E_{kp}(\phi, \lambda, z = 0) &= 30 + \frac{32}{\sin^2\phi} + 1000\exp\{-[\frac{(\lambda - 150)^2}{900} + \frac{(\phi - 35)^2}{50}]\} \\ &\quad -80\exp\{-[\frac{(\lambda - 190)^2}{1600} + \frac{(\phi - 42)^2}{200}]\}, \end{aligned} \tag{4.1}$$

where λ is the longitude from 0° to 360°E, and ϕ is the latitude from 10° to 60°N. The units of E_{kp} are cm^2/s^2.

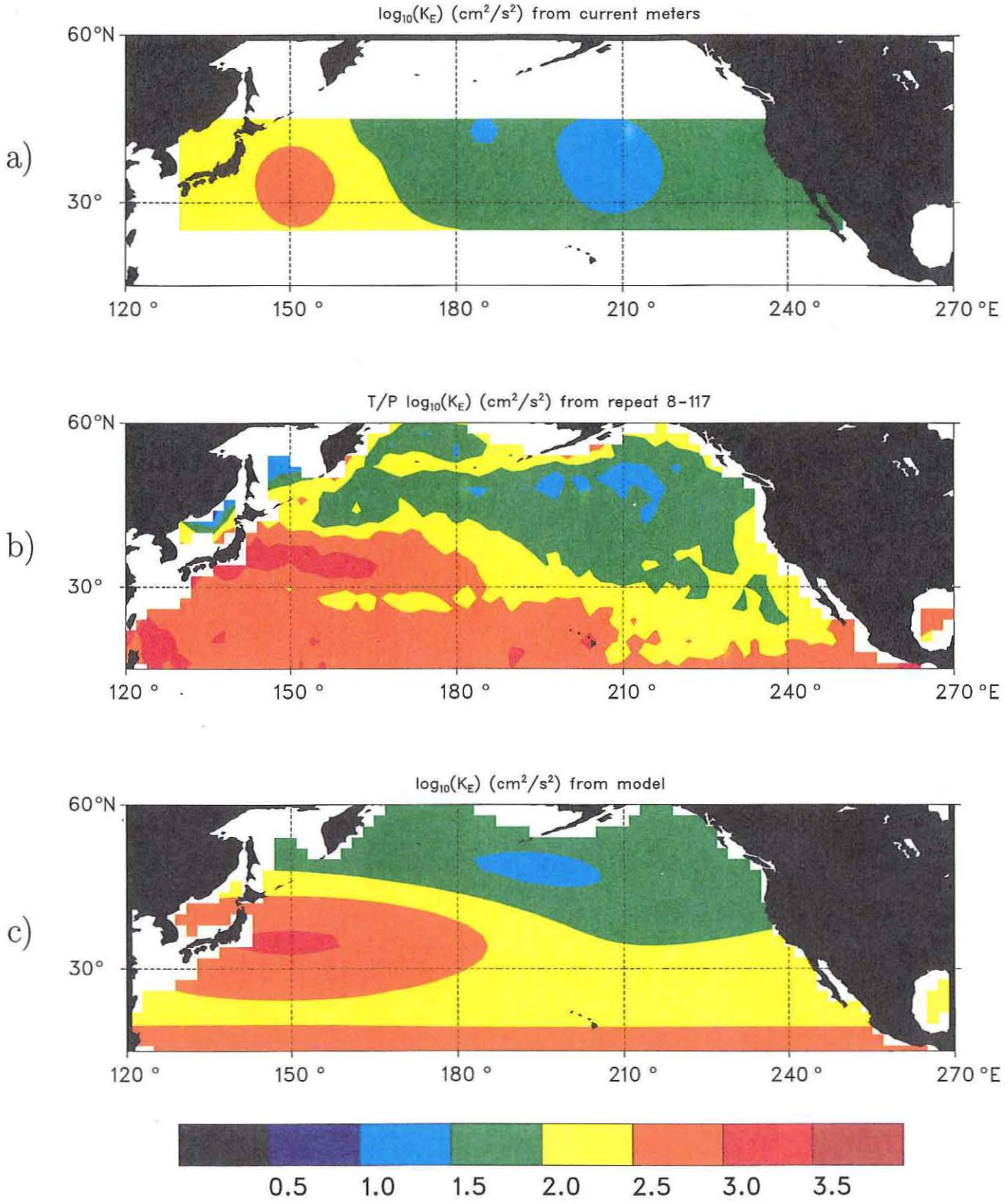

Figure 4-1: Surface eddy kinetic energy in the region of North Pacific. (a) from the current meters (Wunsch, 1997) (b) from TOPEX/POSEIDON data (Stammer, 1997a) (c) from the empirical formula.

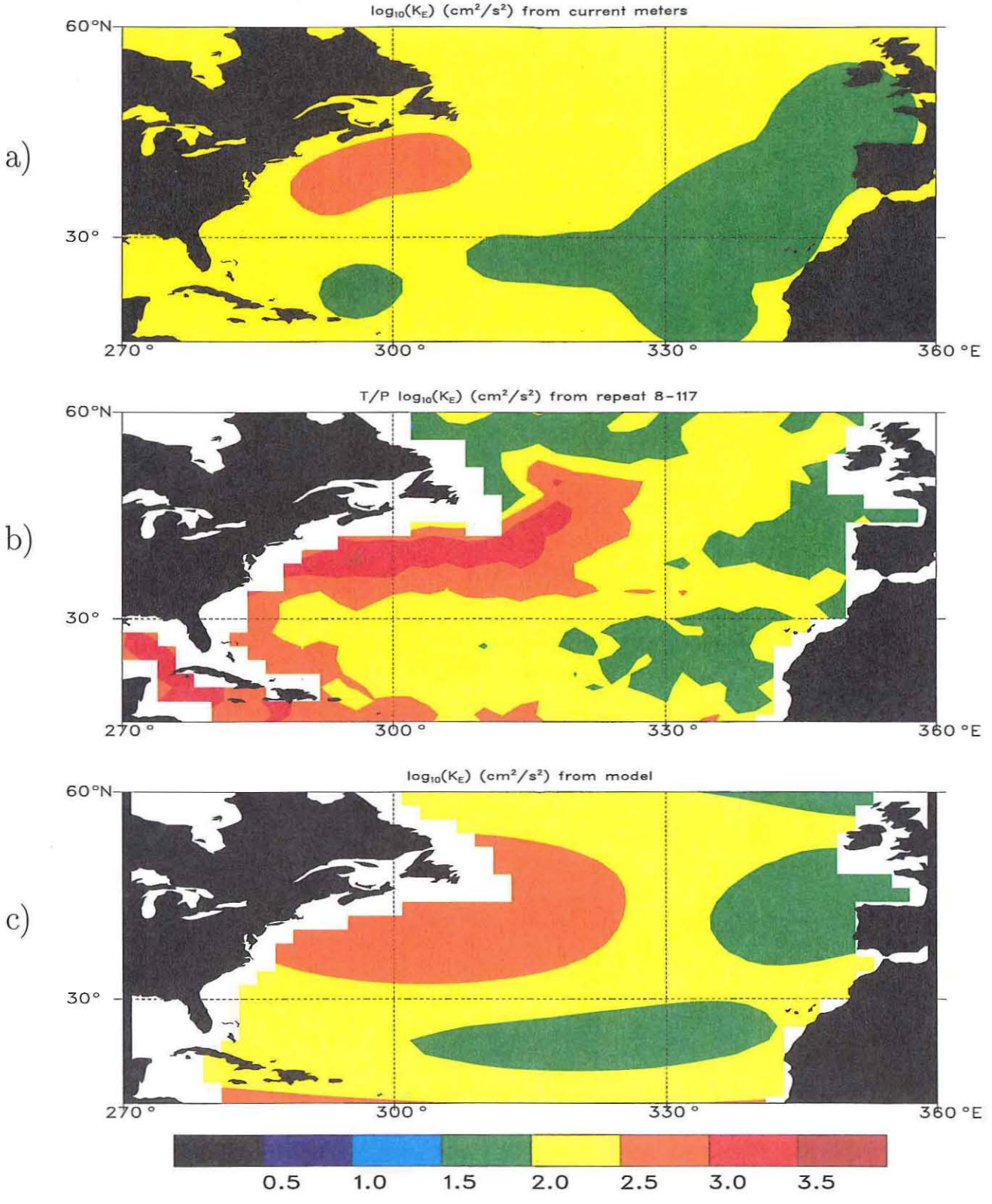

Figure 4-2: Same as in Figure 4-1 except for North Atlantic.

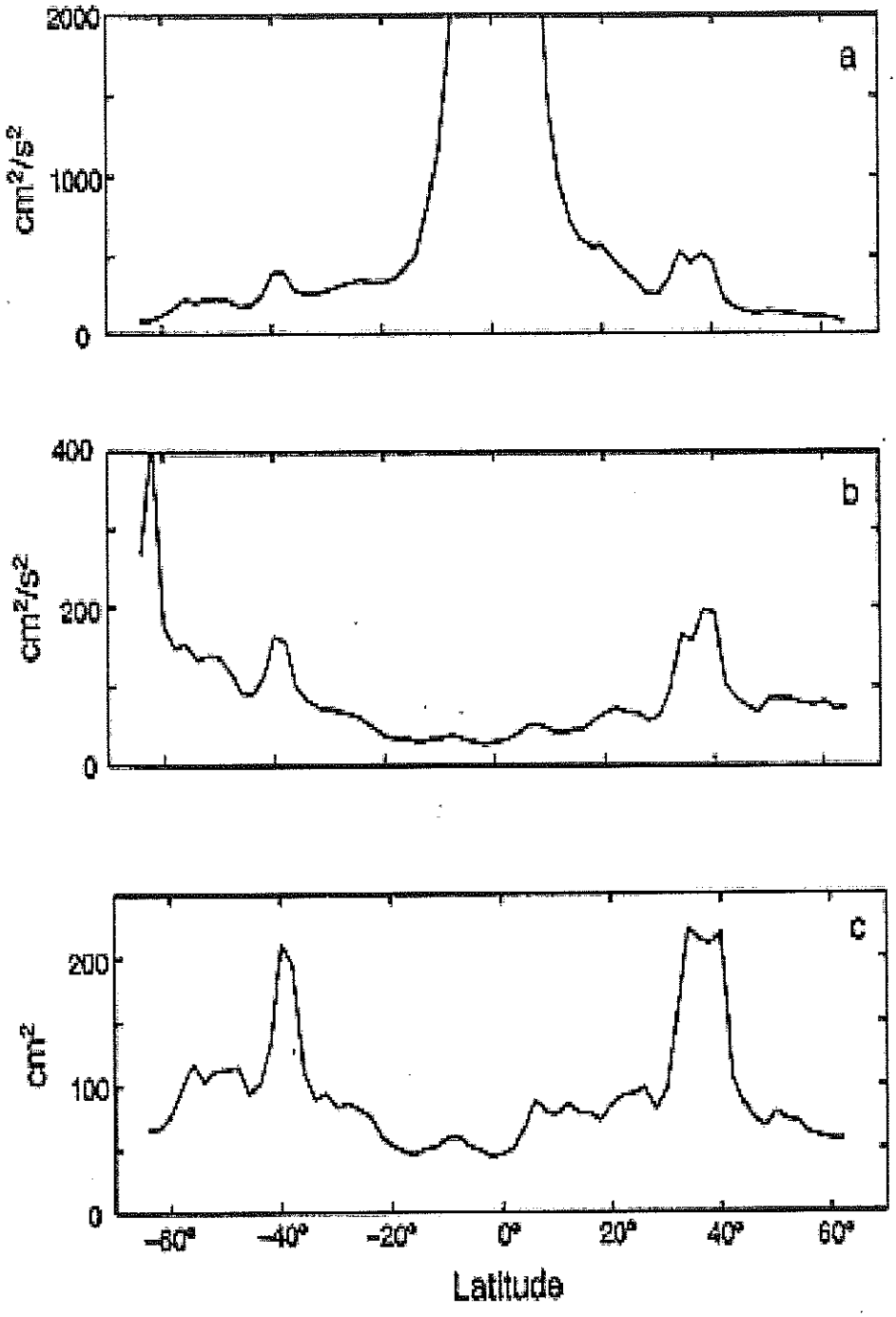

Figure 4-3: Zonal averages between 0° and 360°E of (a) K_E, (b) K_{sl} and (c) SSH variance, plotted against latitude (Stammer 1997a).

The surface eddy kinetic energy in the North Atlantic is expressed as

$$E_{ka}(\phi,\lambda,z=0) = 50 + \frac{35}{\sin^2\phi} + 1000\exp\{-[\frac{(\lambda-305)^2}{400} + \frac{(\phi-43)^2}{80}]\} -$$
$$280\exp\{-[\frac{(\lambda-320)^2}{2000} + \frac{(\phi-16)^2}{200}]\} - 160\exp\{-[\frac{(\lambda-320)^2}{900} + \frac{(\phi-42)^2}{50}]\}, \quad (4.2)$$

in units of cm^2/s^2. The results from equations (4.1) and (4.2) are drawn in figures 4-1.c and 4-2.c, respectively. As shown in figures 4-1 and 4-2, equations (4.1) and (4.2) are reasonable fits to the general pattern of the corresponding observations.

4.2 A first-guess k, l, ω spectral form

The spatial inhomogeneity of oceanic kinetic energy shows that there is no universal form $\Phi(k,l,\omega,n)$ for the low frequency variability. We have to modify the universal form $\Phi(k,l,\omega,n)$ to a regional form $\Phi(k,l,\omega,n,\phi,\lambda)$ so that the model spectrum can fit the corresponding observations at different locations. Suppose that $\Phi(k,l,\omega,n,\phi,\lambda)$ exists and a convenient representation of $\Phi(k,l,\omega,n,\phi,\lambda)$ for each mode is

$$\Phi(k,l,\omega,n,\phi,\lambda) = B_n(k)C_n(l)D_n(\omega)E_0(n)I(\phi,\lambda). \quad (4.3)$$

Here $B_n(k)$ and $C_n(l)$ stand for the zonal- and meridional-wavenumber spectral shape, respectively; $D_n(\omega)$ represents the frequency spectral shape; $E_0(n)$ is a constant associated with each mode which will determine how the energy is divided among vertical modes; and $I(\phi,\lambda)$ is the spatial function that represents how the energy level depends on space. As shown in figure 4-1 and 4-2, in the areas away from major currents and within the horizontal scale of about 1000 km, the energy level can be roughly treated as constant, and thus wavenumber spectrum is a useful representation. In equation (4.3), it is assumed that frequency spectral shape, wavenumber spectral shape, vertical structure and energy level are separable, which is the simplest case for $\Phi(k,l,\omega,n,\phi,\lambda)$. However, as will be seen later, the separated form in equation (4.3)

cannot distinguish westward-going energy from eastward-going one. A sophisticated frequency and wavenumber coupled form is proposed in chapter 7 to solve this problem. In the next section, I will decide on the form of $B_n(k)$, $C_n(l)$, $D_n(\omega)$, and $E_0(n)$ according to different observations.

4.3 Vertical structure of kinetic energy and potential energy

Schmitz (1978, 1988) studied the vertical distribution of kinetic energy at different sites in the Atlantic and Pacific. He concluded that the vertical profile for kinetic energy is independent of geography as a first approximation across the entire mid-latitude band. Eddy kinetic energy K_E dropped exponentially from the surface to a depth of about 1.2 km, then remained almost constant within the abyss.

Wunsch (1997) systematically studied the partition of the kinetic energy of time–varying motions amongst the dynamical modes throughout the water column. He concluded that in the open North Pacific, the water column average kinetic energy was about 35% in the barotropic mode and about 55% in the first baroclinic mode. The North Atlantic contained on average about 40% in the barotropic and 50% in the first baroclinic mode in the middle of the ocean. Strong deviations from these values occur near the Gulf Stream and near the equator, and no attempt to model them in those regions will be made here. The results by Wunsch and Schmitz are consistent. Wunsch's result shows that in the open ocean horizontal kinetic energy is dominated by the barotropic and first baroclinic mode and that the partitioning among barotropic and first baroclinic mode is roughly equal. Because the first baroclinic mode is surface intensified, horizontal kinetic energy will be dominated by the first baroclinic mode in the upper ocean; thus it will decay nearly exponentially in the main thermocline. Within the deep water, horizontal kinetic energy remains almost constant because the deep ocean is dominated by the barotropic mode.

Wunsch (1999b) inferred the vertical displacement of an isopycnal from tempera-

ture measurements and investigated the vertical structure of potential energy in the North Atlantic. He found that the water column average potential energy was about 30-40% in the first baroclinic mode. The ratio of kinetic energy in the first baroclinic mode to potential energy was about 0.2-0.4 in the mid-latitude away from the western boundary. Reader beware that the results for the vertical structure of potential energy are semi-quantitative, because the results are sensitive to the values of $\partial\bar{\theta}/\partial z$ whose reliability is not clear at all, and the number of useful records on each mooring is very limited.

4.4 Observed three-dimensional spectra of SSH

TOPEX/POSEIDON satellite altimeter data provide nearly simultaneous measurements of global sea surface height every 10 days, which provides estimates of the frequency/wavenumber spectra of sea surface height. The spectra were first derived by Wunsch and Stammer (1995) from the spherical harmonic analysis of the $2^\circ \times 2^\circ$ gridded data. Subsequently, Stammer (1997a) obtained the spectra from the Fourier analysis of alongtrack data. The spectra obtained from these two different methods are quite similar (Wunsch and Stammer, 1995). In order to readily compare with model results, I will derive the spectra from the Fourier analysis of gridded data to see how the spectra depend on zonal-wavenumber, meridional-wavenumber and frequency. Moreover, the spectra produced by Wunsch and Stammer (1995) and Stammer (1997a) are scalar in that neither Wunsch and Stammer (1995) nor Stammer (1997a) studied the directional property of the spectrum. In this chapter, I will provide an estimate of what percentage energy in the sea surface height propagates to the east and to the west. The value used here is gridded with a spatial resolution of $0.25^\circ \times 0.25^\circ$ and a temporal resolution of 10 days. These numbers were produced by Le Traon et al. (1998) through combining TOPEX/POSEIDON and ERS-1/2 measurements. Because the low frequency oceanic variability strongly depends on geography as described in section 4.1, I will study the three-dimensional spectrum

region by region. As a representative result, I analyze the three-dimensional spectra of sea surface height anomaly in the area of $25° - 50°$N and $195° - 225°$E in North Pacific. The size of the area is chosen as a result of a compromise between resolution and homogeneity. Because the meridional range of the area is so small, compared with the radius of the earth, this area can be assumed to be in a horizontal plane; that is, the distance of one degree along the zonal direction is independent of latitude. Defining the space-time Fourier transform of sea surface height anomaly $\eta(x, y, t)$ as $\tilde{\eta}(k, l, \omega)$, then

$$\tilde{\eta}(k, l, \omega) = \int_{-\infty}^{+\infty} \int_{-\infty}^{+\infty} \int_{-\infty}^{+\infty} \eta(x, y, t) e^{i2\pi(kx+ly-\omega t)} dx dy dt. \tag{4.4}$$

By definition, the three-dimensional spectrum can be written as

$$\Upsilon_\eta(k, l, \omega) = < |\tilde{\eta}(k, l, \omega)|^2 > . \tag{4.5}$$

Because the data are real, the three-dimensional spectrum is symmetrical in the sense that $\Upsilon_\eta(k, l, \omega) = \Upsilon_\eta(-k, -l, -\omega)$. Hereafter, the discussion is limited to positive frequencies only, though k and l have both signs. To obtain some statistical stability, the spectrum is averaged over three neighboring frequencies. This produces an approximate 6 degrees of freedom. Figure 4-4 shows the smoothed three-dimensional spectrum at periods longer than 60 days plotted as $log[\Upsilon_\eta(k, l)/\Upsilon_{\eta-\max}(k, l)]$, where $\Upsilon_{\eta-\max}(k, l)$ is the peak of the three-dimensional spectrum in each frequency band. The most conspicuous point of figure 4-4 is that, in each frequency band, energy is dominated by long wavelengths. For periods longer than 90 days, the westward-going energy is greater than eastward-going energy over long wavelengths. In each frequency band, the energy distribution tends to be isotropic at wavelengths shorter than 200 km. It is unclear whether this isotropic property is real or if it is the artificial result of the objective mapping. The spatial correlated function used to produce the gridded data is isotropic and has a correlation scale about 200 km in the area we studied (Le Traon, et al., 1998).

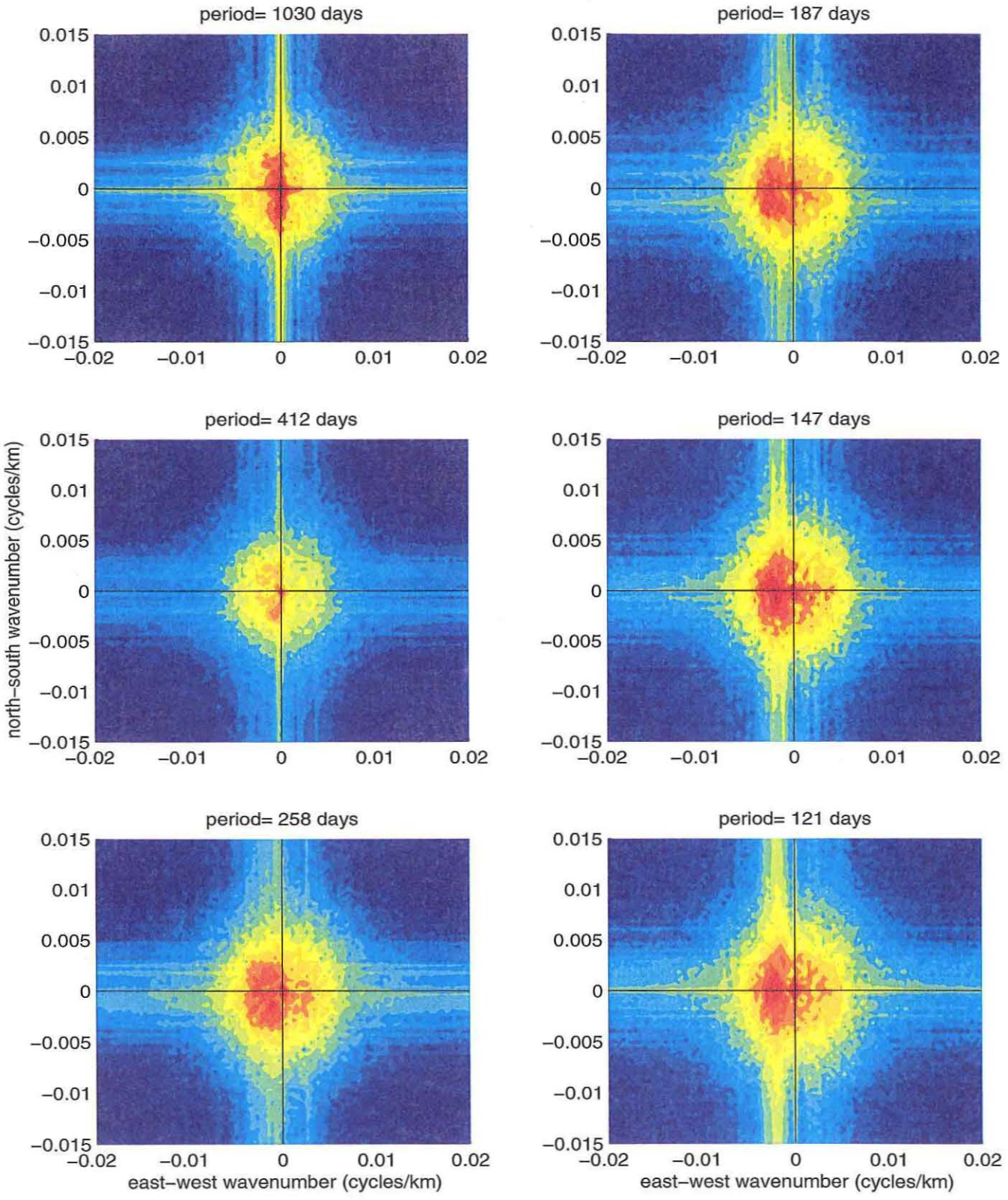

Figure 4-4: To be continued

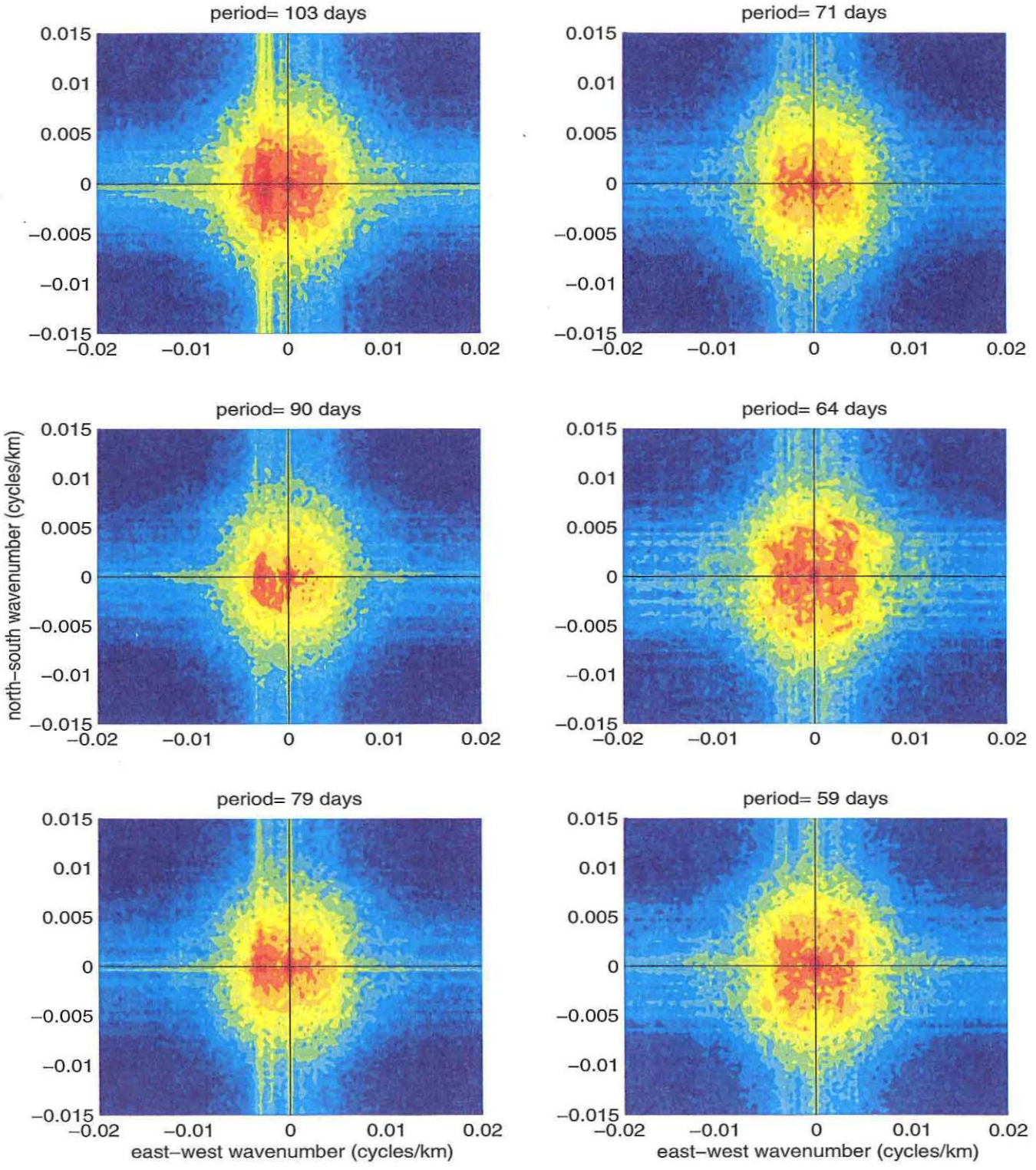

Figure 4-4: The smoothed three-dimensional spectra at periods longer than 59 days. The spectra at shorter periods are similar except that the energy distribution is nearly isotropic.

suggests that ΔCO_3^{2-} estimates are accurate to no better than ±5 to 10 μmol kg^{-1} (Figure 2.12). Given that expected D_{Zn} errors are similarly large (Table 2.3), it is not obvious why the D_{Zn}:ΔCO_3^{2-} relationship appears to be tighter. An important factor is probably the steeper slope for D_{Cd}, *i.e.*, D_{Cd} increases three-fold over ~20 μmol kg^{-1} ΔCO_3^{2-}, while D_{Zn} increases three-fold over ~40 μmol kg^{-1} ΔCO_3^{2-} (Figures 2.7, 2.11). This would cause the uncertainty in ΔCO_3^{2-} to be more important for D_{Cd}.

If the observed scatter in the relationship between D_{Cd} and ΔCO_3^{2-} is mainly the result of these uncertainties, one could speculate that *C. wuellerstorfi* and *Uvigerina* are actually good recorders of seawater Cd and ΔCO_3^{2-}. The precise relationship between D_{Cd} and ΔCO_3^{2-} remains poorly constrained by the current data, however. I therefore propose a pair of very preliminary, simple linear equations for waters deeper than 3000 m (Figure 2.11b):

$$D_{Cd} = 0.1\Delta CO_3^{2-} + 2.5 \text{ (for } \Delta CO_3^{2-} < 5 \text{ μmol kg}^{-1}) \quad (2.12)$$

$$D_{Cd} = 3 \text{ (for } \Delta CO_3^{2-} > 5 \text{ μmol kg}^{-1}) \quad (2.13)$$

For samples from any depth, a depth correction can be applied to these equations as follows:

$$D_{Cd} = (D_{Cd(z)} - 3) + 0.1\Delta CO_3^{2-} + 2.5 \text{ (for } \Delta CO_3^{2-} < 5 \text{ μmol kg}^{-1}) \quad (2.14)$$

$$D_{Cd} = (D_{Cd(z)} - 3) + 3 \text{ (for } \Delta CO_3^{2-} > 5 \text{ μmol kg}^{-1}) \quad (2.15)$$

where $D_{Cd(z)}$ represents the Cd partition coefficient predicted from water depth only. Preliminary equations for $D_{Cd(z)}$ are based on Boyle's (1992) equations, except that the >3000 m maximum value is taken to be 3:

$$D_{Cd(z)} = 1.3 \text{ (for depths } < 1150 \text{ m}) \quad (2.16)$$

$$D_{Cd(z)} = 1.3 + (\text{depth} - 1150)1.7/1850 \text{ (for depths 1150-3000 m)} \quad (2.17)$$

$$D_{Cd(z)} = 3 \text{ (for depths } > 3000 \text{ m}) \quad (2.18)$$

Application of Equations 2.14 and 2.15 to my core top Cd/Ca data significantly improves the agreement between Cd_W and estimated water column Cd concentrations (r^2=0.73; Figure 2.13).

zonal-wavenumber. The spectra of the northward-going $\Upsilon_\eta(l > 0, \omega > 0)$, southward-going $\Upsilon_\eta(l < 0, \omega > 0)$ and standing part $\Upsilon_\eta(l = 0, \omega > 0)$ are shown in figure 4-6. The total energy over the positive frequencies is 14.2 cm^2, among which 2.9 cm^2 is contained in the northward-going, 3.9 cm^2 in the southward-going and 7.4 cm^2 in the standing motions. The total energy of northward-going and southward-going motions is approximately the same as the energy of standing motions. Although there is more energy going-southward, the difference between northward-going and southward-going energy is much smaller than the difference between the eastward-going and westward-going energy.

4.6 Observed one-dimensional spectra of SSH

As discussed in last section, two-dimensional spectra are still fairly complex. They can be further simplified into one-dimensional forms.

The zonal-wavenumber spectra

The integration of zonal-wavenumber/frequency spectrum of the eastward-going motions over frequency produces the zonal-wavenumber spectrum of eastward-going motions,

$$\Upsilon_{\eta e}(k) = \int_0^{+\infty} \Upsilon_\eta(k > 0, \omega) d\omega. \tag{4.7}$$

Similarly, the zonal-wavenumber spectrum of westward-going motions is

$$\Upsilon_{\eta w}(k) = \int_0^{+\infty} \Upsilon_\eta(k < 0, \omega) d\omega. \tag{4.8}$$

The spectra in the T/P data of eastward-going and westward-going motions are displayed in figure 4-7. The most striking feature in figure 4-7 is that the energy level of the spectrum of westward-going motions is higher than that of eastward-going ones by a factor of 3 at wavelengths longer than 250 km. At wavelengths shorter than 250 km, the spectra of westward-going and eastward-going motions are nearly identical.

The general shape of the zonal-wavenumber spectrum of westward-going motions

can be written as

$$\begin{aligned} \Upsilon_{\eta w}(k) &\propto |k|^{-1/2}, \ 0 < |k| \leq 0.0028 \ \text{(cycles per km)} \\ &\propto |k|^{-4}, \quad 0.0028 \leq |k|. \end{aligned} \tag{4.9}$$

For the eastward-going motions, it is

$$\begin{aligned} \Upsilon_{\eta e}(k) &\propto |k|^{-1/2}, \ 0 < |k| \leq 0.004 \ \text{(cycles per km)} \\ &\propto |k|^{-4}, \quad 0.004 \leq |k|. \end{aligned} \tag{4.10}$$

By definition, the scalar zonal-wavenumber spectrum can be written as

$$\Upsilon_{\eta}(k) = \int_{-\infty}^{+\infty} \Upsilon_{\eta}(k,\omega) d\omega = \int_{-\infty}^{0} \Upsilon_{\eta}(k,\omega) d\omega + \int_{0}^{+\infty} \Upsilon_{\eta}(k,\omega) d\omega \tag{4.11}$$

which is symmetrical, $\Upsilon_{\eta}(k) = \Upsilon_{\eta}(-k)$, and hence provides no information on the directional property.

The scalar wavenumber spectrum is the sum of the wavenumber spectrum of eastward-going and westward-going motions in the positive frequencies; that is,

$$\Upsilon_{\eta}(k) = \Upsilon_{\eta w}(-k) + \Upsilon_{\eta e}(k) \ \ k > 0. \tag{4.12}$$

The scalar zonal-wavenumber spectrum is displayed in figure 4-9. The spectrum has a transition point around 300 km. The spectral slope is about $-1/2$ at wavelengths longer than 300 km and increases to about -3 at wavelengths shorter than 300 km, which is similar to that derived by Wunsch and Stammer (1996).

A global wavenumber spectrum of sea surface height has been constructed by Wunsch and Stammer (1995). Subsequently, Stammer (1997) investigated the spectrum of sea surface height region by region. The global averaged wavenumber spectrum of sea surface height can be written as

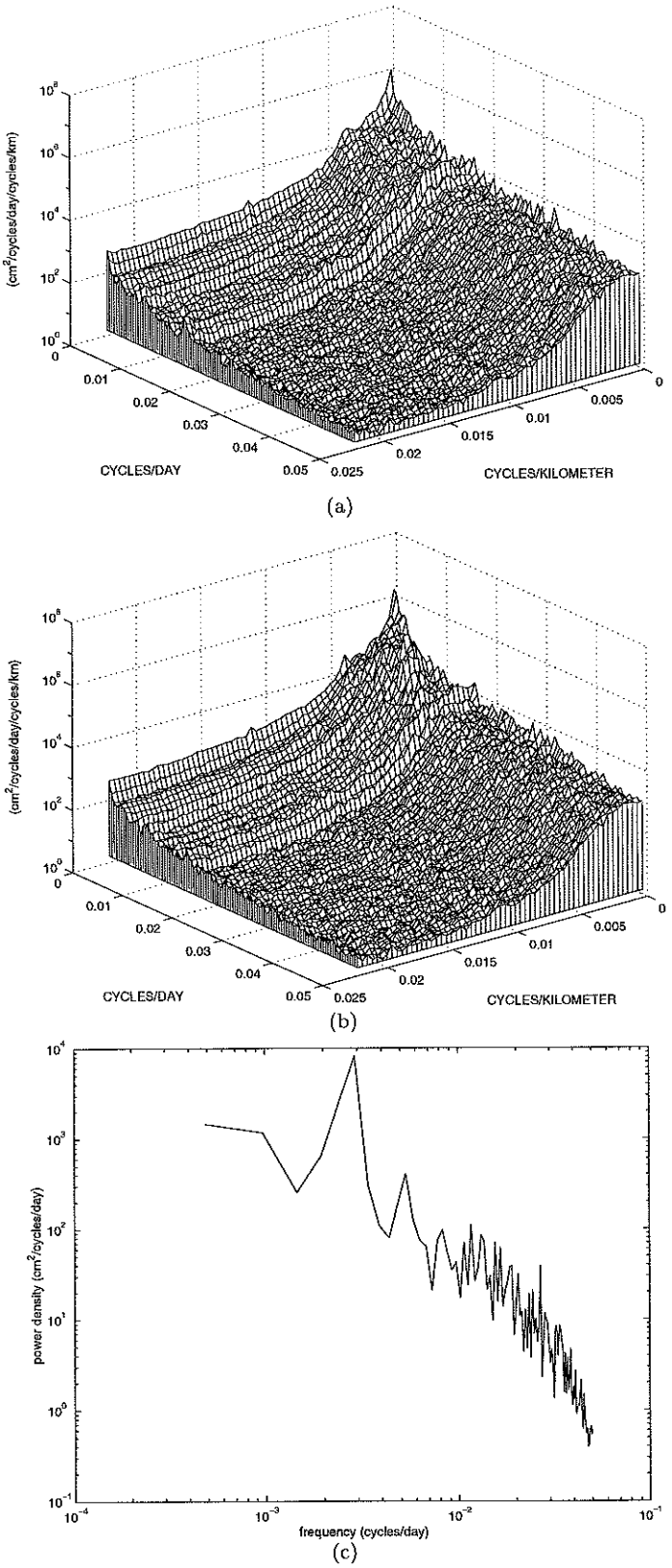

Figure 4-5: The zonal-wavenumber/frequency spectra: (a) eastward-going, (b) westward-going, and (c) standing parts. The annual cycle dominates the frequency spectrum of standing motions.

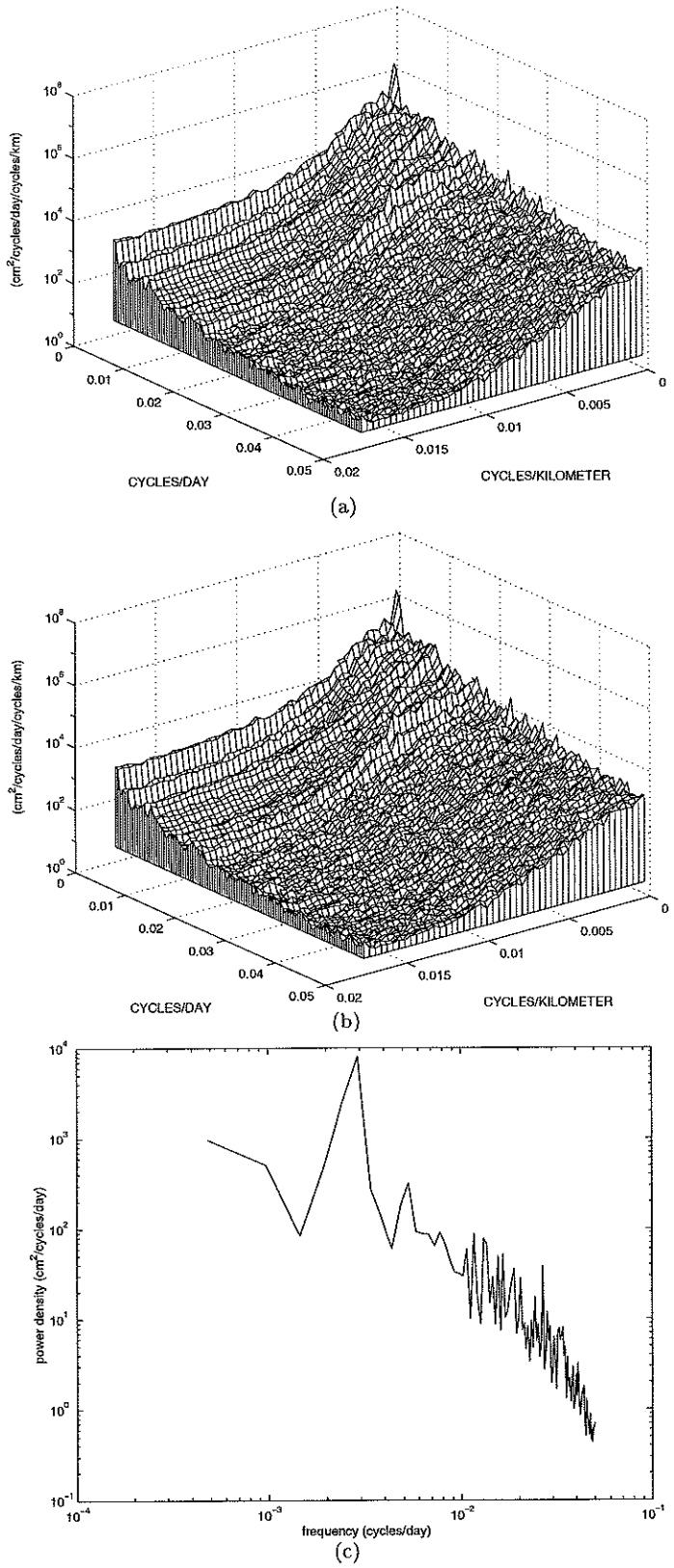

Figure 4-6: The meridional-wavenumber/frequency spectra: (a) northward-going, (b) southward-going, and (c) standing part. The annual cycle dominates the frequency spectrum of standing motions.

$$\begin{aligned}\Upsilon_\eta(k) &\propto |k|^{-1/2},\ 0 < |k| \leq 1/400 \text{ (cycles per km)} \\ &\propto |k|^{-5/2},\ 1/400 \leq |k| \leq 1/150 \text{ (cycles per km)} \\ &\propto |k|^{-4},\ 1/150 \leq |k|. \end{aligned} \tag{4.13}$$

The reader is reminded that there is large uncertainty of the wavenumber spectrum at wavelengths shorter than about 100 km. The measurements of T/P at high wavenumbers are contaminated by measurement noises and aliased by small-scale physical processes such as internal waves and internal tides (Wunsch and Stammer, 1995; Stammer, 1997a). Stammer (1997a) found some universal characteristics for the regional wavenumber spectral shape, which is roughly consistent with the global one. The energy level for the sea surface height and cross-track velocity for wavelengths longer than about 100 km increases greatly from the low energy area in the eastern and central sub-tropical gyre toward the energetic western boundary.

The meridional-wavenumber spectra

The meridional-wavenumber spectra of the northward-going and southward-going motions can be derived in a similar way. Figure 4-8 shows that the meridional-wavenumber spectral shape of northward-going and southward-going motions are similar, and the energy level of southward-going motions is slightly higher at wavelengths longer than 500 km. The scalar meridional-wavenumber spectrum is displayed in figure 4-10. It looks like the scalar zonal-wavenumber spectrum in figure 4-9.

The frequency spectra

By definition, the frequency spectrum of eastward-going energy can be written as

$$\Upsilon_{\eta e}(\omega) = \int_{k>0} \Upsilon_\eta(k,\omega)dk; \tag{4.14}$$

the frequency spectrum of westward-going energy is

$$\Upsilon_{\eta w}(\omega) = \int_{k<0} \Upsilon_\eta(k,\omega)dk; \tag{4.15}$$

and the frequency spectrum of standing waves is $\Upsilon_\eta(k=0,\omega)$. The frequency spectra of the northward-going, southward-going and standing motions can be obtained similarly.

The frequency spectra of eastward-going, westward-going and standing waves are shown in figure 4-11. The peak associated with annual cycle only appears in the spectrum of standing waves. For periods shorter than 100 days, the spectrum of westward-going waves is redder than that of the eastward-going parts. At periods longer than 100 days, the energy level of westward-going motions is about three times as much as that of eastward-going motions. Again, the frequency spectrum of standing motions is dominated by seasonal cycle, and the peak near 60 days is due to the contamination by a residual tidal contribution.

The spectral shape of the frequency spectra of westward-going motions can be approximately written as

$$\begin{aligned} \Upsilon_{\eta w}(\omega) &\propto \omega^{-1/2}, \ 0 < \omega \leq 0.007 \ \text{(cycles per day)} \\ &\propto \omega^{-2}, \quad 0.007 \leq \omega, \end{aligned} \tag{4.16}$$

for the eastward-going motions, it is

$$\begin{aligned} \Upsilon_{\eta e}(\omega) &\propto \omega^{-1/2}, \ 0 < \omega \leq 0.007 \ \text{(cycles per day)} \\ &\propto \omega^{-3/2}, \quad 0.007 \leq \omega, \end{aligned} \tag{4.17}$$

and for the standing motions, it is

$$\begin{aligned} \Upsilon_{\eta 0}(\omega) &\propto \omega^{-3/4}, \ 0 < \omega \leq 0.005 \ \text{(cycles per day)} \\ &\propto \omega^{-2}, \quad 0.005 \leq \omega, \end{aligned} \tag{4.18}$$

Figure 4-12 presents the frequency spectra of northward-going, southward-going and standing waves. Figure 4-12 is similar to figure 4-11 except that the difference between the spectra of northward-going and southward-going motions is much smaller

than that between the spectra of southward-going and westward-going motions.

The scalar frequency spectrum is

$$\Upsilon_\eta(\omega) = \int_{-\infty}^{+\infty}\int_{-\infty}^{+\infty}\Upsilon_\eta(k,l,\omega)dkdl, \tag{4.19}$$

$$= \Upsilon_{\eta e}(\omega) + \Upsilon_{\eta w}(\omega) + \Upsilon_\eta(k=0,\omega) \tag{4.20}$$

$$= \Upsilon_{\eta n}(\omega) + \Upsilon_{\eta s}(\omega) + \Upsilon_\eta(l=0,\omega). \tag{4.21}$$

The scalar frequency spectrum is displayed in figure 4-13. The global averaged frequency spectrum of sea surface height has been constructed by Wunsch and Stammer (1995) and in general the frequency spectrum displayed in figure 4-13 is similar to the global averaged frequency spectrum of sea surface height. On time scales shorter than 100 days the spectra approximately follow an ω^{-2} power law, with an $\omega^{-1/2}$ power law over longer periods (Wunsch and Stammer, 1995).

Stammer (1997) broke the global power density spectrum down into regional structures. An important result is that a very high degree of universality in spectral shape was found—independent of the very large variations in regional energy levels. Stammer (1997) found three different region types: (i) the energetic boundary currents, (ii) the bulk of the extratropical basins, and (iii) the tropical interior oceans. There exists a pronounced similarity in the shape of all the spectra from each dynamical category. In the interior ocean, the general shape of the sea surface height and sea surface slope spectra basically agrees with that of the global average but with less energy. In general, the slope spectral characteristic—with a flat low-frequency part and a steeper decay at higher frequencies–appears qualitatively consistent with results from moored current meter and temperature measurements.

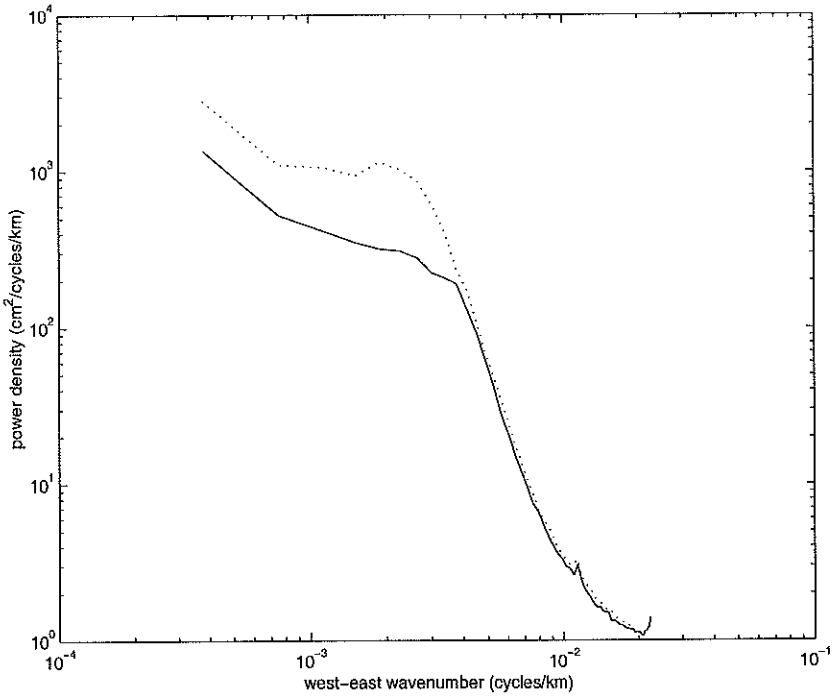

Figure 4-7: The zonal-wavenumber spectra of eastward-going (solid line) and westward-going motions (dotted line) in the T/P data.

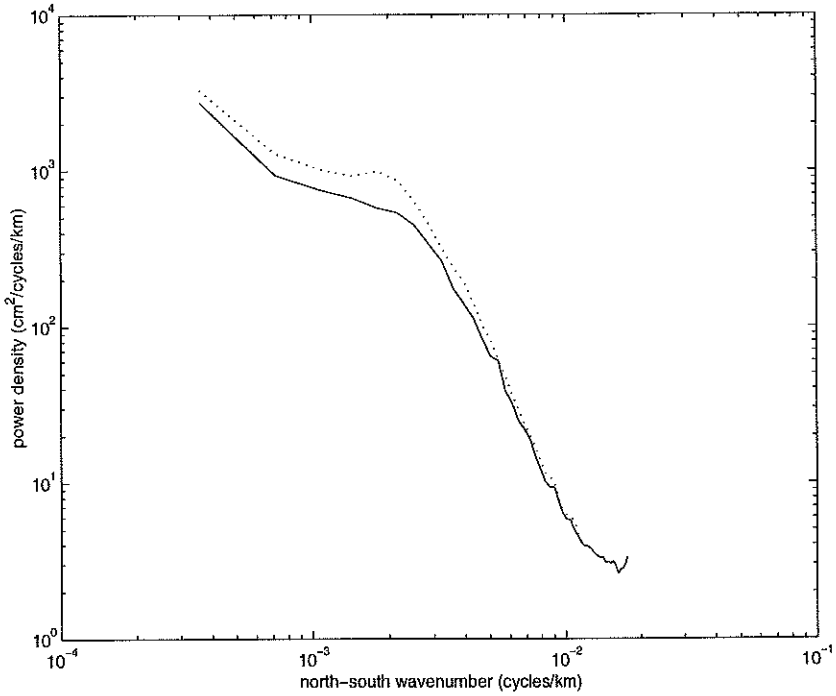

Figure 4-8: The meridional-wavenumber spectra of northward-going (solid line) and southward-going motions (dotted line).

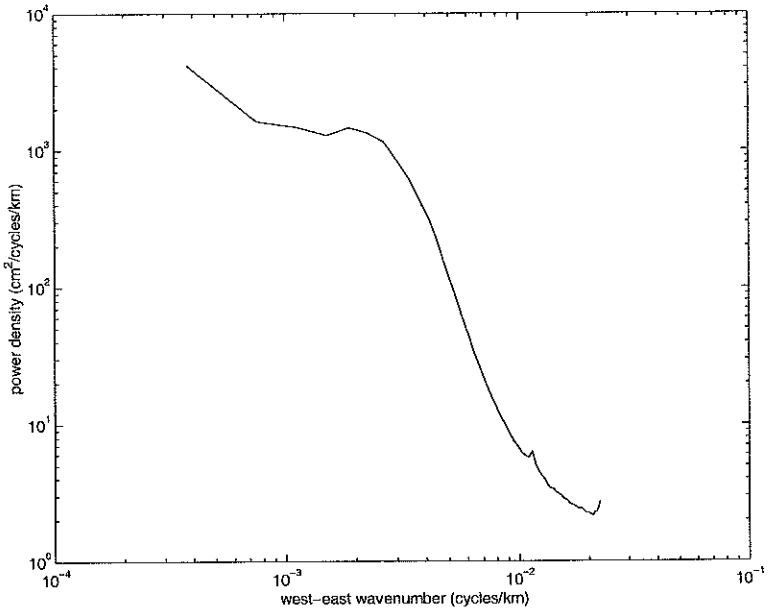

Figure 4-9: The scalar zonal-wavenumber spectra.

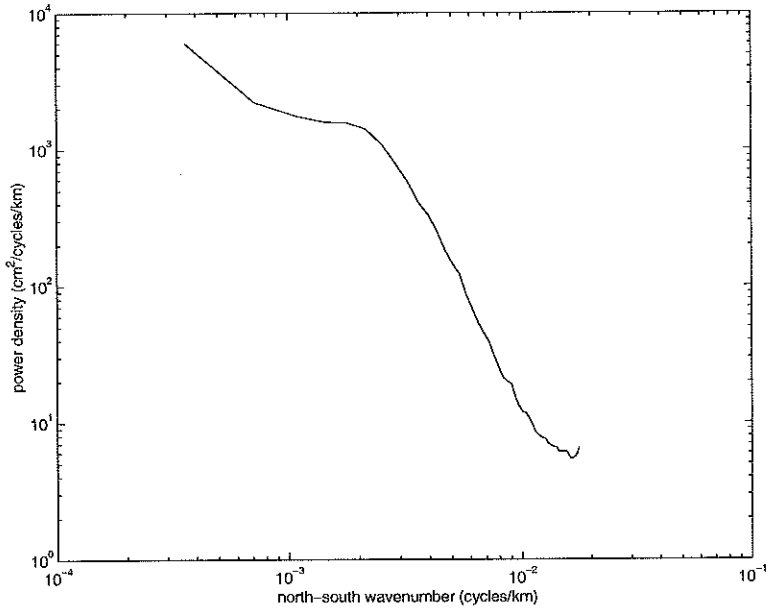

Figure 4-10: The scalar meridional–wavenumber spectra.

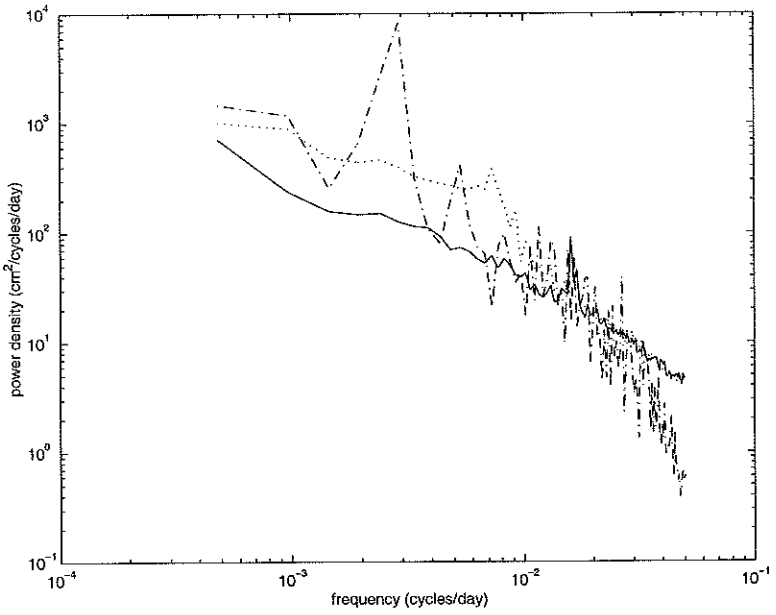

Figure 4-11: The frequency spectra of eastward-going (solid line), westward-going (dotted line) and standing motions (dashdot line). The frequency spectrum of standing motions is dominated by annual cycle.

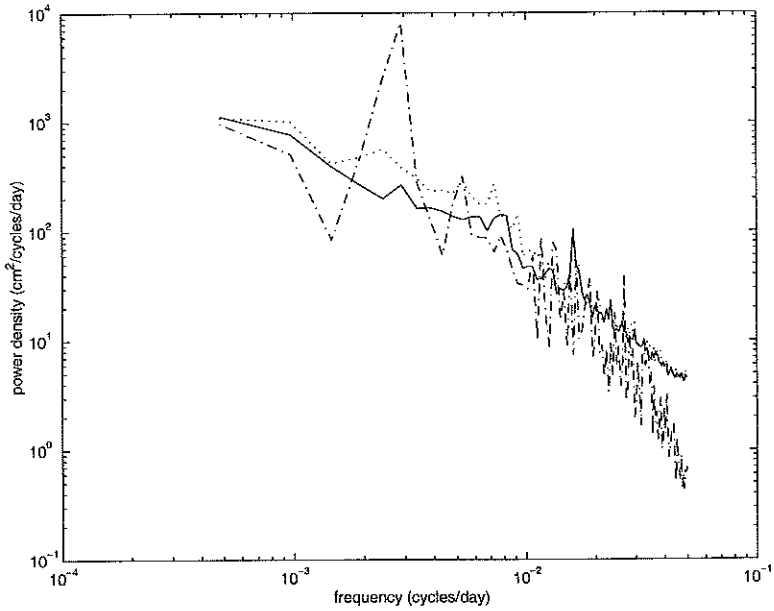

Figure 4-12: The frequency spectra of northward-going (solid line), southward-going (dotted line) and standing motions (dashdot line). The frequency spectrum of standing motions is dominated by annual cycle.

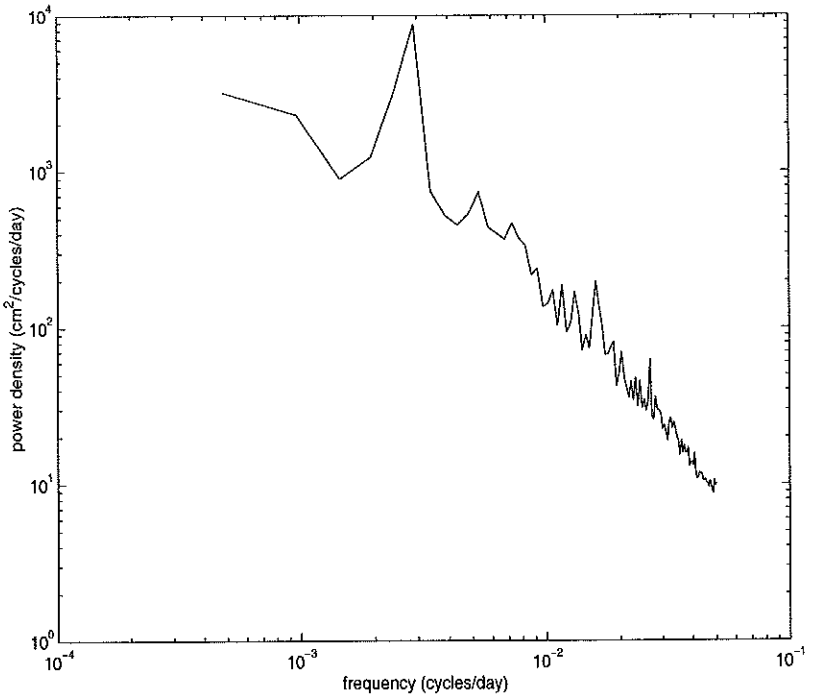

Figure 4-13: The scalar frequency spectrum. The spectrum is dominated by the seasonal cycle.

4.7 Observed temperature wavenumber spectra

The data used here is taken from the repeated XBT lines in the North Pacific between San Francisco and Hawaii. The data have been described in detail by Gilson et al. (1998). The raw data were interpolated onto a grid with 0.1° longitude spacing. The time mean of the objectively mapped data was removed at each grid point. The time-averaged wavenumber spectra of the temperature perturbations at different depths were then estimated.

Figure 4-14 presents the time-averaged wavenumber spectra at different depths. The general spectral shape is independent of depth and can be written as

$$\begin{aligned} \Upsilon_\theta(k) &\propto |k|^{-1/2},\ 0 < |k| \leq 1/400 \text{ (cycles per km)} \\ &\propto |k|^{-5/2},\ 1/400 \leq |k| \leq 1/150 \text{ (cycles per km)} \\ &\propto |k|^{-4},\ 1/150 \leq |k|, \end{aligned} \tag{4.22}$$

which is similar to that of sea surface height perturbations (equation 4.13). In general, the energy level decreases with depth. Roemmich and Cornuelle (1990) analyzed XBT measurements in the South Pacific ocean and found that the wavenumber spectral shape there is similar to those displayed in figure 4-14.

Gilson et al. (1998) studied the relationship of TOPEX/POSEIDON altimetric height to steric height, which is calculated from temperature and salinity measurements along a precisely repeating ship track in the North Pacific over a period of 5 years. They found that on wavelengths longer than 500 km altimetric height variability is highly correlated with the variability of the steric height, with a coherence amplitude of 0.89. About 65% of the total variance is found in the wavelengths longer than 500 km in steric height.

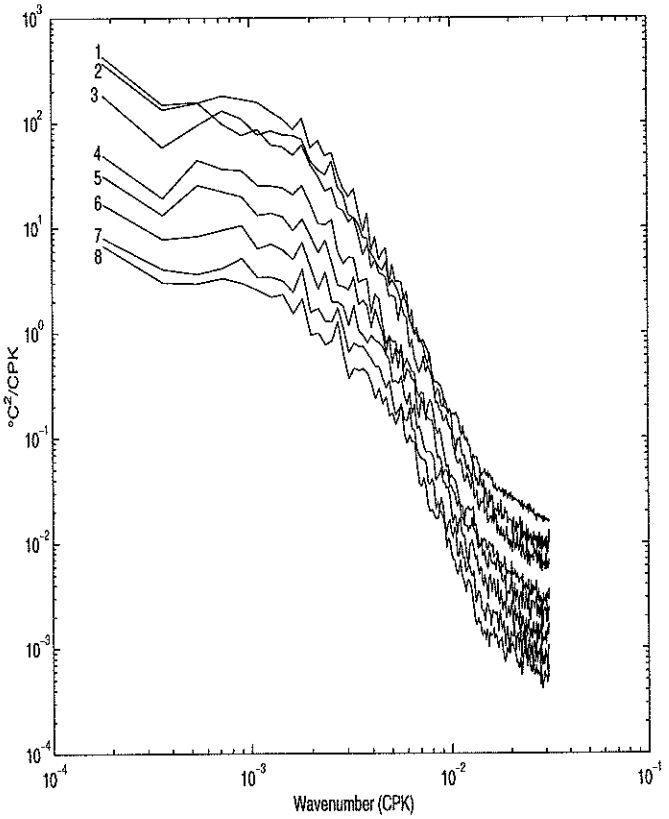

Figure 4-14: The wavenumber spectra of temperature averaged among depths (1) 0-100 m, (2) 100-200 m, ... (8) 700-800 m.

4.8 Observed frequency spectra of velocity and temperature

An early discussion of frequency spectra from current meters was given by Wunsch (1981). Generally speaking, such spectra of velocity show an isotropic high frequencies with a spectral slope of about ω^{-2} followed by an energy-containing band towards longer periods (periods longer than 100 days). In the vertical, the structure is roughly consistent (see Wunsch, 1997) with dominance of the barotropic and first baroclinic modes. Other results were summarized by Schmitz (1978). These results are modified in proximity to major topographic features. Figure 4-14 displays the mean normalized frequency spectra of horizontal velocities in the barotropic and first baroclinic modes from 105 current meter mooring measurements, which has been elaborated on by Wunsch (1997). At each site, the spectra have been normalized by their total energy before the average is performed. The averaged frequency spectra for zonal and meridional velocities in the barotropic and first baroclinic modes are very similar. We shall see later that in most regions the flows are isotropic, in the sense that the difference between the frequency spectra of the two components of horizontal velocities is statistically insignificant. The frequency spectra of the barotropic and first baroclinic modes also display similar structure, which implies that the frequency spectral shape of horizontal velocities is independent of depth. The variance-preserving figures show that kinetic energy are dominated by motions with periods around 100 days.

Moored temperature frequency spectra are not very dependent on geography and exhibit a behavior similar to that of velocity. In the regions away from major topographic features, the frequency spectral shape of the horizontal velocities and temperature is independent of depth, and the energy level of the temperature frequency spectra drops more rapidly with depth than that of the horizontal velocities.

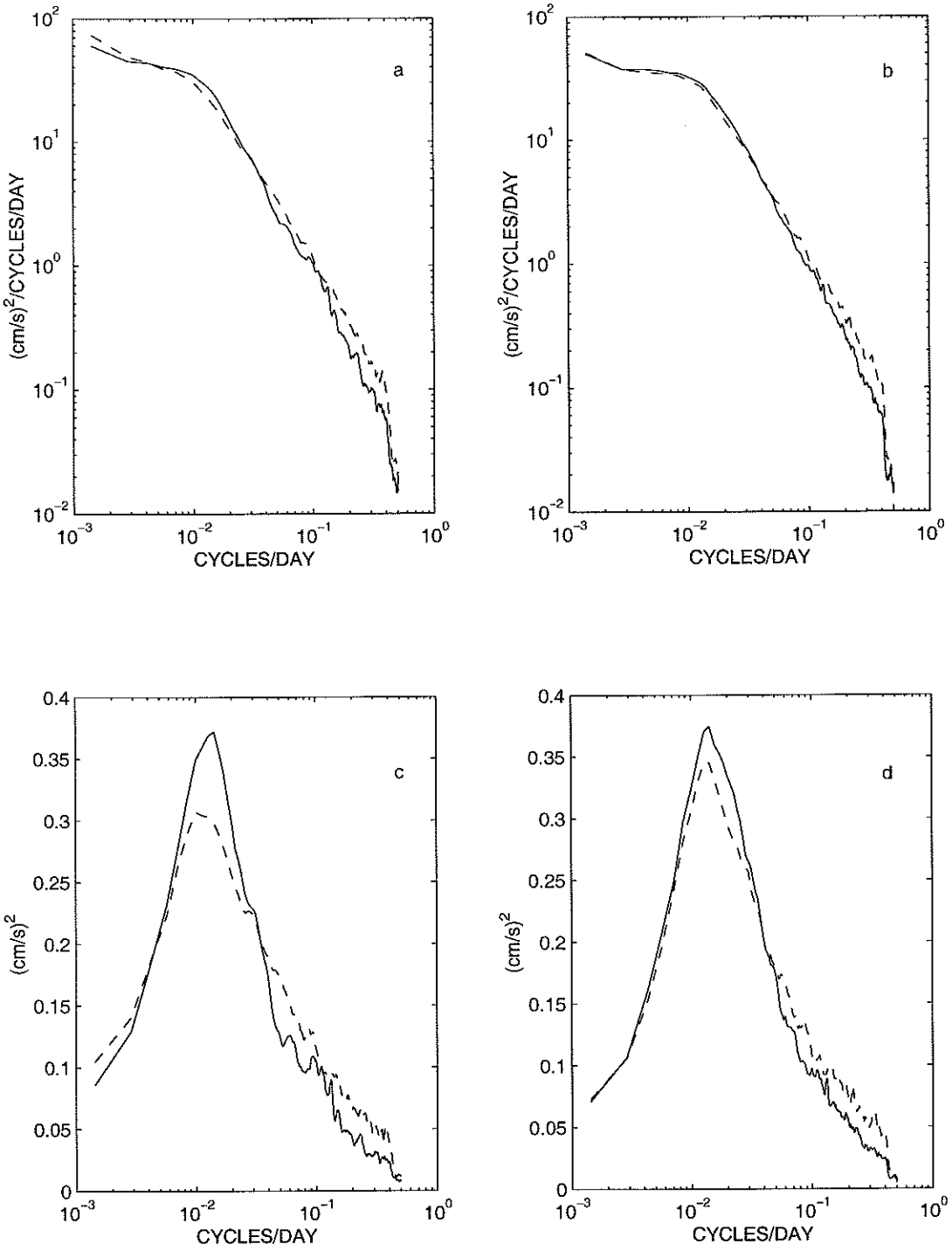

Figure 4-15: The mean normalized frequency spectra of zonal (a) and meridional (b) velocities in the barotropic (solid line) and first baroclinic modes (dashed line) from 105 current meter measurements (see Wunsch 1997). The variance-preserving form of zonal (c) and meridional (d) velocities. At each site, the spectra have been normalized by their total energy before the spatial average is done.

4.9 Heat fluxes

Large portions of the heat fluxes in the ocean-atmosphere system are carried by eddies. The eddy heat fluxes are fundamental to the understanding of climate change, the mechanisms of eddy generation, the interactions between eddy and mean flows and the parameterization of the eddy effect in ocean general circulation models. In spite of the importance of eddy heat fluxes, a quantitative global description of eddy heat fluxes in the ocean is still not available due to the difficulties of observing the ocean with sufficient space and time resolution. Recently, Wunsch (1999a) estimated the eddy heat fluxes based on quasi-global current meter and temperature mooring records. He concluded that eddy heat fluxes are quite small in the ocean interior and are only significant near western boundary current areas. In the western boundary area, significant eddy heat fluxes are confined to the top 1000 m. Because there is no significant eddy heat flux throughout much of the ocean interior, there is no need to parameterize the eddy heat flux there. The heat fluxes of the simple model in Chapter 3 are zero. Therefore in the ocean interior, the data and model are consistent to first order.

Because of the limitation of measurements, the eddy heat fluxes are often estimated indirectly through the theory of baroclinic instability or through eddy-resolved numerical models. For example, using four years of sea surface height measurements from the TOPEX/POSEIDON spacecraft, Stammer (1998) calculated the surface eddy kinetic energy and eddy scales under geostrophic assumptions, from which the global distribution of apparent eddy coefficient was produced. Based on the assumption that the eddy heat fluxes are produced through the baroclinic instability of the large scale geostrophic fields, he calculated the meridional eddy heat fluxes and found that strong meridional eddy fluxes exist in the western boundary current regions of all oceans and in the tropics equatorward of about 15° latitude. The significant eddy heat fluxes near the strong western boundary currents presumably result from the inhomogeneity of the low frequency variability as described in section 4.1.

4.10 Anisotropy

Two types of anisotropy for low frequency oceanic variability are found in this study. First, the energy distribution is not identical in all directions. For example, the three-dimensional spectrum of sea surface height anomaly, as described in previous sections, shows that there is more energy going westward at large scales and low frequencies. The second type of anisotropy is displayed in the form of differences between zonal and meridional components of horizontal velocity, which include the differences in the total energy, the differences in the frequency spectrum and the differences in the wavenumber spectrum. The difference between the frequency spectra of zonal and meridional components of horizontal velocity can be found from current meter records. The wavenumber spectra of zonal and meridional components of velocity can be obtained only from records of simultaneous mooring deployments.

The data used here are from the 105 quasi-global current meter moorings, as described by Wunsch (1997). I calculated the variance of zonal and meridional components of velocity in the barotropic and first baroclinic mode for each site and found that the variance of zonal and meridional velocity typically do not differ by more than a factor of 2 in the barotropic and first baroclinic modes. Because the energy level can not fully describe the current meter records, I further compared the frequency spectrum of zonal and meridional components in the barotropic and first baroclinic mode at each site. It is found that in general the difference between the frequency spectra of zonal and meridional components is statistically insignificant with respect to a 95% confidence interval. Only in the regions close to boundaries and jets, did I find significant anisotropy. Figures 4-16 and 4-17 are two examples where significant anisotropy is found. Figure 4-16 shows that the energy level of the frequency spectrum of the zonal component is over one order of magnitude higher than that of the meridional component at periods longer than 100 days in both the barotropic and first baroclinic modes. The result in figure 4-17 is the opposite; at periods longer than 50 days, the energy level of the meridional component is significantly higher than that of the zonal component in the two modes. The data used in figures 4-16

and 4-17 are taken inside the Gulf Stream and near the eastern boundary of the North Pacific, respectively. Therefore, the difference between the frequency spectrum of the zonal and meridional components in figure 4-16 is presumably related to the strong western boundary current, the Gulf Stream. The difference in figure 4-17 might be due to the meridional California Current system. The results in figure 4-16 and 4-17 suggest that the dynamics in the region close to jets and boundaries are distinct. The reason for the difference between the zonal and meridional components as displayed here awaits further study.

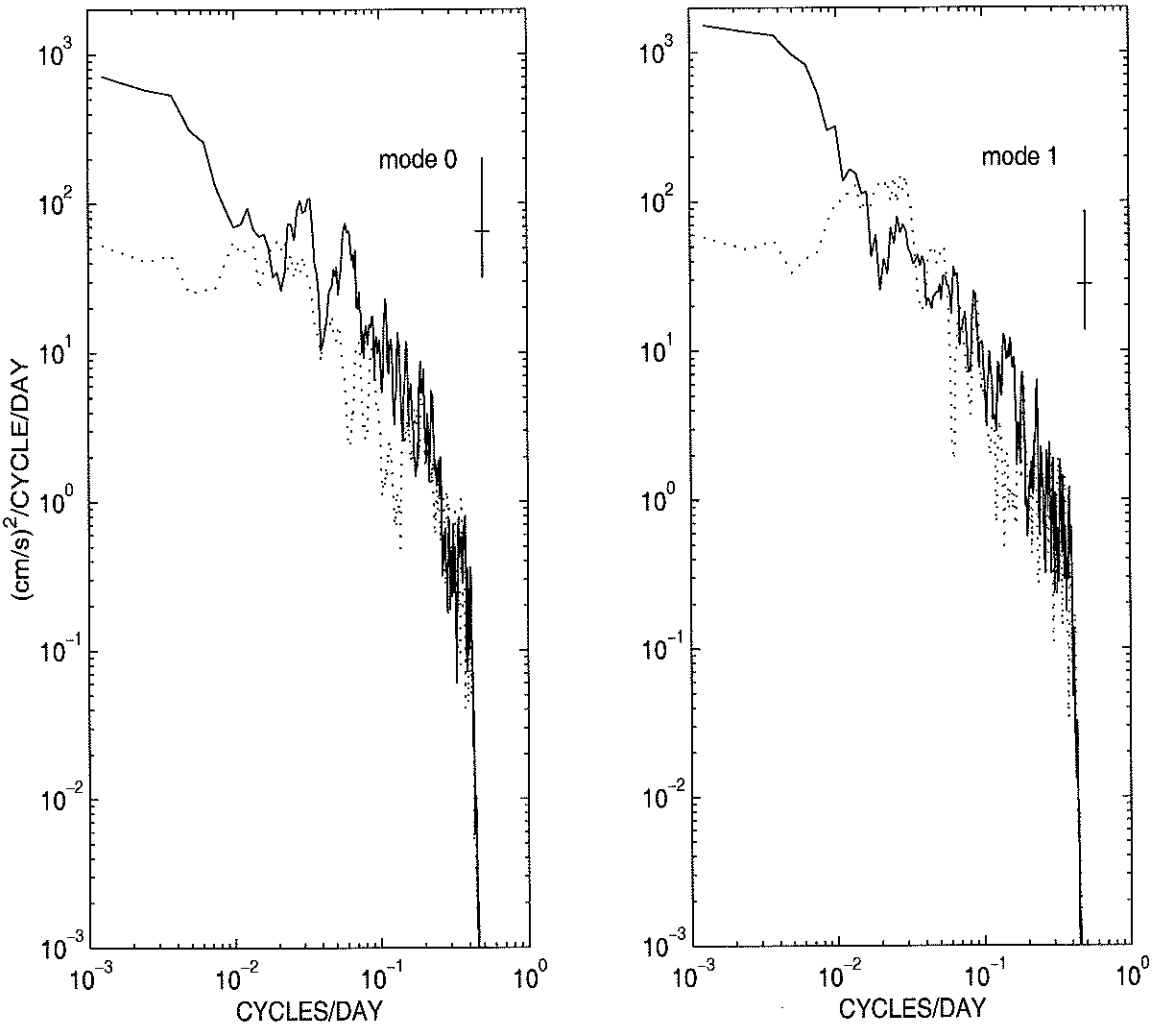

Figure 4-16: Frequency spectra for the zonal (solid line) and meridional (dotted line) component of horizontal velocity in the barotropic and first baroclinic mode at 38.8°N, 68.1°W. The spectra are estimated using D. Thompson's multitaper method (Percival and Walden, 1993). The ratio of the variance of zonal component to that of meridional component in the barotropic and first baroclinic mode is 3.5 and 2.7, respectively.

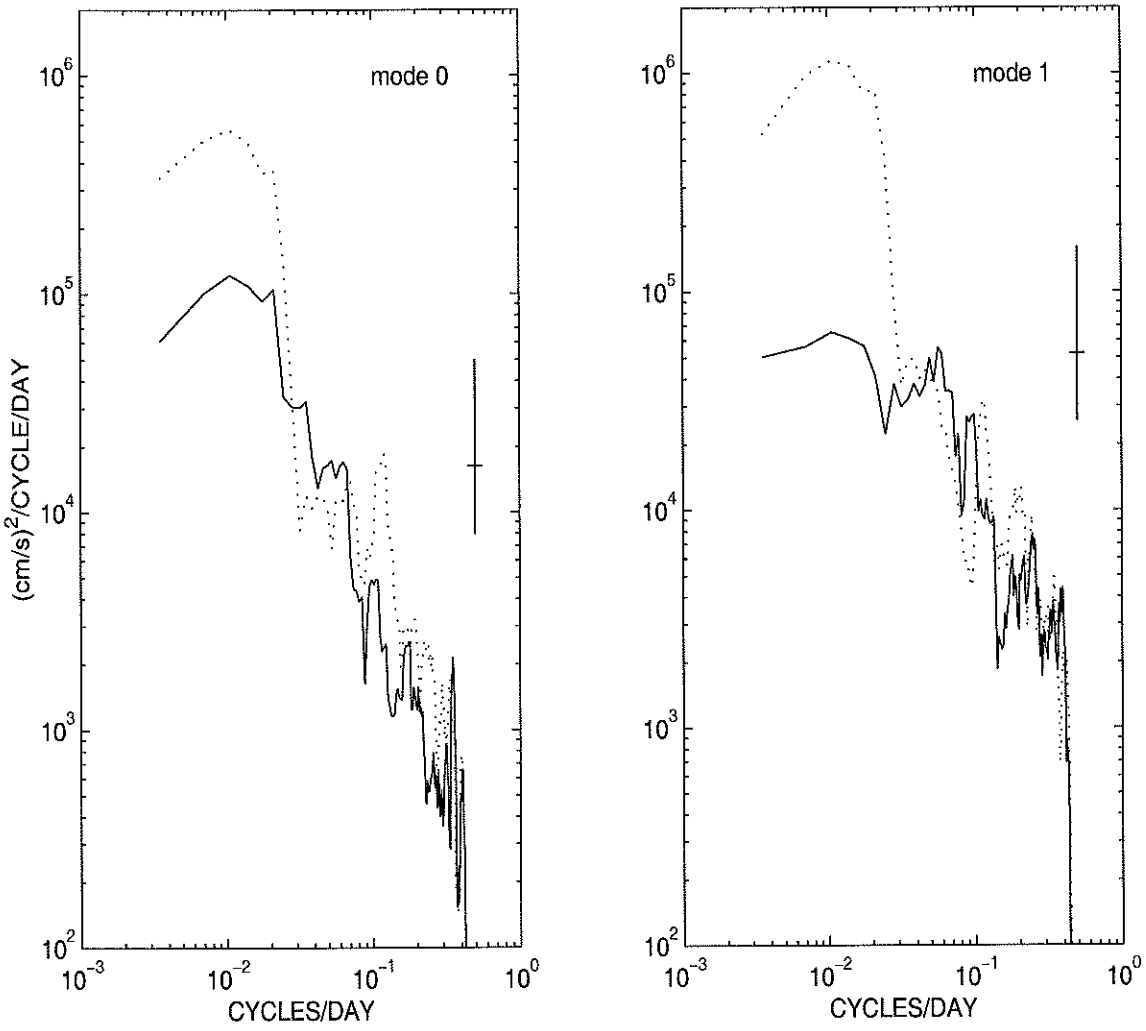

Figure 4-17: Same as figure 4-16 except at 38.2°N, 124.4°W. The ratio of the variance of zonal component to that of meridional component in the barotropic and first baroclinic mode is 0.34 and 0.25, respectively.

Chapter 5

Energy distribution in k, l and ω space part I: a scalar form

5.1 Fitting $\Phi(k, l, \omega, n, \phi, \lambda)$ from observations

Based upon the summary in chapter 4 of observed frequency and wavenumber spectra, I will choose forms for the separated functions making up the full $\Phi(k, l, \omega, n, \phi, \lambda)$. As demonstrated in chapter 3, once the three-dimensional spectrum for pressure of each mode is known, one can estimate $\Phi(k, l, \omega, n, \phi, \lambda)$ through the equation (3.8). Unfortunately, none of the full three-dimensional spectrum of each mode for any variable is available. Because the observed one-dimensional frequency and wavenumber spectral shapes are approximately independent of depth, one can infer that the frequency and wavenumber spectral shapes of each mode are approximately identical, and thus the formula for $\Phi(k, l, \omega, n, \phi, \lambda)$ will be the same for each vertical mode. Because the full three-dimensional spectrum is too complicated to be presented in an analytical form, I start here with the simple form as given by equation (4.3). It is assumed that the frequency spectral shape, wavenumber spectral shape, vertical structure and energy level are separable. The separated form in equation (4.3) is incapable of differentiating the westward-going energy from the eastward-going energy. A more sophisticated frequency and wavenumber coupled form will be produced in

chapter 7. In the following, I will choose the form of $B_n(k)$, $C_n(l)$, $D_n(\omega)$,$E_0(n)$ and $I(\phi, \lambda)$ in equation (4.3) according to the observations. Because most of the region is dominated by the first few modes as seen in the last chapter, only barotropic and first two baroclinic modes are included in my model: n=0, 1, 2. The form of $B_n(k)$, $C_n(l)$ and $D_n(\omega)$ are chosen to fit the globally averaged wavenumber and frequency spectral shape, respectively.

Choosing the $B_n(k)$ to fit the observed zonal-wavenumber spectrum

The $B_n(k)$ is chosen according to the globally averaged wavenumber spectral shape of sea surface height from T/P measurements:

$$B_n(k) = \begin{cases} \alpha_0 |k|^2 & \text{if } 0 < |k| \leq k_0 \\ \alpha_1 |k|^{-1/2} & \text{if } k_0 < |k| \leq k_1 \\ \alpha_2 |k|^{-5/2} & \text{if } k_1 < |k| \leq k_2 \\ |k|^{-4} & \text{if } |k| > k_2 \ , \end{cases} \tag{5.1}$$

where $k_2 = 0.008$ and $k_1 = 0.0025$ (cycles per km). For continuity of $B_n(k)$ at k_2 and k_1, $\alpha_2 = k_2^{-3/2}$ and $\alpha_1 = k_2^{-3/2} k_1^{-2}$. In the ocean, the longest wavelength is limited by the width of the ocean basin or the perimeter of the earth where the ocean circulates around the earth without barriers. Therefore, there is no energy at wavenumbers $0 \leq |k| \leq k_0$, where k_0 corresponds to the wavenumber of longest wave in the ocean. If the spectrum at wavenumbers $0 \leq |k| \leq k_0$ is chosen to be zero, it will be discontinuous at $|k| = k_0$, and thus the so-called Gibbs phenomenon will arise. In order to moderate the Gibbs phenomenon, the spectrum is chosen to diminish smoothly to zero from $k = k_0$ to $k = 0$, while it ensures that the energy at wavelengths longer than the width of the ocean basin is negligible. As displayed in equation (5.1), the wavenumber spectrum is simply chosen to be proportional to $|k|^2$ at wavenumbers $0 < |k| \leq k_0$. For continuity of $B_n(k)$ at k_0, $\alpha_0 = k_2^{-3/2} k_1^{-2} k_0^{-5/2}$. For simplicity, k_0 is assumed to be 0.0001 cycles per km. The corresponding wavelength of k_0 is 10,000 km, which is about as long as the width of the North Pacific ocean.

Equation (5.1) gives

$$\int_{-\infty}^{+\infty} B_n(k)dk = 5.1 \times 10^7. \tag{5.2}$$

Choosing the $C_n(l)$ to fit the observed meridional-wavenumber spectrum

The wavenumber spectra of sea surface height from T/P measurements suggest that $C_n(l)$ has the same form as $B_n(k)$.

Choosing the $D_n(\omega)$ to fit the observed frequency spectrum

The $D_n(\omega)$ is chosen according to the globally averaged frequency spectral shape of horizontal velocity:

$$D_n(\omega) = \begin{cases} \gamma_0 |\omega|^{-1/2} & \text{if } 0 < |\omega| \leq \omega_0 \\ |\omega|^{-2} & \text{if } |\omega| > \omega_0 \ , \end{cases} \tag{5.3}$$

where $\omega_0 = 0.01$ (cycles per day). For continuity of $D_n(k)$ at ω_0, $\gamma_0 = \omega_0^{-3/2}$. Equation (5.3) gives

$$\int_{-\infty}^{+\infty} D_n(\omega)d\omega = 600. \tag{5.4}$$

Now that the wavenumber and frequency spectral shapes have been chosen, the variance for each mode can be obtained

$$\begin{aligned} & \int_{-\infty}^{+\infty}\int_{-\infty}^{+\infty}\int_{-\infty}^{+\infty} \Phi(k,l,\omega,n,\phi,\lambda)dkdld\omega \\ = \ & I(\phi,\lambda)E_0(n)\left[\int_{-\infty}^{+\infty} B_n(k)dk\right]\left[\int_{-\infty}^{+\infty} C_n(l)dl\right]\left[\int_{-\infty}^{+\infty} D_n(\omega)d\omega\right] \\ = \ & 1.6 \times 10^{18} I(\phi,\lambda)E_0(n). \end{aligned} \tag{5.5}$$

The energy level of each mode

The total kinetic energy per unit surface area for each mode is

$$KE(n) = \int_{-\infty}^{+\infty}\int_{-\infty}^{+\infty}\int_{-\infty}^{+\infty} 2\pi^2(k^2+l^2)\Phi(k,l,\omega,n,\phi,\lambda)dkdld\omega$$

$$
\begin{aligned}
&= 2\pi^2 I(\phi,\lambda)E_0(n)\left[\int_{-\infty}^{+\infty} k^2 B_n(k)dk\right]\left[\int_{-\infty}^{+\infty} C_n(l)dl\right]\left[\int_{-\infty}^{+\infty} D_n(\omega)d\omega\right] \\
&\quad +2\pi^2 I(\phi,\lambda)E_0(n)\left[\int_{-\infty}^{+\infty} B_n(k)dk\right]\left[\int_{-\infty}^{+\infty} l^2 C_n(l)dl\right]\left[\int_{-\infty}^{+\infty} D_n(\omega)d\omega\right] \\
&= 6.3\times 10^{14} I(\phi,\lambda)E_0(n). \qquad (5.6)
\end{aligned}
$$

As seen in section 4.3, the vertical structure of eddy kinetic energy can be simply represented by the barotropic and first two baroclinic modes in the middle of the ocean, and roughly speaking, the kinetic energy of the first three modes is in the ratio of 1:1:1/2. Accordingly, if we choose $E_0(0) = 1$, then $E_0(1) = 1$ and $E_0(2) = 0.5$.

Choose $I(\phi,\lambda)$ to fit the observed surface kinetic energy

The surface kinetic energy for the model is

$$
\begin{aligned}
E_k(\phi,\lambda,z=0) &= \sum_{n=0}^{n=2} F_n^2(z=0)\left[\int_{-\infty}^{+\infty}\int_{-\infty}^{+\infty}\int_{-\infty}^{+\infty} 2\pi^2(k^2+l^2)\Phi(k,l,\omega,n,\phi,\lambda)dkdld\omega\right] \\
&= \sum_{n=0}^{n=2} F_n^2(z=0)KE(n) = 2.1\times 10^{12} I(\phi,\lambda). \qquad (5.7)
\end{aligned}
$$

Equation (5.7) yields

$$
I(\phi,\lambda) = \frac{E_k(\phi,\lambda,z=0)}{2.1\times 10^{12}}. \qquad (5.8)
$$

The empirical formulas for the surface kinetic energy in the North Pacific and the North Atlantic are given by equations (4.1) and (4.2), respectively.

The potential energy per unit surface area for each mode

$$
\begin{aligned}
PE(n,\phi,\lambda) &= \frac{1}{2R_n^2}\int_{-\infty}^{+\infty}\int_{-\infty}^{+\infty}\int_{-\infty}^{+\infty}\Phi(k,l,\omega,n,\phi,\lambda)dkdld\omega \\
&= \frac{7.8\times 10^{17} I(\phi,\lambda)E_0(n)}{R_n^2}. \qquad (5.9)
\end{aligned}
$$

The ratio of kinetic energy to potential energy per unit surface area for first baroclinic mode

$$
\frac{KE(1,\phi,\lambda)}{PE(1,\phi,\lambda)} = 8.1\times 10^{-4} R_1^2. \qquad (5.10)
$$

If we take $f = 10^{-4}\text{s}^{-1}$, which is a typical value of f at mid-latitude, equation (2.21) gives $R_1 = 25\text{km}$. Then

$$\frac{KE(1,\phi,\lambda)}{PE(1,\phi,\lambda)} = 0.51. \tag{5.11}$$

The zonal-wavenumber spectrum of sea surface height

$$\begin{aligned}\Upsilon_\eta(k,\phi,\lambda) &= \sum_{n=0}^{n=2} \frac{f^2 F_n^2(z=0)}{g^2} \int_{-\infty}^{+\infty}\int_{-\infty}^{+\infty} \Phi(k,l,\omega,n,\phi,\lambda)dld\omega \\ &= \frac{f^2 I(\phi,\lambda)}{g^2} \sum_{n=0}^{n=2} F_n^2(z=0)E_0(n)\left[\int_{-\infty}^{+\infty} C_n(l)dl\right]\left[\int_{-\infty}^{+\infty} D_n(\omega)d\omega\right] B_n(k). \end{aligned} \tag{5.12}$$

Note the consistency of units for different variables. $\int_{-\infty}^{+\infty}\int_{-\infty}^{+\infty}\Phi(k,l,\omega,n,\phi,\lambda)dld\omega$ has the units of $(\text{cm}^2/s^2)\text{m}/(\text{cycles/km})^3$, the units of $F_n^2(z)$ are m^{-1}, the units of f are s^{-1}, and the units of g are km s^{-2}. If we take $f = 2\Omega sin\phi = 1.45 \times 10^{-4} sin\phi$ s^{-1} and $g = 9.8 \times 10^{-3}\text{km s}^{-2}$, then

$$\begin{aligned}\Upsilon_\eta(k,\phi,\lambda) &= \frac{f^2 I(\phi,\lambda) \times 5.1 \times 10^7 \times 600}{g^2}[F_0^2(z=0) + F_1^2(z=0) + 0.5 \times F_2^2(z=0)]B_1(k) \\ &= 2.2 \times 10^4 sin^2\phi\ I(\phi,\lambda)B_1(k)\ \ [\text{cm}^2/(\text{cycles/km})]. \end{aligned} \tag{5.13}$$

The meridional-wavenumber spectrum of sea surface height

$$\begin{aligned}\Upsilon_\eta(l,\phi,\lambda) &= \sum_{n=0}^{n=2} \frac{f^2 F_n^2(z=0)}{g^2} \int_{-\infty}^{+\infty}\int_{-\infty}^{+\infty} \Phi(k,l,\omega,n,\phi,\lambda)dkd\omega \\ &= \frac{f^2 I(\phi,\lambda)}{g^2} \sum_{n=0}^{n=2} F_n^2(z=0)E_0(n)\left[\int_{-\infty}^{+\infty} B_n(k)dk\right]\left[\int_{-\infty}^{+\infty} D_n(\omega)d\omega\right] C_n(l) \\ &= 2.2 \times 10^4 sin^2\phi\ I(\phi,\lambda)C_1(l)\ \ [\text{cm}^2/(\text{cycles/km})]. \end{aligned} \tag{5.14}$$

The variance of sea surface height

$$\begin{aligned}\sigma_\eta^2(\phi,\lambda) &= \sum_{n=0}^{n=2} \frac{f^2 F_n^2(z=0)}{g^2} \int_{-\infty}^{+\infty}\int_{-\infty}^{+\infty}\int_{-\infty}^{+\infty} \Phi(k,l,\omega,n,\phi,\lambda)dkdld\omega \\ &= 1.1 \times 10^{12} sin^2\phi\ I(\phi,\lambda)\end{aligned}$$

$$= \quad 0.52 sin^2\phi \; E_k(\phi, \lambda, z = 0) \quad [\mathrm{cm}^2]. \tag{5.15}$$

The zonal-wavenumber spectrum of temperature

$$\Upsilon_\theta(k, z, \phi, \lambda) = \sum_{n=0}^{n=2} f^2 G_n^2(z) (\frac{\partial \theta_0}{\partial z})^2 \int_{-\infty}^{+\infty} \int_{-\infty}^{+\infty} \Phi(k, l, \omega, n, \phi, \lambda) dl d\omega$$

$$= f^2 I(\phi, \lambda) (\frac{\partial \theta_0}{\partial z})^2 [G_1^2(z) + 0.5 \times G_2^2(z)] \left[\int_{-\infty}^{+\infty} C_1(l) dl\right] \left[\int_{-\infty}^{+\infty} D_1(\omega) d\omega\right] B_1(k)$$

$$= 6.4 \times 10^4 sin^2\phi I(\phi, \lambda) [G_1^2(z) + 0.5 \times G_2^2(z)] (\frac{\partial \theta_0}{\partial z})^2 B_1(k) \quad [^\circ\mathrm{C}^2/(\mathrm{cycles/km})], \tag{5.16}$$

where the units of $G_n^2(z)$ are $\mathrm{s}^4\mathrm{m}^{-3}$ and the units of $\partial\theta_0/\partial z$ are $^\circ$C/m.

The meridional-wavenumber spectrum of temperature

$$\Upsilon_\theta(l, z, \phi, \lambda) = \sum_{n=0}^{n=2} f^2 G_n^2(z) (\frac{\partial \theta_0}{\partial z})^2 \int_{-\infty}^{+\infty} \int_{-\infty}^{+\infty} \Phi(k, l, \omega, n, \phi, \lambda) dk d\omega$$

$$= f^2 I(\phi, \lambda) (\frac{\partial \theta_0}{\partial z})^2 [G_1^2(z) + 0.5 \times G_2^2(z)] \left[\int_{-\infty}^{+\infty} B_1(k) dk\right] \left[\int_{-\infty}^{+\infty} D_1(\omega) d\omega\right] C_1(l)$$

$$= 6.4 \times 10^4 sin^2\phi \; I(\phi, \lambda) [G_1^2(z) + 0.5 \times G_2^2(z)] (\frac{\partial \theta_0}{\partial z})^2 C_1(l) \quad [^\circ\mathrm{C}^2/(\mathrm{cycles/km})], \tag{5.17}$$

where the units of $G_n^2(z)$ are $\mathrm{s}^4\mathrm{m}^{-3}$ and the units of $\partial\theta_0/\partial z$ are $^\circ$C/m.

The frequency spectrum of sea surface height

$$\begin{aligned}
\Upsilon_\eta(\omega, \phi, \lambda) &= \sum_{n=0}^{n=2} \frac{f^2 F_n^2(z=0)}{g^2} \int_{-\infty}^{+\infty} \int_{-\infty}^{+\infty} \Phi(k, l, \omega, n, \phi, \lambda) dk dl \\
&= \frac{f^2 I(\phi, \lambda)}{g^2} \sum_{n=0}^{n=2} F_n^2(z=0) E_0(n) \left[\int_{-\infty}^{+\infty} B_n(k) dk\right] \left[\int_{-\infty}^{+\infty} C_n(l) dl\right] D_n(\omega) \\
&= 1.9 \times 10^9 sin^2\phi \; I(\phi, \lambda) D_1(\omega) \quad [\mathrm{cm}^2/(\mathrm{cycles/km})] \; .
\end{aligned} \tag{5.18}$$

The frequency spectrum of zonal velocity

$$\Upsilon_u(\omega, z, \phi, \lambda) = \sum_{n=0}^{n=2} \int_{-\infty}^{+\infty} \int_{-\infty}^{+\infty} 4\pi^2 l^2 F_n^2(z) \Phi(k, l, \omega, n, \phi, \lambda) dk dl$$

$$= 4\pi^2 I(\phi, \lambda) \sum_{n=0}^{n=2} E_0(n) F_n^2(z=0) \left[\int_{-\infty}^{+\infty} B_n(k) dk\right] \left[\int_{-\infty}^{+\infty} l^2 C_n(l) dl\right] D_n(\omega)$$

$$= 1.1 \times 10^{12} \left[F_0^2(z) + F_1^2(z) + 0.5 \times F_2^2(z)\right] D_1(\omega) \quad [\mathrm{cm}^2/\mathrm{s}^2/(\mathrm{cycles/day})], \tag{5.19}$$

where the units of $F_n^2(z)$ are m^{-1}.

The frequency spectrum of meridional velocity

$$\Upsilon_v(\omega,z,\phi,\lambda)=\sum_{n=0}^{n=2}\int_{-\infty}^{+\infty}\int_{-\infty}^{+\infty}4\pi^2k^2F_n^2(z)\Phi(k,l,\omega,n,\phi,\lambda)dkdl$$
$$=4\pi^2I(\phi,\lambda)\sum_{n=0}^{n=2}F_n^2(z)E_0(n)\left[\int_{-\infty}^{+\infty}k^2B_n(k)dk\right]\left[\int_{-\infty}^{+\infty}C_n(l)dl\right]D_n(\omega)$$
$$=1.1\times10^{12}\left[F_0^2(z)+F_1^2(z)+0.5\times F_2^2(z)\right]D_1(\omega)\ \ [\mathrm{cm}^2/\mathrm{s}^2/(\mathrm{cycles/day})],\quad(5.20)$$

where the units of $F_n^2(z)$ are m^{-1}. Note that the frequency spectra of zonal and meridional velocities are the same.

The frequency spectrum of temperature

$$\Upsilon_\theta(\omega,z,\phi,\lambda)=\sum_{n=0}^{n=2}f^2G_n^2(z)(\frac{\partial\theta_0}{\partial z})^2\int_{-\infty}^{+\infty}\int_{-\infty}^{+\infty}\Phi(k,l,\omega,n,\phi,\lambda)dkdl$$
$$=f^2I(\phi,\lambda)(\frac{\partial\theta_0}{\partial z})^2[G_1^2(z)+0.5\times G_2^2(z)]\left[\int_{-\infty}^{+\infty}B_1(k)dk\right]\left[\int_{-\infty}^{+\infty}C_1(l)dl\right]D_1(\omega)$$
$$=5.4\times10^9sin^2\phi\ I(\phi,\lambda)[G_1^2(z)+0.5\times G_2^2(z)](\frac{\partial\theta_0}{\partial z})^2D_1(\omega)\ \ [^\circ\mathrm{C}^2/(\mathrm{cycles/day})],(5.21)$$

where the units of $G_n^2(z)$ are $\mathrm{s}^4\mathrm{m}^{-3}$, the units of $\partial\theta_0/\partial z$ are $^\circ$C/m.

5.2 Model and data comparison

In the above section, I have specified the formula for each component of $\Phi(k,l,\omega,n,\phi,\lambda)$: $B_n(k)$, $C_n(l)$, $D_n(\omega)$, $E_0(n)$ and $I(\phi,\lambda)$, based on different observations. There may be, however, some incompatibilities among different observations. For example, the vertical structure of the model is specified according to the observed vertical structure of kinetic energy. However, it is unclear whether the vertical structure of the temperature (potential energy) is dynamically consistent with that of the kinetic energy. Another example is the wavenumber spectral shape. Both T/P and XBT measurements can provide estimates of wavenumber spectral shape. If they are not dynamically consistent, the function $\Phi(k,l,n,\omega,\lambda)$ through which diverse observations can be rec-

onciled will not exist. In this section, I will make model/data comparisons to see how well each model spectrum fits the corresponding observation with the $\Phi(k, l, \omega, n, \phi, \lambda)$ we chose. We do not expect the model to fit the observations perfectly, because the different wavenumber, frequency and vertical mode structure found in different places have been neglected, the seasonal cycle is not considered either, etc.

Zonal-wavenumber, meridional-wavenumber and frequency spectrum of sea surface height

The model and observed zonal-wavenumber, meridional-wavenumber and frequency spectra are plotted in figure 5-1, 5-2 and 5-3. The observed spectra come from the area of 25° – 50°N and 195° – 225°E with a center latitude at 37.5°N, which have been described in detail in section 4.4. The energy level inside this area is relatively uniform. According to the equation (4.1), the average value $E_k(\phi, \lambda, z = 0)$ in this area is about 94 cm^2/s^2; therefore, $I(\phi, \lambda) = 4.5 \times 10^{-11}$. Figures 5-1, 5-2 and 5-3 show that the model spectra are reasonable fits to the observations in general. One major difference between the observations and the model is that at wavelengths shorter than 200 km, the observed wavenumber spectrum is redder than the model spectrum. As discussed in section 4.4, there is some uncertainty of the observed wavenumber spectral shape at wavelengths less than 200 km. Another obvious difference is that the observed frequency spectrum is slightly redder than the model spectrum at periods longer than 100 days.

Temperature wavenumber spectrum

The observed temperature wavenumber spectrum in figure 5-4 is from the XBT data in the eastern North Pacific described in section 4.7. The XBT line ranges from (236°E, 38°N) to (202°E, 21°N) and the center latitude is 30°N. The surface eddy kinetic energy along this XBT line is relatively homogeneous. According to equation (4.1), the mean value of surface kinetic energy along this XBT line is about 150 cm^2/s^2. Because the vertical gradient of mean temperature changes strongly with location in the upper ocean, which violates the assumption of horizontal homogeneity, we compare the model spectrum with the observations at the depth of 700 m as

a representative result. The vertical gradient of mean temperature along the XBT line at this depth changes relatively less sharply. The mean value of $\partial\theta_0/\partial z$ is about 0.0041°C/m. With this choice of energy level and vertical gradient of mean temperature, the model temperature wavenumber spectrum is plotted in figure 5-4. As displayed in figure 5-4, the model spectrum fits the observations very well in terms of spectral shape and energy level.

Frequency spectrum of horizontal velocities and temperature

One set of current meter mooring data is analyzed here, which is located at (39.5°N, 232.3°E) inside the low energy area in the eastern North Pacific. It has current and temperature meters at nominal depths of 160, 580, 595, 1230, 3000 and 3800 m. The measurements at 3800 m are neglected because the signal for temperature perturbations is very weak and the record is primarily dominated by the noise. From equation (4.1), $E_k(39.5°N, 232.3°E, z = 0) = 86\text{cm}^2/\text{s}^2$. Therefore, $I(39.5°N, 232°E) = 4.1 \times 10^{-11}$. The vertical gradients of the mean temperature at depths of 160, 580, 595, 1230,and 3000 are 0.020, 0.0042, 0.0040, 0.0019 and 0.00024°C/m, respectively. The model and observed spectra are plotted in figure 5-5. The general agreement between the model and the observed spectra is quite pleasing.

Ratio of kinetic energy to potential energy

The ratio of kinetic energy to potential energy of the first baroclinic mode is 0.51 in mid-latitudes (equation 5.11). This value is consistent with the result obtained by Wunsch(1999b) from current meter and temperature mooring measurements.

5.3 Summary

In this chapter, a regional model for the energy density $\Phi(k, l, \omega, n, \phi, \lambda)$ of the low frequency variability in the ocean is produced. Only the first three modes are included in my model: the barotropic and first two baroclinic modes. For each mode I choose

$$\Phi(k, l, \omega, n, \phi, \lambda) = B_n(k)C_n(l)D_n(\omega)E_0(n)I(\phi, \lambda), \tag{5.22}$$

and based on various observations, I obtain:

(1) the meridional- and zonal-wavenumber spectral shape

$$C_n(l) = B_n(k) = \begin{cases} 2.2 \times 10^{18}|k|^2 & \text{if } 0 < |k| \leq k_0 \\ 2.2 \times 10^{8}|k|^{-1/2} & \text{if } k_0 < |k| \leq k_1 \\ 1.4 \times 10^{3}|k|^{-5/2} & \text{if } k_1 < |k| \leq k_2 \\ |k|^{-4} & \text{if } |k| > k_2 \ , \end{cases} \tag{5.23}$$

where $k_2 = 0.008$, $k_1 = 0.0025$ and $k_0 = 0.0001$ (cycles per km).

(2) the frequency spectral shape

$$D_n(\omega) = \begin{cases} 1000|\omega|^{-1/2} & \text{if } 0 < |\omega| \leq \omega_0 \\ |\omega|^{-2} & \text{if } |\omega| > \omega_0 \ , \end{cases} \tag{5.24}$$

where $\omega_0 = 0.01$ (cycles per day).

(3) the partition among vertical modes

$$E_0(0) = 1, E_0(1) = 1, E_0(2) = 0.5. \tag{5.25}$$

(4) the energy magnitude

$$I(\phi, \lambda) = \frac{E_k(\phi, \lambda, z = 0)}{2.1 \times 10^{12}}. \tag{5.26}$$

The empirical formula for the surface kinetic energy in the North Pacific is

$$\begin{aligned} E_k(\phi, \lambda, z = 0) \ &= \ 30 + \frac{32}{\sin^2\phi} + 1000\exp\{-[\frac{(\lambda - 150)^2}{900} + \frac{(\phi - 35)^2}{50}]\} \\ &\quad -80\exp\{-[\frac{(\lambda - 190)^2}{1600} + \frac{(\phi - 42)^2}{200}]\}, \end{aligned} \tag{5.27}$$

where λ is the longitude , ϕ is the latitude and the units of E_k are $\mathrm{cm}^2/\mathrm{s}^2$.

The empirical formula for the surface kinetic energy in the North Atlantic is

$$E_k(\phi,\lambda,z=0) = 50 + \frac{35}{\sin^2\phi} + 1000\exp\{-[\frac{(\lambda-305)^2}{400} + \frac{(\phi-43)^2}{80}]\} -$$
$$280\exp\{-[\frac{(\lambda-320)^2}{2000} + \frac{(\phi-16)^2}{200}]\} - 160\exp\{-[\frac{(\lambda-320)^2}{900} + \frac{(\phi-42)^2}{50}]\} \quad (5.28)$$

where the units of E_k are $\mathrm{cm}^2/\mathrm{s}^2$.

The frequency spectral shape, wavenumber spectral shape and vertical structure are universal in my model; only the energy level is a function of geography. The parameters for the wavenumber and frequency spectral shape in my model are primarily chosen to fit the globally averaged spectra of the observations. This empirical model is a good first-order approximation to the true ocean, because the observed frequency, wavenumber and mode structure displays strikingly universal characteristics. Nonetheless, we need to keep in mind that the frequency, wavenumber and mode structure do show some variations from region to region, even if these variations are very small compared with the variations of eddy kinetic energy with geography. These changes of frequency, wavenumber and vertical structure with location are of great importance to the understanding of eddy generation mechanism (Stammer, 1997a). Based on different observations, a rough estimate of the uncertainty of my empirical model is provided here. First, the transitional wavenumber k_1 in equation (5.1) is assumed to be universal, and $k_1 = 0.0025$ cycles/km. The study by Stammer (1997a) shows that k_1 is a function of latitude, and it increases with latitude, ranging from 0.002 cycles/km at 15°N to 0.005 cycles/km at 60°N. Let us assume $B_n(k) \propto k^p$ and $D_n(\omega) \propto \omega^r$. The values of p and r at different wavenumber and frequency bands in my model are given in equation (5.1) and (5.3), respectively. In general, the uncertainty of p is greater at high wavenumbers. At wavelengths longer than about 400 km, the global average value of p is -0.5. The study by Stammer (1997a) showed that the spectral slope p at this wavenumber band is nearly independent of location (his figure 16), and that p changes from about -3.0 to -2.2 over the wavelengths between about 100 and 400 km from region to region. There is great uncertainty associated with the

wavenumber spectral shape from T/P measurements at wavelengths less than about 100 km because of the measurement noise and aliasing of interval waves. Wunsch and Stammer (1995) obtained a $k^{-4/3}$ power law at this high wavenumber band and argued that this is dominated by noise. The wavenumber spectra of high-quality XBT measurements in chapter 4 show that the slope is about -4 at wavelengths less than 150 km. Overall, the change of p with location is within about 15% in respect to the global averaged value of p except for the wavelengths less than 100 km. There is some uncertainty of the frequency spectral shape also. The globally averaged spectral slope of horizontal velocity is -0.5 at periods longer than 100 days; however, the spectral slope of sea surface hight is about -0.8 and some local current meter measurements show that the spectrum of horizontal velocity is nearly white at periods longer than 100 days. Although the study by Wunsch (1997) showed that on average the partitioning of kinetic energy among barotropic and first baroclinic mode is roughly equal, the exact value for it is a function of location. For example, the mid-Atlantic ridge region shows strong first baroclinic mode contribution. Interested readers should consult Wunsch (1997).

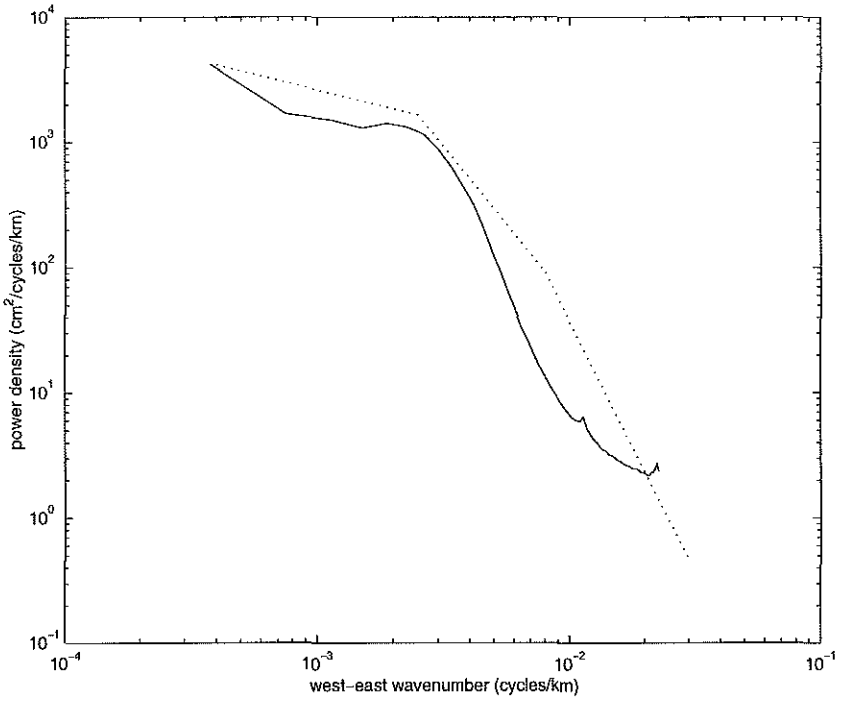

Figure 5-1: Zonal-wavenumber spectrum of sea surface height. Solid line is the observed spectrum. Dotted line is the corresponding model spectrum.

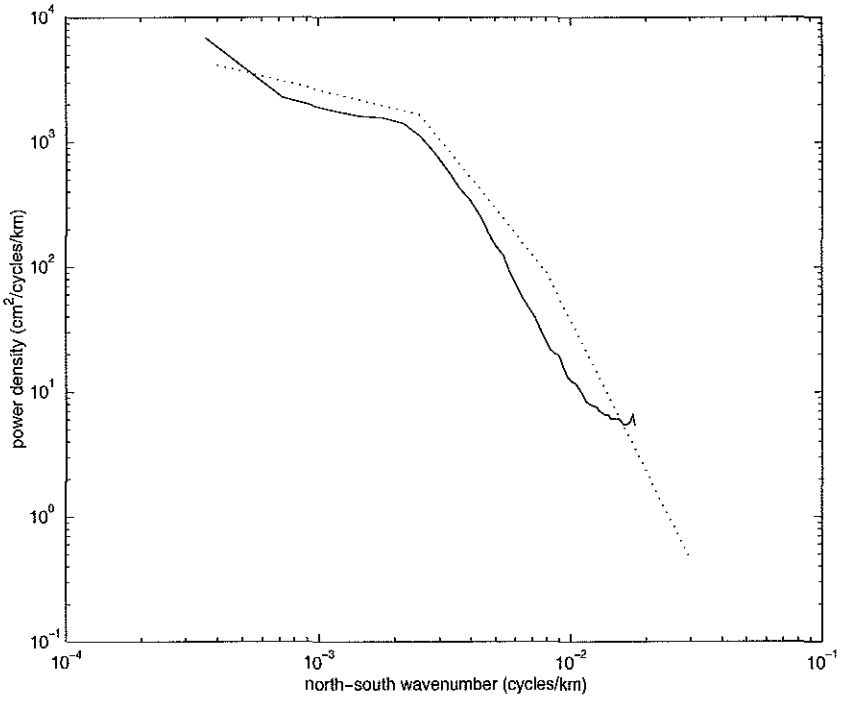

Figure 5-2: Meridional-wavenumber spectrum of sea surface height. Solid line is the observed spectrum. Dotted line is the corresponding model spectrum.

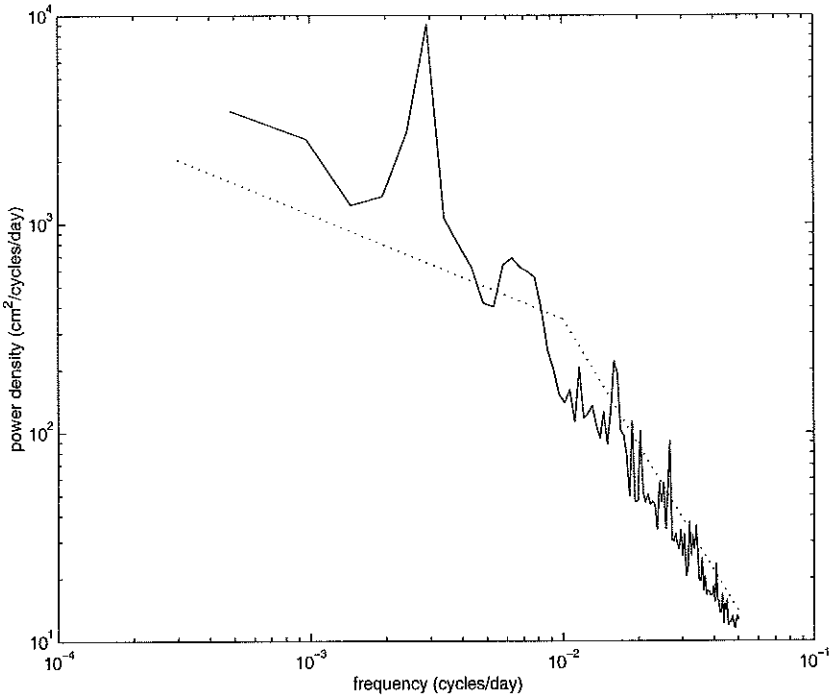

Figure 5-3: Frequency spectrum of sea surface height. Solid line is the observed spectrum. Dotted line is the corresponding model spectrum. There is a striking peak at the annual period on the observed spectrum.

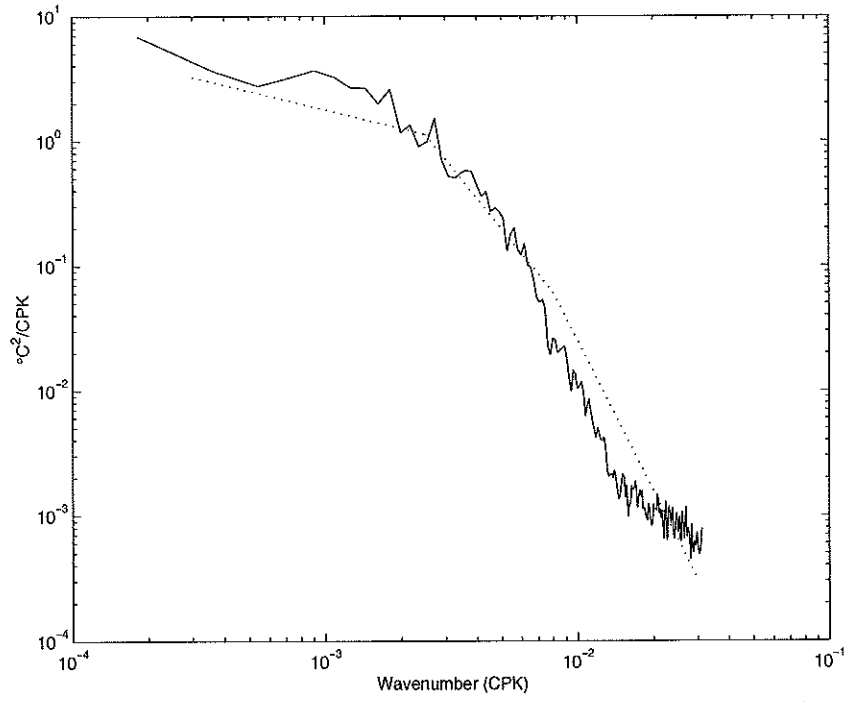

Figure 5-4: Zonal-wavenumber spectrum of temperature. Solid line is the observed spectrum. Dotted line is the corresponding model spectrum.

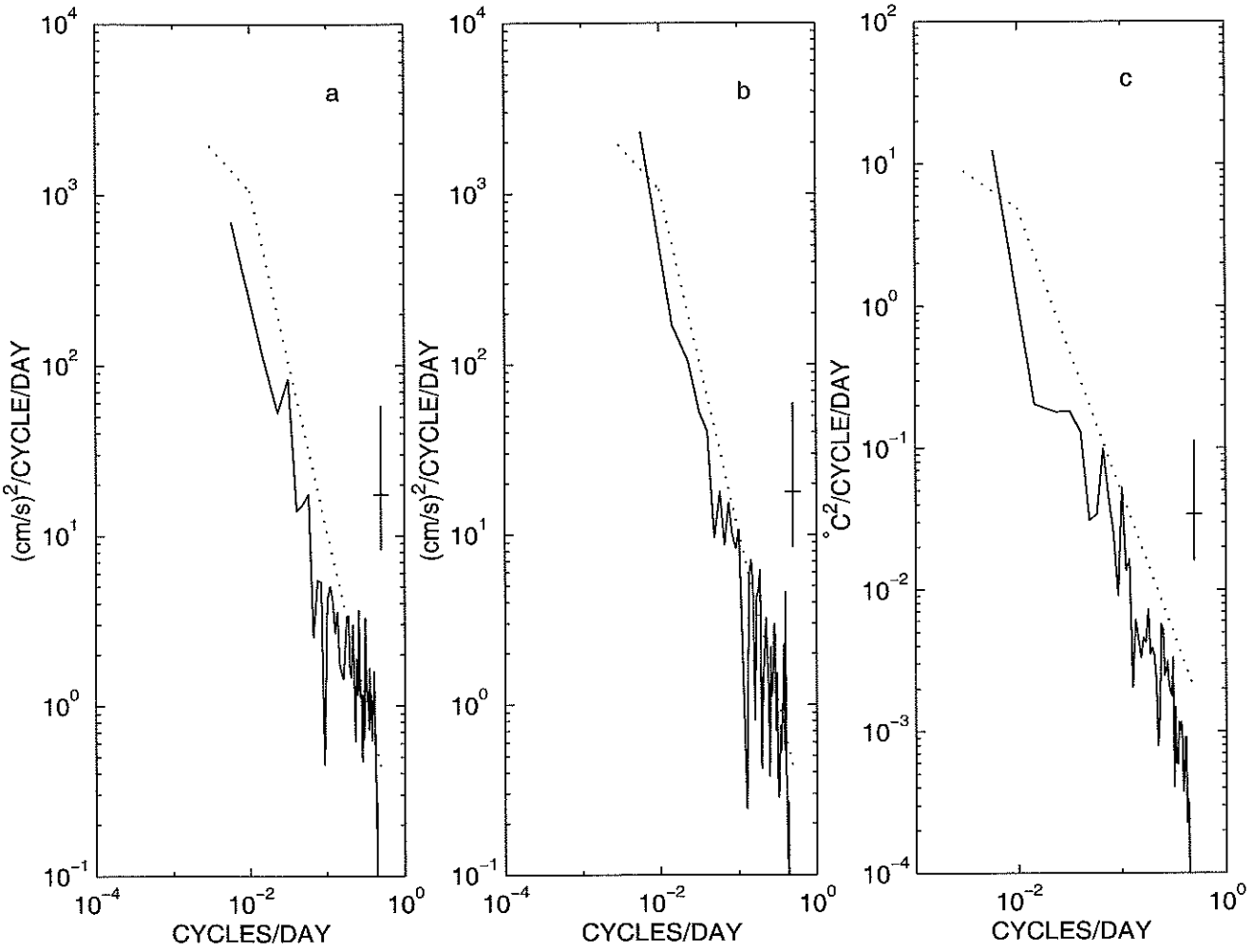
a
b
c
(cm/s)^2/CYCLE/DAY
(cm/s)^2/CYCLE/DAY
°C^2/CYCLE/DAY
CYCLES/DAY
CYCLES/DAY
CYCLES/DAY

(i)

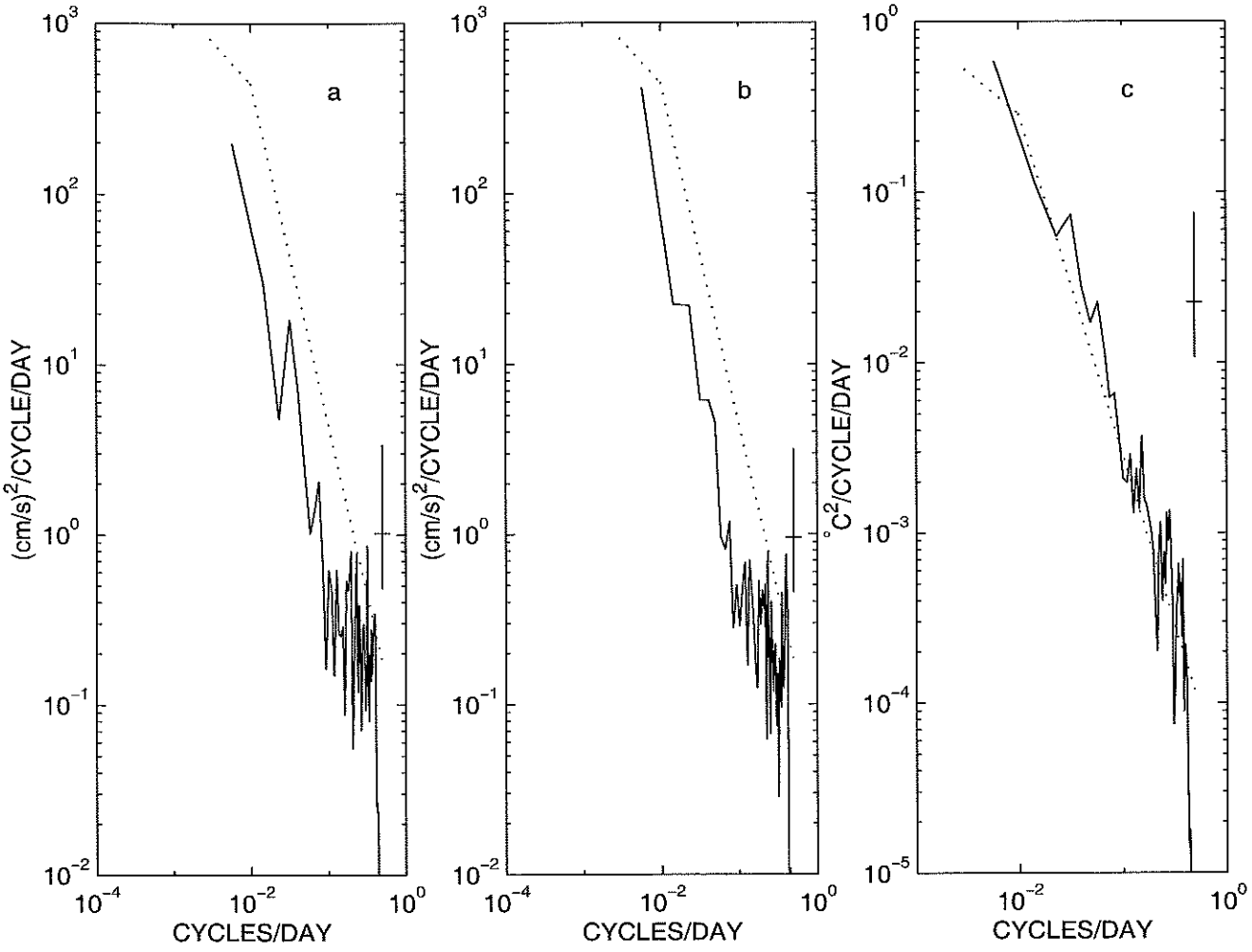
a
b
c
(cm/s)^2/CYCLE/DAY
°C^2/CYCLE/DAY
CYCLES/DAY
10^3
10^2
10^1
10^0
10^{-1}
10^{-2}
10^{-3}
10^{-4}
10^{-5}

(ii)

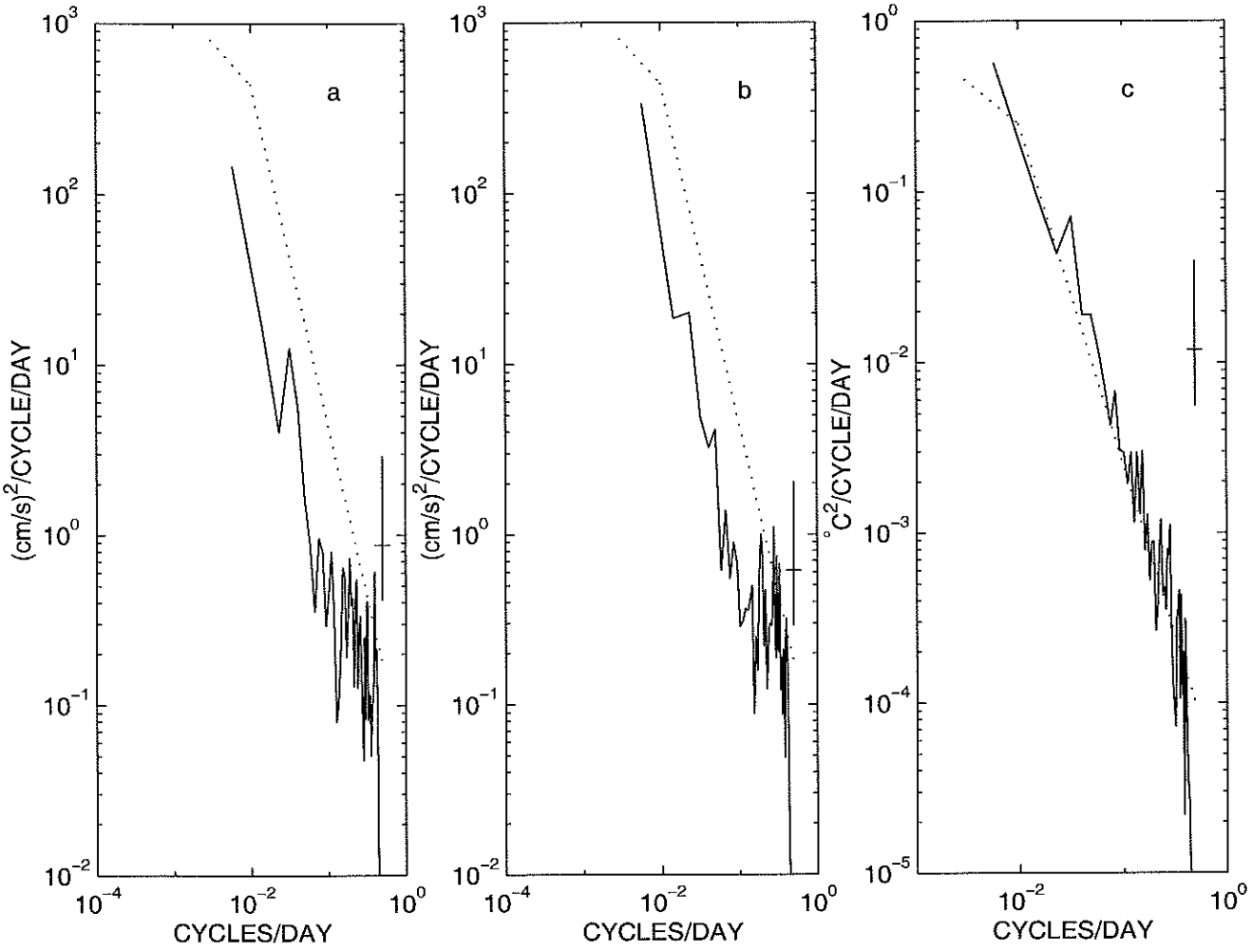
a
b
c
(cm/s)^2/CYCLE/DAY
(cm/s)^2/CYCLE/DAY
°C^2/CYCLE/DAY
CYCLES/DAY
CYCLES/DAY
CYCLES/DAY

(iii)

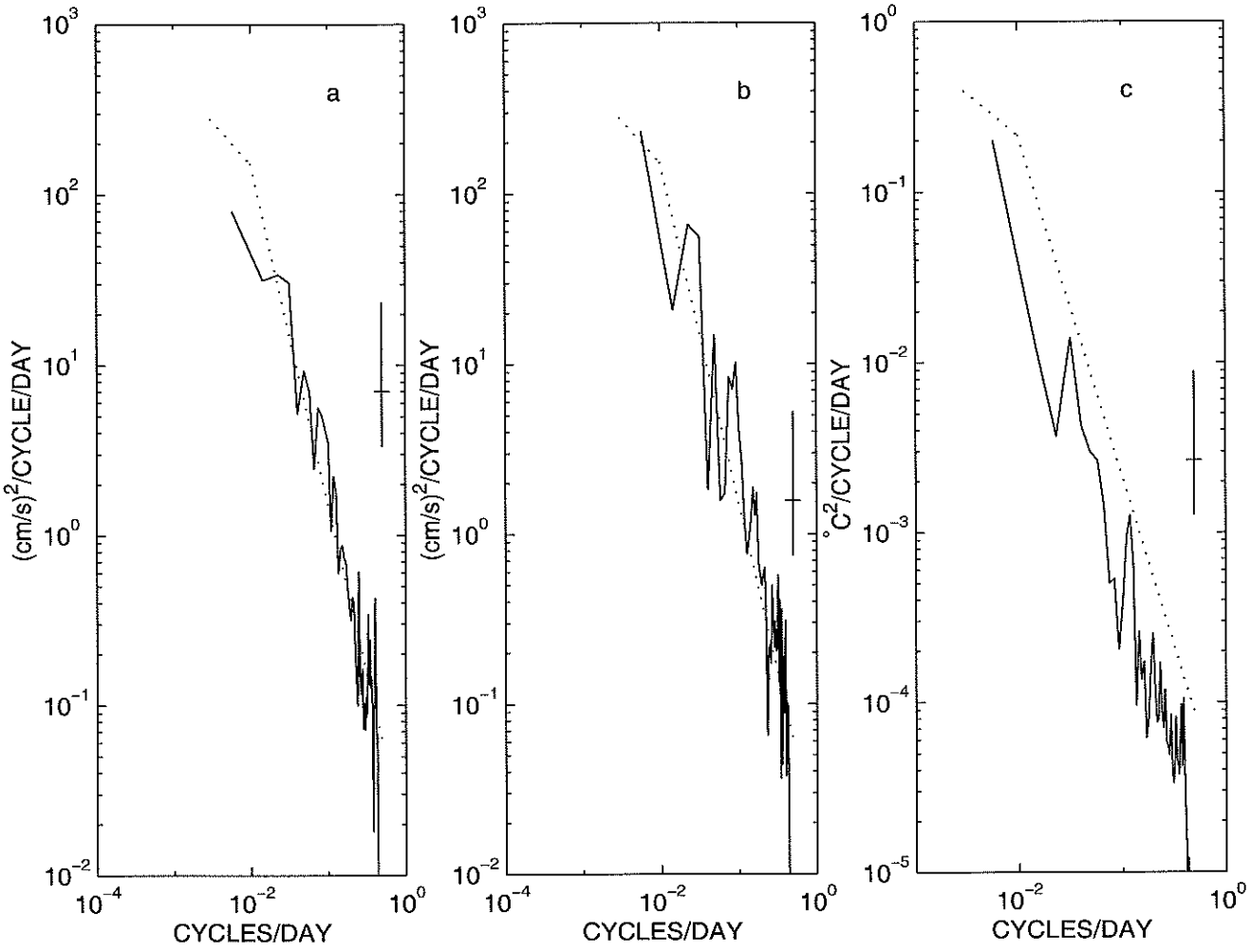
a
b
c
(cm/s)^2/CYCLE/DAY
(cm/s)^2/CYCLE/DAY
°C^2/CYCLE/DAY
CYCLES/DAY
CYCLES/DAY
CYCLES/DAY

(iv)

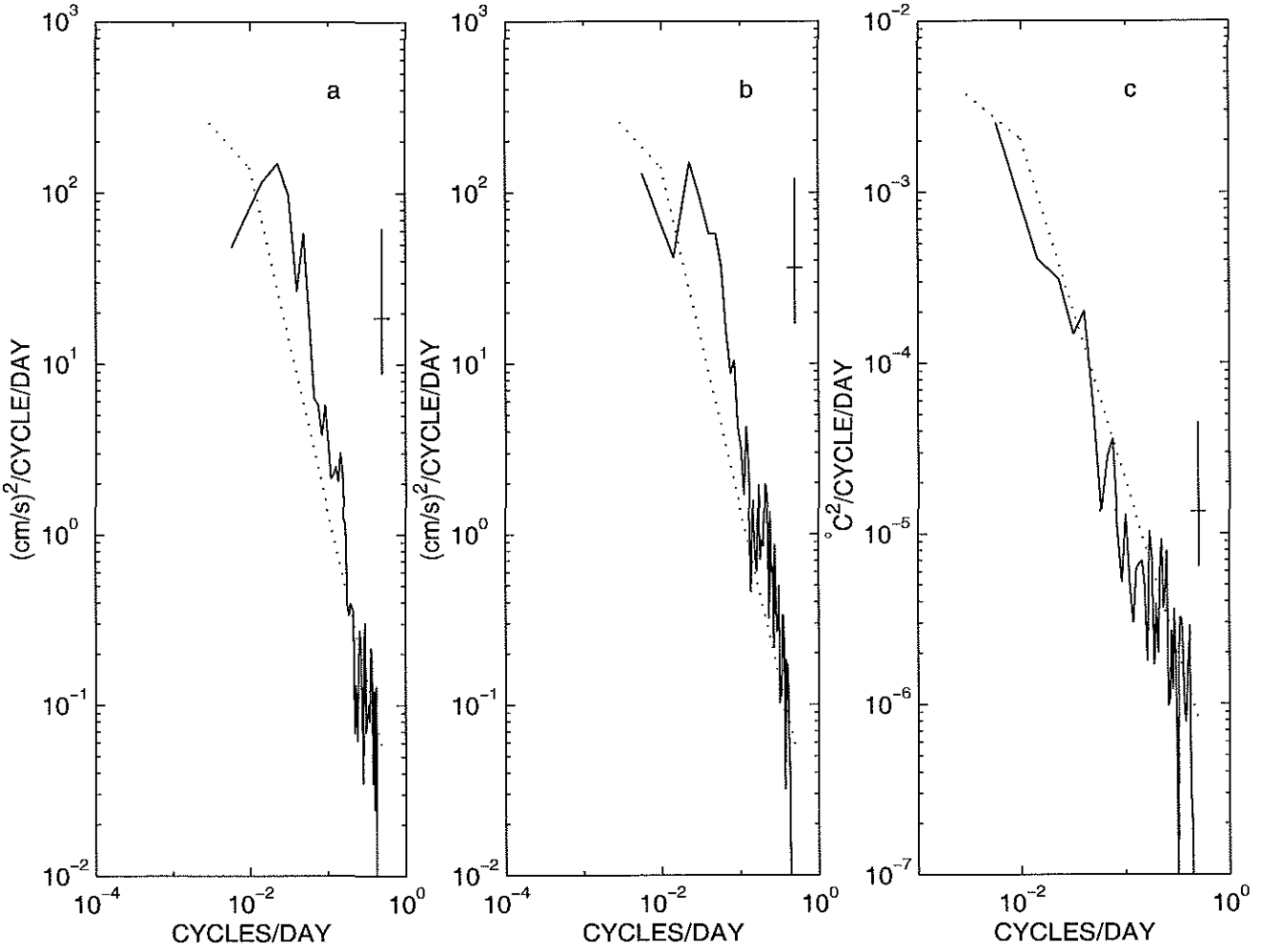

(v)

Figure 5-5: Frequency spectra of zonal (a), meridional velocity (b) and temperature (c) at depths of 160 m (i), 580 m (ii), 595 m (iii), 1230 m (iv) and 3000 m (v). Solid line is the observed spectrum, and the dotted line is the model spectrum.

Chapter 6

Application

A first order spectral description of low frequency oceanic variability has been constructed; however, I have arbitrarily ignored the contributions of higher modes, the different structure found in intense current systems, the equatorial region, etc. Nonetheless, the present first approximation does have some useful applications. The followings describe four examples of the uses of the spectra.

6.1 Covariance functions

The Fourier transform of the wavenumber (frequency) spectrum is the spatial (temporal) covariance. For example, the zonal autocovariance of temperature is

$$R_\theta(r_x,\phi,\lambda,z)=\sum_{n=0}^{n=2}\int_{-\infty}^{+\infty}\int_{-\infty}^{+\infty}\int_{-\infty}^{+\infty}|\theta_a(k,l,\omega,z,n)|^2\Phi(k,l,\omega,n,\phi,\lambda)cos(2\pi kr_x)dkdld\omega. \tag{6.1}$$

Knowledge of the covariance function is useful for many purposes, such as objective mapping and the estimation of integral scales of variability. In order to conveniently compare data with different scales, the autocorrelation function is often calculated instead. The autocorrelation of temperature as a function of zonal separation distance is displayed in figure 6-1. The temperature autocorrelation function shows an exponential decay with e-folding spatial scales of about 120 km. Because the meridional

wavenumber spectrum of temperature is the same as the zonal wavenumber spectrum, the meridional autocorrelation function and the zonal autocorrelation function are the same also. Figure 6-2 shows the autocorrelation of zonal and meridional velocity as a function of zonal separation distance. The autocorrelation function of meridional velocity has a zero crossing at 50 km. The most striking feature in figure 6-2 is that the autocorrelation function of zonal velocity decays with zonal lag much faster than that of meridional velocity, which means that along zonal direction, zonal velocity has longer spatial scales than meridional velocity. This is due to the fact that zonal wavenumber spectrum of zonal velocity is redder than that of meridional velocity, the ratio of zonal wavenumber spectrum of zonal velocity to that of meridional velocity is proportional to k^{-2}. The meridional autocorrelation functions are the same as the zonal autocorrelation functions except that autocorrelation function of zonal velocity and autocorrelation function of meridional velocity are interchanged. My result is consistent with the theory of turbulence. Batchelor (1953) found that for incompressible fluid, the *longitudinal* velocity autocorrelation, which stands for autocorrelation of the velocity parallel to the separation vector, is always higher than the *lateral* velocity autocorrelation which represents autocorrelation of the velocity normal to the separation vector. As discussed at the end of chapter 5, the universal wavenumber spectral shape in my model has some uncertainty. Overall, the uncertainty of wavenumber spectral slope is within 15% in respect to the universal spectral slope in my model at wavelengths longer than 100 km. Figure 6-3 shows how sensitive the autocorrelation function is to the wavenumber spectral shape. As displayed there, the variations of the autocorrelation associated with the changes of spectral shape are less than 0.1 everywhere. The most sensitive place is at the zonal lag between 200 and 400 km where the maximum variations occur. The reader is reminded that the energy of the temperature is concentrated at the spatial scale around 200 to 400 km. The dashdot line in figure 6-3 has higher autocorrelation for the same separation distance, because it corresponds to the redder wavenumber spectrum.

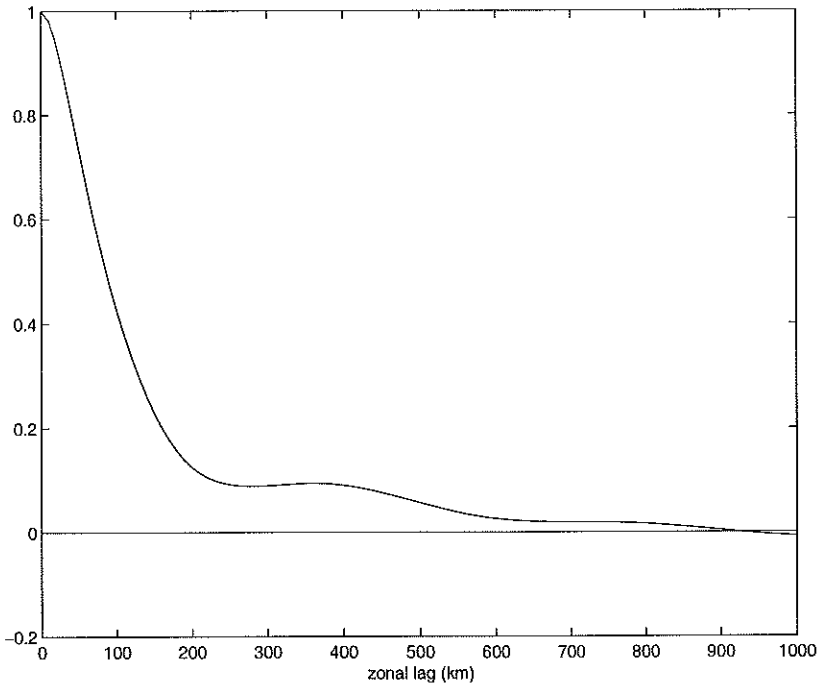

Figure 6-1: Temperature autocorrelation as a function of zonal separation distance.

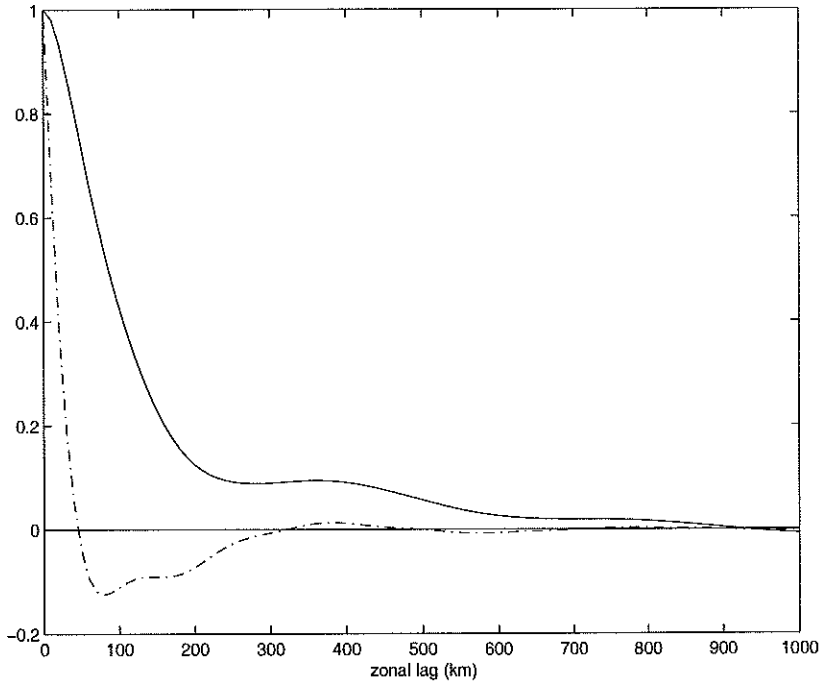

Figure 6-2: Autocorrelation of zonal velocity (solid line) and meridional velocity (dashdot line) as a function of zonal separation distance.

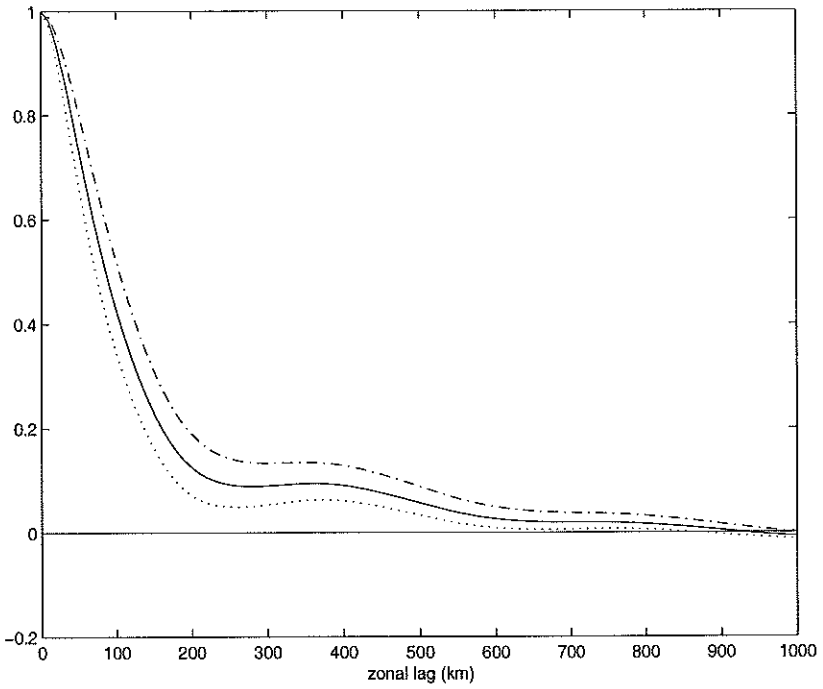

Figure 6-3: Uncertainty of the autocorrelation function. The solid line represents the autocorrelation function corresponding to the universal wavenumber spectrum in my model. The dashdot and dotted line correspond to the wavenumber spectrum with a slope of 15% more and 15% less than the slope of my universal spectrum, respectively.

6.2 Variability of volume flux and heat content

Large-scale long-term change of temperature in the ocean has attracted much attention in the last decade. The hydrographic section along 24°N in the North Atlantic provides unique data to detect climate change of large scale temperature and volume transport in the ocean, because it has been repeated three times during 1957, 1981 and 1992. By comparing the 1981 and 1957 surveys, Roemmich and Wunsch (1984) first identified significant warming in an ocean-wide band from 700 to 3000 m with a maximum temperature difference of 0.2°C. Recently Parrilla et al. (1994) and Arbic and Owens (2000) used all three surveys along 24°N and found that the waters between 800 and 2500 m have consistently warmed over the past 35 years. In climate study, the natural variability is often regarded as noise and the long term trend is

considered to be the signal. It is highly desirable not only to estimate the difference between measurements taken at two different times, but also to determine whether such a difference is significant relative to natural variability.

The volume transport of the ocean is often estimated from hydrographic measurements through inverse modeling (Wunsch, 1996). It varies with time, and the variability depends on the horizontal distance of the hydrographic section. So does the heat content in the region bounding the hydrographic section. To which extent estimates of heat content and volume flux from one-time hydrographic survey can represent their mean values is the issue to be address here. As detailed later, the method used by Parrilla et al. (1994) and Arbic and Owens (1999) to estimate uncertainty in average temperature (heat content) is empirical. Here I will provide a more rigorous estimate of uncertainty for the volume transport and heat content (average temperature).

Suppose that the hydrographic section runs in the east-west direction and is bounded at both ends with the zonal length of L km. The volume transport across this section from a depth of $-h_2$ to $-h_1$ m for each mode can be written as

$$V(L, y, n, t) = \int_0^L \int_{-h_2}^{-h_1} v(x, y, z, n, t) dz dx, \tag{6.2}$$

and the heat content in the region bounding the hydrographic section is

$$\Theta(L, y, n, t) = \int_0^L \int_{-h_2}^{-h_1} \rho_0 c_p \theta(x, y, z, n, t) dz dx. \tag{6.3}$$

Because the value of the density ρ_0 changes little with location and time, here it is treated as a constant, $\rho_0 = 1.027 \times 10^3$ kg/m^3. One important and widely used factor associated with heat content is the average temperature in the region bounding the hydrographic section. By definition, the average temperature can be written as

$$[\theta](L, y, n, t) = \frac{1}{hL} \int_0^L \int_{-h_2}^{-h_1} \theta(x, y, z, n, t) dz dx, \tag{6.4}$$

where $h = h_2 - h_1$. In chapter 3, I have derived an analytic formula for the frequency spectrum of tomographic data, equation (3.37). From that formula, the variance of the average temperature can be readily obtained

$$\sigma^2_{[\theta]}(L,n,\lambda,\phi) = \left(\frac{1}{h}\int_{-h_2}^{-h_1}\frac{\partial\theta_0}{\partial z}G_n(z)dz\right)^2 \int_{-\infty}^{+\infty}\int_{-\infty}^{+\infty}\int_{-\infty}^{+\infty} f^2\Phi(k,l,\omega,n,\lambda,\phi)W(k,L)d\omega dkdl. \tag{6.5}$$

The variance of the average meridional velocity can be obtained in a similar way:

$$\sigma^2_{[v]}(L,n,\lambda,\phi) = \left(\frac{1}{h}\int_{-h_2}^{-h_1}F_n(z)dz\right)^2 \int_{-\infty}^{+\infty}\int_{-\infty}^{+\infty}\int_{-\infty}^{+\infty} 4\pi^2k^2\Phi(k,l,\omega,n,\lambda,\phi)W(k,L)d\omega dkdl, \tag{6.6}$$

where $W(k,L)$ is defined in equation (3.38). Note that $W(k,L)$ decreases with L and $W(k,L=0)=1$. The variances of the average temperature and average meridional velocity decrease with L because more energy is filtered out as L increases. $\sigma^2_{[\theta]}(L,n,\lambda,\phi)$ and $\sigma^2_{[v]}(L,n,\lambda,\phi)$ depend on location as well as the zonal length L. At each site $\sigma^2_{[\theta]}(L,n,\lambda,\phi)$ and $\sigma^2_{[v]}(L,n,\lambda,\phi)$ are normalized by their maximum values, $\sigma^2_{[\theta]}(L=0,n,\lambda,\phi)$ and $\sigma^2_{[v]}(L=0,n,\lambda,\phi)$, so that they only depend on the zonal length L. As displayed in figure 6-4, the normalized $\sigma^2_{[\theta]}(L,n,\lambda,\phi)$ and $\sigma^2_{[v]}(L,n,\lambda,\phi)$ decrease with the zonal length L. This suggests that the longer the zonal length of the hydrographic section, the less variable the average temperature and mass transport. The most striking property of figure 6-4 is that $\sigma^2_{[\theta]}(L,n,\lambda,\phi)$ decreases with zonal length L much less rapidly than $\sigma^2_{[v]}(L,n,\lambda,\phi)$. For average temperature, half of the energy is filtered out when the zonal length is about 350 km; for average meridional velocity, 90% of the variance is removed due to filtering when the zonal distance is 250 km. This difference arises because the zonal spatial scale of meridional velocity is shorter than that of temperature, as discussed in section 6.1.

The variance of heat content is

$$\sigma^2_{\Theta}(L,n,\lambda,\phi) = \rho^2c_p^2h^2L^2\sigma^2_{[\theta]}(L,n,\lambda,\phi), \tag{6.7}$$

and the variance of volume flux is

$$\sigma_V^2(L,n,\lambda,\phi) = h^2L^2\sigma_{[v]}^2(L,n,\lambda,\phi). \tag{6.8}$$

From equation (6.7) and (6.8), we can see that $\sigma_\Theta^2(L,n,\lambda,\phi)$ and $\sigma_V^2(L,n,\lambda,\phi)$ does not simply increase with L^2. How $\sigma_\Theta^2(L,y,n)$ and $\sigma_V^2(L,y,n)$ depend on L is displayed in figure 6-5. The variance of volume flux increases rapidly as L increases from 0 to 200 km, then it increases very slowly. As L increases from 200 km to 2000 km, the variance of volume flux only increases by about 10%. This phenomenon can be rationalized in the following way: because the zonal length scale of mesoscale eddies is about 200 km, the hydrographic section contains less than one mesoscale eddy when L is shorter than 200 km, and the variability will increase with L until L reaches 200 km. As L is longer than 200 km, the number of mesoscale eddies in the region bounding the hydrographic section will be greater than one and increases with L; the variability of total volume flux will be the average of variability of different eddies. Therefore, it changes slowly when the zonal length is greater than 200 km. However, because the zonal length scale of temperature is much larger than that of meridional velocity, the variance of heat content still increases smoothly with L after L is greater than 200 km (figure 6-5).

The variances of volume transport and heat content depend on location as well as L. As an example, the standard deviation of the volume flux and heat content for the hydrographic section at 24°N is estimated. The zonal range of the hydrographic section is assumed to be from 25°W to 75°W, which nearly coincides with the actual hydrographic section. The function for $\Phi(k,l,\omega,n,\lambda,\phi)$ along this section can be derived according to the formulas produced in chapter 5. For the volume transport, I choose the vertical integration to be from the surface to the depth of 2000 meters, while for heat content (temperature), the vertical integration is taken from 1000 meters to 2000 meters because the signal-to-noise ratio for temperature is largest within this range. The standard deviation of volume flux, average temperature and heat content for this particular hydrographic section are listed in table 6-1. As

displayed in the table, the variability of barotropic volume flux and baroclinic volume flux is roughly the same. For the average temperature, the variability in the second baroclinic mode is larger than that in the first baroclinic mode.

	σ_V (0-2000 m)	$\sigma_{[\theta]}$ (1000-2000 m)	σ_Θ (1000-2000 m)
n=0	2.9 (Sv)		
n=1	2.0 (Sv)	0.01 (°C)	1.7×10^{14} (J/m)
n=2	1.1 (Sv)	0.018 (°C)	2.9×10^{14} (J/m)
total	3.7 (Sv)	0.021 (°C)	3.4×10^{14} (J/m)

Table 6-1: Standard deviation of volume flux, average temperature and heat content for the first three modes and the standard deviation of the total variability.

Arbic and Owens (2000) calculated the zonal average and standard deviation of the temperature difference between 1981 and 1957. They assumed that the standard error uncertainty in the zonally averaged temperature difference is mainly due to mesoscale eddies that have a horizontal length scale of about 100 km and obtained the error uncertainty by dividing the standard deviation by the square root of the number of mesoscale eddy length scales in the 5,000 km width of the 24°N. The zonally and vertically (from 1000 to 2000 m) averaged temperature difference between 1984 and 1957 is 0.11°C and the error uncertainty is 0.024°C, which is very close to my estimate.

Ganachaud (1999) estimated the uncertainty in volume flux through an eddy-resolving oceanic general circulation model and he found that the variability in baroclinic volume flux through 24° above 2000 m is about 4 Sv (personal communication), which is larger than the value of 2.4 Sv I obtained.

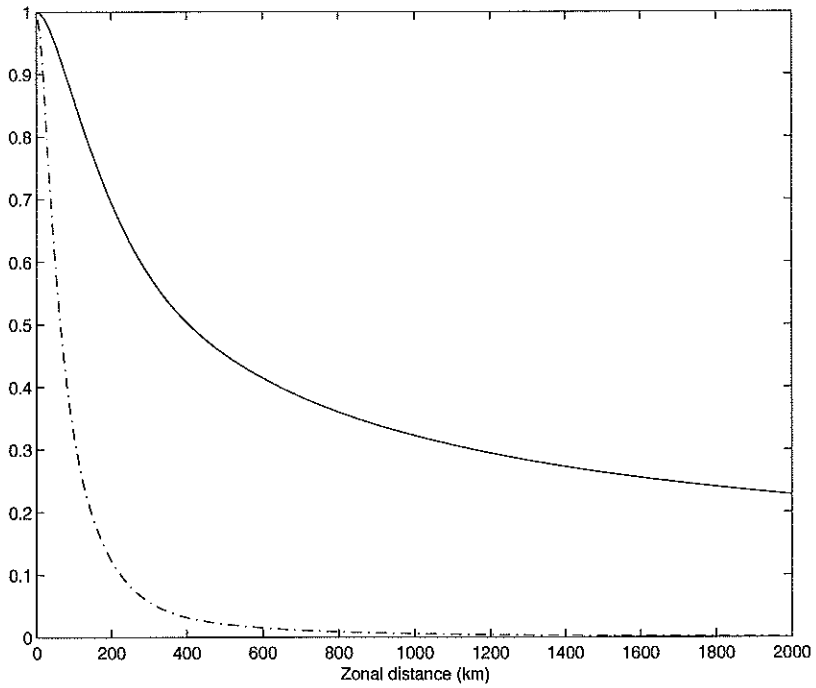

Figure 6-4: The normalized $\sigma^2_{[\theta]}(L, n, \lambda, \phi)$ (solid line) and $\sigma^2_{[v]}(L, n, \lambda, \phi)$ (dashdot line) as a function of L. $\sigma^2_{[\theta]}(L, n, \lambda, \phi)$ and $\sigma^2_{[v]}(L, n, \lambda, \phi)$ are normalized by $\sigma^2_{[\theta]}(L = 0, n, \lambda, \phi)$ and $\sigma^2_{[v]}(L = 0, n, \lambda, \phi)$, respectively.

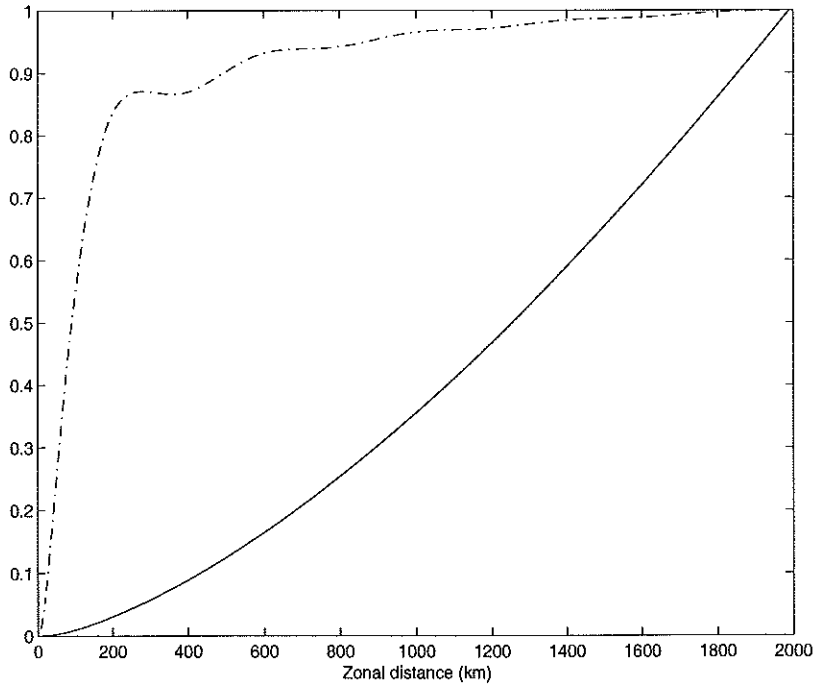

Figure 6-5: The normalized $\sigma^2_{\Theta}(L, n, \lambda, \phi)$ (solid line) and $\sigma^2_{V}(L, n, \lambda, \phi)$ (dashdot line) as a function of L. $\sigma^2_{\Theta}(L, n, \lambda, \phi)$ and $\sigma^2_{V}(L, n, \lambda, \phi)$ are normalized by $\sigma^2_{\Theta}(L = 2000, n, \lambda, \phi)$ and $\sigma^2_{V}(L = 2000, n, \lambda, \phi)$, respectively.

6.3 Design of an observational network

Fluctuations of heat storage in the ocean are key factors in understanding the general circulation of the ocean and climate change. Because the area of the ocean is vast, it is very expensive to monitor the climatic variability of heat content. The oceanic variability is continuous in space and time. The measurements, however, are sparse and subject to noise. There is no doubt that the higher the sampling density, the more accurate the estimates. Nonetheless, there is an inevitable trade-off between cost and sampling density. It is impossible and unnecessary to make the sampling spacing infinitesimal. It is desirable to evaluate the effectiveness of different sampling strategies before the monitoring network is put into use. The particular question posed here is: to what extent can the finite and discrete observations can represent the actual oceanic variability? One closely related question is: what is the minimum sampling density in order to resolve and detect the climate change with certain accuracy?

6.3.1 Optimal interpolation

Optimal estimation methods have been applied by a few authors to the design of observational networks in oceanography (e.g., Bretherton et al., 1976; White and Bernstein, 1979; Bretherton et al, 1984; White, 1995). The advantage of optimal estimation theory is that one can quantitatively estimate the impact of sampling strategy and measurement noise on the final product. An important factor in applying this theory is the knowledge of the statistical structure of the variable to be analyzed. Once the autocorrelation and signal-to-noise ratio are determined, then the least sampling rates that produce the desirable interpolation error can be estimated. The general approach to estimate the *random* vector $\mathbf{X}$ from its measurements $\mathbf{Y}$ in statistical estimation theory is the so-called Bayesian least-squares estimation method (Papoulis, 1991). The key factor of this approach is the conditional probability $p_{\mathbf{x}|\mathbf{y}}(\mathbf{X}|\mathbf{Y})$, which fully characterizes the relationship between the signal vector $\mathbf{X}$ and the observation vector $\mathbf{Y}$. In general, this estimator is a nonlinear function

of the data and it yields the least uncertainty (in terms of error variance) among all estimators (Willsky et al., 1998). The difficulty inherent in this method is the derivation of the conditional probability $p_{\mathbf{x}|\mathbf{y}}(\mathbf{X}|\mathbf{Y})$, which often is not available. Another widely used approach is minimum variance (Gauss-Markov) estimator. By assuming that the estimator to be a linear function of the data, this estimator requires only the first and second statistical moments: mean and covariance distribution of the signal and noise. The minimum variance estimation method was first introduced into meteorology by Gandin (1963) to estimate the value of the field at a point based on randomly distributed measurements. Its application to oceanographic problems was reviewed by Wunsch (1996). Assuming that the field and noise are jointly Gaussian distributed, Bretherton et al. (1984) applied the Bayesian least-squares estimation method to the design study of measurements of heat storage. Under this assumption, the Bayesian least-squares method and linear least-squares method produce the same estimate and the same uncertainty (Willsky et al., 1998). In the following I will use the linear minimum variance method to evaluate the effectiveness of different sampling strategies.

The minimum variance estimator

Let $\mathbf{r_i} = \mathbf{r_1}, \mathbf{r_2}, ..., \mathbf{r_K}$ denote the locations where the measurements are made, and let $\mathbf{s_m} = \mathbf{s_1}, \mathbf{s_2}, ..., \mathbf{s_L}$ denote the positions where the estimates are sought and which are usually at grid point. Define the measurement at the point $\mathbf{r_i}$ as $y(\mathbf{r_i})$, which is the actual value plus some random noise

$$y(\mathbf{r_i}) = x(\mathbf{r_i}) + w(\mathbf{r_i}), \quad 1 \leq i \leq K. \tag{6.9}$$

I assume that the noise has zero mean, the noise at different points is uncorrelated and the noise is uncorrelated with the actual value of the underlying process; that is

$$< w(\mathbf{r_i}) >= 0, \quad < w(\mathbf{r_i})w(\mathbf{r_j}) >= \sigma_w^2(\mathbf{r_i})\delta_{ij}, \quad < (x(\mathbf{r_i}) - \overline{x}(\mathbf{r_i}))w(\mathbf{r_j}) >= 0, \tag{6.10}$$

where $\overline{x}(\mathbf{r_i})$ represents the mean value of $x(\mathbf{r_i})$.

The estimate at the location $\mathbf{s_m}$ is assumed to be an linear combination of the measurements,

$$\tilde{x}(\mathbf{s_m}) = a(\mathbf{s_m}) + \sum_{i=1}^{K} b(\mathbf{s_m}, \mathbf{r_i}) y(\mathbf{r_i}). \tag{6.11}$$

In order for the estimate to be unbiased, I choose

$$a(\mathbf{s_m}) = \overline{x}(\mathbf{r_i}) - \sum_{i=1}^{K} b(\mathbf{s_m}, \mathbf{r_i}) \overline{y}(\mathbf{r_i}). \tag{6.12}$$

The weighting coefficient $b(\mathbf{s_m}, \mathbf{r_i})$, which minimizes the mean-square error, is determined by the following simultaneous equations

$$\sum_{j=1}^{K} b(\mathbf{s_m}, \mathbf{r_j}) \rho_{xx}(\mathbf{r_i}, \mathbf{r_j}) + \gamma^{-2} b(\mathbf{s_m}, \mathbf{r_i}) = \rho_{xx}(\mathbf{s_m}, \mathbf{r_i}), \quad 1 \leq i \leq K, \tag{6.13}$$

where $\rho_{xx}(\mathbf{r_i}, \mathbf{r_j})$ is the autocorrelation between signals at the location $\mathbf{r_i}$ and $\mathbf{r_j}$, $\rho_{xx}(\mathbf{s_m}, \mathbf{r_i})$ is the signal autocorrelation between the point where the interpolation takes place and the surrounding points where observations are made, and γ^2 is the ratio of signal variance to noise variance.

$$\gamma^2 = \frac{\sigma_x^2}{\sigma_w^2} \tag{6.14}$$

The corresponding mean-square error is

$$\sigma_e^2(\mathbf{s_m}) = \sigma_x^2 [1 - \sum_{i=1}^{K} b(\mathbf{s_m}, \mathbf{r_i}) \rho_{xx}(\mathbf{s_m}, \mathbf{r_i})]. \tag{6.15}$$

Define the normalized error as

$$P = \frac{\sigma_e(\mathbf{s_m})}{\sigma_x}, \tag{6.16}$$

therefore

$$P = \sqrt{1 - \sum_{i=1}^{K} b(\mathbf{s_m}, \mathbf{r_i}) \rho_{xx}(\mathbf{s_m}, \mathbf{r_i})}. \tag{6.17}$$

Equation (6.17) was derived by Alaka and Elvander (1972) and used by White and Bernstein (1979) to design an oceanographic network. Equation (6.17) states that the interpolation error depends only on the autocorrelation function, interpolation scheme and weighting coefficients. It is independent of the values of measurements. Therefore, the interpolation error can be estimated before any measurements are made as long as the autocorrelation function and error statistics are known.

The correlation functions for temperature and two components of horizontal velocity have been obtained in section 6.1. The signal is often defined by the scales of interest to the observer and usually stands for large scale perturbations. The noise, on the other hand, has two sources: one is the instrumental error, and the other is the subgrid ambient variability in the field itself. In the literature, the noise is often considered to be dominated by the second source. Once the wavenumber spectrum of field and sampling spacing are known, the variance of noise due to subgrid aliasing can be easily calculated. Based on the zonal-wavenumber spectrum of temperature obtained in last chapter, it is found that 41% of the variance is distributed at zonal-wavelengths longer than 1000 km, 64% at zonal-wavelengths longer than 500 km and 92% at zonal-wavelengths longer than 200 km. Therefore, the ratio of signal variance to error variance is about 0.7:1 for the sampling array with the zonal spacing of 500 km. It increases to 1.8:1 for zonal spacing of 250 km and to 12:1 for the zonal spacing of 100 km. The above discussion is about temperature. The results for horizontal velocities are different. Because the zonal-wavenumber spectrum of temperature is redder than that of meridional component of horizontal velocities, the ratio of zonal-wavenumber spectrum of temperature to the zonal-wavenumber spectrum of meridional velocity is proportional to k^{-2}. It is found that only 10% of the variance of meridional velocity is at zonal-wavelengths longer than 500 km and 33 % at wavelengths longer than 200 km. Therefore, for the meridional velocity, the ratio of signal variance to error variance is about 0.11:1 for the sampling array with the zonal spacing of 250 km and 0.5:1 for the zonal spacing of 100 km. The ratio of signal variance to error variance for temperature is much higher than that for meridional

velocity for the sampling array with zonal spacing larger than 100 km. Here I am not going to specify the value of the signal-to-noise ratio. Instead, I let it to be a controllable variable, and I will study how the interpolation error depends on signal-to-noise ratio as well as sampling density.

In the most general cases, the interpolation is four-dimensional in zonal, meridional, temporal and vertical directions. Here, I consider the interpolation to be two-dimensional and in the horizontal plane. In this case, the autocorrelation function is two-dimensional: $R_\theta(r_x, r_y) = R_\theta(r_x)R_\theta(r_y)$, where $R_\theta(r_x)$ and $R_\theta(r_y)$ are the one-dimensional zonal autocorrelation function and meridional autocorrelation function, respectively, and have been obtained in section 6.1. White (1995) compared the results in different dimensions and found that the interpolation error decreases as dimension increases because there are greater independent observations for higher dimensions.

As an illustration of how the normalized interpolation error varies with sampling density, I choose a 12-point interpolation scheme, which is displayed in figure 6-6. I want to estimate the temperature at the center point based on measurements at the surrounding 12 points. As displayed in figure 6-7, the interpolation error drops as sampling density increases, more rapidly in the beginning. The less accurate the observations, the more the interpolation error. The structure of mapping errors in figure 6-7 suggests that optimal sampling occurs at spacing about 40-50 km, because interpolation error decreases rapidly for sampling spacing greater than 50 km, then very slowly.

As mentioned before, my model is a first-order approximation to the actual ocean variability. The dependence of spectral shape on geography has been simply neglected. However, as described by Stammer (1997), the observed spectral shape does depend on geography and latitude. Therefore, for a more precise design for sampling some particular regions, the particular statistics of those regions should be used. Figure 6-8 shows how sensitive the interpolation error is to the spectral shape. The three curves in figure 6-8 display a similar structure, which suggests that the optimal sampling

spacing for the three different spectral shapes is roughly the same, around 40-50 km. When the spectral slope changes by 15%, the variations of the normalized error is less than 0.1.

The strategy for monitoring horizontal velocities should be different from the strategy for measuring temperature, because horizontal velocities have distinct auto-covariance structure. The most important property of the auto-covariance of horizontal velocities is anisotropy; the zonal decorrelation scales are longer than the meridional scales for zonal component, and the reverse is true for meridional component.

There is an emerging program, named Argo, which is going to deploy a global array of 3,000 profiling floats to measure the temperature and salinity of the ocean's upper layer. If the 3,000 floats are deployed regularly in the global ocean, the spacing will be about 340 km by 340 km. The wavenumber spectrum of temperature suggests that 56% of the variance is at wavelengths longer than 680 km; therefore, the ratio of signal variance to noise variance, γ^2, is about 1.3 for the sampling array with 340 km spacing. Figure 6-7 shows that when the ratio of signal variance to noise variance is 1.5, 50 km sampling spacing is preferable. If we further double the sampling density—sampling spacing is decreased from 50 km to 25 km—the interpolation error will decrease only 10%. If the floats are regularly distributed with spacing 50 km, about 140,000 floats are needed to cover the global ocean. Therefore, the proposed 3000 floats cannot monitor the dominant variability over the global ocean.

6.3.2 Optimal averaging

In the above, I studied how to estimate the value at a point, based on some observations surrounding that point. For the study of climate change, it is highly desirable to obtain estimates of the value averaged over a large area, rather than the value at a point. Kagan (1997) gave a comprehensive and detailed discussion of statistical averaging of meteorological fields.

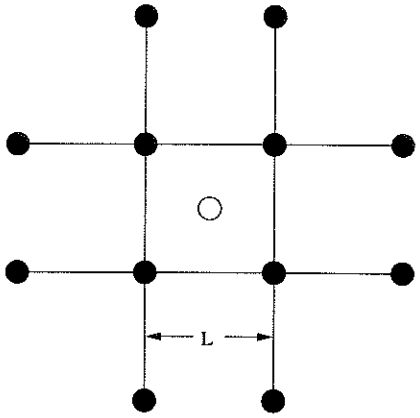

Figure 6-6: The interpolation scheme used in this study. The solid circles represent the places where the measurements are made and the open circle stands for the location where the estimate to be obtained.

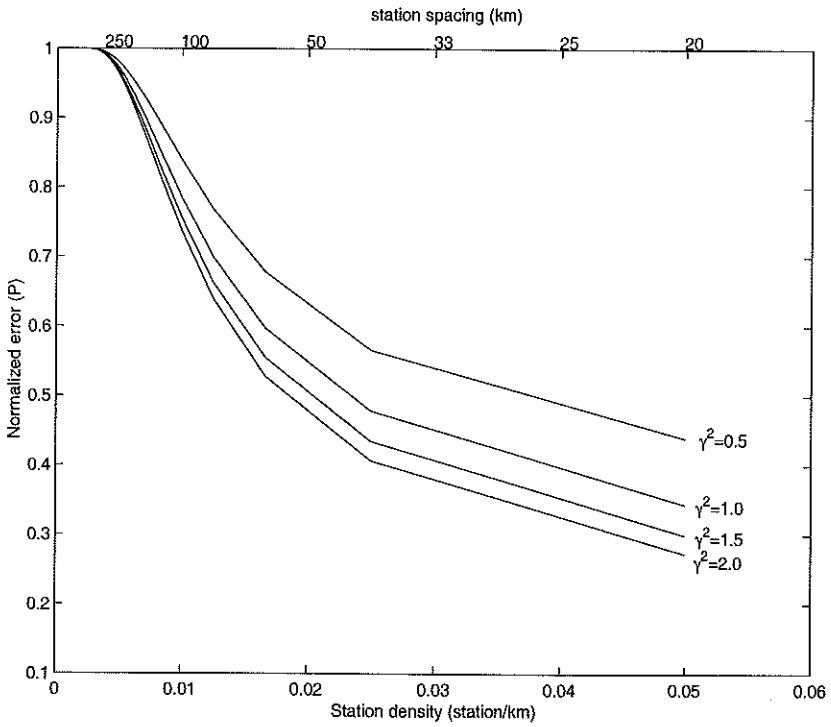

Figure 6-7: Normalized interpolation error of temperature versus sampling density for different values of γ^2, the ratio of signal variance to noise variance.

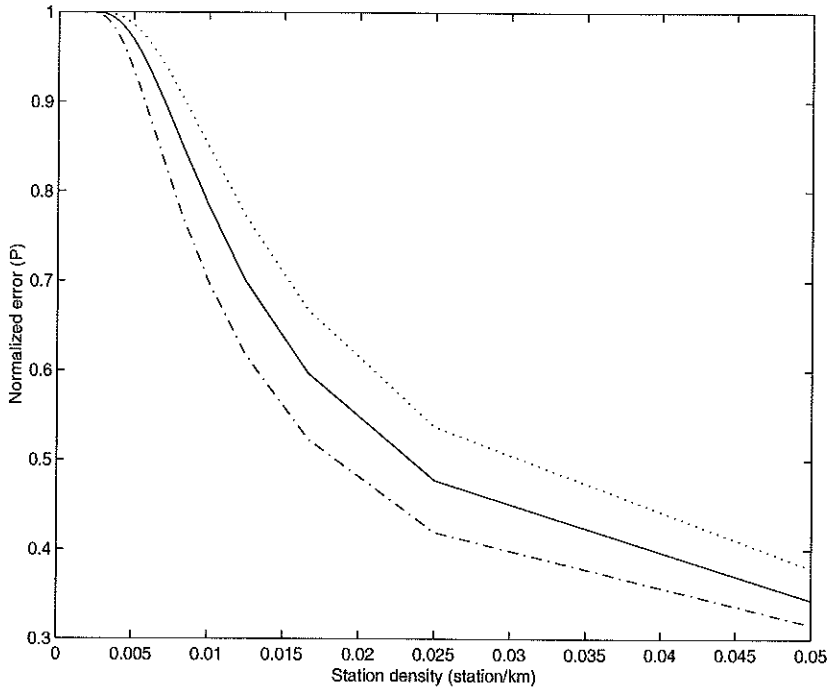

Figure 6-8: The normalized error for different wavenumber spectral shapes with signal-to-noise ratio of 1.0. The solid line corresponds to the globally averaged wavenumber spectral shape, while the dashdot and dotted line correspond to the wavenumber spectrum with slope 15% more and 15% less than that of the globally averaged one, respectively.

In the following, the optimal averaging method will be applied to the design of oceanographic monitoring network, with a focus on studying how the error associated with determining averaged value depends on sampling density. I assume that the averaging is two-dimensional and in the horizontal plane. If $F(x, y)$ is defined to be the averaged value of the field $f(x, y)$ (figure 6-9), then

$$F(x_s, y_s) = \frac{1}{L_x L_y} \int_{x_s - L_x/2}^{x_s + L_x/2} \int_{y_s - L_y/2}^{y_s + L_y/2} f(\xi_1, \xi_2) d\xi_1 d\xi_2. \tag{6.18}$$

Let $g(x_i, y_i)$ be the measurement at the point (x_i, y_i), which is the true value $f(x_i, y_i)$ plus some noise $w(x_i, y_i)$, so that

$$g(x_i, y_i) = f(x_i, y_i) + w(x_i, y_i). \tag{6.19}$$

The estimate of $F(x,y)$ is assumed to be an linear combination of surrounding measurements:

$$\tilde{F}(x_s,y_s)=\sum_{i=1}^{n}p_i g(x_i,y_i), \tag{6.20}$$

where p_i is the weighting factor for the measurement at the point (x_i,y_i).

For a homogeneous process, in order to get unbiased estimate, p_i needs to satisfy

$$\sum_{i=1}^{n}p_i=1, \tag{6.21}$$

unless $< f >= 0$. In this study, I assume that the time-mean has been removed before the spatial average is made. I further assume that actual value is uncorrelated with noise, noises at different places are uncorrelated and that noises have zero mean. The mean-square error is

$$E^2(x_s,y_s)=< [\tilde{F}(x_s,y_s)-F(x_s,y_s)]^2 > . \tag{6.22}$$

For an unbiased estimate,

$$E^2(x_s,y_s)=\sigma_F^2-2\sum_{i=1}^{n}p_i R_{Ff_i}+\sum_{i=1}^{n}\sum_{j=1}^{n}p_i p_j R_{ij}+\sigma_w^2\sum_{i=1}^{n}p_i^2, \tag{6.23}$$

where σ_F^2 is the variance of the average value, R_{ij} is the covariance between signals at the point (x_i,y_i) and (x_j,y_j), σ_w^2 is variance of noise and R_{Ff_i} is the covariance between the average value and the value at the point (x_i,y_i),

$$R_{Ff_i}=< [f(x_i,y_i)-< f(x_i,y_i) >][F(x_s,y_s)-< F(x_s,y_s) >] > . \tag{6.24}$$

Substitution of equation (6.18) into (6.24) yields

$$R_{Ff_i}=\frac{1}{L_x L_y}\int_{x_s-L_x/2}^{x_s+L_x/2}\int_{y_s-L_y/2}^{y_s+L_y/2}R_f(x_i-\xi_1,y_i-\xi_2)d\xi_1 d\xi_2, \tag{6.25}$$

where $R_f(x_i-\xi_1,y_i-\xi_2)$ is covariance between values at point (x_i,y_i) and (ξ_1,ξ_2).

Equation (6.25) suggests that covariance between the average value and the value at the point (x_i, y_i) is the average of the covariances between the value at point (x_i, y_i) and at every point inside the area where the average to be estimated.

For simplicity, define (r_x, r_y) to be the separation distance between the point (x_i, y_i) and the center of the area where the average value to be estimated,

$$r_x = x_i - x_s, \quad r_y = y_i - y_s, \tag{6.26}$$

so that equation (6.25) can be simplified as

$$R_{Ff_i} = \frac{1}{L_x L_y} \int_{r_x - L_x/2}^{r_x + L_x/2} \int_{r_y - L_y/2}^{r_y + L_y/2} R_f(\tau_1, \tau_2) d\tau_1 d\tau_2. \tag{6.27}$$

Normalize (6.23) by the variance of field f, σ_f^2,

$$\epsilon^2 = \frac{E^2(x_s, y_s)}{\sigma_f^2} = \mu - 2\sum_{i=1}^{n} p_i \beta_i + \sum_{i=1}^{n}\sum_{j=1}^{n} p_i p_j r_{ij} + \gamma^{-2} \sum_{i=1}^{n} p_i^2, \tag{6.28}$$

where

$$\mu = \frac{\sigma_F^2}{\sigma_f^2}, \quad \beta_i = \frac{R_{Ff_i}}{\sigma_f^2}, \quad r_{ij} = \frac{R_{ij}}{\sigma_f^2}. \tag{6.29}$$

Note that the variance of the average value is not equal to the average of the variance at single point. In fact the variance of the average value is always less than variance of the value at a point, $\mu \leq 1$, because variability associated with small scales is filtered out due to averaging. For temperature, the variance at a point is

$$\sigma_f^2 = \int_{-\infty}^{+\infty} \int_{-\infty}^{+\infty} \int_{-\infty}^{+\infty} |\theta_a|^2 \Phi(k, l, \omega, n, \lambda, \phi) dk dl d\omega, \tag{6.30}$$

and the variance of the average value is

$$\sigma_F^2 = \int_{-\infty}^{+\infty} \int_{-\infty}^{+\infty} \int_{-\infty}^{+\infty} |\theta_a|^2 \Phi(k, l, \omega, n, \lambda, \phi) \frac{sin^2(2\pi k L_x/2)}{(2\pi k L_x/2)^2} \frac{sin^2(2\pi l L_y/2)}{(2\pi l L_y/2)^2} dk dl d\omega. \tag{6.31}$$

If $L_x = 1000$ km and $L_y = 1000$ km, then $\mu = 0.05$.

The optimal weight is obtained by minimizing the error variance ϵ^2. Therefore, p can be obtained by solving

$$\sum_{j=1}^{n} p_j r_{ij} + p_i \gamma^{-2} = \beta_i, \tag{6.32}$$

and the corresponding error is

$$\epsilon^2 = \mu - \sum_{i=1}^{n} p_i \beta_i. \tag{6.33}$$

The error depends on the size of the area where the average value to be estimated, the number of observations, the sampling density and signal-to-noise ratio. The following discussions describe two simple cases. First, the averaging area is fixed to be 1000 km by 1000 km, the number of observations is fixed to be 12, and the average scheme is shown in figure 6-9. Figure 6-10 shows how the error depends on sampling spacing and signal-to-noise ratio. As shown there, the normalized error is always less than 0.22, which is the square root of the normalized variance of the average value. This means that variance of the error cannot exceed the variance of the average value. The most striking property in figure 6-8 is that the minimum errors are obtained at the sampling spacing around 220 km. This is because the number of observations is fixed to be 12. When the measurements are too close to each other, they just duplicate one another. Some improvements can be achieved by mutual canceling of random error in the data by repeated sampling. If they are too far away from each other, however, they will miss the dominant variability of the underlying process. In the second case, the averaging area is also fixed to be 1000 km by 1000 km. However, the number of observations is not fixed, and I assume that all observations are located within the area where the average value is estimated (figure 11). As shown in figure 6-12, the error associated with determining the average value decays smoothly with sampling density and more rapidly at sampling density less than 0.012 station/km; and it is much less than the error associated with estimating the value at a point (figure 6-7). Because

the root mean square of the average value is about 0.22, the error associated with determining the average value is always less than 0.22. Both of the two cases studied here have limitations. In the first one, the number of observations used to estimate the average value is fixed to 12; in the second case no observations outside the average area have been used to estimate the average value. In order to fully understand the relationship among the error, samping density, number of observations, and sampling geometry, further study is needed.

6.4 Lagrangian correlation

Recently, there have been an increasing number of observations from drifting floats. It is of interest to find out how to combine float data with other measurements such as XBT and altimeter data for the purpose of understanding the ocean general circulation. The relationship between Lagrangian and Eulerian statistics is fundamental to the understanding of turbulent diffusion. A number of theories claim to give the relationship between the velocity statistics of Lagrangian particles and the statistics of the Eulerian flow (see the review by Davis, 1981). These theories enable one to relate the Lagrangian autocovariance function to the Eulerian energy wavenumber and frequency spectra. Therefore, given Eulerian energy wavenumber and frequency spectra, one can predict the Lagrangian autocovariance function (frequency spectrum) based on various theories. The crucial factor to test these theories is the three-dimensional spectrum of the Eulerian flow. The motivation here is to test one of the theories by comparing the predicted Lagrangian autocorrelation function with that of observations. One widely used approximation for the relationship between Lagrangian and Eulerian statistics in the literature was originally proposed by Corrsin (1959) and applied by Saffman (1963). The theory by Corrsin will be evaluated here.

I assume that the particle trajectory is in the horizontal plane and let $(X(t), Y(t))$ be the trajectory of the particle, which was deployed at the position of $(X(t) = 0, Y(t) = 0)$ at time $t = 0$; then the trajectory satisfies the equations

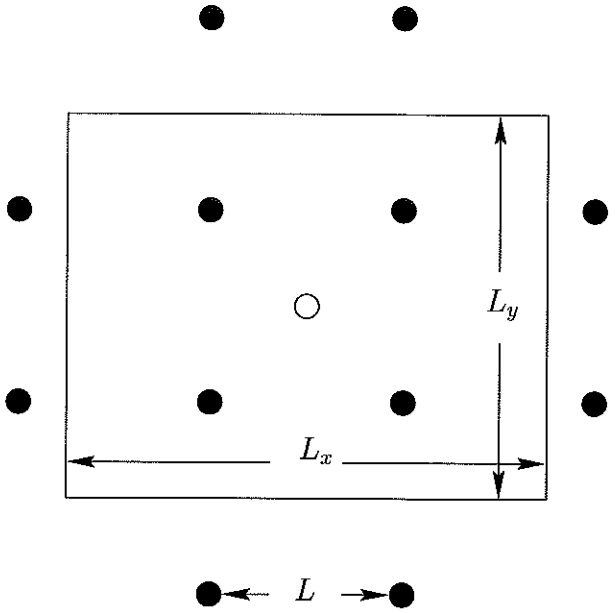

Figure 6-9: The optimal averaging scheme used in this study. The solid circles represent the places where the measurements are made and the open circle stands for the center of the area where the average are performed.

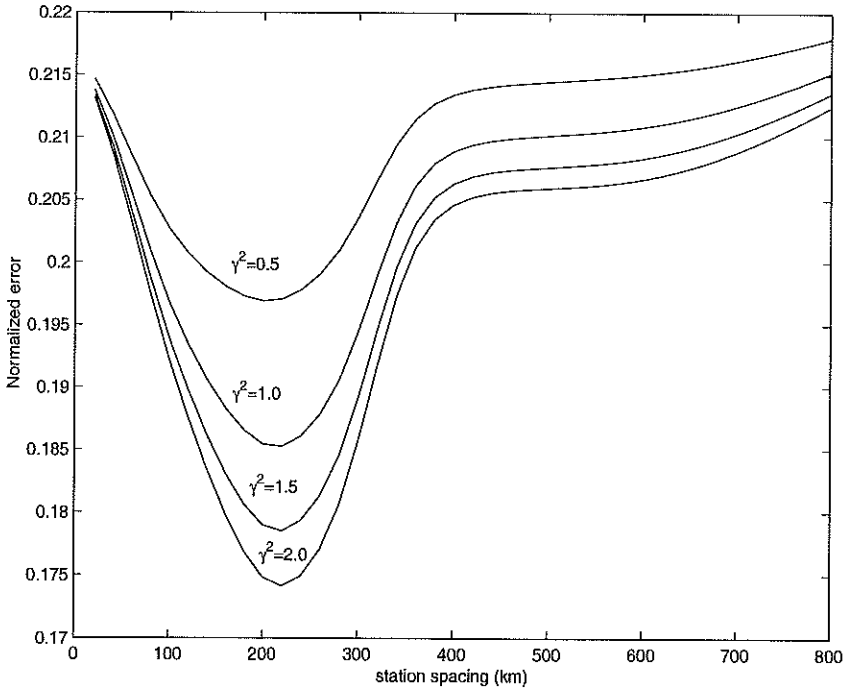

Figure 6-10: Normalized interpolation error of temperature versus sampling spacing for different values of γ^2, the ratio of signal variance to noise variance.

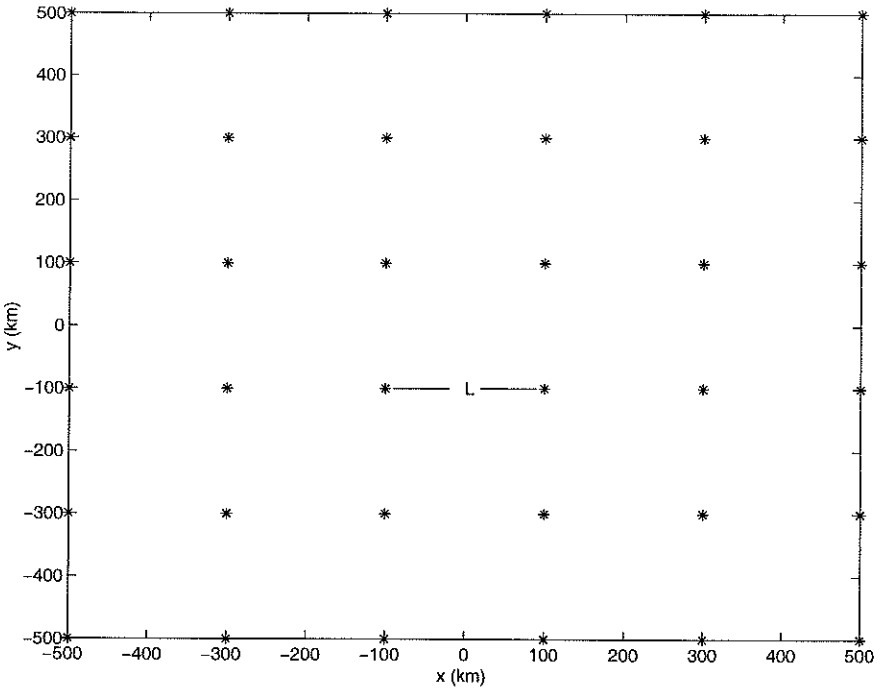

Figure 6-11: The optimal averaging scheme for the second case. Observations are all located inside the area where the average is made and are regularly distributed. The spacing will decrease as the number of observations increases.

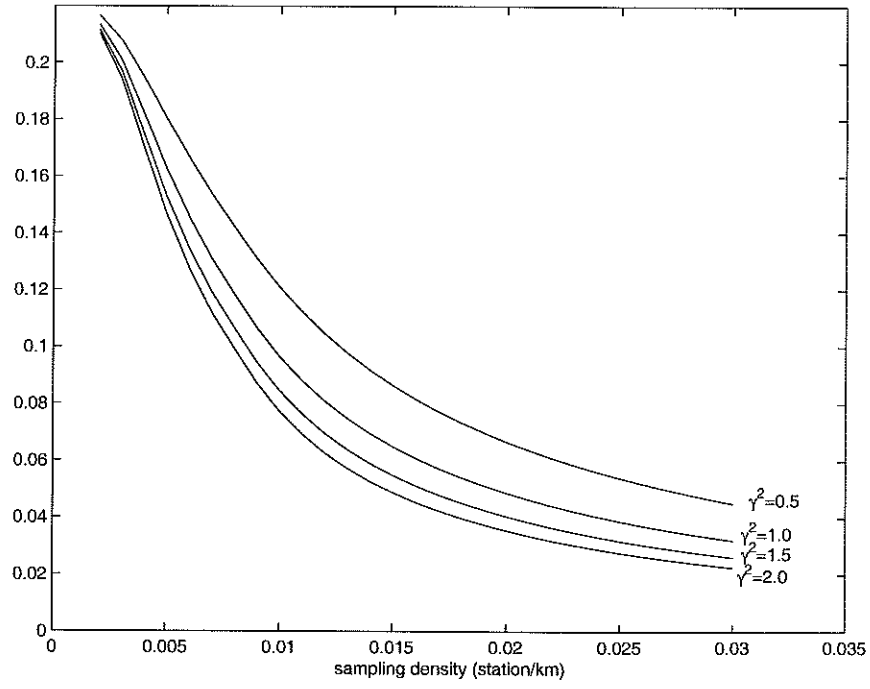

Figure 6-12: Normalized interpolation error of temperature versus sampling spacing for different values of γ^2, the ratio of signal variance to noise variance.

$$\frac{dX(t)}{dt} = u_L(t) = u(X(t), Y(t), t), \tag{6.34}$$

$$\frac{dY(t)}{dt} = v_L(t) = v(X(t), Y(t), t), \tag{6.35}$$

where $u_L(t)$ and $v_L(t)$ are zonal and meridional components of Lagrangian horizontal velocities, and where $u(X(t), Y(t), t)$ and $v(X(t), Y(t), t)$ are zonal and meridional Eulerian horizontal velocities at the position $(X(t), Y(t))$ at time t. The autocovariance function of the Lagrangian velocity $u_L(t)$ is defined as

$$R_{Lu}(t) =< u_L(0)u_L(t) >=< u(0,0,0)u(X(t), Y(t), t) > . \tag{6.36}$$

The particle displacement in the direction of x-axis at time t is

$$X(t) = \int_0^t u_L(t')dt'. \tag{6.37}$$

Let $\sigma^2(t)$ be the mean square particle displacement in the direction of x-axis, then

$$\sigma^2(t) =< X^2(t) > . \tag{6.38}$$

It is readily proved that

$$\sigma^2(t) = 2\int_0^t (t-\tau)R_{Lu}(\tau)d\tau. \tag{6.39}$$

Taking the second derivative of equation (6.39) gives

$$\frac{d^2\sigma^2(t)}{d^2t} = 2R_{Lu}(t). \tag{6.40}$$

Equation (6.36) can be written as

$$R_{Lu}(t) = \int_{-\infty}^{+\infty}\int_{-\infty}^{+\infty} < u(0,0,0)u(r_x, r_y, t)\ \delta\left[r_x - X(t), r_y - Y(t)\right] > dr_x dr_y, \tag{6.41}$$

where $\delta[r_x - X(t), r_y - Y(t)]$ is a two-dimensional delta function. The reader is reminded that $[x(t), y(t)]$ is the position of the particle at time t and is random, while $[r_x, r_y]$ is the position of a point in two-dimensional space and is deterministic. $\delta[r_x - X(t), r_y - Y(t)] = 0$ except when $X(t) = r_x$ and $Y(t) = r_y$. So $\delta[r_x - X(t), r_y - Y(t)] = 0$ is the marker of a fluid particle. For convenience, define a new variable as

$$P(r_x, r_y, t) = < \delta[r_x - X(t), r_y - Y(t)] >, \tag{6.42}$$

which stands for the probability density of the position of a particle at time t.

If we assume that $u(0,0,0)u(r_x, r_y, t)$ and $\delta[r_x - X(t), r_y - Y(t), t]$ in equation (6.41) are statistically independent, equation (6.41) becomes

$$R_{Lu}(t) = \int_{-\infty}^{+\infty}\int_{-\infty}^{+\infty} R_u(r_x, r_y, t)P(r_x, r_y, t)dr_x dr_y. \tag{6.43}$$

This is the independence approximation suggested by Corrsin (1959). The essence of the independence approximation is that after a long time, the diffusion process is effectively the same as a random walk. For a random walk, the local velocity and the displacement of a particle after a few steps are uncorrelated. Weinstock (1976) investigated the validity of this approximation. He showed that it is the first term in a systematic expansion of the Lagrangian function and that the independence approximation is satisfied for homogeneous turbulence. Equation (6.43) suggests that the Lagrangian autocovariance is the average of the Eulerian autocovariance, and the average is taken with respect to the probability of the position of the particle.

The distribution of $P(r_x, r_y, t)$ is assumed to be isotropic and normal

$$P(r_x, r_y, t) = \frac{1}{2\pi\sigma^2(t)} \exp\left(-\frac{r_x^2 + r_y^2}{2\sigma^2(t)}\right). \tag{6.44}$$

Substitution of equation (6.44) into (6.43) and use of Parseval's theorem yield

$$R_{Lu}(t) = \int_{-\infty}^{+\infty}\int_{-\infty}^{+\infty}\Upsilon_u(k,l,t)e^{-2\pi^2(k^2+l^2)\sigma^2(t)}dkdl, \tag{6.45}$$

where

$$\Upsilon_u(k,l,t) = \int_{-\infty}^{+\infty}\int_{-\infty}^{+\infty}R_u(r_x,r_y,t)e^{2\pi(kr_x+lr_y)}dr_xdr_y. \tag{6.46}$$

Because $X(0) = 0$ and $\sigma^2(t) =< X^2(t) >$, the initial conditions are

$$\sigma^2(t) = 0, \quad \frac{d\sigma^2(t)}{dt} = 0 \quad \text{at} \ \ t = 0. \tag{6.47}$$

The reader is reminded that the Eulerian covariance function is

$$R_u(t) = \int_{-\infty}^{+\infty}\int_{-\infty}^{+\infty}\Upsilon_u(k,l,t)dkdl. \tag{6.48}$$

It follows from equation (6.45) that

$$|R_{Lu}(t)| \begin{cases} = |R_u(t)| & \text{if } t = 0 \\ < |R_u(t)| & \text{if } t \neq 0\ , \end{cases} \tag{6.49}$$

which shows that the Lagrangian autocorrelation is less than the Eulerian autocorrelation except at $t = 0$.

Substitution of equation (6.45) into (6.40) yields

$$\frac{d^2\sigma^2(t)}{d^2t} = 2\int_{-\infty}^{+\infty}\int_{-\infty}^{+\infty}\Upsilon_u(k,l,t)e^{-2\pi^2(k^2+l^2)\sigma^2(t)}dkdl. \tag{6.50}$$

This is an integro-differential equation for $\sigma^2(t)$ in terms of the Eulerian spectrum function $\Upsilon_u(k,l,t)$. The formula for $\Upsilon_u(k,l,t)$ can be derived from chapter 5,

$$\Upsilon_u(k,l,n,z,t) = E_0(n)I(\phi,\lambda)F_n^2(z)B_n(k)4\pi^2l^2C_n(l)\int_{-\infty}^{+\infty}D_n(\omega)cos(2\pi\omega t)d\omega \tag{6.51}$$

Given $\Upsilon_u(k,l,t)$, equation (6.50) can be solved numerically with the initial conditions given in equation (6.47). Lundgren and Pointin (1976) assumed some idealized forms for $\Upsilon_u(k,l,t)$ and estimated the Lagrangian velocity autocorrelation function. They found that the results based on the independence approximation by Corrsin (1959) are consistent with numerical simulations. Because equation (6.50) is nonlinear, the solution depends not only on the spectral shape but also the energy level. As an example, I choose the energy magnitude to be 120 cm^2/s^2, which is a typical value in the mid-ocean. The Lagrangian and Eulerian autocorrelation functions of the first baroclinic mode at the sea surface are displayed in figure 6-13. As displayed there, both Eulerian and Lagrangian autocorrelation functions decay exponentially with time lag. The most striking feature in figure 6-13 is that the Lagrangian autocorrelation is much smaller than the Eulerian autocorrelation. The e-folding temporal scales of Lagrangian and Eulerian correlation are 4 and 40 days, respectively. There are very few observational studies in the literature about the relationship between Eulerian and Lagrangian statistics. Using the Lagrangian correlation predicator from Corrsin (1959), Middleton (1985) explored in detail the relationships between Lagrangian statistics and Eulerian frequency and wavenumber spectra. He found that in general Lagrangian statistics are insensitive to the details of Eulerian frequency and wavenumber spectrum. However, Lagrangian frequency spectrum depends on the integral length and time scale of the Eulerian velocity field. Davis (1985) analyzed the drifter measurements made off the Northern California coast and found that the Lagrangian time scale is significantly shorter than the Eulerian time scale. This suggests that the independence approximation theory is consistent with the observations.

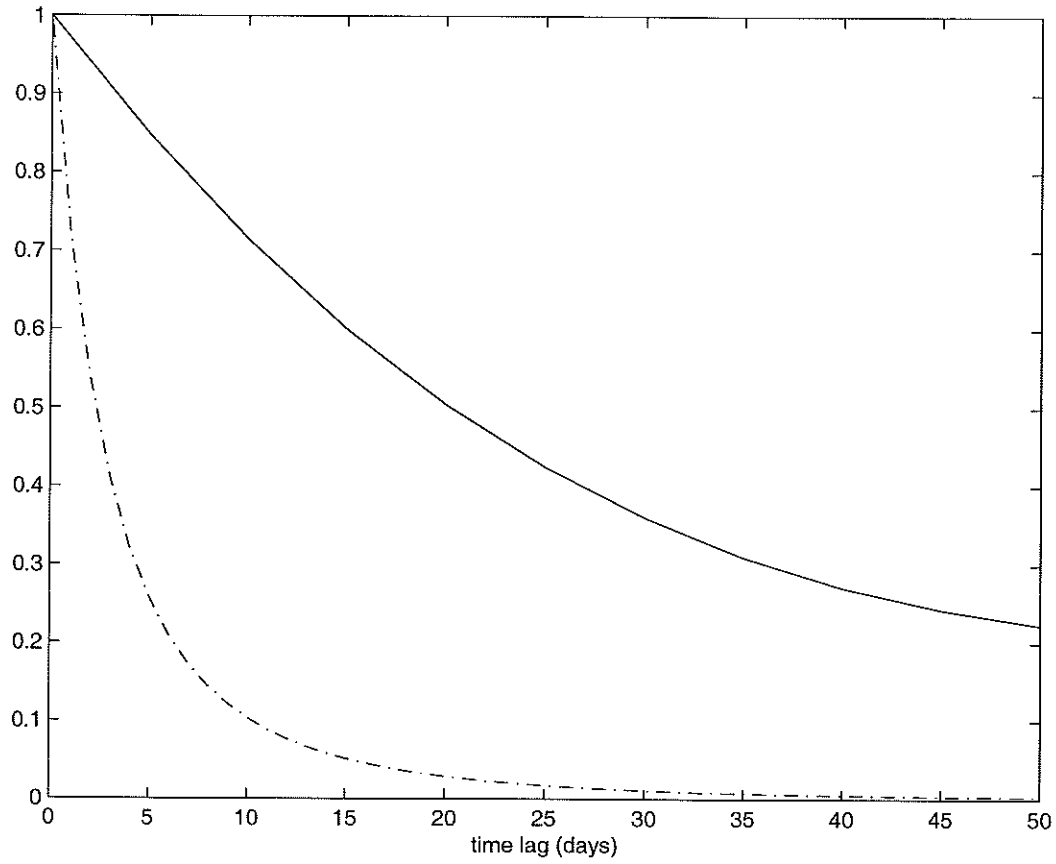

Figure 6-13: Eulerian (solid line) and Lagrangian autocorrelation (dashdot line) of the first baroclinic mode at $z = 0$ with the energy magnitude of 120 cm^2/s^2.

Chapter 7

Energy distribution in k, l and ω space part II: a directional form

7.1 Fitting $\Phi(k, l, \omega, n, \phi, \lambda)$ from observations

One of the important properties of low frequency variability is anisotropy: the energy of the sea surface height is not evenly distributed traveling in all directions. As shown in chapter 4, the energy of westward-going motions is higher than that of eastward-going motions by a factor of three at low frequencies and large scales in the area of 25°-50°N and 195°-225°E. However, as will be seen in chapter 8, the partition of energy among eastward-going, westward-going and standing motions depends on geography. In general, the energy associated with westward-going motions decreases with latitude and there is more energy going westward west of major topographic features. In this chapter, I am trying to model the directional property of the observed spectrum described. This model is not universal: it only applies to the particular region in the North Pacific ocean where the full three-dimensional spectra were analyzed. As shown in chapter 4, the difference between the energy going southward and northward is so little that it is simply ignored here. Because the frequency and wavenumber separate form, equation (4.3), cannot provide any information about the directional property of the spectrum, a frequency/zonal-wavenumber coupled form is chosen here

to differentiate the energy of eastward-going motions from that of westward-going motions. Again, because the spectrum is symmetrical, in the sense that $\Upsilon(k,l,\omega) = \Upsilon(-k,-l,-\omega)$, I am only concerned with positive frequencies, while k and l have both signs. Equation (4.3) is now modified to

$$\Phi(k,l,\omega,n,\phi,\lambda) = \Pi_n(k,\omega)C_n(l)E_0(n)I(\phi,\lambda). \tag{7.1}$$

$\Pi_n(k,\omega)$ has distinct forms for eastward-going, westward-going and standing motions,

$$\Pi_n(k,\omega) = \begin{cases} Q_{n-w}B_{n-w}(k)D_{n-w}(\omega) & for \;\; k < -k_0, \omega > 0 \\ Q_{n-e}B_{n-e}(k)D_{n-e}(\omega) & for \;\; k > k_0, \omega > 0 \\ Q_{n-0}B_{n-0}(k)D_{n-0}(\omega) & for \;\; -k_0 \leq k \leq k_0, \omega > 0 \end{cases} \tag{7.2}$$

where $B_{n-w}(k)$, $B_{n-e}(k)$ and $B_{n-0}(k)$ represent the wavenumber spectral shape of eastward-going, westward-going and standing motions, respectively; $D_{n-w}(\omega)$, $D_{n-e}(\omega)$ and $D_{n-0}(\omega)$ stand for the corresponding frequency spectral shape; and Q_{n-w}, Q_{n-e} and Q_{n-0} determine the relative energy level of eastward-going, westward-going and standing motions. Theoretically, the wavenumber of standing motions is zero and the energy distribution for standing motions is a delta function at $k = 0$. However, the spatial length of the actual data is finite; therefore, any motion with wavelengths longer than the spatial length of the data can not be resolved and is treated as standing waves. In order to be consistent with observations, I define k_0 as the smallest wavenumber which can be resolved by the data and treat the motions with wavenumbers less than k_0 as standing waves in my model. For the case analyzed in chapter 4, k_0 is about 0.0004 cycles per km.

Choosing the $\Pi_n(k,\omega)$ to fit the observed zonal-wavenumber/frequency spectrum of sea surface height

For westward-going motions ($k < -k_0, \omega > 0$)

Choosing the $B_{n-w}(k)$ to fit the observed zonal-wavenumber spectrum of westward-going motions

$$B_{n-w}(k) = \begin{cases} \alpha_1 |k|^{-0.5} & \text{if } -k_1 \leq k < -k_0 \\ |k|^{-4} & \text{if } k \leq k_1 \ , \end{cases} \tag{7.3}$$

where $k_1 = 0.0028$ (cycles per km). For continuity of $B_n(k)$ at k_1, $\alpha_1 = k_1^{-3.5}$. Equation (7.3) gives

$$\int_{-\infty}^{-k_0} B_{n-w}(k)dk = 7.2 \times 10^7. \tag{7.4}$$

Choosing the $D_{n-w}(\omega)$ to fit the observed frequency spectrum of westward-going motions

$$D_{n-w}(\omega) = \begin{cases} \gamma_0 \omega^{-0.5} & \text{if } 0 < \omega \leq \omega_0 \\ \omega^{-2} & \text{if } \omega \geq \omega_0 \ , \end{cases} \tag{7.5}$$

where $\omega_0 = 0.007$ (cycles per day). For continuity of $D_n(k)$ at ω_0, $\gamma_0 = \omega_0^{-1.5}$. Equation (7.5) yields

$$\int_0^{+\infty} D_{n-w}(\omega)d\omega = 429. \tag{7.6}$$

For eastward-going motions $(k > k_0, \omega > 0)$

Choosing the $B_{n-e}(k)$ to fit the observed zonal-wavenumber spectrum of eastward-going motions

$$B_{n-e}(k) = \begin{cases} \alpha_2 |k|^{-0.5} & \text{if } k_0 < k \leq k_2 \\ |k|^{-4} & \text{if } k \geq k_2 \ , \end{cases} \tag{7.7}$$

where $k_2 = 0.004$ (cycles per km). For continuity of $B_n(k)$ at k_2, $\alpha_2 = k_2^{-3.5}$. Equation (7.7) gives

$$\int_{+k_0}^{+\infty} B_{n-e}(k)dk = 2.7 \times 10^7. \tag{7.8}$$

Choosing the $D_{n-e}(\omega)$ to fit the observed frequency spectrum of eastward-going motions

$$D_{n-e}(\omega) = \begin{cases} \gamma_1 \omega^{-0.5} & \text{if } 0 < \omega \leq \omega_0 \\ \omega^{-1.5} & \text{if } \omega \geq \omega_0 \ , \end{cases} \tag{7.9}$$

where $\omega_0 = 0.007$ (cycles per day). For continuity of $D_n(k)$ at ω_0, $\gamma_1 = \omega_0^{-1}$. It follows from equation (7.9) that

$$\int_0^{+\infty} D_{n-e}(\omega) d\omega = 48. \tag{7.10}$$

For standing motions $(-k_0 \leq k \leq k_0, \omega > 0)$

Because the observations provide no information on the wavenumber spectrum at wavenumbers $-k_0 \leq k \leq k_0$, I simply assume that the energy of standing motions is evenly distributed within $-k_0 \leq k \leq k_0$:

$$B_{n-0}(k) = 1 \qquad \text{if } -k_0 \leq k \leq k_0, \tag{7.11}$$

which gives

$$\int_{-k_0}^{k_0} B_{n-0}(k) dk = 2k_0 = 0.0008. \tag{7.12}$$

Choosing the $D_{n-0}(\omega)$ to fit the observed frequency spectrum of standing motions

$$D_{n-0}(\omega) = \begin{cases} \gamma_2 \omega^{-0.75} & \text{if } 0 < \omega \leq \omega_1 \\ \omega^{-2} & \text{if } \omega \geq \omega_1 \ , \end{cases} \tag{7.13}$$

where $\omega_1 = 0.005$ (cycles per day). For continuity of $D_n(k)$ at ω_1, $\gamma_2 = \omega_1^{-1.25}$. Equation (7.13) gives

$$\int_0^{+\infty} D_{n-0}(\omega) d\omega = 1000. \tag{7.14}$$

By definition, the partitioning of the variance of sea surface height among eastward-

going, westward-going and standing motions for the model is

$$\sigma^2_{\eta e} : \sigma^2_{\eta w} : \sigma^2_{\eta 0} = \int_{k_0}^{+\infty}\int_{0}^{+\infty} Q_{n-e}B_{n-e}(k)D_{n-e}(\omega)d\omega dk$$
$$: \int_{-\infty}^{-k_0}\int_{0}^{+\infty} Q_{n-w}B_{n-w}(k)D_{n-w}(\omega)d\omega dk : \int_{-k_0}^{+k_0}\int_{0}^{+\infty} Q_{n-0}B_{n-0}(k)D_{n-0}(\omega)d\omega dk. \quad (7.15)$$

Substitution of equation (7.3) to (7.13) into equation (7.15) gives

$$\sigma^2_{\eta e} : \sigma^2_{\eta w} : \sigma^2_{\eta 0} = 1.5 \times 10^9 Q_{n-e} : 3.8 \times 10^{10} Q_{n-w} : 0.2 Q_{n-0}. \quad (7.16)$$

The observations in chapter 4 show that the energy of eastward-going, westward-going and standing motions is approximately in the ratio of 1:2:4. If we choose $Q_{n-e} = 1.0$, then according to equation (7.16), $Q_{n-w} = 0.084$ and $Q_{n-0} = 6.5 \times 10^9$.

Choosing the $C_n(l)$ to fit the observed meridional-wavenumber spectrum of sea surface height

$$C_n(l) = \begin{cases} \beta_0 & \text{if } |l| \le l_0 \\ \beta_1 |l|^{-1/2} & \text{if } l_0 < |l| \le l_1 \\ \beta_2 |l|^{-5/2} & \text{if } l_1 \le |l| \le l_2 \\ |l|^{-4} & \text{if } |l| \ge l_2 \ , \end{cases} \quad (7.17)$$

where $l_0 = 0.0004$; $l_1 = 0.0025$; and $l_2 = 0.008$ cycles per km. For continuity of $C_n(l)$ at l_1 and l_2, $\beta_1 = l_2^{-3/2} l_1^{-2}$ and $\beta_2 = l_2^{-3/2}$. Motions within $|l| \le l_0$ are treated as standing waves and it is assumed that the energy is constant within $-l_0 \le l \le l_0$. Equation (7.17) gives

$$\int_{l_0}^{+\infty} C_n(l) dl = 2.0 \times 10^7, \quad (7.18)$$

and

$$\int_{0}^{l_0} C_n(l) dl = \beta_0 l_0 = 0.0004 \beta_0. \quad (7.19)$$

The ratio of the energy of propagating motions, which includes the energy of northward-

going and southward-going motions, to that of standing motions for the model is

$$\sigma^2_{lpr} : \sigma^2_{lst} = 2.0 \times 10^7 : 0.0004\beta_0. \tag{7.20}$$

The measurements in chapter 4 show that the ratio of the total energy of northward-going and southward-going motions to that of standing motions is roughly 1:1. Accordingly,

$$\beta_0 = 5.0 \times 10^{10}. \tag{7.21}$$

Equation (7.3) to (7.17) yield

$$\int_{-\infty}^{+\infty}\int_{-\infty}^{+\infty}\int_{-\infty}^{+\infty}\Phi(k,l,\omega,n,\phi,\lambda)dkdld\omega = 1.46 \times 10^{18} I(\phi,\lambda)E_0(n). \tag{7.22}$$

The energy level of each mode

The total kinetic energy per unit surface area for each mode

$$\begin{aligned} KE(n) &= \int_{-\infty}^{+\infty}\int_{-\infty}^{+\infty}\int_{-\infty}^{+\infty}2\pi^2(k^2+l^2)\Phi(k,l,\omega,n,\phi,\lambda)dkdld\omega \\ &= 3.0 \times 10^{14} I(\phi,\lambda)E_0(n). \end{aligned} \tag{7.23}$$

As seen in chapter 4, the vertical structure of eddy kinetic energy can be simply represented by the barotropic and first two baroclinic modes in the middle of the ocean and roughly speaking, the kinetic energy of the first three modes is in the ratio of 1:1:1/2. Accordingly, if we choose $E_0(0) = 1$, then $E_0(1) = 1$ and $E_0(2) = 0.5$.

Choose the $I(\phi,\lambda)$ to fit the observed surface kinetic energy

The surface kinetic energy for the model is

$$\begin{aligned} E_k(\phi,\lambda,z=0) &= \sum_{n=0}^{n=2} F_n^2(z=0)\left[\int_{-\infty}^{+\infty}\int_{-\infty}^{+\infty}\int_{-\infty}^{+\infty}2\pi^2(k^2+l^2)\Phi(k,l,\omega,n,\phi,\lambda)dkdld\omega\right] \\ &= 9.9 \times 10^{11} I(\phi,\lambda). \end{aligned} \tag{7.24}$$

Equation (7.24) yields

$$I(\phi,\lambda) = \frac{E_k(\phi,\lambda,z=0)}{9.9\times10^{11}}. \tag{7.25}$$

The potential energy per unit surface area for each mode

$$\begin{aligned} PE(n,\phi,\lambda) &= \frac{1}{2R_n^2}\int_{-\infty}^{+\infty}\int_{-\infty}^{+\infty}\int_{-\infty}^{+\infty}\Phi(k,l,\omega,n,\phi,\lambda)dkdld\omega \\ &= \frac{1.5\times10^{18}I(\phi,\lambda)E_0(n)}{2R_n^2}. \end{aligned} \tag{7.26}$$

The ratio of kinetic energy to potential energy per unit surface area for first baroclinic mode

If we take $f = 10^{-4}\mathrm{s}^{-1}$, $R_1 = 25$ km and

$$\frac{KE(1,\phi,\lambda)}{PE(1,\phi,\lambda)} = 0.26. \tag{7.27}$$

The variance of sea surface height

$$\begin{aligned} \sigma_\eta^2(\phi,\lambda) &= \sum_{n=0}^{n=2}\frac{f^2F_n^2(z=0)}{g^2}\int_{-\infty}^{+\infty}\int_{-\infty}^{+\infty}\int_{-\infty}^{+\infty}\Phi(k,l,\omega,n,\phi,\lambda)dkdld\omega \\ &= 1.1\times10^{12}sin^2\phi\ I(\phi,\lambda) = 1.1sin^2\phi\ E_k(\phi,\lambda,z=0)\ \ [\mathrm{cm}^2]. \end{aligned} \tag{7.28}$$

The zonal-wavenumber spectrum of westward-going motions of sea surface height $(k<-k_0,\omega>0)$

$$\begin{aligned} \Upsilon_{\eta w}(k,\phi,\lambda) &= \sum_{n=0}^{n=2}\frac{f^2F_n^2(z=0)}{g^2}\int_0^{+\infty}\int_{-\infty}^{+\infty}Q_{n-w}B_{n-w}(k)D_{n-w}(\omega)C_n(l)E_0(n)I(\phi,\lambda)dld\omega \\ &= 2.1\times10^3sin^2\phi\ I(\phi,\lambda)B_{n-w}(k)\ \ [\mathrm{cm}^2/(\mathrm{cycles/km})]. \end{aligned} \tag{7.29}$$

The zonal-wavenumber spectrum of eastward-going motions of sea surface height $(k>k_0,\omega>0)$

$$\begin{aligned} \Upsilon_{\eta e}(k,\phi,\lambda) &= \sum_{n=0}^{n=2}\frac{f^2F_n^2(z=0)}{g^2}\int_0^{+\infty}\int_{-\infty}^{+\infty}Q_{n-e}B_{n-e}(k)D_{n-e}(\omega)C_n(l)E_0(n)I(\phi,\lambda)dld\omega \\ &= 2.8\times10^3sin^2\phi\ I(\phi,\lambda)B_{n-e}(k)\ \ [\mathrm{cm}^2/(\mathrm{cycles/km})]. \end{aligned} \tag{7.30}$$

The scalar zonal-wavenumber spectrum of sea surface height ($k > k_0$)

$$\begin{aligned}
\Upsilon_\eta(k,\phi,\lambda) &= \int_{-\infty}^{+\infty}\int_{-\infty}^{+\infty} F_\eta(k,l,\omega,\phi,\lambda)dld\omega \\
&= F_{\eta w}(k,\phi,\lambda) + F_{\eta e}(k,\phi,\lambda) \\
&= sin^2\phi\ I(\phi,\lambda)\,[2100B_{n-w}(k) + 2800B_{n-e}(k)] \quad [\mathrm{cm}^2/(\mathrm{cycles/km})]. \quad (7.31)
\end{aligned}$$

The scalar meridional-wavenumber spectrum of sea surface height ($l > l_0$)

$$\begin{aligned}
\Upsilon_\eta(l,\phi,\lambda) &= \sum_{n=0}^{n=2} \frac{f^2F_n^2(z=0)}{g^2} \int_{-\infty}^{+\infty}\int_{-\infty}^{+\infty} \Pi_n(k,\omega)C_n(l)E_0(n)I(\phi,\lambda)dld\omega \\
&= 1.3\times10^4 sin^2\phi\ I(\phi,\lambda)C_n(l) \quad [\mathrm{cm}^2/(\mathrm{cycles/km})]. \quad (7.32)
\end{aligned}$$

The frequency spectrum of westward-going motions of sea surface height ($k < -k_0, \omega > 0$)

$$\begin{aligned}
\Upsilon_{\eta w}(\omega,\phi,\lambda) &= \sum_{n=0}^{n=2} \frac{f^2F_n^2(z=0)}{g^2} \int_{-\infty}^{+\infty}\int_{-\infty}^{-k_0} Q_{n-w}B_{n-w}(k)D_{n-w}(\omega)C_n(l)E_0(n)I(\phi,\lambda)dkdl \\
&= 3.5\times10^8 sin^2\phi\ I(\phi,\lambda)D_{n-w}(\omega) \quad [\mathrm{cm}^2/(\mathrm{cycles/day})]. \quad (7.33)
\end{aligned}$$

The frequency spectrum of eastward-going motions of sea surface height ($k > k_0, \omega > 0$)

$$\begin{aligned}
\Upsilon_{\eta e}(\omega,\phi,\lambda) &= \sum_{n=0}^{n=2} \frac{f^2F_n^2(z=0)}{g^2} \int_{-\infty}^{+\infty}\int_{k_0}^{+\infty} Q_{n-e}B_{n-e}(k)D_{n-e}(\omega)C_n(l)E_0(n)I(\phi,\lambda)dkdl \\
&= 1.6\times10^9 sin^2\phi\ I(\phi,\lambda)D_{n-e}(\omega) \quad [\mathrm{cm}^2/(\mathrm{cycles/day})]. \quad (7.34)
\end{aligned}$$

The frequency spectrum of standing motions of sea surface height ($-k_0 \le k \le k_0, \omega > 0$)

$$\begin{aligned}
\Upsilon_{\eta 0}(\omega,\phi,\lambda) &= \sum_{n=0}^{n=2} \frac{f^2F_n^2(z=0)}{g^2} \int_{-\infty}^{+\infty}\int_{-k_0}^{k_0} Q_{n-0}B_{n-0}(k)D_{n-0}(\omega)C_n(l)E_0(n)I(\phi,\lambda)dkdl \\
&= 3.0\times10^8 sin^2\phi\ I(\phi,\lambda)D_{n-0}(\omega) \quad [\mathrm{cm}^2/(\mathrm{cycles/day})]. \quad (7.35)
\end{aligned}$$

The scalar frequency spectrum of sea surface height ($\omega > 0$)

$$\Upsilon_\eta(\omega,\phi,\lambda) = \Upsilon_{\eta w}(\omega,\phi,\lambda) + \Upsilon_{\eta e}(\omega,\phi,\lambda) + \Upsilon_{\eta 0}(\omega,\phi,\lambda)$$
$$= sin^2\phi\ I(\phi,\lambda)\left[3.5\times10^8 D_{n-w}(\omega) + 1.6\times10^9 D_{n-e}(\omega) + 3.0\times10^8 D_{n-0}(\omega)\right], \quad (7.36)$$

in the units of $\mathrm{cm}^2/(\mathrm{cycles/day})$.

The scalar zonal-wavenumber spectrum of temperature ($k > k_0$)

$$\begin{aligned}\Upsilon_\theta(k,z,\phi,\lambda) &= \sum_{n=0}^{n=2} f^2 G_n^2(z)(\frac{\partial\theta_0}{\partial z})^2 E_0(n) I(\phi,\lambda)\int_{-\infty}^{+\infty}\int_{-\infty}^{+\infty}\Pi(k,\omega)C_n(l)dld\omega \\ &= 6.1\times10^3 sin^2\phi\ I(\phi,\lambda)(\frac{\partial\theta_0}{\partial z})^2\left[G_1^2(z) + 0.5\times G_2^2(z)\right] \\ &\quad [B_{n-w}(k) + 1.4\times B_{n-e}(k)]\quad [^\circ\mathrm{C}^2/(\mathrm{cycles/km})]. \end{aligned} \quad (7.37)$$

The scalar meridional-wavenumber spectrum of temperature ($l > l_0$)

$$F_\theta(l,z,\phi,\lambda) = \sum_{n=0}^{n=2} f^2 G_n^2(z)(\frac{\partial\theta_0}{\partial z})^2\int_{-\infty}^{+\infty}\int_{-\infty}^{+\infty}\Pi(k,\omega)dkd\omega C_n(l)E_0(n)I(\phi,\lambda)$$
$$= 3.8\times10^4 sin^2\phi\ I(\phi,\lambda)(\frac{\partial\theta_0}{\partial z})^2[G_1^2(z) + 0.5\times G_2^2(z)]C_n(l)\quad [^\circ\mathrm{C}^2/(\mathrm{cycles/km})]. \quad (7.38)$$

The frequency spectrum of zonal velocity ($\omega > 0$)

$$\Upsilon_u(\omega,z,\phi,\lambda) = \sum_{n=0}^{n=2}\int_{-\infty}^{+\infty}\int_{-\infty}^{+\infty} 4\pi^2 l^2 F_n^2(z)\Phi(k,l,\omega,n,\phi,\lambda)dkdl$$
$$= 1.25\times10^{11} I(\phi,\lambda)\left[F_0^2(z) + F_1^2(z) + 0.5F_2^2(z)\right]$$
$$\times[D_{n-w}(\omega) + 4.5\times D_{n-e}(\omega) + 0.87\times D_{n-0}(\omega)]\quad [\mathrm{cm}^2/\mathrm{s}^2/(\mathrm{cycles/day})] \quad (7.39)$$

The frequency spectrum of meridional velocity ($\omega > 0$)

$$\Upsilon_v(\omega,z,\phi,\lambda) = \sum_{n=0}^{n=2}\int_{-\infty}^{+\infty}\int_{-\infty}^{+\infty} 4\pi^2 k^2 F_n^2(z)\Phi(k,l,\omega,n,\phi,\lambda)dkdl$$
$$= 1.3\times10^{11} I(\phi,\lambda)\left[F_0^2(z) + F_1^2(z) + 0.5F_2^2(z)\right]$$
$$\times\left[D_{n-w}(\omega) + 8.7\times D_{n-e}(\omega) + 7.0\times10^{-3} D_{n-0}(\omega)\right], \quad (7.40)$$

in the units of $cm^2/s^2/(cycles/day)$.

The frequency spectrum of temperature ($\omega > 0$)

$$\Upsilon_\theta(\omega, z, \phi, \lambda) = \sum_{n=0}^{n=2} f^2 G_n^2(z)(\frac{\partial \theta_0}{\partial z})^2 \int_{-\infty}^{+\infty}\int_{-\infty}^{+\infty} \Phi(k, l, \omega, n, \phi, \lambda) dk dl$$
$$= 1.0 \times 10^9 sin^2\phi \; I(\phi, \lambda)[G_1^2(z) + 0.5 \times G_2^2(z)](\frac{\partial \theta_0}{\partial z})^2$$
$$\times [D_{n-w}(\omega) + 4.5 \times D_{n-e}(\omega) + 0.85 \times D_{n-0}(\omega)] \quad [°C^2/(cycles/day)]. \quad (7.41)$$

7.2 Model and data comparison

As in chapter 5, the model spectra will be compared with the corresponding observations. The data used here are the same as those used in chapter 5.

The frequency/wavenumber spectrum of sea surface height

The frequency and wavenumber spectra of westward-going and eastward-going motions in sea surface height are displayed in figure 7-1. The model spectra fit the observations quite well in terms of both spectral shape and energy level (figure 7-1). As shown in figures 7-2 and 7-3, the scalar zonal-wavenumber spectrum and meridional-wavenumber spectrum of the model are in rough agreement with the corresponding observations. The energy level of model frequency spectra in figures 7-2 to 7-5 are systematically higher than the observations and the differences are within a factor of 2. Figure 7-4 shows that superimposed on the background continuum, there is a striking peak at the annual period on the observed spectrum. The peak associated with annual cycle only appears on the frequency spectrum of sea surface height: there is no significant peak at the period of one year on the frequency spectra of horizontal velocities and temperature. The seasonal cycles should be treated exclusively. This is left for future study.

The scalar wavenumber spectrum of temperature

The scalar zonal-wavenumber spectrum of temperature is shown in figure 7-6. As shown there, the agreement between the model spectrum and the observed spectrum is quite pleasing.

The scalar frequency spectrum of horizontal velocities and temperature

Figure 7-7 displays the frequency spectra of two components of horizontal velocities and temperature at 5 different depths. Because the data sets are short, the spectra have large confidence intervals. The model spectra are indistinguishable from the observations with respect to a 95% confidence interval.

7.3 Summary

The directional form for the energy density $\Phi(k, l, \omega, n, \phi, \lambda)$ is produced in this chapter. Compared with the model produced in chapter 5, this one can differentiate westward-going energy from eastward-going energy; however it is more complex. Only the first three modes are included in my model: the barotropic and first two baroclinic modes. For each mode I choose

$$\Phi(k, l, \omega, n, \phi, \lambda) = \Pi_n(k, \omega) C_n(l) E_0(n) I(\phi, \lambda). \tag{7.42}$$

$\Pi_n(k, \omega)$ has distinct forms for eastward-going, westward-going and standing motions,

$$\Pi_n(k, \omega) = \begin{cases} Q_{n-w} B_{n-w}(k) D_{n-w}(\omega) & for \;\; k < -k_0, \omega > 0 \\ Q_{n-e} B_{n-e}(k) D_{n-e}(\omega) & for \;\; k > k_0, \omega > 0 \\ Q_{n-0} B_{n-0}(k) D_{n-0}(\omega) & for \;\; -k_0 \leq k \leq k_0, \omega > 0 \end{cases} \tag{7.43}$$

where $k_0 = 0.0004$ cycles/km. Based on various observations, I obtain

(1) the zonal-wavenumber/frequency spectral shape $\Pi_n(k, \omega)$

For westward-going motions $(k < -k_0, \omega > 0)$

$$B_{n-w}(k) = \begin{cases} 8.6 \times 10^8 |k|^{-0.5} & \text{if } -k_1 \leq k < -k_0 \\ |k|^{-4} & \text{if } k \leq k_1 \;, \end{cases} \tag{7.44}$$

where $k_1 = 0.0028$ cycles per km.

$$D_{n-w}(\omega) = \begin{cases} 1.7 \times 10^3 \omega^{-0.5} & \text{if } 0 < \omega \leq \omega_0 \\ \omega^{-2} & \text{if } \omega \geq \omega_0 \ , \end{cases} \tag{7.45}$$

where $\omega_0 = 0.007$ cycles per day.

$$Q_{n-w} = 0.084 \tag{7.46}$$

For eastward-going motions $(k > k_0, \omega > 0)$

$$B_{n-e}(k) = \begin{cases} 2.5 \times 10^8 |k|^{-0.5} & \text{if } k_0 < k \leq k_2 \\ |k|^{-4} & \text{if } k \geq k_2 \ , \end{cases} \tag{7.47}$$

where $k_2 = 0.004$ cycles per km.

$$D_{n-e}(\omega) = \begin{cases} 143 \omega^{-0.5} & \text{if } 0 < \omega \leq \omega_0 \\ \omega^{-1.5} & \text{if } \omega \geq \omega_0 \ , \end{cases} \tag{7.48}$$

where $\omega_0 = 0.007$ cycles per day.

$$Q_{n-e} = 1.0 \tag{7.49}$$

For standing motions $(-k_0 \leq k \leq k_0, \omega > 0)$

$$B_{n-0}(k) = 1 \qquad \text{if } -k_0 \leq k \leq k_0, \tag{7.50}$$

$$D_{n-0}(\omega) = \begin{cases} 752 \omega^{-0.75} & \text{if } 0 < \omega \leq \omega_1 \\ \omega^{-2} & \text{if } \omega \geq \omega_1 \ , \end{cases} \tag{7.51}$$

where $\omega_1 = 0.005$ cycles per day.

$$Q_{n-0} = 6.5 \times 10^9. \tag{7.52}$$

(2) the meridional-wavenumber spectral shape

$$C_n(l) = \begin{cases} 2.5 \times 10^{11} & \text{if } |l| \leq l_0 \\ 2.2 \times 10^8 |l|^{-1/2} & \text{if } l_0 < |l| \leq l_1 \\ 1.4 \times 10^3 |l|^{-5/2} & \text{if } l_1 \leq |l| \leq l_2 \\ |l|^{-4} & \text{if } |l| \geq l_2 \ , \end{cases} \tag{7.53}$$

where $l_0 = 0.0001$, $l_1 = 0.0025$, and $l_2 = 0.008$ cycles per km.

(3) the partition among vertical modes

$$E_0(0) = 1, E_0(1) = 1 and E_0(2) = 0.5. \tag{7.54}$$

(4) the energy magnitude

$$I(\phi, \lambda) = \frac{E_k(\phi, \lambda, z = 0)}{9.9 \times 10^{11}}. \tag{7.55}$$

The empirical formula for the surface kinetic energy in the North Pacific is

$$\begin{aligned} E_k(\phi, \lambda, z = 0) \quad = \quad & 30 + \frac{32}{\sin^2 \phi} + 1000 \exp\{-[\frac{(\lambda - 150)^2}{900} + \frac{(\phi - 35)^2}{50}]\} \\ & -80 \exp\{-[\frac{(\lambda - 190)^2}{1600} + \frac{(\phi - 42)^2}{200}]\}, \end{aligned} \tag{7.56}$$

where λ is the longitude , ϕ is the latitude and the units of E_k are cm^2/s^2.

The scalar formula for $\Phi(k, l, \omega, n, \phi, \lambda)$, which is produced in chapter 5, can be obtained from the directional form by adding up the energy of eastward-going, westward-going, and standing motions.

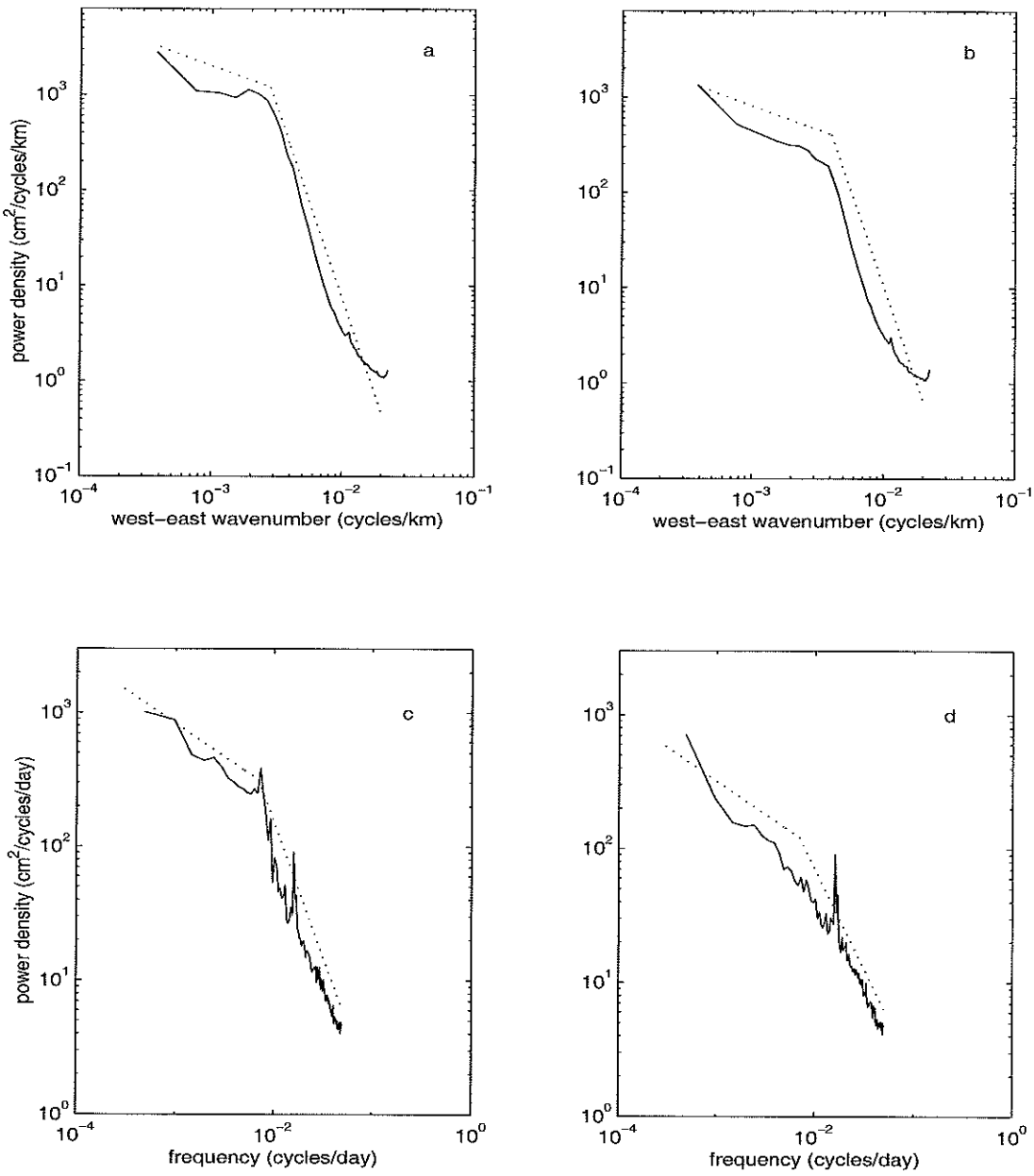

Figure 7-1: The zonal-wavenumber spectrum of westward-going motions (a) and eastward-going motions (b), and the frequency spectrum of westward-going motions (c) and eastward-going motions (d) of sea surface height. The spectra of measurements and model are plotted in solid lines and dotted lines, respectively. The peak at the period about 60 days in figure (c) and (d)is due to tidal aliasing.

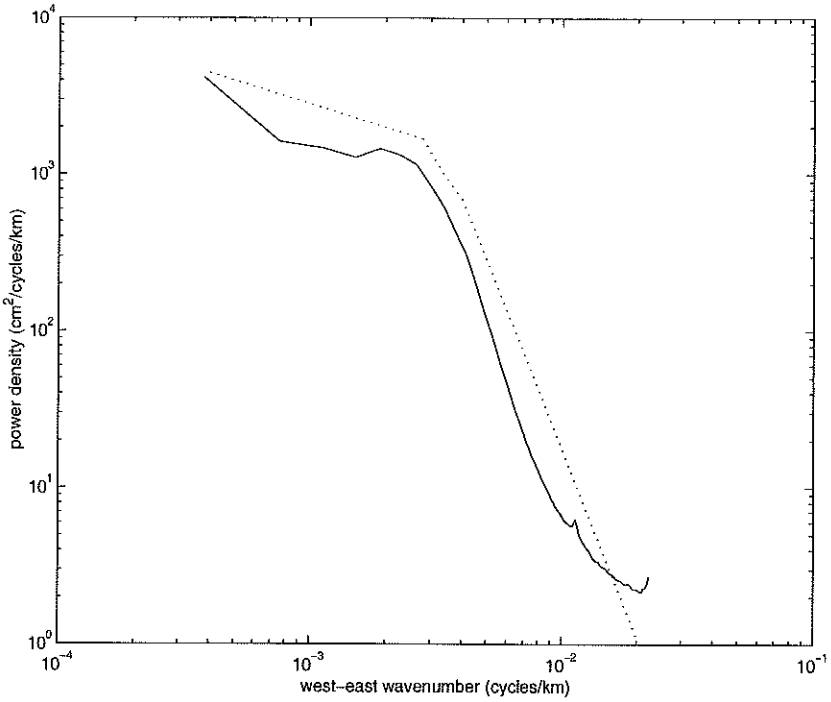

Figure 7-2: Scalar zonal-wavenumber spectrum of sea surface height. Solid line is the observed spectrum. Dotted line is the corresponding model spectrum.

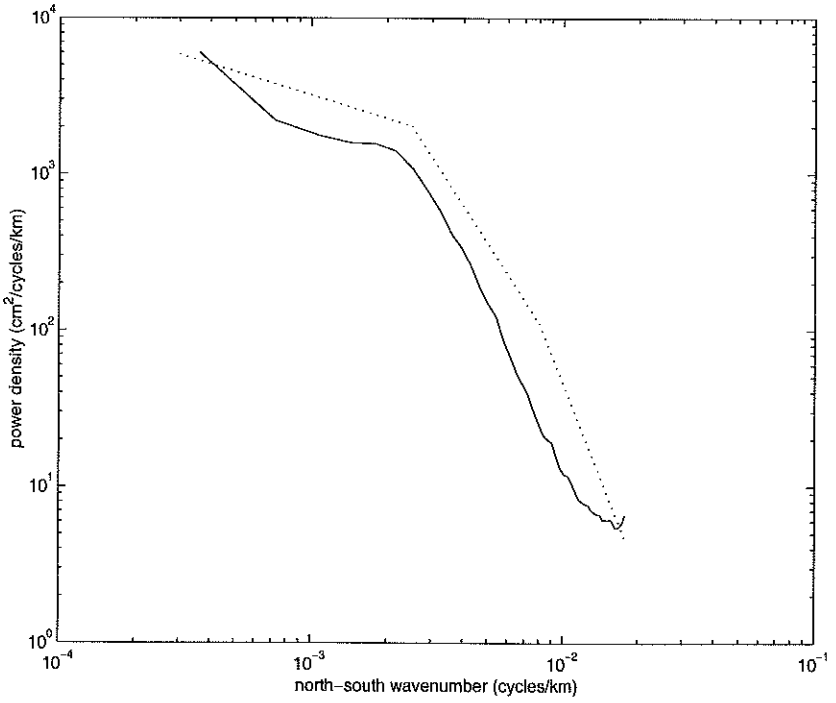

Figure 7-3: Scalar meridional-wavenumber spectrum of sea surface height. Solid line is the observed spectrum. Dotted line is the corresponding model spectrum.

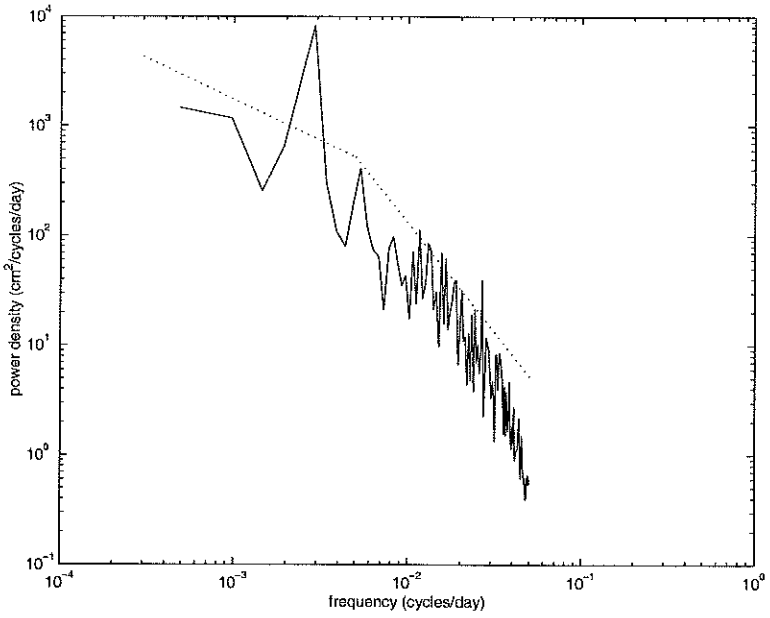

Figure 7-4: Frequency spectrum of standing motions of sea surface height. Solid line is the observed spectrum. Dotted line is the corresponding model spectrum. Superimposed on the background continuum, there is a striking peak at the annual period.

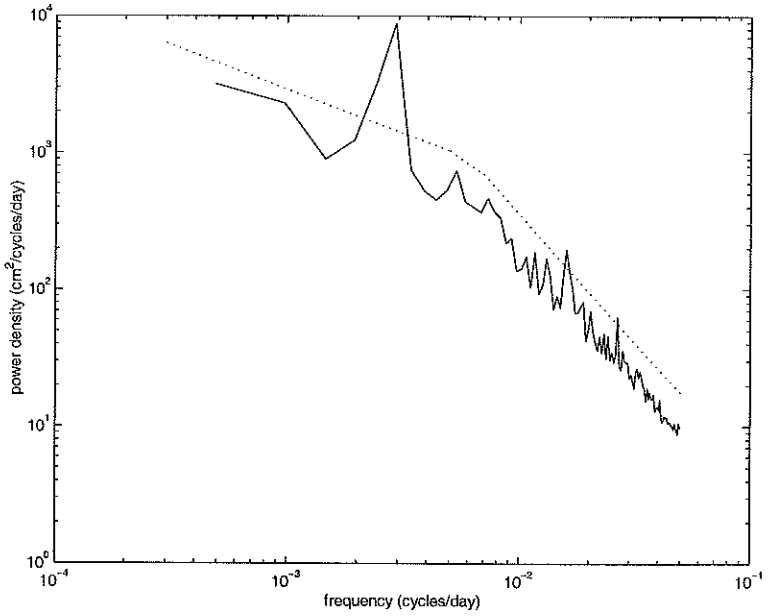

Figure 7-5: Scalar frequency spectrum of sea surface height. Solid line is the observed spectrum. Dotted line is the corresponding model spectrum. The observed spectrum is dominated by the annual cycle.

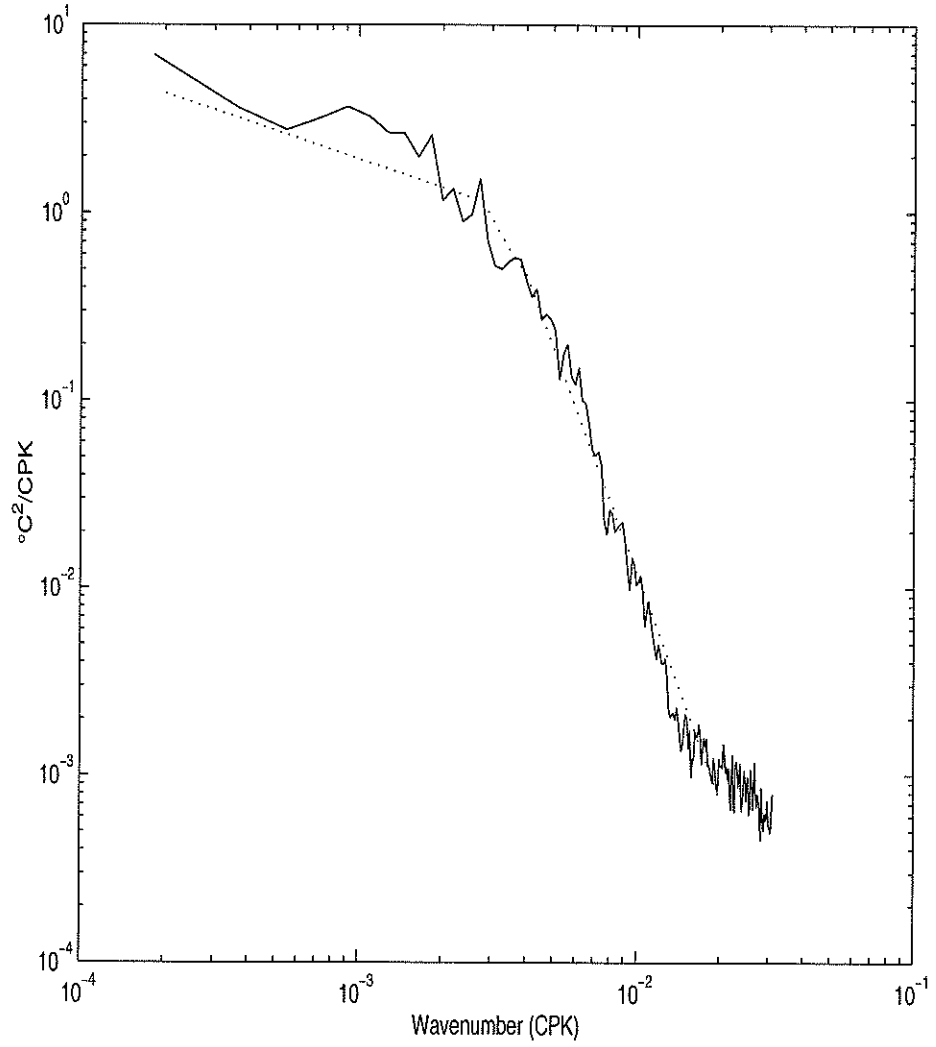

Figure 7-6: Scalar zonal-wavenumber spectrum temperature. Solid line is the observed spectrum. Dotted line is the corresponding model spectrum.

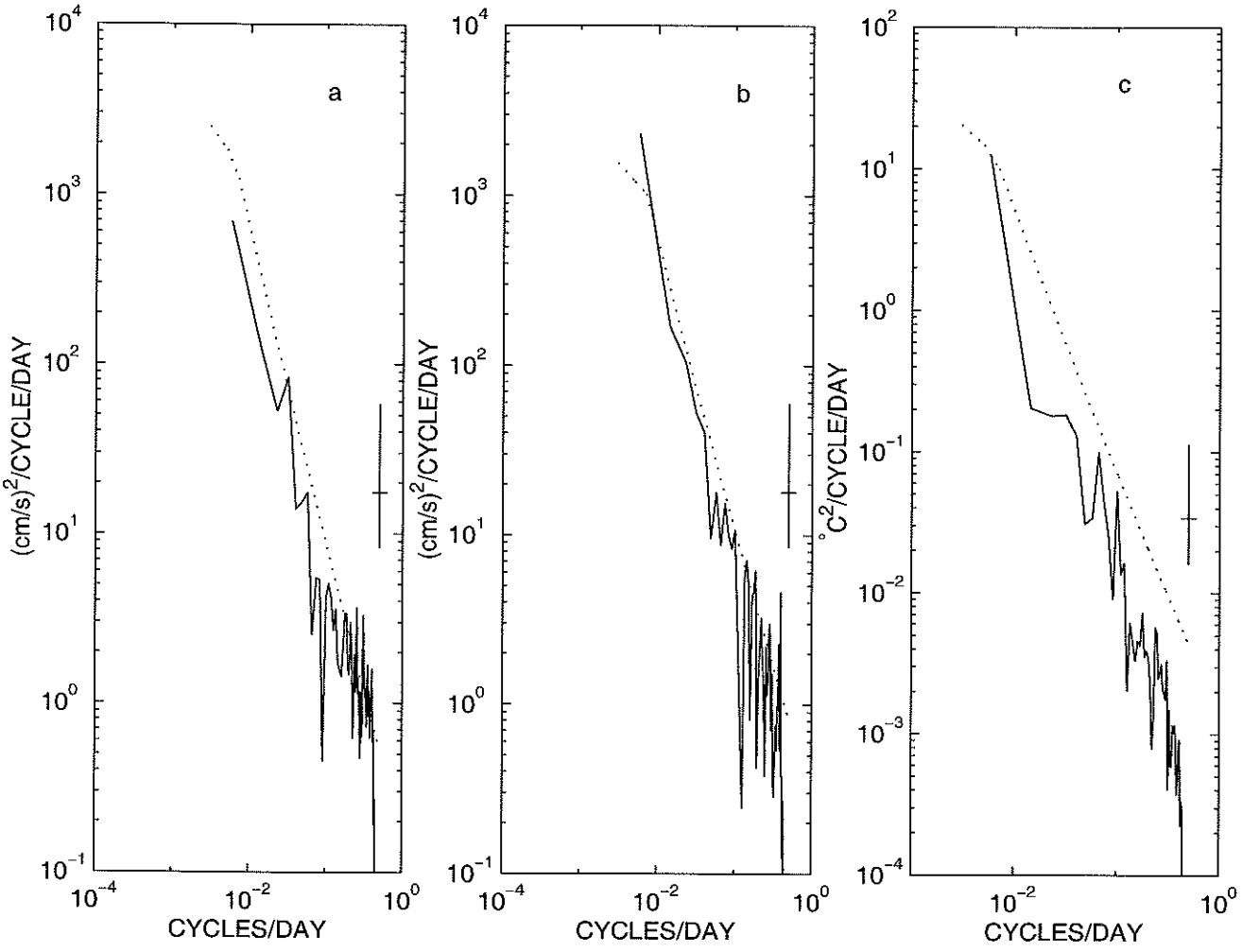
a
b
c
(cm/s)^2/CYCLE/DAY
(cm/s)^2/CYCLE/DAY
°C^2/CYCLE/DAY
CYCLES/DAY
CYCLES/DAY
CYCLES/DAY

(i)

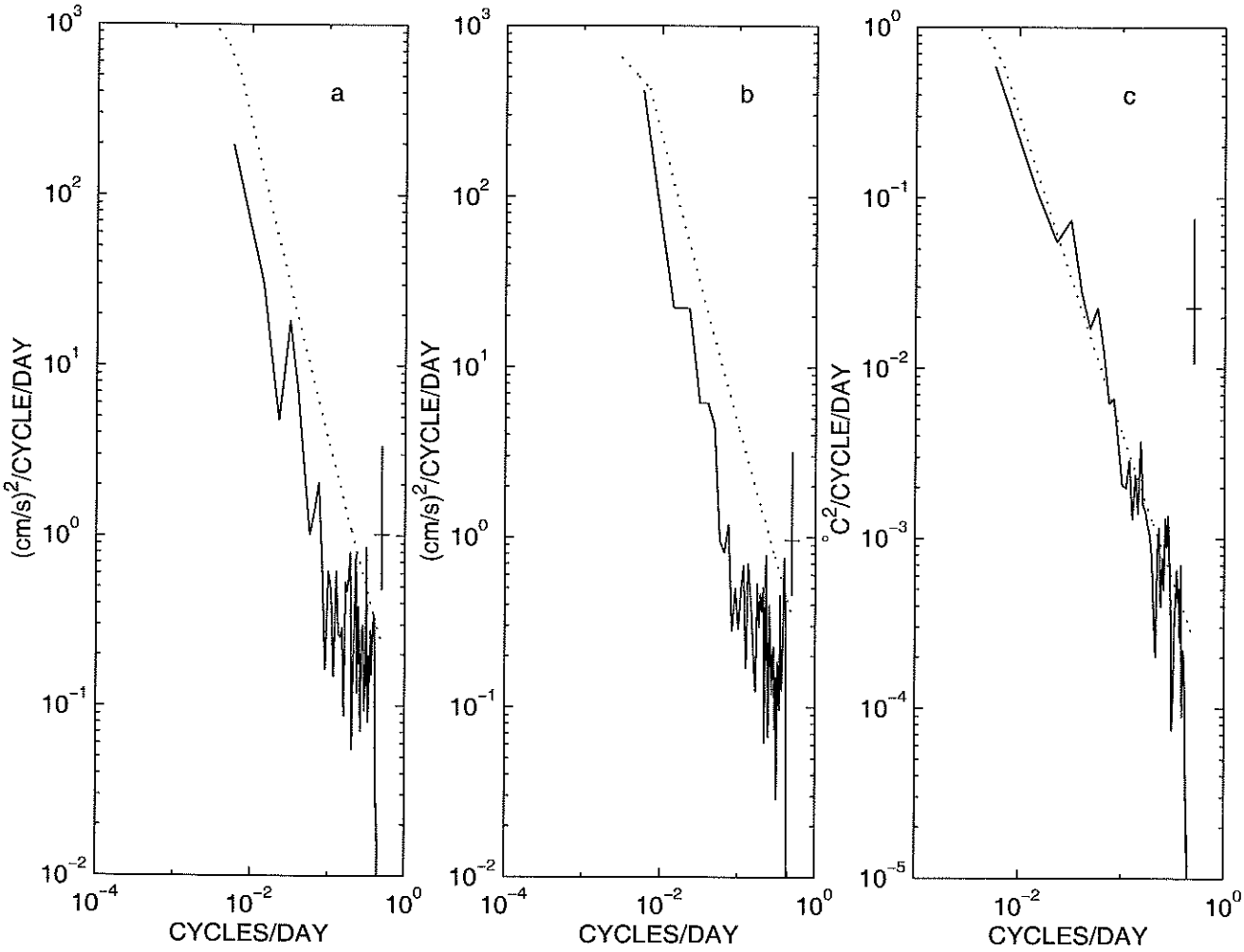
a
b
c
(cm/s)^2/CYCLE/DAY
(cm/s)^2/CYCLE/DAY
°C^2/CYCLE/DAY
CYCLES/DAY
CYCLES/DAY
CYCLES/DAY

(ii)

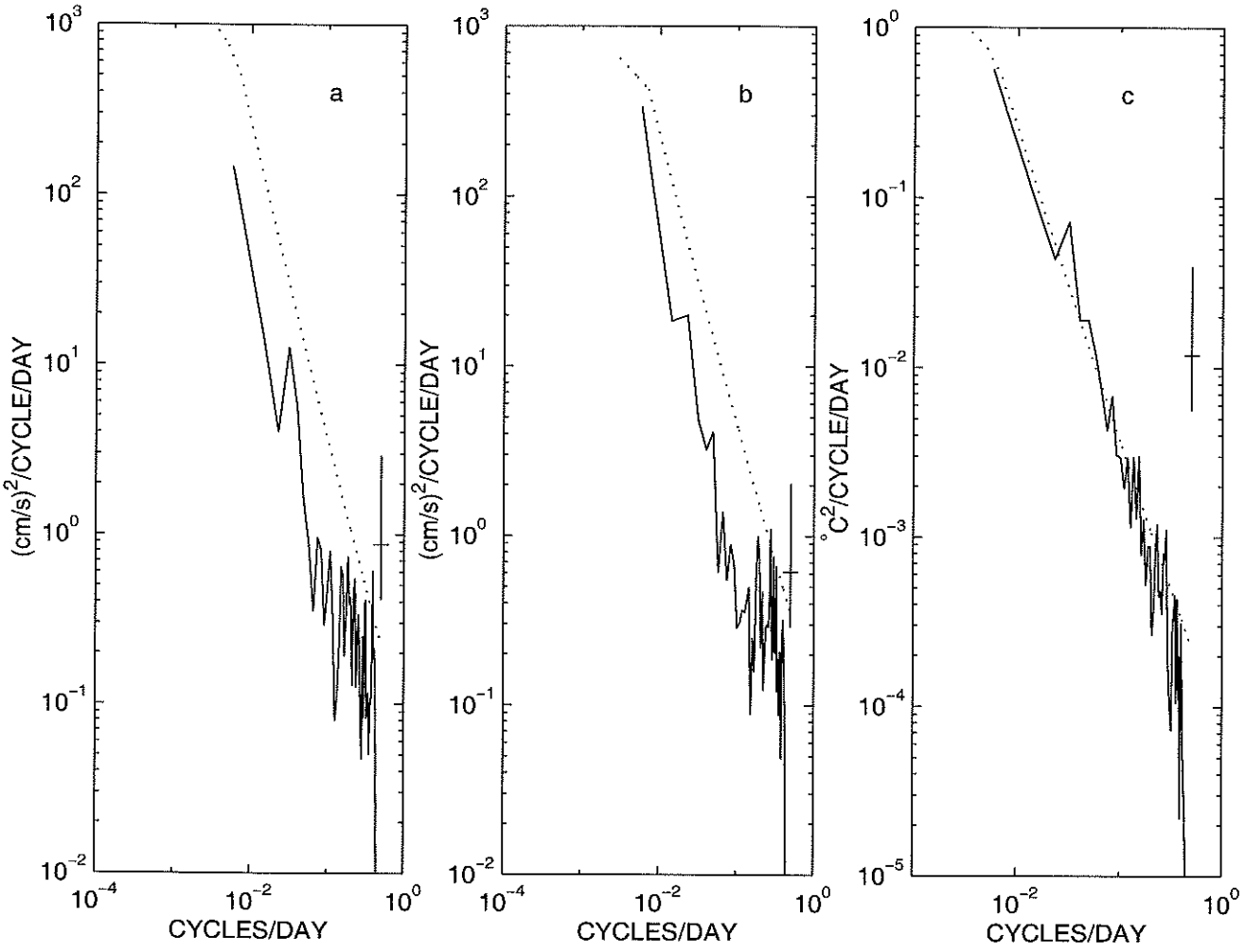
a
b
c
(cm/s)^2/CYCLE/DAY
(cm/s)^2/CYCLE/DAY
°C^2/CYCLE/DAY
CYCLES/DAY
CYCLES/DAY
CYCLES/DAY

(iii)

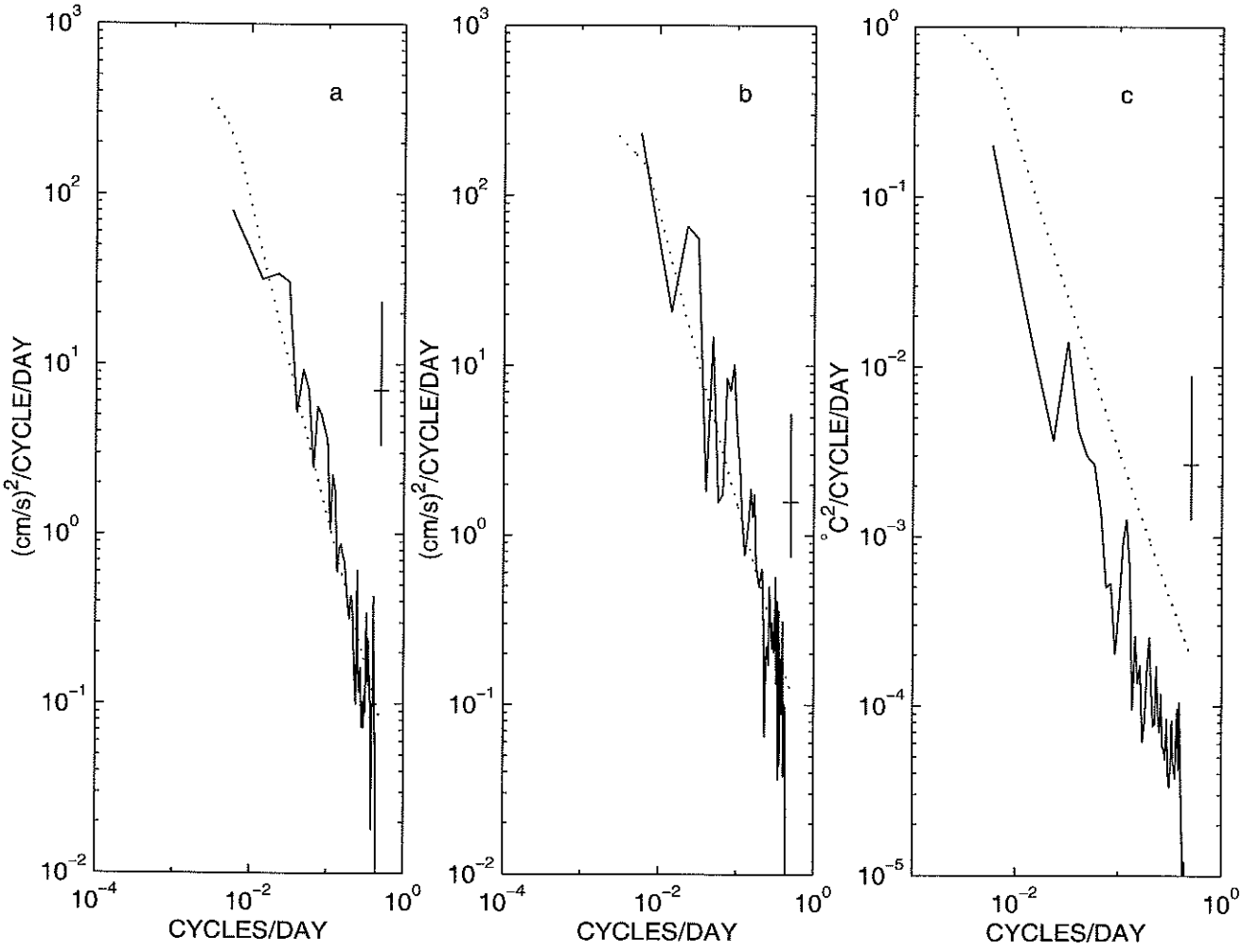
a
b
c
(cm/s)²/CYCLE/DAY
°C²/CYCLE/DAY
CYCLES/DAY
CYCLES/DAY
CYCLES/DAY

(iv)

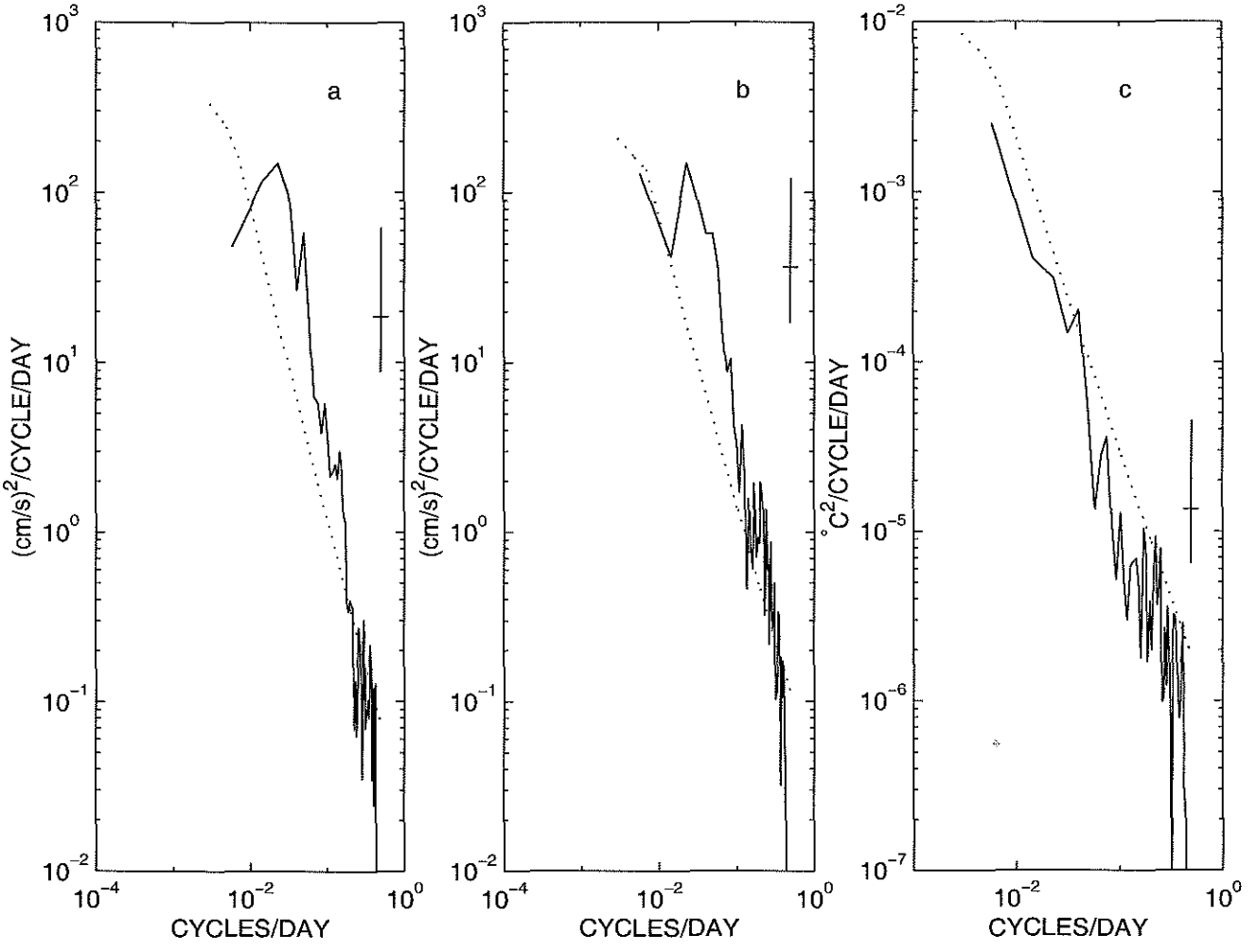

(v)

Figure 7-7: Scalar frequency spectra of zonal (a), meridional velocity (b) and temperature (c) at depths of 160m (i), 580m (ii), 595m (iii), 1230m (iv) and 3000m (v). The solid line is the observed spectrum and the dotted line is the model spectrum.

Chapter 8

The observed dispersion relationship for North Pacific Rossby wave motions

8.1 Introduction

Most of this chapter was published by Zang and Wunsch (1999). In the preceding chapters, efforts are made to produce a universal continuous spectrum for low frequency variability. The low frequency variability consists of Rossby waves, eddies and etc. Rossby waves are important parts among the continuous spectrum we produced in previous chapters. What percentage of the ocean variability can be explained by the linear Rossby wave theory is of interest not only for their links to the forecast of low frequency oceanic variability but also from a theoretical point of view. Rossby waves play an important role in maintaining the western boundary layer and the transient adjustment of ocean circulation to changes in atmospheric forcing. The presence of the first baroclinic long Rossby waves was found early from upper-ocean temperature data (White, 1977; Kessler, 1990). White (1977) analyzed the XBT data for the tropical North Pacific and discovered that the annual vertical displacements in the main thermocline propagate westward as long baroclinic waves, with a phase

speed twice that of free first baroclinic Rossby waves. Recently, Chelton and Schlax (1996) performed an analysis of the 3-year high quality TOPEX/POSEIDON altimeter data. They filtered out high frequency and small scale variabilities to highlight the long Rossby waves and found that the disagreement between the apparent phase speeds of Rossby waves and the theoretically predicted values is universal. Poleward of the tropical band from 10°S to 10°N, the apparent phase speeds are systematically greater than those predicted by standard theory for free first baroclinic long Rossby waves (Figure 8-1).

The difference between the apparent phase speeds and those predicted by standard theory has been attributed by several authors (e.g., Qiu et al., 1997; Killworth, 1997) to the breakdown of one or more of the assumptions inherent in the linear theory. Possible mechanisms include atmospheric forcing, wave and mean flow interactions, wave and wave interaction, coupling of vertical modes and topography. Some of these factors will be examined in the following.

White (1977) studied the ocean response to annual wind forcing. He showed that when superimposed on the local response, the free long Rossby wave yields a long wave which propagates at a phase speed twice that of the free long Rossby wave. Qiu et al. (1997) extended the theory by White (1977). They investigated what the phase speed of the total response was when in the presence of the forced wave response to wind forcing in the interior ocean, the eastern boundary generated free Rossby wave and dissipation. They showed that the forced wave pattern propagates westward at $2c_r$, where c_r is the speed of the free first baroclinic long Rossby wave. In low latitudes the westward phase speed of the total response favors the speed of $1c_r$ because of the boundary-generated free Rossby waves. Toward higher latitudes, the boundary-generated free waves become highly dissipative, the interior-forced wave motion becomes dominant. Thus the total response tends to propagate at $2c_r$.

Killworth et al. (1997) investigated the effect of mean zonal flow on the propagation of first baroclinic long Rossby waves. Using historical hydrographic data, they

obtained the climatological buoyancy frequency profiles and the vertical shear of the mean flow. They found that the effect of the mean barotropic zonal flow is purely a Doppler shift and the inclusion of the barotropic flow has small and mixed effects on the phase speed of the first baroclinic Rossby wave. The major changes to the Rossby wave phase speed are caused by the presence of second baroclinic zonal mean flow, which modifies the potential vorticity gradient. Assuming some idealized form for the model buoyancy and mean shear flow, Dewar (1998) performed a similar study and found that baroclinic waves are accelerated through the interactions of the waves with the background potential vorticity field. de Szoeke and Chelton (1999) further investigated what features in the mean flow and stratification cause the acceleration of the long baroclinic Rossby waves. By studying a simple three-layer model, they concluded that the modification of long baroclinic Rossby waves is associated with potential vorticity homogenization.

So far, all studies attribute the difference between observations and theory to the limitation of the simple linear theory. One important fact has been neglected. The observed phase speed obtained by Chelton and Schlax (1996) is not the phase speed of free first baroclinic Rossby waves. As seen in chapter 4, the sea surface height variability is a broad band process. It is made up of many different signals such as free Rossby waves, forced waves, etc. Moreover, although in general sea surface height variability mainly reflects the first baroclinic mode, the barotropic mode and high baroclinic modes play an important role over many parts of the ocean (Wunsch, 1997). Therefore, not all the sea surface height variability is necessarily first baroclinic Rossby waves. The observed phase speed obtained by Chelton and Schlax (1996) is not the phase speed of free first baroclinic Rossby waves, but the phase speed of the total response which is composed of barotropic Rossby waves, first and second baroclinic Rossby waves, forced waves, etc. Although the linear Rossby wave theory is a first-order good approximation to oceanic low frequency variability, the actual ocean is turbulent and much of the actual time-dependent motion can not be adequately described by linear wave models. How to separate the free Rossby

waves from other waves and to which extent the linear Rossby wave theory is a good representation of the true ocean variability are the incentive for this work. Because the standard theory for free Rossby waves is expressed in terms of frequency and wavenumber, the best way to compare observations with theory is to express the data in Fourier space, that is, analyze the three dimensional spectrum of the data. The determination of the frequency/wavenumber structure of the wave field is one of the most powerful techniques for the study of the properties of ocean variability. The frequency/wavenumber spectrum yields the direction and phase speed of wave propagation, and therefore helps us to forecast the propagating signals and clarify the fundamental processes of wave generation. It can also help us separate different physical processes by taking advantage of the fact that different waves have different frequency and wavenumber characteristics. Cipollini et al. (1997) performed Fourier transforms of TOPEX/POSEIDON altimeter data and ERS-1 along-track scanning radiometer sea surface temperature data near 34°N in the Northeast Atlantic. They observed westward propagating signals with three distinct speeds. However, they neither compared the observations with the theory nor provided estimates of uncerntainty. Using a filter in time and a wavelet transform in space, Wang et al. (1998) analyzed the gridded sea surface height data and identified two types of Rossby waves with different frequencies and wavenumbers along 25°S in the South Pacific. No estimates of uncertainty was provided. Here we apply array signal processing technique to the original along track sea surface height data. We will provide estimates of uncertainty and compare the observations with the theoretical dispersion relationships for Rossby waves.

The presentation of this chapter is organized as follows. The array processing method will be reviewed in section 2. Section 3 presents data and data processing. The results are discussed in section 4. A brief summary is drawn in section 5.

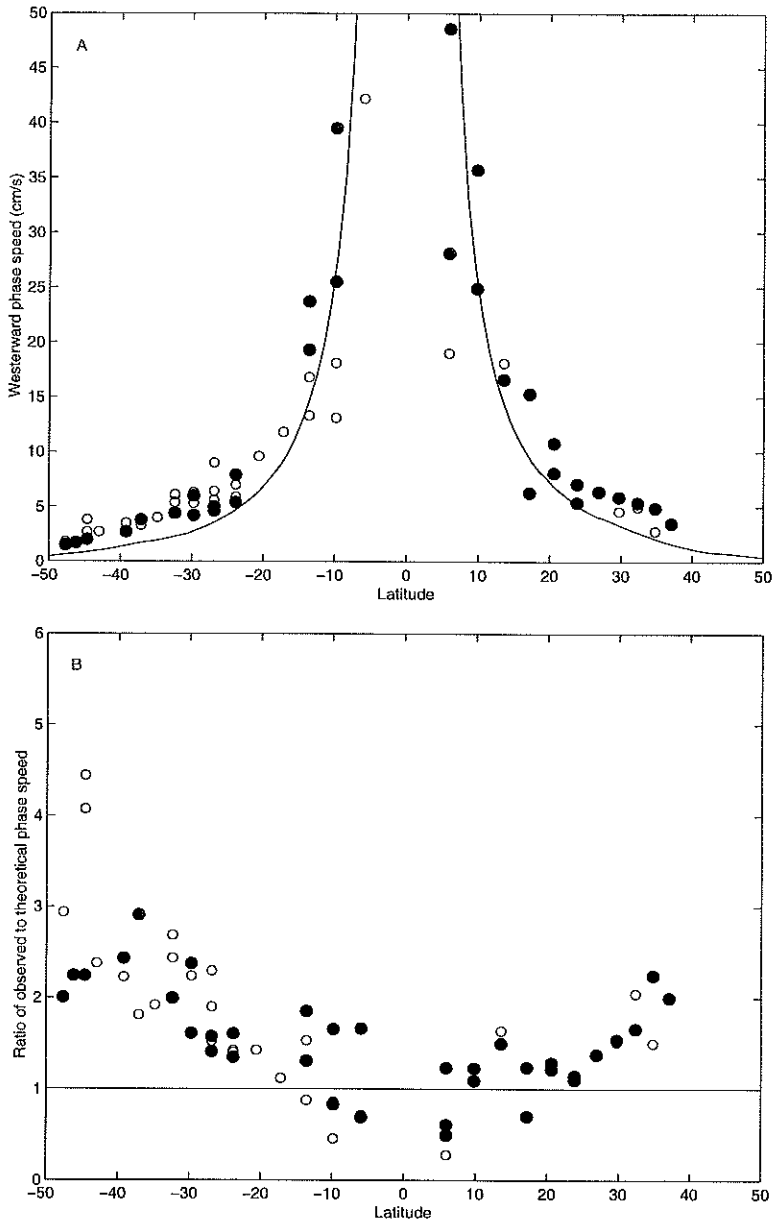

Figure 8-1: (A) Gloabally distributed estimates of the phase speeds of westward-propagating sea level signals. The solid circles correspond to Pacific estimates, and the open circles correspond to Atlantic and Indian Ocean estimates. The continuous line stands for the global average latitudinal variation of the phase speed predicted by the standard theory for extratropical freely propagating, linear, first baroclinic mode long Rossby waves. (B) Ratio of the observed phase speeds to the phase speeds predicted by the standard theory at the same geographical locations as the observations (Chelton and Schlax, 1996).

8.2 Beam-forming method

Two types of beam-forming methods will be used here, that is, classic beam-forming technique and minimum variance estimator. Classic beam-forming techniques are a "delay-and-sum" form of processing in the Fourier frequency/wavenumber domain. Data, $x_i(t)$, at each position are temporally band-pass filtered, by ordinary fast-Fourier transform, in a narrow-band surrounding temporal frequency σ, generating the Fourier transforms $\hat{x}_i(\omega)$. All cross-power combinations $R_{ij}(\omega) =< \hat{x}_i(\omega)\hat{x}_j(\omega)^* >$ are formed (the * denotes complex conjugation and the bracket average is estimated by frequency-band averaging). Denote the vector separation between positions i, j as $\Delta\mathbf{r}_{ij}$. The estimated dominant wavenumber present is obtained from the maximum over all plausible wavenumbers, $\mathbf{k}$ of

$$\Phi(\omega, \mathbf{k}) = \Phi(\omega, k, l) = \sum_{ij} w_i w_j^* R_{ij}(\omega) exp(-i\mathbf{k} \cdot \Delta\mathbf{r}_{ij}), \tag{8.1}$$

where w_i are weights which are used to control the shape of the wavenumber window. The "beam-pattern" is the field Φ over $\mathbf{k}$ evaluated in the presence of a single, monochromatic plane wave $exp(i\mathbf{k}_0 \cdot \mathbf{r} - i\omega t)$. Unlike methods based upon multi-dimensional fast Fourier methods, the spatial separations $\Delta\mathbf{r}_{ij}$ can be quite irregular. As demonstrated by Capon (1969), equation (8.1) is a biased estimator of the actual three-dimensional spectrum as a result of window tapering. Therefore, corrections must be made to compensate for the loss of energy due to window tapering (see Capon, 1969). Oceanographic applications of this and related methods may be seen, e.g. in Wunsch and Hendry (1972), and elsewhere.

The basic frequency resolution of this form of analysis is given by the reciprocal of the data duration, reduced by the frequency-band averaging as in an ordinary power density spectral estimate; the highest frequency estimated is given by the normal Nyquist criterion (data are uniformly spaced in time). Wavenumber resolution is similarly determined by the zonal array dimension with the spatial Nyquist deter-

mined, theoretically, by the smallest available zonal spatial separation. Because the data positions need not be uniformly spaced, the actual practical Nyquist wavenumber is dependent upon the array geometry and signal-to-noise ratio.

The minimum variance estimator is a high resolution array processing method which is due to Capon (1969). It is sometimes termed the "maximum-likelihood method", because the form of this estimator is similar to that in the maximum-likelihood estimation of the amplitude of a sine wave of known frequency in Gaussian random noise (Capon et al., 1967). The array output power contains not only the desired energy along the look direction but also the undesired one from other directions. The minimum variance estimator adaptively constructs a weighting function to minimize the array output power while maintaining the gain along the look direction to be unity (Pillai, 1989).

Let $\mathbf{R}$ be the cross-power spectral matrix and $\mathbf{w}$ be the weighting vector to be specified, then the output power is

$$S(\omega) = \mathbf{w}^{+}\mathbf{R}\mathbf{w}. \tag{8.2}$$

Capon's Estimator is equivalent to the following problem (Pillai, 1989)

$$\min_{\mathbf{w}} \ \mathbf{w}^{+}\mathbf{R}\mathbf{w} \quad \text{subject to} \quad \mathbf{w}^{+}\mathbf{a} = \mathbf{1} \tag{8.3}$$

where $\mathbf{a}$ is the steering vector

$$\mathbf{a} = [\mathbf{e}^{\mathbf{i}\vec{\mathbf{k}}\vec{\mathbf{x}}_1}, \mathbf{e}^{\mathbf{i}\vec{\mathbf{k}}\vec{\mathbf{x}}_1}, ...\mathbf{e}^{\mathbf{i}\vec{\mathbf{k}}\vec{\mathbf{x}}_N}]^{\mathbf{T}} \tag{8.4}$$

The constrained minimization can be found by using a Lagrangian multiplier λ to construct an new function

$$T = \mathbf{w}^{+}\mathbf{R}\mathbf{w} + \lambda(\mathbf{w}^{+}\mathbf{a} - \mathbf{1}) \tag{8.5}$$

If the matrix $\mathbf{R}$ is positive-definite, the optimum weight vector is readily given by

$$\mathbf{w} = \frac{\mathbf{R^{-1}a}}{\mathbf{a^{+}R^{-1}a}}. \tag{8.6}$$

The corresponding output power with this optimum weight vector is

$$\Phi(\omega, k, l) = \frac{1}{\mathbf{a^{+}Qa}} = \frac{1}{\sum\limits_{j,l=1}^{N} q_{jl}(\omega) \exp[i\vec{k}(\vec{x}_j - \vec{x}_l)]}. \tag{8.7}$$

which is defined as the three dimensional estimator. $\mathbf{Q}$ is the inverse of the matrix $\mathbf{R}$. Assuming the sensor outputs to be stationary Gaussian processes, Capon and Goodman(1970) showed that the random variable $\Phi(\omega, k, l)$ is a multiple of a chi-square variable with $2M$ degrees-of-freedom, where M is the number of frequency bands averaged. In this study, we choose $m = 3$ then there are thus about six degrees-of-freedom.

The reader beware that the necessary condition for equation (8.7) to hold is that the cross spectral matrix $\mathbf{R}$ must be positive-definite. This necessary condition is often unattainable. The singular covariance matrix is a well known problem in the array signal processing literature and can be fixed in a number of ways. Diagonal loading is one of the common methods (Baggeroer and Cox, 1999). However, when diagonal loading is applied, bias will be introduced into the spectral estimates. This issue has been examined recently by Baggeroer and Cox (1999). When diagonal loading is applied the cross spectral matrix $\mathbf{R}$ is replaced by

$$\mathbf{R}(\delta) = \mathbf{R} + \delta\mathbf{I}, \tag{8.8}$$

where δ represents the noise power which is added to make the spectral matrix non-singular. With this cross spectral matrix, the weight vector of the minimum variance beamformer becomes

$$\mathbf{w}(\delta) = \frac{\mathbf{R}(\delta)^{-1}\mathbf{a}}{\mathbf{a^{+}R}(\delta)^{-1}\mathbf{a}}. \tag{8.9}$$

If the above weight vector is applied to the unloaded sample cross spectral matrix, the beam output is

$$\Phi_1(\omega, k, l) = \mathbf{w}(\delta)^{+}\mathbf{R}\mathbf{w}(\delta). \tag{8.10}$$

On the other hand, if the loaded cross spectral matrix is used, the beam output is

$$\Phi_2(\omega, k, l) = \left[\mathbf{a}^{+}\mathbf{R}(\delta)^{-\mathbf{1}}\mathbf{a}\right]^{-1}. \tag{8.11}$$

These formulas were derived by Baggeroer and Cox (1999). There are no analytic solutions of the bias due to diagonal loading. However, the bias can be estimated through Monte Carlo methods (Baggeroer and Cox, 1999). The effect of diagonal loading on the confidence limit of minimum variance estimator is still unclear and is an outstanding problem in array signal processing (Baggeroer, personal communication).

8.3 Data and data processing

Here, following CS, we use TOPEX/POSEIDON(T/P) altimeter data, from the period 1 January 1993 to 21 September 1997, edited and corrected as described by King et al. (1994) except for the use of a more recent tidal model. The data set available to CS spanned about three years. Here the five years of data improves both the frequency resolution and the statistical reliability. T/P provides global sea surface height observations every 9.91 days. Data within an orbit cycle were assigned to a common time. This assignment will have a distorting effect on the result, but as will be seen, the results suggest it is not of first-order importance. The time-mean was removed from each along-track point to obtain the time dependent part, then a three block non-overlapping time average was performed to filter out all motions with periods shorter than 59.5 days. The result is an array of elevation anomalies $\eta'(\phi_i, \lambda_i, t)$ where ϕ is the latitude, λ the longitude and $t = 1\Delta t, 2\Delta t, ..., 58\Delta t$, is a time index, with Δt =29.7 days. A large, and large-scale, steric component exists at the annual period in the altimetric data (see Stammer, 1997b); because dynamical

effects at one year are of interest here, this contribution was not removed, and we rely upon the wavenumber rejection capability of our method to separate the $k = 0$ contributions from others.

One of the difficulties with the study of Rossby waves is that the propagation is not only anisotropic, but also inhomogeneous. In particular, because the meridional variation of $f(y)$ is not linear, and R_n, is a function of y (and x) the phase velocities are functions of latitude. Phase lines initially aligned with a meridian will "turn" because the phase velocity is greater at low latitudes than at high latitudes (see Schopf et al., 1981). If the ocean occupied the entire globe, the proper basis set would be the spherical harmonics. In the present situation we represent the waves as sines and cosines in narrow latitude bands in a series of boxes depicted in Figure 8-2 and listed in Table 8-1. The latitude range is restricted to 0.2° so that the meridional changes are negligible. The longitude bands are sufficiently restricted that zonal variations in R_n are slight.

Seven boxes, chosen somewhat arbitrarily to represent low, middle and high Pacific latitudes as well as some degree of east-west dependence, are used. Consider any box centered at latitude ϕ_0. Then within the box, we can think of each position of an altimetric time series as though it were part of an array (see Fig. 8-2),

$$\{x_i(t)\} = \{\eta'(\phi_i, \lambda_i, t)\}, 1 \leq i \leq N, 1\Delta t \leq t \leq 58\Delta t, \tag{8.12}$$

where $x_i(t)$ is the time series at pseudo-sensor, i, and analyze it by standard "beam-forming" techniques (e.g. Capon, 1969; Lacoss, 1971; Båth, 1974). An alternative procedure would be direct three dimensional least-squares fitting of sines and cosines; array processing procedures are however, efficient and convenient.

Because of the "diamond-pattern" in which the satellite ground-tracks cover the ocean, we can choose analysis positions ϕ_i, λ_i within the boxes either with a regular or irregular spacing along and between these tracks. The zonal spacing between

sensors is vanishingly small near where the descending and ascending arcs intersect. So-called data-adaptive techniques for array processing are well known, especially Capon's (1969) method. These methods are most powerful when arrays are small and irregular, and the plane-wave signal-to-noise ratio is large. In the present case, we arrange for the data coverage to be fairly uniform and large-scale, and the Capon method did not produce better results than did the more robust and conventional beamforming method. An attempt to examine high wavenumbers by employing a very disparate array spacing and the Capon method will be described briefly at the end.

After filtering, each "sensor" has an altimetric time series, $x_i(t)$, at intervals, $\Delta t = 29.7$ days, with duration $T = 58\Delta t$. To stabilize the cross-power estimates, frequency-band averaging was done over three adjacent values which thus sets the approximate frequency resolution of the analysis. Let the zonal width of the array (its aperture) be L, and let the smallest zonal spacing between any two elements be Δr (in kilometers). Beamforming produces estimates of the power density, $\Phi(\sigma, k, l)$, in a band of zonal wavenumbers, $2\pi/L \leq k \leq \pi/(\Delta r)$. Each box extends sufficiently far in the zonal direction to distinguish the first mode baroclinic wave from motions at or near $k = 0$. This $k-$wavenumber band is separately computed for each of the resolved frequencies. Because the meridional aperture is so small, there is almost no resolving power in the meridional direction (wavenumber l) which is therefore, indistinguishable from $l = 0$ in the results.

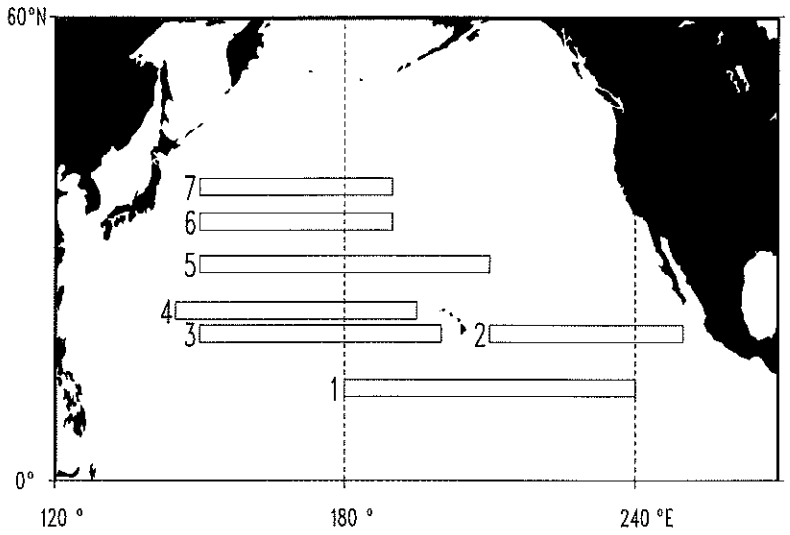

Figure 8-2: Rectangles are the seven regions chosen to study the frequency wavenumber spectrum of sea surface height variability.

Area	Latitude	Longitude	R_1 (km)	$c_{1-\max}$ (cm/s)	$T_{1-\min}$ (days)
1	11.9–12.1°N	180–240° E	91	-18.6	71
2	18.9–19.1°N	210–250°E	58	-7.4	116
3	18.9–19.1°N	150–200°E	67	-9.7	100
4	21.9–22.1°N	145–195°E	60	-7.5	114
5	27.9–28.1°N	150–210°E	47	-4.4	154
6	33.4–33.6°N	150–190°E	38	-2.7	200
7	37.9–38.1°N	150–190°E	30	-1.6	270

Table 8-1: Areas chosen to analyze the frequency/wavenumber spectra. Zonal and meridional ranges, first baroclinic Rossby radius of deformation R_1 (Chelton et al., 1998), theoretical fastest phase speed of the first baroclinic long Rossby wave $c_{1-max} = -\beta R_1^2$, and the minimum period of the first baroclinic Rossby waves in each region $T_{1-min} = 2\pi/\sigma_{1-max}$.

8.4 Results

Area 4.

Consider Area 4, northwest of the Hawaiian chain. Figure 8-3 depicts positions for which altimetric time series were generated, thus defining the array. Fig.8-4a shows the so-called beam-pattern of the array and which can be interpreted as the apparent wavenumber spectrum which would be centered on wavenumber (k_0,l_0) if there were a monochromatic wave of this wavenumber at a fixed frequency crossing the array. Notice that only a very narrow meridional wavenumber band is shown because of the lack of resolution in the north-south direction. Figures 8-4b-f show the result of the analysis at frequencies plotted as $log_{10}\left[\Phi\left(\sigma,k,l\right)/\Phi_{max}\left(\sigma,k,l\right)\right]$ with a $*$ denoting the position of the computed maximum. As expected, the energy density is generally much larger for negative wavenumbers (westward phase velocity) than for eastward going motions. There is a finite background energy at all wavenumbers upon which the peaks are superimposed. This background continuum, which generally has more energy than is found in the plane-wave peak, requires separate study.

Because the analysis is essentially a two-dimensional (σ,k) one, and the $l=0$ waves are the fastest ones, Fig. 8-5 depicts the dispersion relations for the barotropic and first baroclinic modes in Area 4, with $l=0$ (first baroclinic Rossby radii are from Chelton et al., 1998). The observed spectral peaks have been transferred from Fig. 8-4 to Fig. 8-5, and an uncertainty estimate is generated from the confidence limits derived by Capon and Goodman (1970). An indication of the relative strength of the peak is provided by the circle diameter. The only observed spectral peaks are on the longwave branch (wavenumbers below the wavenumber corresponding to the maximum frequency for mode 1). With one exception, at a frequency near 0.008 cycles/day (period 123 days), the observed peaks are indistinguishable within error estimates from the conventional linear dispersion curves. For the comparatively weak motions lying at frequencies $\sigma > \sigma_{1-max}$ the motions cannot be explained as linear baroclinic waves. The fraction of the energy lying in the observed peak varies from

about 43% near 862 days period declining monotonically to about 11% at 157 days period.

The zonal group velocity vanishes at $\sigma = \sigma_{n-max}$ and under some circumstances (e.g., Wunsch and Gill, 1976) one anticipates an energy density maximum here in a form of resonance. We see no evidence for such motions.

Phase Speed

By definition, the (zonal) phase speed of a wave is $c = \sigma/k$, the slope of the dispersion curve. For those frequencies and wavenumbers in Fig. 8-5 lying on or near the dispersion curves, the observed and theoretical phase speeds are in accord within the uncertainty limits. At higher frequencies (or absolute wavenumbers), the observed frequencies are systematically higher than the first baroclinic dispersion curve would permit. The average slope of the empirical dispersion curve, is higher than the theoretical mean slope and one thus has a positive phase speed bias. If we rule out the possibility that the waves are barotropic motions with *too low* a phase speed, then one could fairly conclude that these waves are moving faster than theory permits.

Equally appealing however, would be their description as motions not simply consistent with linear dynamics. Many sources of such motions are known, including wind-forcing, instabilities, non-linear self-interactions etc. On smaller scales (mesoscale), the existence of baroclinic motions not satisfying linear dispersion relations has been known for a long time (e.g., The MODE Group, 1978). Thus, if all the motions lying within a finite frequency band are used to compute an apparent overall phase velocity, irrespective of the physics present, there is clearly a bias toward large values. But the separation into distinct frequency and wavenumber regions shows that much of the motion is not in conflict with the simplest linear theory.

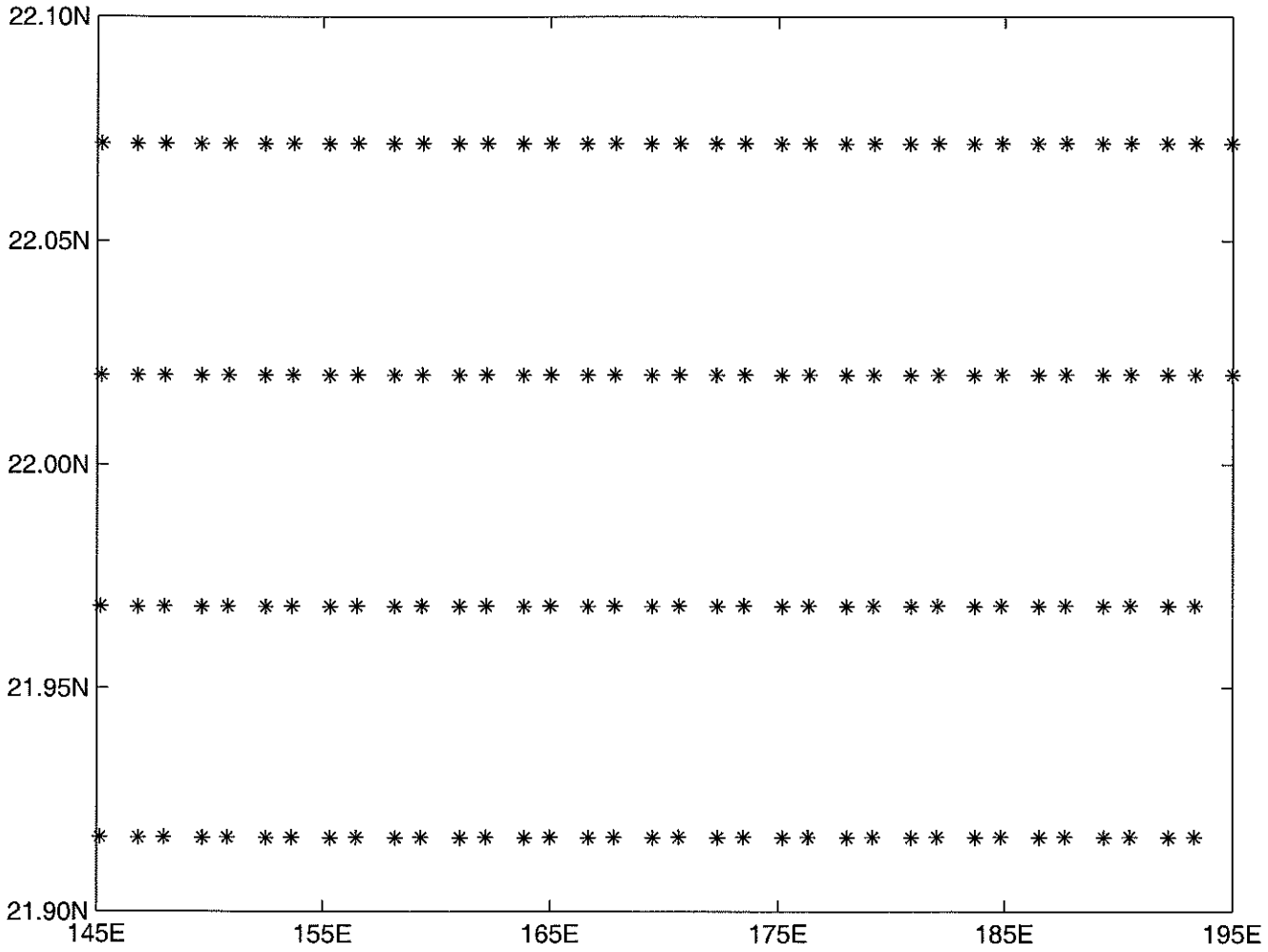

Figure 8-3: Array geometry in region 4. The position of each "sensor" is marked by a star and corresponds to a position on the TOPEX/POSEIDON sub-satellite track.

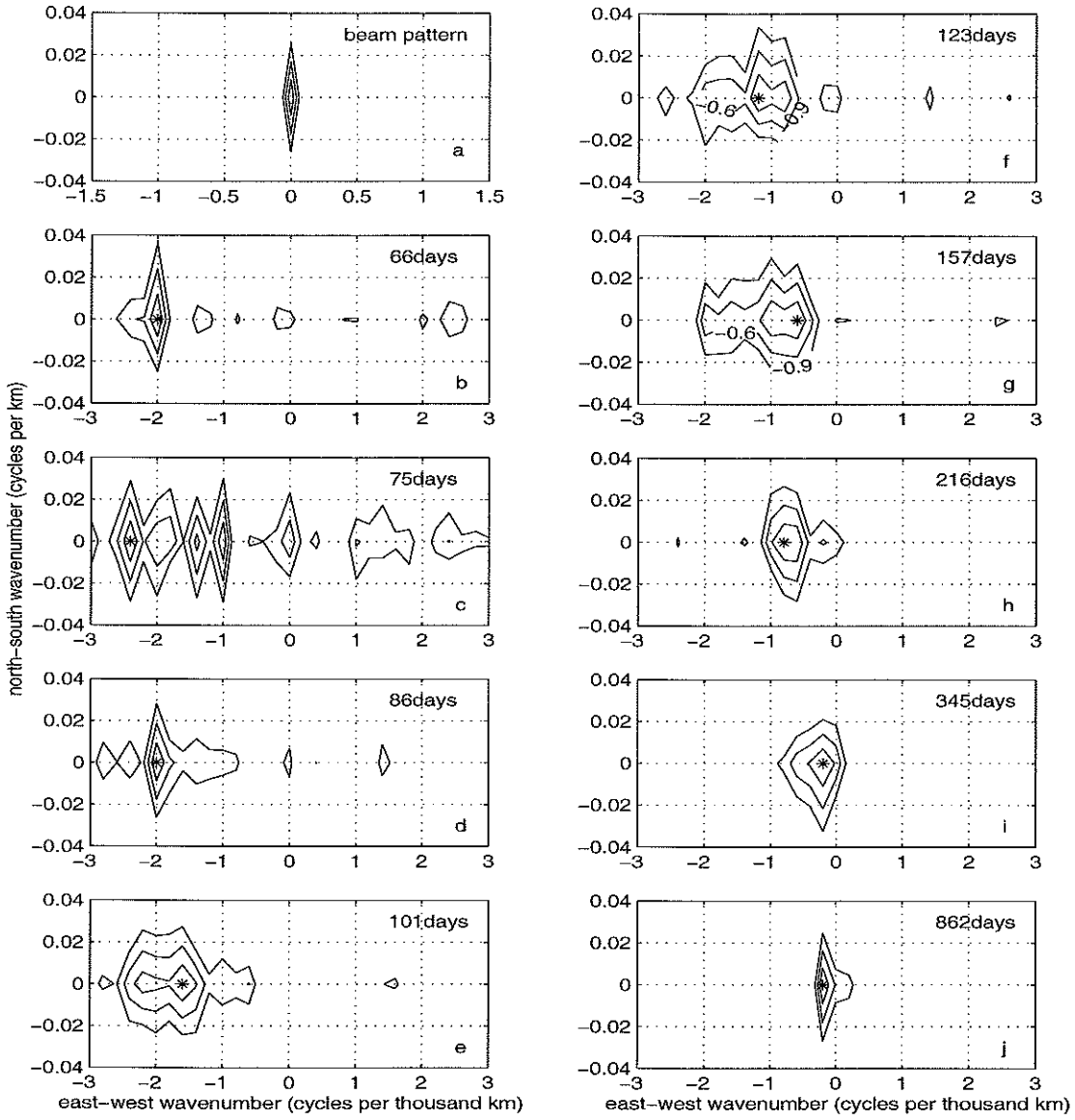

Figure 8-4a The beam pattern for the array in Fig. 8-3. Fig. 8-4b-j., The frequency-wavenumber spectra $\Phi(\omega, k, l)$ at periods $T = 2\pi/\sigma$ (in days) (b) 66. (c) 75. (d) 86. (e) 101. (f) 123. (g) 157. (h) 216. (i) 345. and (j) 862 (days). The contour levels are the same in each panel and vary from 0 to -0.9 in steps of -0.3. The units of east-west wavenumber and north-south wavenumber are cycles per thousand km and cycles per km, respectively. The observed spectral peak in each frequency band is marked by a star.

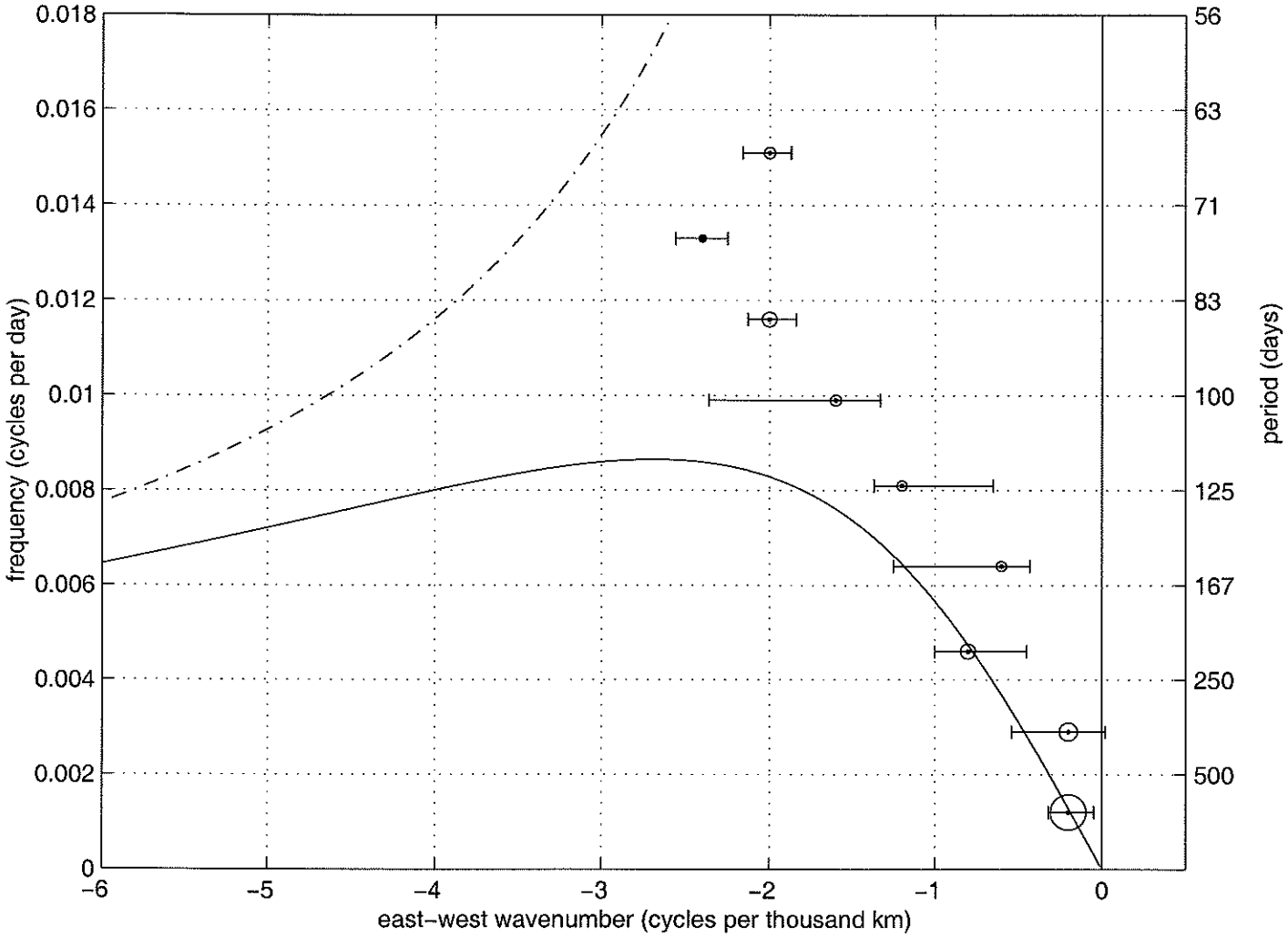

Figure 8-5: Frequency-zonal wave number spectra of region 4. The peak in each frequency band in Fig.8-4 is indicated by a dot here. The magnitude of each peak is denoted by the size of the circle around that peak. The dash-dot and solid curves denote the barotropic and first baroclinic Rossby wave dispersion curves with $l = 0$, respectively. At the lowest frequencies, the barotropic curve is visually indistinguishable from $k = 0$. Uncertainty estimates are derived from the 95% confidence interval (Capon and Goodman, 1970) for the peak values. The zonal wavenumber interval represents those wavenumbers where the background energy surrounding the apparent peak is larger than or equal to the lower limit of the confidence interval.

Other Areas.

The frequency/zonal-wavenumber spectra for the remaining areas analyzed here are shown in Fig. 8-6. In Area 1 (Fig. 8-6a) , most peaks are located at $k = 0$. These motions have zonal scales larger than the array aperture and can be due to large-scale barotropic motions or steric forcing on large zonal scales (annual cycle heating) or both. Only two peaks are not located at $k = 0$ and they agree very well with the dispersion curve for first baroclinic Rossby waves, but carry only about 10% of the energy. Here again, a lumped apparent phase speed would be biassed high.

As shown in Fig. 8-1, the latitudes of Areas 2 and 3 are the same, east and west respectively of the Hawaiian chain. The frequency zonal-wavenumber spectra for these areas are shown in Fig. 8-6b,c. As indicated in Table 8-1, long first baroclinic mode waves propagate faster in the western parts of the basin. This zonal change of phase speed is a result of the deepening of the thermocline in the west (Chelton et al., 1998). At the annual frequency band, Area 3 is dominated by a first baroclinic Rossby wave, whereas Area 2 is dominated by a signal indistinguishable from zonal uniformity ($k = 0$), and which is presumably the steric contribution alluded to above. One explanation for this difference (e.g., Chelton and Schlax, 1996) is that the Hawaiian Ridge generates a westward moving train of annual period Rossby waves. Fig. 8-6b and 8-6c show that at low frequencies the observed spectral peaks are located either very close to the baroclinic dispersion curve (around 20% of the total energy) or at the axis, $k = 0$. At frequencies higher than σ_{1-max}, the observed spectral peaks are situated between the barotropic and first baroclinic Rossby wave dispersion curves.

As the latitude increases, the maximum frequency and the phase speed of the lowest baroclinic mode (the fastest baroclinic mode) decreases. Whatever baroclinic motion is present above σ_{1-max}, it cannot be a linear flat-bottom mode. Even where the waves are present in linear theory, they become much more susceptible to the various effects described by Killworth et al. (1997) and others.

White (1977) inferred the existence of annual-period baroclinic Rossby waves in the tropical Pacific and he suggested that they are generated by the annual-period

wind forcing. Here we find that only Areas 3 and 4 show such waves significantly present. Other regions are dominated by energy indistinguishable from $k = 0$ and which may be spectral leakage from the annual period.

Within the equatorial band from 10°N to 10°S, CS (their Fig. 5) found that apparent westward phase speeds were smaller than the theoretical value. At these latitudes, one expects that higher modes should become more prominent, and this is observed in current meter records (e.g., Wunsch, 1997) and in data from profiling devices (e.g., Eriksen, 1981). The unaccounted-for-presence of high modes is consistent with a negatively biassed value for c_1. Furthermore, around the equator eastward propagating Kelvin and mixed-Rossby-gravity wave modes become possible. The equatorial band is thus worthy of special attention, and it will not be further discussed here.

The Short-Wavelength Limit

High-resolution methods permit one to use irregularly spaced arrays to seek waves whose wavelengths are set by the Nyquist wavelength of the shortest lateral separation. Robustness of the results is dependent upon signal-to-noise ratios and the actual array configuration. An attempt was made in Area 4 to determine the wavenumber spectrum at wavenumbers beyond those corresponding to σ_{1-max}, the short-wavelength branch. No statistically significant peaks above the background energy could be found, and we will not discuss these results any further.

8.5 Discussion

We find a significant fraction of the energy present in the North Pacific Ocean is consistent with the linear Rossby wave dispersion relation Eq. (2.36). The remaining energy is not so consistent, and believe that the results of CS are readily explained through the general mechanisms, if not all the details, described by Qiu et al. (1997), Killworth et al. (1997) and the wider literature on generalizations to more complex conditions of the linear theory. One has in part an interference pattern of free motions consistent with linear physics, superimposed upon forced motions of various types .

In any fixed wavenumber band, there exists some motions with frequencies lying above the dispersion curve for first baroclinic modes. These motions produce lumped westward phase speeds which are generally too high for the linear theory. It is almost a semantic distinction as to whether the motion is best described as linear Rossby waves with the "wrong" frequency, or simply as oceanic motions not satisfying the dispersion relation. At most latitudes, there *is* significant energy which does appear consistent within present error estimates with the linear dispersion relationship.

The question raised by CS as to why c_n is too large, now becomes instead the question of why frequencies become preferentially too high as wavenumber magnitudes increase? Presumably the answer to this question is some combination of the answer given by Killworth et al. (1997), the mode coupling of the barotropic and baroclinic modes known to occur in some regions (e.g., Wunsch, 1997), and the space/time structure of the atmospheric forcing. Many reasons can be found for the existence of motions inconsistent with the first baroclinic mode of a resting flat-bottom ocean, including the presence of the barotropic mode, higher baroclinic modes, advection, topography and forcing.

At higher latitudes, as the waves slow, and ultimately disappear at frequencies accessible with existing data sets, non-linear effects as well as background distortions of the potential vorticity gradient (e.g. Killworth, et al., 1997) can dominate the spectrum and eventually there is no evidence for linear waves at all.

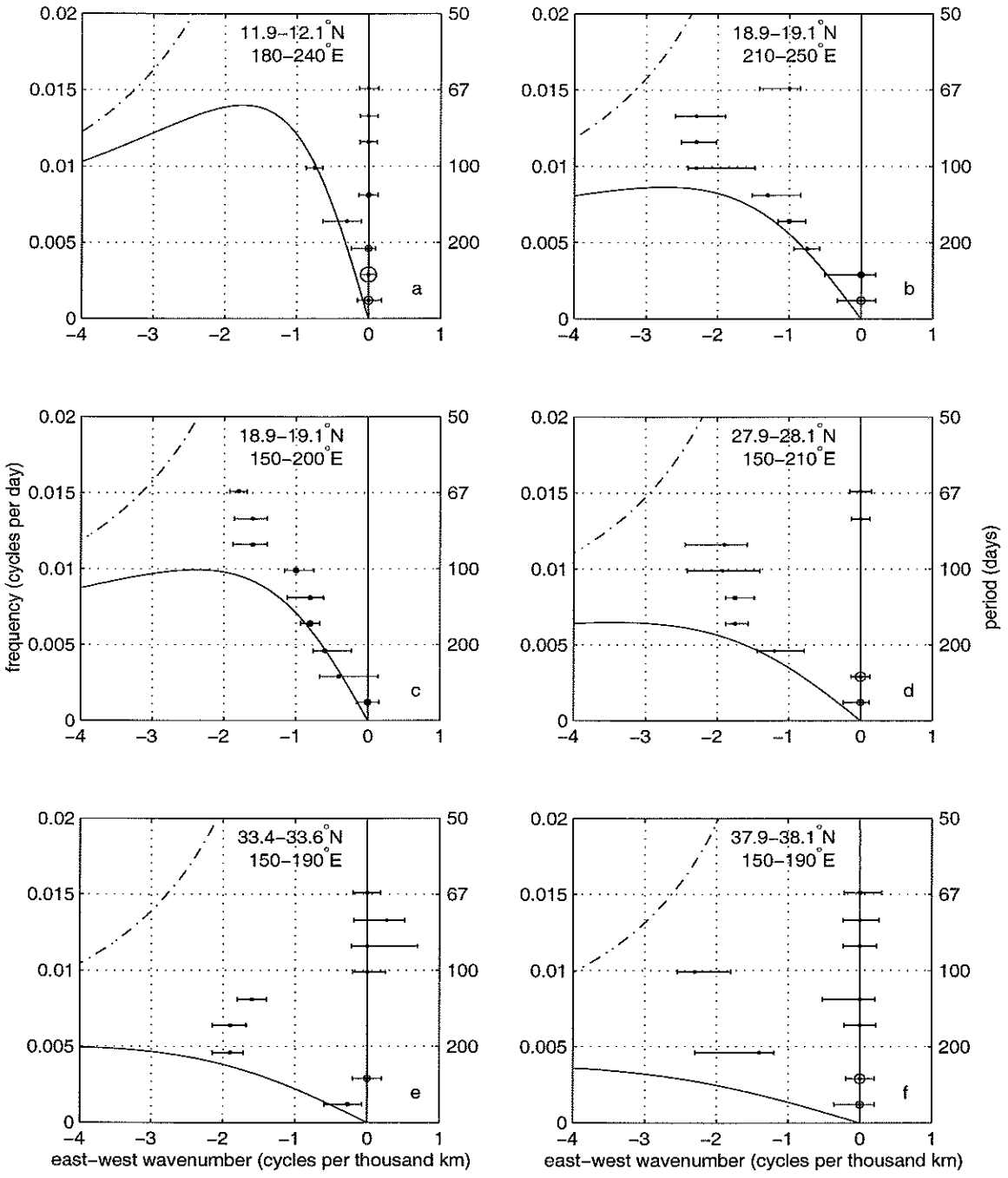

Figure 8-6: Same as in figure 8-5 except (a) for region 1. (b) Region 2. (c) Region 3. (d) Region 5. (e) Region 6. (f) Region 7.

Chapter 9

Conclusions and discussion

This thesis work can be summarized as producing an approximate basic spectral description of low frequency oceanic variability by using a simple dynamical model with various observations. First, this study shows that a single function of $\Phi(k, l, \omega, n, \lambda, \phi)$ *does* exist, and all measurements can be simplified as a certain function of $\Phi(k, l, \omega, n, \lambda, \phi)$. It implies that various data are consistent with linear equations of fluid dynamics to first order approximation. This work provides estimates of how the energy of low frequency oceanic variability depends on two components of horizontal wavenumbers, frequency, vertical mode and geography, and what percentage of energy propagates westward and eastward. The only geography-dependent part is the energy level. It also provides estimates of some physical variables in which no observations are available, such as the wavenumber spectrum of horizontal velocities. With the aid of Gauss-Markov estimation method, the spectrum is applied to the design of observational strategy. If the regional model $\Phi(k, l, \omega, n, \lambda, \phi)$ is normalized by the geography-dependent factor $I(\phi, \lambda)$, we will obtain a universal spectral model $\Phi(k, l, \omega, n)$. The vertical structure is governed by the barotropic and first two baroclinic modes, and the frequency and wavenumber structure of each mode is displayed in figure 9-1.

The low frequency variability is a broad-band process and Rossby waves are particular parts of it. The sea surface height measurements in the North Pacific are analyzed, and it is found that about 10-40% of the total variance in each frequency

band are indistinguishable from the simplest theoretical Rossby wave description. Toward higher latitudes, both amplitudes and phase speeds of linear waves decrease. Non-equatorial latitudes display some energy with frequencies too high for consistency with linear theory; this energy produces a positive bias if a lumped average westward phase speed is computed for all the motions present.

The model produced here is not final and will become obsolete with the coming of new observations. For example, the vertical structure of kinetic energy has been obtained by Wunsch (1997) from current meter data; however, each mode cannot be completely represented by the energy level alone. Each vertical mode is a function of two components of horizontal wavenumber and frequency. So far, complete frequency and wavenumber structure of barotropic and baroclinic modes of any field still does not exist except that a few current meter moorings can provide an estimate of it; however, the resolution and reliability of such estimate are very low. The coming Gravity Recovery and Climate Experiment (GRACE) project will enable oceanographers to measure ocean bottom pressure fluctuations from space with extraordinary accuracy through measuring the time-dependent gravity. Simultaneous measurements of sea surface height and ocean bottom pressure will greatly enhance our knowledge of the ocean circulation. Among other things, this can help us to estimate how ocean variability is partitioned between barotropic and baroclinic motions and the space and time scales of barotropic motions, which could be used to improve the energy density model produced in this thesis. The present model has the following assumptions:

(1) observations at different times can be reasonably related, which implies the oceanic variability is stationary in time,

(2) the process is linear,

(3) the basic state is at rest,

(4) the bottom of the ocean is flat,

(5) there is no forcing, and

(6) the buoyancy frequency $N(z)$ is universal and can be modeled by an idealized exponential form.

The empirical model produced in this thesis can only be applied to the mid-ocean away from the equator and boundaries. Regions close to the equator and western boundary have distinct dynamics. Near the western boundary currents, the barotropic mode dominates (Wunsch, 1997); the effect of mean flow cannot be neglected and there exist significant differences between the energy level of zonal and meridional components of horizontal velocity. The frequency and wavenumber spectral shape near the western boundary is different from that in the interior ocean (Stammer, 1997). In the areas close to the equator, high modes become more important (Wunsch, 1997; Eriksen, 1981), and the geostrophic balance doesn't hold. As discussed in chapter 2, my model cannot represent temperature variations in the mixed layer and at sea surface. Most data used in this study span a few years. The frequency and wavenumber spectrum for very low frequencies—decadal and even longer period—is unclear. The seasonal cycle requires further study also. As displayed in chapter 5, there is a striking peak associated with the seasonal cycle of the frequency spectrum of sea surface height. However, the seasonal cycle is not significant on the frequency spectrum of horizontal velocity and temperature below the mixed layer.

Why $\Phi(k, l, \omega, n)$ has a particular universal spectral shape is of great interest from the theoretical point of view. The generation mechanism of ocean variability includes atmospheric wind and thermal forcing, barotropic and baroclinic instability, and the interaction of mean flow with topography. The lowest-mode character of low frequency variability is attributed to quasi-geostrophic nonlinear interactions, which drives the motion toward larger scales both in the vertical and horizontal direction (Charney, 1971; Rhines, 1975; Fu and Flierl, 1979). In the ocean and atmosphere, wavenumber spectral shape is often rationalized by geostrophic turbulence theory. In the absence of forcing and dissipation, two-dimensional flow is peculiar in that total kinetic energy and enstrophy are conserved. Therefore, kinetic energy must be transferred simultaneously from small to larger scales and large to smaller scales through nonlinear interactions between different scales of motion (Fjörtoft 1953). This led Krainchnan (1967) to postulate that there exists two distinct "inertial"

subranges of two-dimensional turbulence. The large-scale subrange has a kinetic energy spectrum of $k^{-3/5}$, while the kinetic energy spectrum of small-scale subrange is proportional to k^{-3}. Charney (1971) also obtained a -3 law at the tail of the kinetic energy spectrum from a quasi-geostrophic model and conjectured that in this region there would be equipatition between the two components of the kinetic energy and the potential energy. Rhines (1979) further argued that kinetic energy should exhibit a maximum at the wavelength close to the "Rhines scale", $l \propto \sqrt{u/\beta}$, where u is the root-mean-square of the fluctuating speed. The results from numerical simulation are quite similar (Lilly, 1969; McWilliams and Chow, 1981). For the ocean, two-dimensional turbulence theory only offers an explanation for the spectral shape at wavelengths smaller than 400 km. It is unclear why the wavenumber spectra of sea surface height and temperature are proportional to $k^{-1/2}$ at wavelengths longer than 400 km. The frequency spectral shape is explained as an integral response of the ocean to continuous random forcing of the atmosphere (Hasselman, 1976). Using a conceptual model with atmospheric forcing, Hasselman (1976) and Frankignoul and Hasselman (1977) found that although the frequency spectrum of atmospheric forcing is white at periods longer than one week, the frequency spectrum of the ocean should be red and proportional to ω^{-2} at periods from a few days to about 150 days because the ocean acts as a first order Markov integrator of atmospheric input. At periods longer than a year, the frequency spectrum of the ocean turns white, because negative feedbacks become important. Frankignoul and Müller (1979) and Willebrand et al. (1980) further investigated the response of the ocean to stochastic forcing by the atmosphere using linear quasi-geostrophic model. Willebrand et al. (1980) found that the ocean response is essentially barotropic at periods between the inertial period and about 300 days. Most of the theories only provide qualitative explanation with focus on predicting the wavenumber and frequency spectral shape. Even the state-of-art general circulation model cannot predict both spectral shape and energy levels correctly (Stammer et al., 1996). More work needs to be done along these lines in the future.

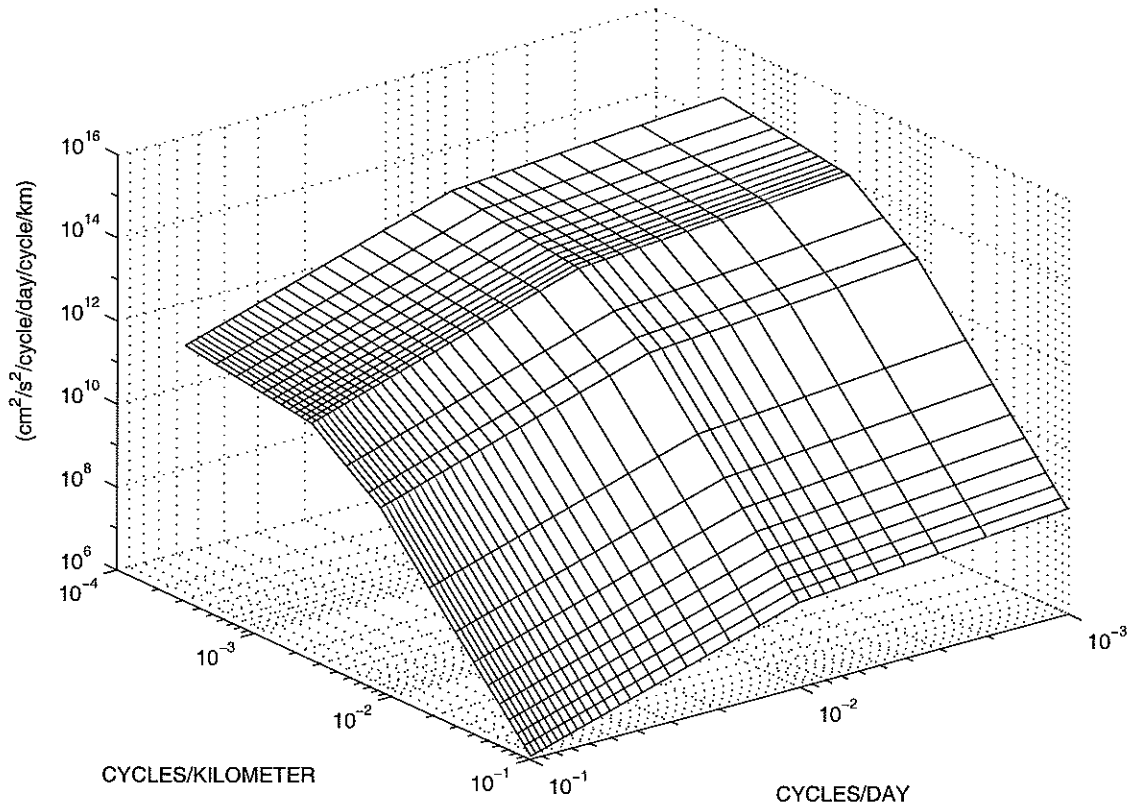

Figure 9-1: Two-dimensional zonal-wavenumber and frequency spectrum. Meridional-wavenumber and frequency spectrum is the same.

Appendix A

Rossby waves and the mid-Atlantic ridge

A.1 Introduction

Rossby waves are large scale and low frequency phenomena in the ocean. The detection of Rossby waves is only possible with a global data set. Satellite altimetry enables oceanographers to monitor the global ocean variability continuously for years for the first time. The Rossby waves have been identified by many oceanographers from the satellite altimeter data (e.g., Chelton and Schlax, 1996; Wang et al, 1998; Zang and Wunsch, 1999). The generation mechanism of Rossby wave includes: (1) atmospheric wind forcing and buoyancy forcing acting on the sea surface, (2) either along-shore wind stress or coastally trapped Kelvin waves along the eastern boundary, and (3) the interaction between the mean flow and topography. The generation of Rossby waves by wind stress has received much attention in the literature (e.g., Veronis and Stommel, 1956; Anderson and Gill, 1975; White, 1977; and Qiu et al., 1997). Chelton and Schlax (1996) found that only in low latitudes, could boundary-generated Rossby waves propagate across the ocean basin. Towards high latitudes, the boundary-originated waves were trapped near the east coast. This feature was also found in numerical ocean modeling (Qiu et al., 1997). Recent theoretical studies

suggest that the ocean general circulation is strongly influenced by mid-ocean ridge system, which acts as an incomplete barrier to the ocean circulation (Pedlosky et al., 1997; Pedlosky and Spall, 1999). One open question is whether the Rossby waves generated at the eastern boundary can cross the mid-ocean ridge. If the anomalies originated from the eastern boundary can be transmitted across the mid-ocean ridge as westward-going Rossby waves, they will affect the western boundary currents; thus influence the climate in other regions. Using a quasi-geostrophic model, Barnier (1988) investigated the influence of the mid-Atlantic ridge on first baroclinic Rossby waves generated by seasonal wind fluctuations at the eastern boundary. He found that the ridge blocked the waves coming from the eastern boundary but generated new waves whose phase vector was almost normal to the ridge crest west of the ridge.

In general, the propagation of Rossby waves can be represented by three different ways. The direct method is to present the measurements in space and time domain: the so-called hovmoller diagram. Strictly speaking, this method is useful only when the signal is made up of a single wave. If the data is composed of waves with different frequencies and wavenumbers, the spectral method is required. The spectral method enables one to quantitatively determine the wavenumbers and frequencies of dominant signals in the data. It also makes it easy to compare observations with theory. However, the spectrum provides no information about time and space. If the signal undergoes abrupt changes over time or space, the Fourier method is not suitable to detect these abrupt changes. The third way of presenting propagation of Rossby waves is wavelet transforms. The main advantage of wavelets is that they contain information about both frequency (wavenumber) and time (space). A wavelet transform is a powerful tool for the study of a rapidly changing wave field during wave generation, growth or decay.

In this chapter, the array signal processing technique will be used with wavelet method to study how the properties of Rossby waves change across the mid-Atlantic ridge. First, the array signal processing technique will be applied to TOPEX/POSEIDON satellite altimeter data to find out the period and wavelength of dominant Rossby

waves. Then, the wavelet technique will be used to investigate how the property of dominant Rossby waves changes with space and time. The objective here is to find out whether Rossby waves west of major ocean ridges are generated locally by the topography or originate from the eastern boundary and amplify over the mid-ocean ridge.

A.2 Data and data processing

TOPEX/POSEIDON altimeter along track data from cycle 11 to 212 (December 31, 1992 to June 15, 1998) is used here. In order to study the effect of the mid-ocean ridge on Rossby waves, one particular box in the North Atlantic, which crosses the mid-Atlantic ridge, is chosen to study. The spatial distribution of measurements within the box is fairly regular (Figure A-1). TOPEX/POSEIDON provides global sea surface height measurements every 9.91 days. The measurements within one orbit cycle are assumed to be synchronous. First the time mean of the sea surface height at each spatial point is removed, then a three block non-overlapping time average was done to remove motions with periods shorter than 59.5 days.

A.3 Wavelet analysis

Wavelet method was developed in last decade, since then it has been applied to the study of various fields such as decadal variability, atmospheric turbulence and ocean wind waves (see Kumar and Foufoula-Georgiou, 1997 for a review). Wavelet method provides quantitative information about not only the wavenumber, frequency and phase speed of propagating waves but also spatial and temporal modulation of energy amplitude. Wavelet transform and the relationship between wavelet transform and Fourier transform are briefly summarized here.

A.3.1 Wavelet transform

The continuous wavelet transform $S(b,a)$ of a real signal $f(t)$ with respect to the mother wavelet, $g(t)$, is defined as

$$S(b,a) = \int_{-\infty}^{+\infty} f(t) g_{ab}^{*}(t) dt, \tag{A.1}$$

where

$$g_{ab}(t) = \frac{1}{\sqrt{a}} g(\frac{t-b}{a}) \tag{A.2}$$

represents a set of functions, that is, wavelets, which are constructed from the mother wavelet $g(t)$ by translating and dilating. Here a is a scale parameter, b is a local parameter and * stands for complex conjugate. The normalizing constant $\frac{1}{\sqrt{a}}$ is chosen so that $g_{ab}(t)$ has the same energy for all scales a:

$$||g_{ab}(t)|| = \int_{-\infty}^{+\infty} g_{ab}(t) dt = 1. \tag{A.3}$$

The inverse wavelet transform is given by

$$f(t) = \frac{1}{C_{\psi}} \int_{-\infty}^{+\infty} \int_{0}^{+\infty} \frac{S(b,a) g_{ab}(t)}{a^2} da db, \tag{A.4}$$

where

$$C_{\psi} = 2\pi \int_{-\infty}^{+\infty} \frac{|G(\omega)|^2}{|\omega|} d\omega, \tag{A.5}$$

where $G(\omega)$ is the Fourier transform of $g(t)$,

$$G(\omega) = \frac{1}{2\pi} \int_{-\infty}^{+\infty} g(t) e^{-i\omega t} dt. \tag{A.6}$$

Using Parseval's theorem, one can write the function $S(b,a)$ in terms of $F(\omega)$ and $G(\omega)$, which are the Fourier transforms of $f(t)$ and $g(t)$:

$$S(b,a) = \sqrt{a} \int_{-\infty}^{+\infty} F(\omega) G^{*}(a\omega) e^{ib\omega} d\omega. \tag{A.7}$$

A.3.2 Wavelet and Fourier transform

The advantages of wavelet transform have been discussed in the introduction; however, wavelet analysis has its own limitations. Fourier transform is orthogonal and is a standard procedure to solve partial differential equations analytically. Moreover, because most theory on waves is expressed in terms of frequency and wavenumber, it is straightforward to compare spectrum of the observations with theory. However, continuous wavelet transform is not orthogonal; thus it cannot be used to solve partial differential equations analytically. In addition, because the wavelet transform is not orthogonal, the wavelet transform may produce some false correlations (see Farge, 1992). One must beware of this redundancy when applying the wavelet transform to the actual data.

As indicated by equation (A.7), the wavelet transform depends on both the signal and the choice of wavelet. The choice of wavelet is contingent on what kind of information one wants to extract from the data. The Morlet wavelet has been widely used in atmosphere and oceanography because Morlet wavelet is suitable for the study of wave propagation and it is easy to compare the Morlet wavelet transform with Fourier transform.

The Morlet wavelet is defined as

$$g(t) = \pi^{-1/4} e^{-ict} e^{-t^2/2}, \tag{A.8}$$

which is a periodic function modulated by a Gaussian envelop. It is complexed-valued; therefore, it enables one to extract the information about the amplitude and phase of the data being analyzed. In order to satisfy the admissibility condition, it is necessary to take $c > 5$ (Farge, 1992).

In order to compare wavelet transform of observations with wave theory, one needs to understand the relationship between the wavelet transform and Fourier transform, particularly, what is the relationship between wavelet scales and Fourier periods? and

what is the relationship between wavelet amplitude and Fourier amplitude? Meyers et al. (1993) demonstrated that in the case of Morlet wavelet, the relationship between Wavelet scales and Fourier periods could be derived analytically. They showed that the scale, a_0, where the Morlet wavelet transform of a periodic signal $A_0 e^{i2\pi t/T_0}$ reached its maximum was related to the period of the signal, T_0 through

$$a_0 = [\frac{c + (2 + c^2)^{1/2}}{4\pi}]T_0, \tag{A.9}$$

where c is the parameter of Morlet wavelets. If one chooses

$$c = 2\pi - \frac{1}{4\pi}, \tag{A.10}$$

then the scale of wavelet transform equals the period of the signal:

$$a_0 = T_0. \tag{A.11}$$

It is ready to demonstrate that the corresponding relationship between the maximum of the square amplitudes of the wavelet transform $S(b, a)$ and the amplitude of the wave A_0 is

$$|S(b, a)|^2_{\max} = 2\pi^{-1/2} e^{1/(4\pi)^2} |A_0|^2 a. \tag{A.12}$$

Therefore, the amplitude of wavelet transform not only depends on the amplitude of the wave but also depends on the scale (period) of the wave. In order to compare the true energy at different scales unbiasly, it is desirable to present $|S(b, a)|^2/a$, rather than $|S(b, a)|^2$, which is widely used in the literature.

A.4 Application

A.4.1 Frequency and wavenumber spectrum

The three-dimensional spectrum of sea surface height anomalies is obtained by using the conventional array signal processing method. Non-overlap averaging over three adjacent frequency bands is performed so that statistical stable estimates are obtained. The three-dimensional spectrum is plotted in figure A-2 as $log_{10}\left[\Phi\left(\omega,k,l\right)/\Phi_{max}\left(\omega,k,l\right)\right]$ with a $*$ denoting the position of the computed maximum. As displayed in figure A-2, the peak at each frequency band occurs either at the axis of negative zonal wavenumbers or at the origin. There is more energy going westward just as expected. The annual frequency band is dominated by stationary waves, which is presumably due to uniform atmospheric forcing. At the periods of 178 and 245 days, the fraction of the energy lying in the observed peak is about 15%, which is higher than that at other periods. The zonal wavelength of the observed peak at 178 and 245 days is 700 and 930 km, respectively. The observed phase speeds at these two periods are very close, roughly 4.4 cm/s.

The averaged variance of sea surface height anomaly in the area studied here is about 45 cm^2, among which about 7 cm^2 is contained in eastward-going motions, 22 cm^2 in westward-going motions and 16 cm^2 in stationary motions. Figure A-3a shows the frequency spectra of eastward-going, westward-going and stationary motions. There is a pronounced peak at the period of one year in the frequency spectrum of stationary motions. The energy of westward-going motions is higher than the energy of eastward-going motions at almost all frequency bands. The frequency spectrum of eastward-going motions is red, and the frequency spectrum of westward-going motions is dominated by motions with periods from 150 days to 300 days. The frequency spectrum of westward-going motions is red at periods shorter than 150 days and is blue at periods longer than 300 days. The wavenumber spectra of eastward-going and westward-going motions are displayed in figure A-3b. Most striking property in figure A-3b is that there is a peak at the wavelength about 750

km in the wavenumber spectrum of westward-going motions.

Because the meridional range of the area in figure A-1 is so small that the analysis is a two-dimensional one in essence. The barotropic and baroclinic dispersion curves for classic Rossby theory with $l = 0$ are displayed in figure A-4. Each dot in figure A-4 corresponds to the observed spectral peak at each frequency band in figure A-3. The size of the circle stands for the relative amplitude of the peak. The error bar is produced according to Capon and Goodman (1971). The result in figure A-4 is consistent with those found by Zang and Wunsch (1999) in North Pacific. The observed spectral peaks are all located on the longwave branch and the peaks fall between the barotropic and baroclinic dispersion curves. The frequencies of the observed peaks are systematically higher than those of the first baroclinic dispersion, and lower than those of the barotropic dispersion. Therefore, the observed phase speeds are between first baroclinic Rossby wave speeds and barotropic Rossby wave speeds.

A.4.2 Wavelet transform

As shown in figure A-1, data inside the box are nearly uniformly-distributed. Here they are mapped into one and half degree regular grid along 28.3°N using linear interpolation technique. Since the signal of Rossby waves within the periods between 150 and 300 days is stronger than those at other periods, my concern here is focused on the frequency band between 1/300 and and 1/150 cycles per day. The steric height is extracted by fitting the data with annual harmonics and is then substracted from the data. Then, a zero-phase bandpass filter is applied to extract the signals with periods between 150 and 300 days from the residuals. The Hovmoller diagram of the filtered data is shown in figure A-5. As displayed there, there is a systematic westward propagation. West of 315°E, the amplitudes of westward propagating signals are much larger. Moreover, the slope of constant phase line is steeper east of 295°E; thus, the phase speed is higher in the region close to western boundary. The change of phase speed with longitude results from the fact that thermocline is shallower

in the east. Figure A-5 also shows that westward propagation changes with time. There is an increase of energy around 900 days. The hovemoller diagram provides only qualitative description of spatial and temporal variations wave propagation. To be quantitative, one can resort to windowed Fourier transform or wavelet technique. Compared with windowed Fourier transform, wavelet method is more flexible and convenient. I perform one-dimensional wavelet transform of the filtered sea surface height data $\eta(x,t)$ with respect to x. The mother wavelet used here is Morlet wavelet with $c = 2\pi - 1/2\pi$. The final product is a three-dimensional one: $|S(a,x,t)|^2/a$, where a is the characteristic scale (wavelength). The temporal average of $|S(a,x,t)|^2/a$ is displayed in figure A-6. As displayed there, the variability has a dominant characteristic zonal scale, about 730 km and is much stronger west of the mid-Atlantic ridge. To highlight the variations of energy amplitude with longitude, the temporal average of $|S(a,x,t)|^2/a$ with the characteristic scale $a = 730$ km is plotted in figure A-7, which shows that variability with wavelength about 750 km increases rapidly from 340°E to 300°E and reaches its maximum near 300°E. Figure A-8 displays the time evolution of $|S(a,x,t)|^2/a$ with scale of 730 km. There are two obvious sudden increases of energy in time: one near 900 days and the other near 1600 days. The reason for these two sudden changes requires further study, presumably associated with variations of wind forcing. The corresponding phase change with time and space is shown in figure A-9, which indicates that variability propagates westward systematically. The period is about 200 days and the phase speed is 4.2 cm/s. Figure A-9 shows that although the amplitude of the Rossby waves is much stronger west of topography, the propagation of Rossby wave west of mid-Atlantic ridge originates from the eastern boundary. This suggests that the Rossby waves west of mid-Atlantic ridge is generated along the east boundary and suddenly amplifies over topography.

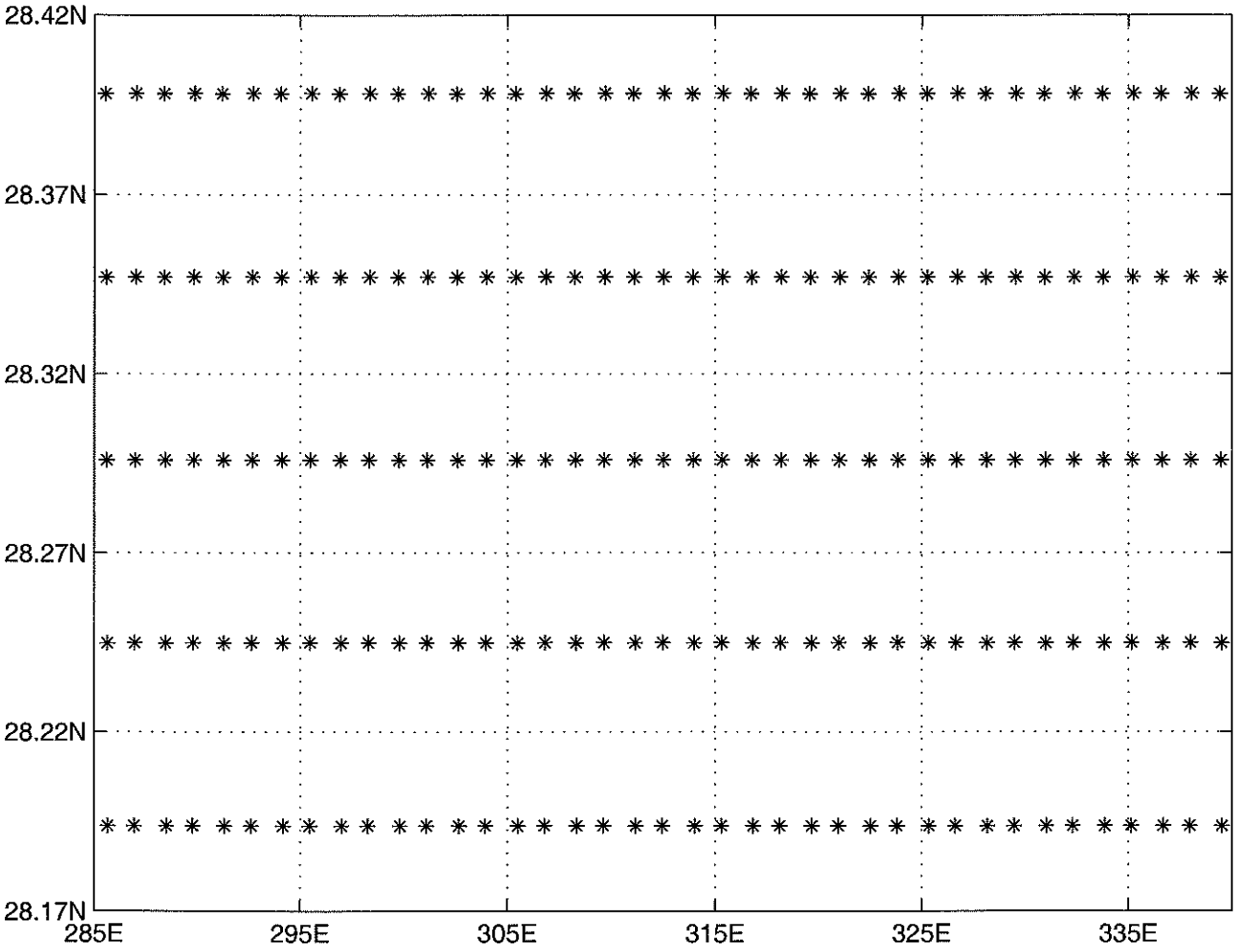

Figure A-1: Array geometry in the area chosen to study. The position of each "sensor" is marked by a star and corresponds to a position on the TOPEX/POSEIDON sub-satellite track.

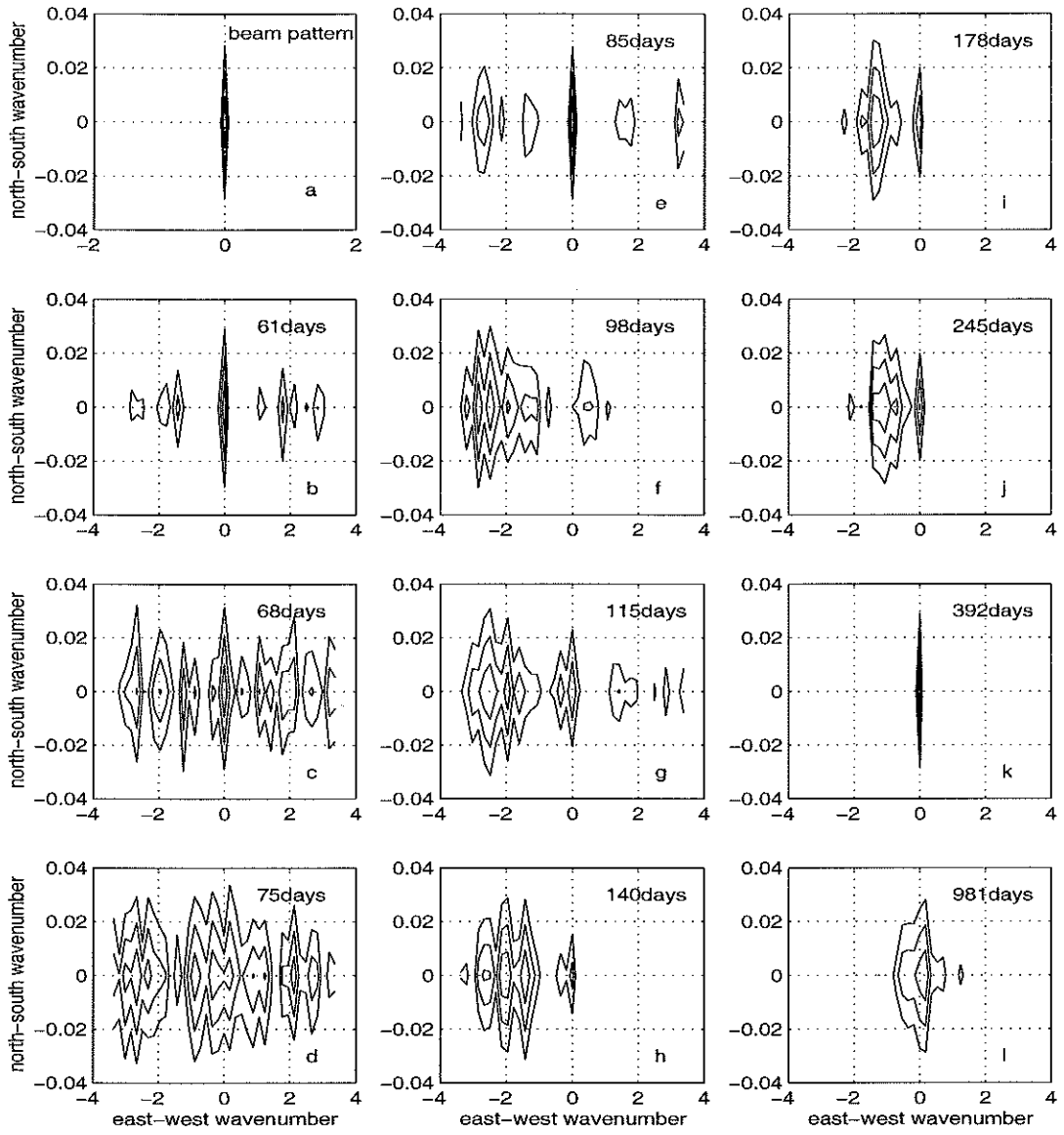

Figure A-2a The beam pattern for the array in Fig. 1. Fig. A-2b-j., The frequency-wavenumber spectra $\Phi(\omega, k, l)$ at periods $T = 2\pi/\sigma$ (in days) (b) 61. (c) 68. (d) 75. (e) 85. (f) 98. (g) 115. (h) 140. (i) 178. (j) 245. (k) 392. and (i) 981 days. The contour levels are the same in each panel and vary from 0 to -0.9 in steps of -0.3. The units of east-west wavenumber and north-south wavenumber are cycles per thousand km and cycles per km, respectively. The observed spectral peak in each frequency band is marked by a star.

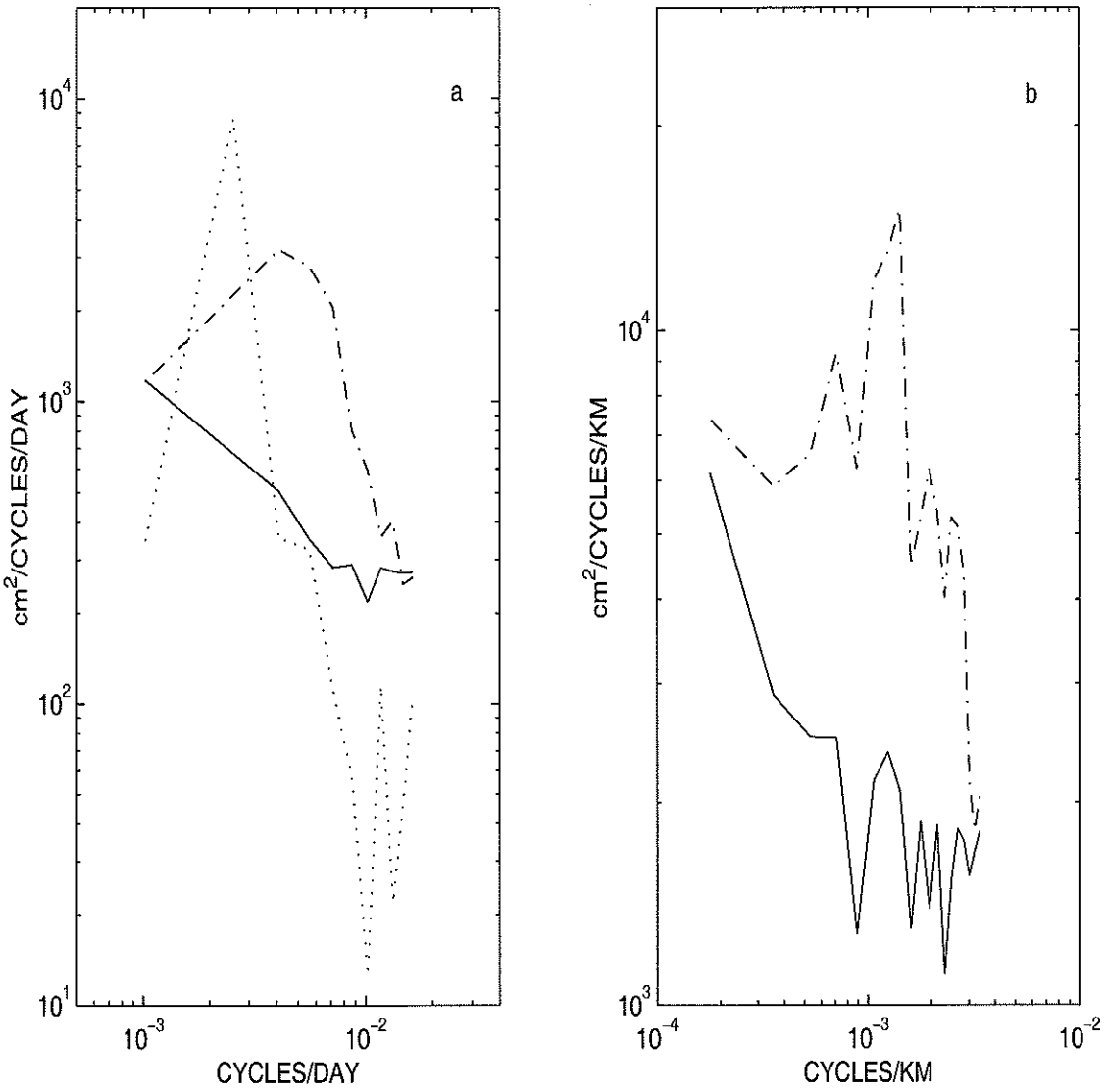

Figure A-3a: The frequency spectrum of eastward-going motions (solid line), westward-going motions (dash-dotted line) and stationary waves (dotted line). The annual peak is most conspicuous in the spectrum of stationary motions. Figure A-3b The wavenumber spectrum of eastward-going motions (solid line) and westward-going motions (dash-dotted line).

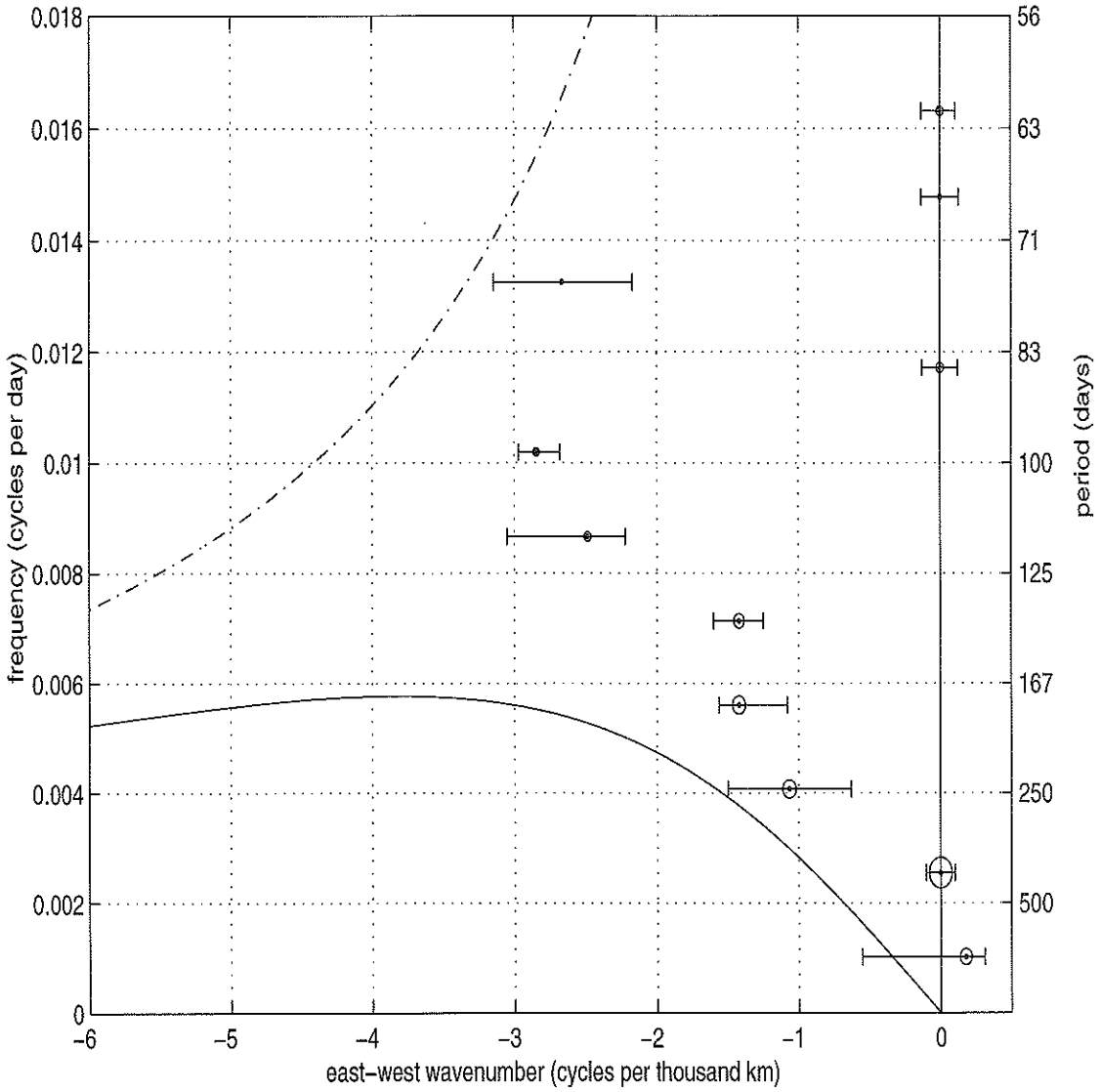

Figure A-4: Frequency-zonal wave number spectra. The peak in each frequency band in Fig. A-3 is indicated by a dot here. The magnitude of each peak is denoted by the size of the circle around that peak. The dash-dot and solid curves denote the barotropic and first baroclinic Rossby wave dispersion curves with $l = 0$, respectively. At the lowest frequencies, the barotropic curve is visually indistinguishable from $k = 0$. Uncertainty estimates are derived from the 95% confidence interval (Capon and Goodman, 1970) for the peak values. The zonal wavenumber interval represents those wavenumbers where the background energy surrounding the apparent peak is larger than or equal to the lower limit of the confidence interval.

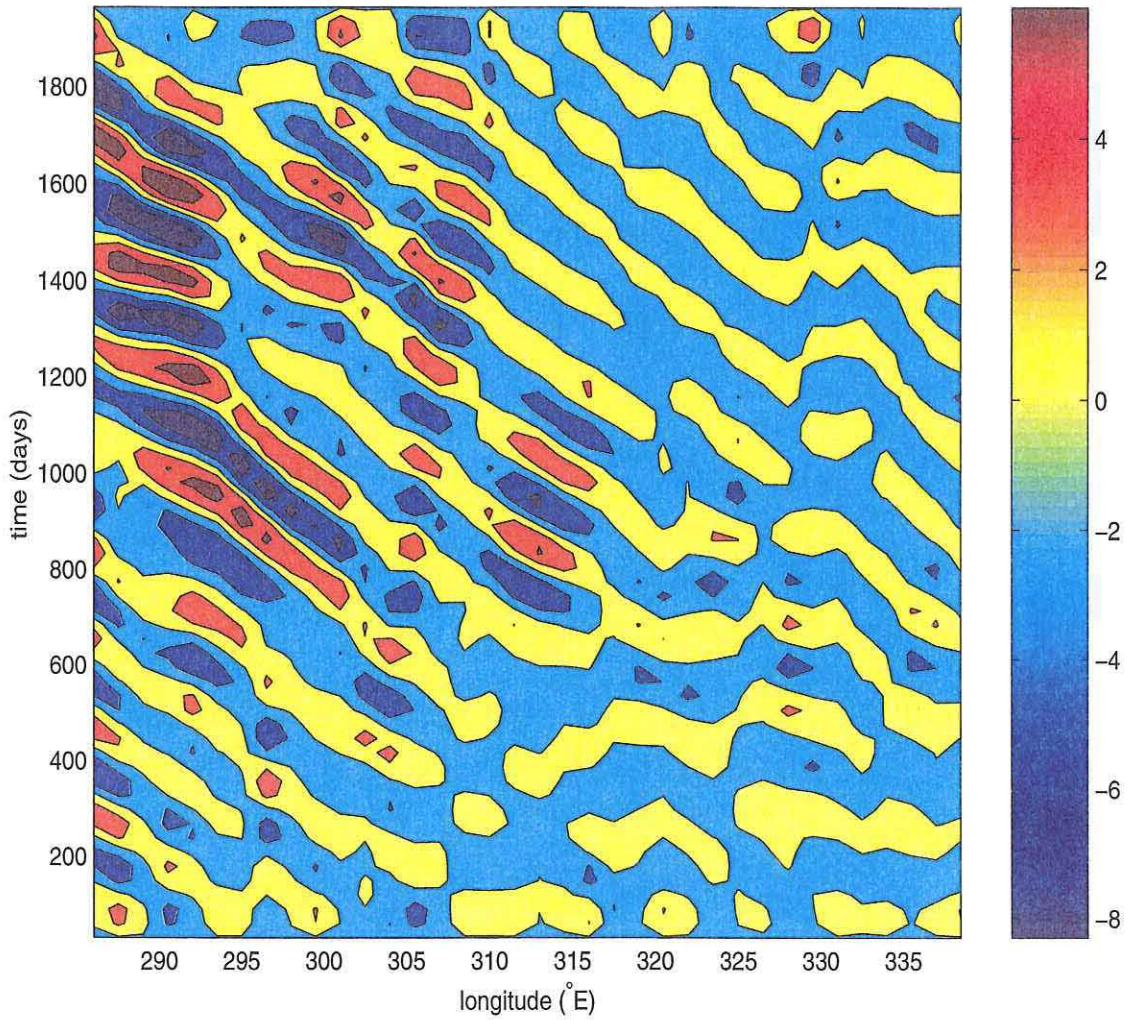

Figure A-5: Hovmoller diagram of filter sea surface height data along 28.3°N.

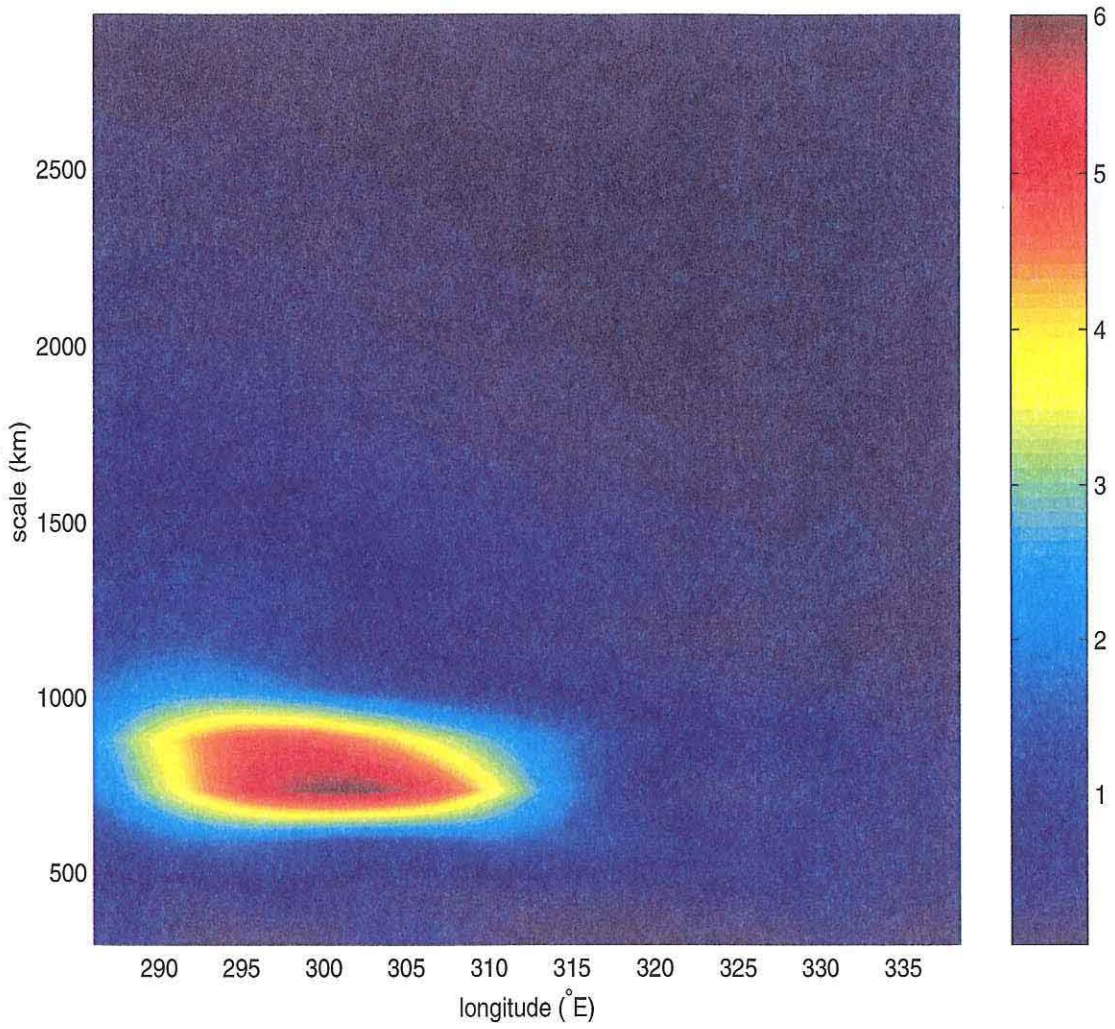

Figure A-6: Temporally averaged energy magnitude.

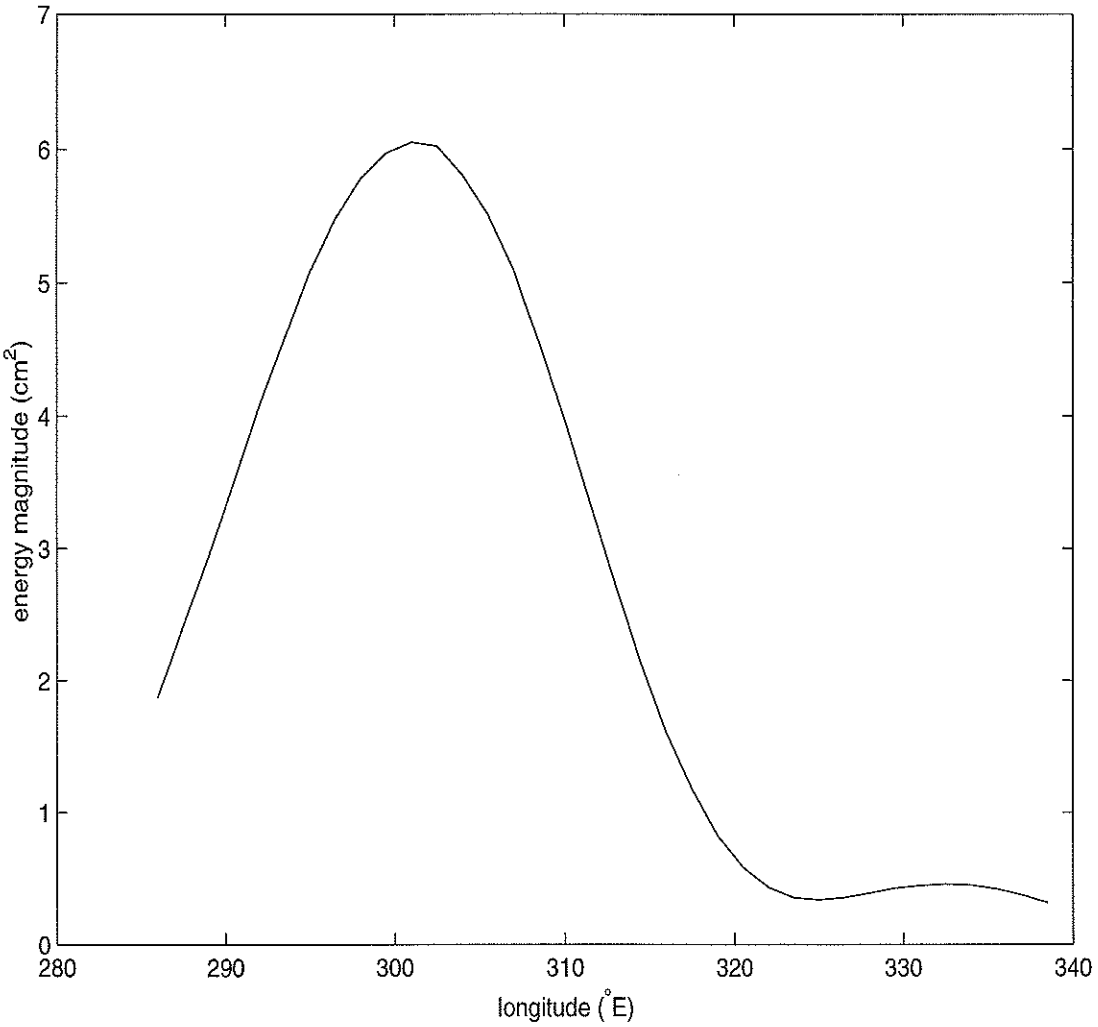

Figure A-7: Temporally averaged energy magnitude of motions with the characteristic zonal scale 730 km.

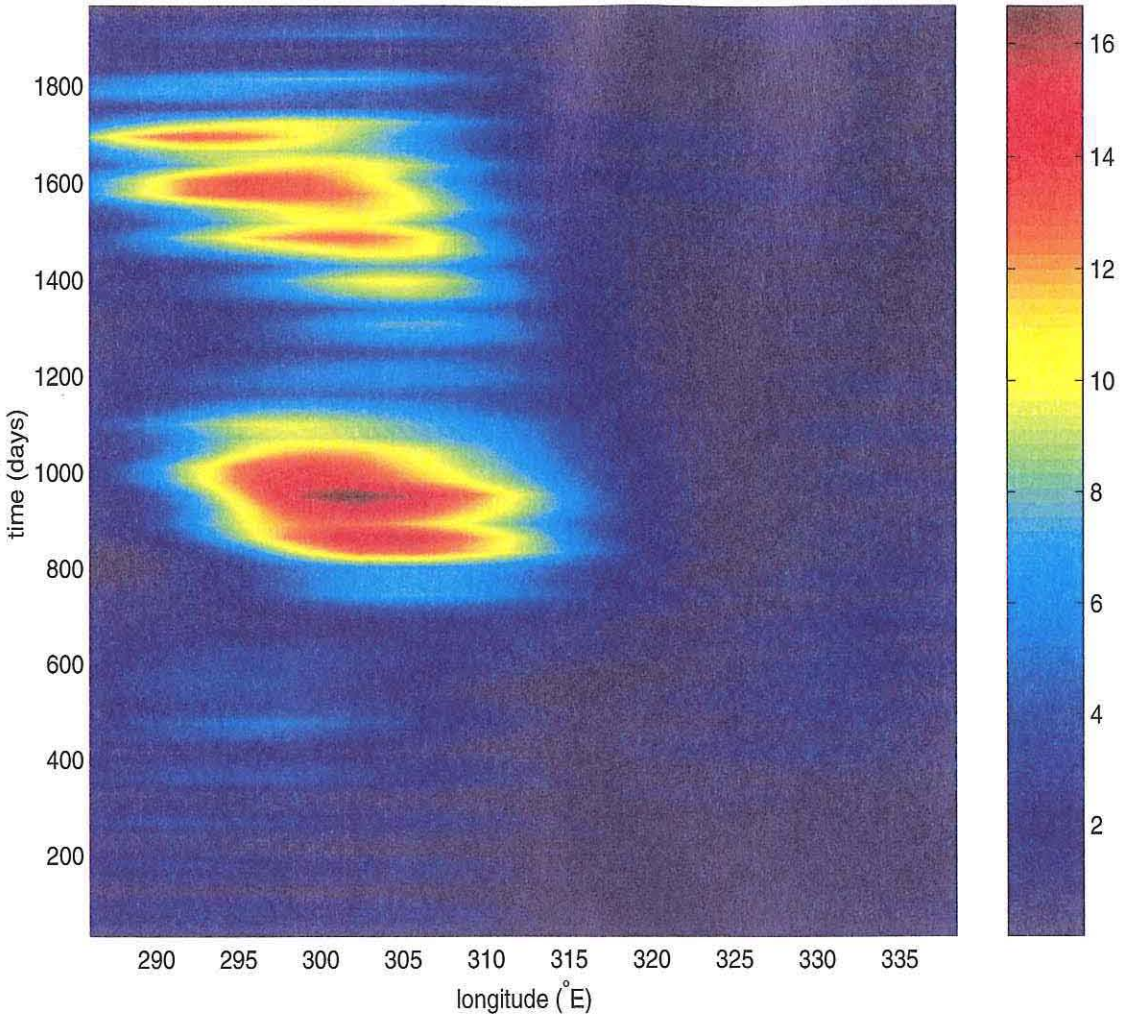

Figure A-8: The temporal evolution of the energy magnitude of motions with the characteristic zonal scale 730 km.

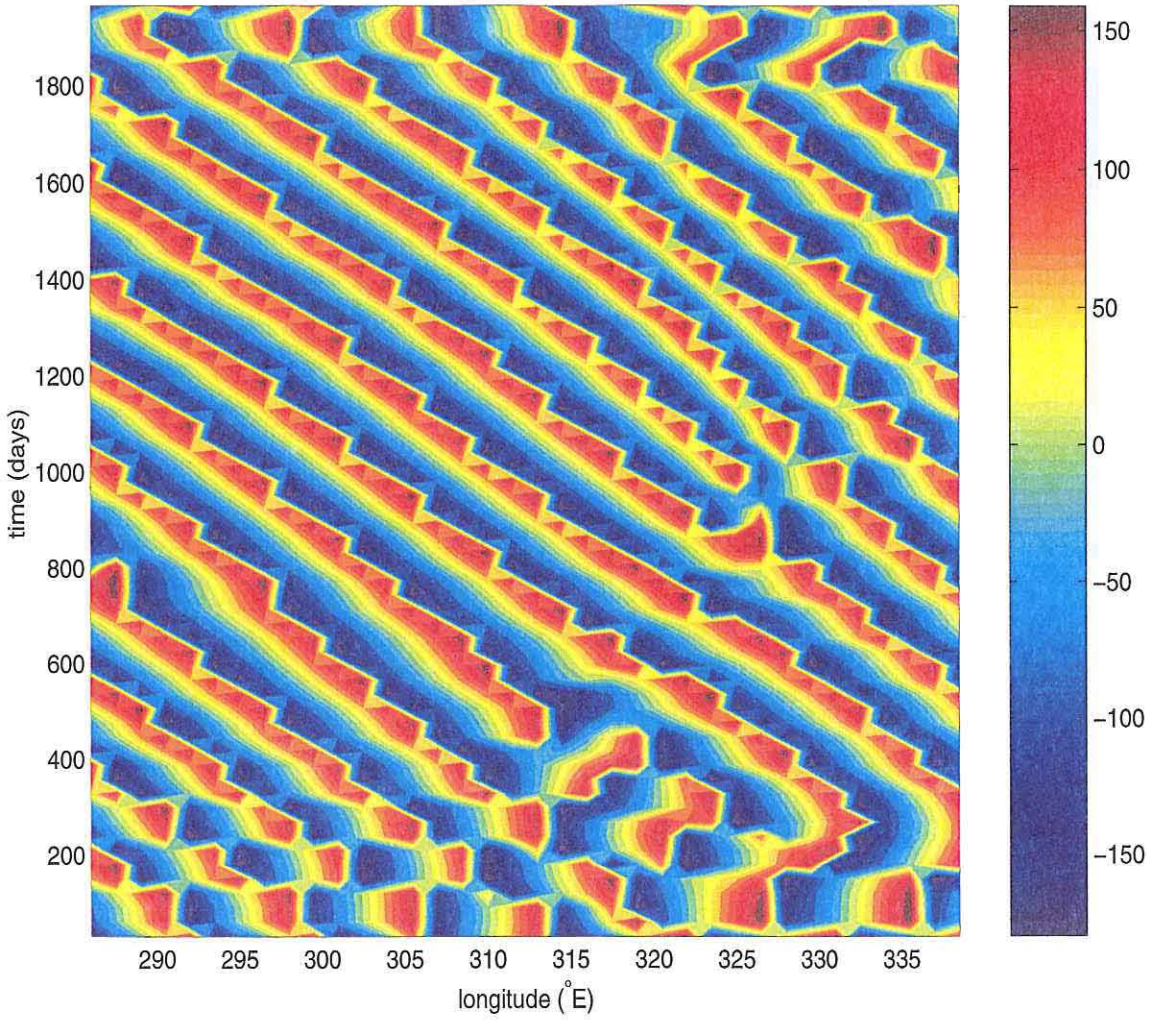

Figure A-9:The temporal evolution of the phase of motions with the characteristic zonal scale 730 km.

Bibliography

[1] Abramowitz, M., and I. A. Stegun, Eds., 1964: *Handbook of Mathematical Functions with formulas, graphs, and mathematical tables.* Washington, U.S. Govt. Print. Off., 1046 pp.

[2] Alaka, H. A., and R. C. Elvander, 1972: Optimum interpolation from observations of mixed quality. *Mon. Wea. Rev.*, 100, 612-624.

[3] Anderson, D. L. T., and A. E. Gill, 1975: Spin-up of a stratified ocean, with application to upwelling. *Deep-sea Res.*, 22, 583-596.

[4] Arbic, B., and B. Owens, 2000: Climatic warming of Atlantic Intermediate Waters. In preparation.

[5] Baggeroer, A., and H. Cox. 1999: Passive sonar limits upon nulling multiple moving ships with large aperture arrays. *Proceedings of the 1999 Asilomar conference of signal and systems.* IEEE press.

[6] Barnier, B., 1988: A numerical study on the influence of the mid-Atlantic ridge on nonlinear first-mode baroclinic Rossby waves generated by seasonal winds. *J. Phys. Oceanogr.*, 18, 417-433.

[7] Batchelor, G. K. (1953): *The theory of homogeneous turbulence.* Cambridge Univ. Press, 197 pp.

[8] Båth, M., 1974: *Spectral Analysis in Geophysics.* Elsevier., New York, 563 pp.

[9] Bretherton, F. P., R. E. Davis and C. B. Faundry, 1976: A technique for objective analysis and design of oceanographic experiments applied to MODE-73. *Deep-sea Res.*, 23, 559-582.

[10] Bretherton, F. P., M. J. McPhaden and E. B. Kraus, 1984: Design studies for climatological measurements of heat storage. *J. Phys. Oceanogr.*, 14, 318-337.

[11] Capon, J., 1969: High resolution frequency-wavenumber spectrum analysis. *Proc. IEEE,* 57, 1408-1418.

[12] Capon, J., R. J. Greenfield, and R. J. Kolker, 1967: Multidimensional maximum-likelihood processing of a large aperture seismic array. *Proc. IEEE,* 55, 192-211.

[13] Capon, J., and N. R. Goodman, 1970: Probability distributions for estimators of the frequency-wavenumber spectrum. *Proc. IEEE,* 58, 1785-1786.

[14] Charney, J. G., 1971: Geostrophic turbulence. *J. Atmos. Sci.*, 28, 1087-1095.

[15] Chelton, D. B., and M. G. Schlax, 1996: Global observations of oceanic Rossby waves. *Science,* 272, 234-238.

[16] Chelton, D. B., R. A. de Szoeke, M. G. Schlax, K. El Naggar, and N. Siwertz, 1998: Geographical variability of the first baroclinic Rossby radius of deformation. *J. Phys. Oceanogr.*, 28, 433-460.

[17] Cipollini, P., D. Cromwell, M. S. Jones, G. D. Quartly and P. G. Challenor, 1997: Concurrent altimeter and infrared observations of Rossby wave propagation near 34°N in the North Atlantic. *Geophys. Res. Lett.*, 24, 889-892.

[18] Corrsin, S. 1959: Progress report on some turbulent diffusion research. *Advances in Geophysics.*, 6, Academic Press, NY, 161-162.

[19] Davis, R. E., 1981: On relating Eulerian and Lagrangian velocity statistics: single particles in homogeneous flows. *J. Fluid Mech.*, 114, 1-26.

[20] Davis, R. E., 1985: Drifter observations of coastal surface currents during CODE: the statistical and dynamical views. *J. Geophys. Res.*, 90, 4756-4772.

[21] de Szoeke R. A., and D. Chelton, 1999: The enhancement of planetary wave speeds by homogeneous potential vorticity layers. *J. Phys. Oceanogr.*, 29, 500-511.

[22] Dewar, W. K., 1998: On "too fast" baroclinic planetary waves in the general circulation. *J. Phys. Oceanogr.*, 28, 1739-1758.

[23] Eriksen, C. C., 1981: Deep currents and their interpretation as equatorial waves in the western Pacific Ocean. *J. Phys. Oceanogr.*, 11, 48-70.

[24] Farge, M., 1992: Wavelet transforms and their applications to Turbulence. *Annu. Rev. Fluid Mech.*, 24, 395-457.

[25] Fjörtoft, R., 1953: On the changes in the spectral distribution of kinetic energy for two-dimensional, nondivergent flow. *Tellus*, 5, 225-230.

[26] Frankignoul, C., and K. Hasselmann, 1976: Stochastic climate models. Part 2, Application to sea-surface temperature anomalies and thermocline variability. *Tellus*, 29, 289-305.

[27] Frankignoul, C., and P. müller, 1979: Quasi-geostrophic response of an infinite beta-plane ocean to schochastic forcing by the atmosphere. *J. Phys. Oceanogr.*, 9, 104-127.

[28] Fu, L.-L., and G. Flierl, 1980: Nonlinear energy and enstrophy transfers in a realistically stratified ocean. *Dyn. Atmos. Oceans.*, 4, 219-246.

[29] Fukumori, I. R. Raghunath, and L.-L. Fu, 1998: Nature of global large-scale sea level variability in relation to atmospheric forcing: a modeling study. *J. Geophys. Res.*, 103, 5493-5312.

[30] Ganachaud, S. A., 1999: Large-scale oceanic circulation and fluxes of freshwater, heat, nutrients and oxygen. Ph.D. thesis MIT/WHOI Joint Program, 266 pp.

[31] Gandin, L. S., 1963: *Objective Analysis of Meteorological Fields* Leningrad, Gidrometeorizdat, 266 pp.

[32] Garrett, C., and W. Munk, 1972: Space-time scales of internal waves. *Geophys. Fluid Dyn.,* 2, 225-264.

[33] Garrett, C., and W. Munk, 1975: Space-time scales of internal waves–a progress report. *J. Geophys. Res.,* 80, 291-297.

[34] Gill, A. E., 1982: *Atmosphere-Ocean Dynamics.* Academic Press, 662 pp.

[35] Gilson, J., D. Roemmich, B. Cornuelle and L. -L. Fu, 1998: The relationship of TOPEX/POSEIDON altimetric height to steric height and circulation in the North Pacific. *J. Geophys. Res.,* 103, 27947-27965.

[36] Hasselmann, K., 1976: Stochastic climate models. Part I, theory. *Tellus,* 28, 473-485.

[37] Kagan, R. L., 1997: *Averaging of meteorological fields.* Kluwer Academic Publishers, 279 pp.

[38] Kessler, W. S., 1990: Observations of long Rossby waves in the northern tropical Pacific. *J. Geophys. Res.,* 95, 5183-5217.

[39] Killworth, P. D., D. B. Chelton, and R. A. de Szoeke, 1997: The speed of observed and theoretical long extra-tropical planetary waves. *J. Phys. Oceanogr.,* 27, 1946-1966.

[40] King, C., D. Stammer, and C. Wunsch, 1994: *The CMPO/MIT TOPEX/-POSEIDON altimetric data set.* Center for Global Change Science, Massachusetts Institute of Technology, Rep. 30, 33 pp. plus color plates.

[41] Kraichnan, R. H., 1967: Inertial ranges in two dimensional turbulence. *Phys. Fluids,* 10, 1417-1423.

[42] Kumar, P., and E. Foufoula-Geogiou, 1997: Wavelet analysis for geophysical applications. *Rev. Geophys.*, 35, 385-412.

[43] Lacoss, R. T., 1971: Data adaptive spectral analysis methods. *Geophysics*, 36, 661-675.

[44] Le Traon, P. Y., F. Nadal, N. Ducet, 1998: An improvement mapping method of multi-satellite altimeter data. *J. Atm. Ocean. Techn.*, 25, 522-534.

[45] Lilly, D. K., 1969: Numerical simulation of two-dimensional turbulence. *Phys. Fluids*, 12, 240-249.

[46] Lundgren T. S. and Y. B. Pointin, 1976: Turbulent self-diffusion. *Phys. Fluids*, 19, 355-358.

[47] McWilliams, J. C. and H. H. S. Chow, 1981: Equilibrium geostrophic turbulence I: A reference solution in a $\beta-$plane channel. *J. Phys. Oceanogr.*, 11, 921-949.

[48] Meyers, S. D., B. G. Kelly and J. J. O'Brien, 1993: An introducation to wavelet analysis in oceanography and meteorology: with application to the dispersion of Yanai waves. *Mon. Wea. Rev.*, 121, 2858-2866.

[49] Middleton, J. F., 1985: Drifter spectra and diffusivities. *J. Mar. Res.*, 43, 37-55.

[50] MODE Group, The 1978: The Mid-ocean dynamics experiment. *Deep-Sea Res.*, 25, 859-910.

[51] Munk, W., P. F. Worcester and C. Wunsch, 1996: *Ocean Acoustic Tomography.* Cambridge Univ. Press, 433 pp.

[52] Papoulis, A., 1991: *Probability, random variables, and stochastic processes.* McGraw-Hill, New York, 666 pp.

[53] Parrilla, G., Lavin, A., Bryden, H., Garcia, M., and R., Millard, 1994: Rising temperature in the subtropical North Atlantic Ocean over the past 35 years. *Nature*, 369, 48-51.

[54] Pedlosky J., 1987: *Geophysical fluid dynamics.* 2nd ed., Springer-Verlag, 710 pp.

[55] Pedlosky J., L. J. Pratt, M. A. Spall, and K. R. Helfrich, 1997: Circulation around islands and ridges. *J. Mar. Res.*, 55, 1199-1251.

[56] Pedlosky J., and M. A. Spall, 1999: Rossby normal modes in basins with barriers. Submitted for publication.

[57] Percival, D. B. and A. T. Walden, 1993: Spectral Analysis for Physical Applications. Multitaper and Conventional Univariate Techniques. Cambridge Univ. Press, Cambridge, 583 pp.

[58] Pillai, S. U., 1989: *Array signal processing.* Springer-Verlag, New York. 221 pp.

[59] Platzman, G. W., 1968: The Rossby wave. *Q. J. Roy. Met. Soc.,* 94, 225-246.

[60] Qiu, B., W. Miao, and P. Müller, 1997: Propagation and decay of forced and free baroclinic Rossby waves in off-equatorial oceans. *J. Phys. Oceanogr.,* 27, 2405-2417.

[61] Rhines, P. B., 1975: Waves and turbulence on a β-plane. *J. Fluid Mech.*, 69, 417-443.

[62] Roemmich, D., and B. Cornuelle, 1990 : Observing the fluctuations of gyre-scale ocean circulation: a study of the subtropical South Pacific. *J. Phys. Oceanogr.,* 20, 1919-1930.

[63] Roemmich, D., and C. Wunsch, 1984: Apparent changes in the climatic state of the deep North Atlantic Ocean. *Nature*, 307, 447-450.

[64] Saffman. P. G., 1963: An approximate calculation of the Lagrangian autocorrelation coefficient for stationary, homogeneous turbulence. *Appl. Sci. Res.,* A11, 245-255.

[65] Schmitz, W. J., Jr., 1978: Observations of the vertical distribution of low frequency kinetic energy in the western North Atlantic. *J. Mar. Res.,* 36, 295-310.

[66] Schmitz, W. J., Jr., 1988: Exploration of the eddy field in the mid-latitude North Pacific. *J. Phys. Oceanogr.*, 18, 459-468.

[67] Schopf, P., D. L. T. Anderson, and R. Smith, 1981: Beta-dispersion of low frequency Rossby waves. *Dyn. Atmos. Oceans,* 5, 187-214.

[68] Stammer,D., 1997a: Global characteristic of ocean variability estimated from regional TOPEX/POSEIDON altimeter measurements. *J. Phys. Oceanogr.*, 27, 1743-1770.

[69] Stammer, D. 1997b: Steric and wind-induced changes in TOPEX/POSEIDON large-scale sea surface topography observations. *J. Geophys. Res.*, 102, 20,987-21,009.

[70] Veronis, G., and H. Stommel, 1956: The action of variable wind stresses on stratified ocean. *J. Mar. Res.*, 15, 43-75.

[71] Wang, L., C. Koblinsky, S. Howden, and B. Beckley, 1998: Large-scale Rossby wave in the South Pacific. *Geophys. Res. Lett.*, 25, 179-182.

[72] Weinstock, J. 1976: Lagrangian-Eulerian relations and the independence approximation. *Phys. Fluids,* 19, 1702-1711.

[73] White, W. B., 1977: Annual forcing of baroclinic long waves in the tropical North Pacific. *J. Phys. Oceanogr.*, 7, 50-61.

[74] White, W. B., 1995: Design of a global observing system for gyre-scale upper ocean temperature variability. *Prog. Oceanog.*, 36, 169-217.

[75] White, W. B., and R. L. Berstein, 1979: Design of an oceanographic network in the midlatitude North Pacific. *J. Phys. Oceanogr.*, 9, 592-606.

[76] Willebrand, J., S. G. H. Philander, and R. C. Pacanowski, 1980: The oceanic response to large-scale atmospheric disturbances. *J. Phys. Oceanogr.*, 10, 411-429.

[77] Willsky, A. S., G. W. Wornell, and J. H. Shapiro, 1998: Stochastic processes, detection and estimation. Course notes. 314 pp.

[78] Wunsch,C. 1981: Low-frequency variability in the sea. In: *Warren,B.A., and C. Wunsch (Eds.):* Evolution of physical oceanography. MIT-Press, Cambridge, Mass.

[79] Wunsch,C. 1996: *The ocean circulation inverse problem.* Cambridge Univ. Press, Cambridge, 442 pp.

[80] Wunsch,C. 1997: The vertical partition of oceanic horizontal kinetic energy. *J. Phys. Oceanogr.*, 27, 1770-1794.

[81] Wunsch, C., 1999a: Where do ocean eddy heat fluxes matter? *J. Geophys. Res.*, 104, 13,235-13,249.

[82] Wunsch, C., 1999b: A summary of North Atlantic baroclinic variability. *J. Phys. Oceanogr.*, 29, 3161-3166.

[83] Wunsch, C., and A. E. Gill, 1976: Observations of equatorially trapped waves in Pacific sea level variations. *Deep Sea Res.*, 23, 371-390.

[84] Wunsch, C. and R. Hendry, 1972: Array measurements of the bottom boundary layer and internal wave field on the continental slope. *Geophys. Fl. Dyn.*, 4, 101-145.

[85] Wunsch, C., and D. Stammer, 1995: The global frequency-wavenumber spectrum of oceanic variability estimated from TOPEX/POSEIDON altimeter measurements. *J. Geophys. Res.*, 100, 24,895-24,910 .

[86] Wunsch, C., and D. Stammer, 1997: Atmospheric loading and the oceanic "inverted barometer" effect. *Rev. Geophys.*, 35, 79-107.

[87] Wunsch. C., and D. Stammer, 1998: Satellite altimetry, the marine geoid and the oceanic general circulation. *Ann. Revs. Earth Plan. Scis.*, 26, 219-253.

[88] Zang, X., 1998: Space and time scales of low frequency variability in the ocean, S.M. thesis, MIT/WHOI Joint Program, 120 pp.

[89] Zang, X. and C. Wunsch, 1999: The observed dispersion relation for North Pacific Rossby wave motions. *J. Phys. Oceanogr.*, 29, 2183-2190.